UNIVERSITY OF MARIBOR
FACULTY OF MECHANICAL ENGINEERING

Doctoral dissertation

APPLICATION OF NORMALIZATION METHOD TO FRACTURE TOUGHNESS TESTING OF WELDS WITH PRONOUNCED STRENGTH HETEROGENEITY

September, 2022 Primož Štefane

UNIVERSITY OF MARIBOR

FACULTY OF MECHANICAL ENGINEERING

Doktorska disertacija

UPORABA NORMALIZACIJSKE METODE ZA TESTIRANJE LOMNE ŽILAVOSTI ZVARNIH SPOJEV Z IZRAZITO HETEROGENO TRDNOSTJO

Doctoral dissertation

APPLICATION OF NORMALIZATION METHOD TO FRACTURE TOUGHNESS TESTING OF WELDS WITH PRONOUNCED STRENGTH HETEROGENEITY

September, 2022	Author:	Primož ŠTEFANE
	Mentor:	prof. dr. Nenad GUBELJAK
	Co-mentor:	prof. dr. Stijn HERTELÉ
	UDK:	620.178.2:621.791.053(043.3)

ACKNOWLEDGEMENTS

I express my sincere gratitude to my supervisors Prof. Nenad Gubeljak and Prof. Stijn Hertelé who continually extended their guidance and supervision for successful accomplishment of my doctoral thesis. Without their expertise and competence, this work would not have been possible. I would like to thank the funding organization “Slovenian Research Agency” (“Agencija za Raziskovalne Zadeve Republike Slovenije - ARRS”) who made this work possible by allocating the funds to undertake this research (grant no. N2-0030). I am highly grateful to our collaborations with Prof. Stijn Hertelé, Prof. Wim De Waele and Mr. Sameera Naib for their contribution towards this project.

I am thankful to Mr. Anton Kresnik, prof. Tomaž Vuherer and Vili Šprah for offering technical support and assistance for conducting experiments during this research. I am thankful to prof. Jožef Predan and doc. Matej Borovinšek for offering counselling on finite element analysis.

During the undertaking of this work, I was consistently encouraged and motivated by my colleagues doc. Mitja Kastrevc, Marjana Milković, Lucija Jurko, Fernanda Tello, Filip Jerenec, Robi Kuserbanj, Matej Vesenjak and Peter Čakš. My special acknowledgment to Gregor Strniša and Vesna Cacio for their assistance in editing of this manuscript.

I praise my friends – Martin Rakovnik, Jana Boškovič, Matej Slatinek, Alja Parežnik Slatinek, Barbara Furman, Filip Mlinšek, Anna Ropret, Tomislav Pučnik and Timi Karner for their consistent support and companionship.

My deepest gratitude to my family for their support and encouragement in my everyday life. Without expertise of my father Srečko Štefane and goodness of my mother Zdenka Štefane I would not have become who I am. A special gratitude goes to my sister Vita Štefane, who reminded me every day to have a positive look on life and not to grow too old too soon.

UPORABA NORMALIZACIJSKE METODE ZA TESTIRANJE LOMNE ŽILAVOSTI ZVARNIH SPOJEV Z IZRAZITO HETEROGENO TRDNOSTJO

Ključne besede: zvar, trdnostno neujemanje, lom, normalizacijska metoda, plastični korekcijski faktorji, vpenjalna priprava, SE(B) preizkušanec, J-R odpornostna krivulja

POVZETEK

V doktorski disertaciji so predstavljeni rezultati obsežnega programa lomno mehanskih preizkusov zvarov z izrazito heterogenimi mehanskimi lastnostmi. Namen tega eksperimentalnega programa je bil določitev lomne žilavosti za heterogene zvare. Uporaba standardnih metod za določitev lomne žilavosti v takšnem primeru daje precenjeno ali podcenjeno lomno žilavost zvarov, kar vodi do napak pri oceni celovitosti konstrukcij. To je poseben izziv, ki do danes ni povsem razrešen. Razlog je ta, da regije zvara z različnimi mehanskimi lastnostmi vplivajo na razvoj polja deformacij na konici razpoke in posledično na gonilno silo za razvoj razpoke. Z namenom, da se ta izziv reši, so bili zvari najprej detajlno preučeni, kot je opisano v 2. poglavju te disertacije.

Pri eksperimentalnem delu, ki je bilo opravljeno v sklopu te raziskave, so bili najprej pripravljeni vzorčni zvari. Ti so bili izdelani z varjenjem plošč iz nizko legiranega visoko trdnostnega jekla S690 QL, ki se v industriji pogosto koristi za gradnjo zahtevnih konstrukcij. Za varjenje je bil uporabljen MAG postopek. Posebna značilnost izdelanih zvarov je ta, da sta pri izdelavi bili uporabljeni dve varilni žici, ki sta se razlikovali po mehanskih lastnostih. Prva varilna žica je imela višjo mejo plastičnosti, druga pa nižjo v primerjavi z osnovnim materialom. Meje plastičnosti uporabljenih varilnih žic so se v tem primeru razlikovale več kot 30 % glede na mejo plastičnosti osnovnega materiala. Na ta način so bile v vzorčnih zvarih umetno poustvarjene povečane neenakosti v trdnosti posamičnih regij zvara. Natančneje, pol žleba, ki je bil izdelan na ploščah pred varjenjem, je bilo polnjenega z varilno žico, ki ima višjo trdnost. Druga polovica žleba je bila polnjena z varilno žico, ki ima nižjo trdnost. Takšno stanje se v praksi pogosto ustvari pri popravljanju obstoječih zvarov, kjer se za popravilo uporabi drugačna elektroda ali varilna žica kot za izdelavo zvara. Za primerjavo so bili izdelani še

zvari, ki so bil polnjeni samo z eno varilno žico. Izdelani zvari so bili detajlno preučeni. Najprej so bile opravljene metalografske preiskave, ki so pokazale na povečano vsebnost bainita in martenzita v mikrostrukturi. Omenjena mikrokonstituenta sta posledica kompleksne termalne zgodovine zaradi varjenja z več varki in pomembno vplivata na trdnost zvarnega materiala. V naslednjem koraku so bile opravljene meritve trdote po Vickersu na vzorcu zvara. Opravljene meritve so pokazale velika nihanja trdote med regijami v osnovnem stanju in pogretimi regijami posamičnih varkov. Povečana trdota je bila opažena tudi v toplotno vplivanem področju (TVP). To nakazuje, da je med varjenjem prišlo do utrjevanja TVP. Dodatno so bile določene lokalne mehanske lastnosti v posameznih regijah zvara z nateznim testiranjem miniaturnih preizkušancev. Preizkusi so pokazali, da mehanske lastnosti, v smislu meje plastičnosti in natezne trdnosti, nihajo v zvaru skladno z izmerjeno trdoto. Hkrati so rezultati preizkusov pokazali, da material zvara z višjo trdnostjo kaže dodatno utrjevanje v pogretem področju. Nasprotno je bilo opaženo pri testiranju materiala zvara z nižjo trdnostjo. V tem primeru pride do mehčanja materiala v pogretem področju. Največji meji plastičnosti in natezne trdnosti sta bili izmerjeni v finozrnatem delu TVP. Dodatno so bili izvedeni še natezni preizkusi standardnih nateznih preizkušancev valjaste oblike. Ti preizkusi so podali povprečne mehanske lastnosti materiala v zvaru in osnovnega materiala. Rezultati teh preizkusov so pokazali relativno dobro ujemanje z rezultati miniaturnih nateznih preizkusov. To pomeni, da je za poenostavljene analize heterogenih zvarov možno koristiti povprečne mehanske lastnosti za izdelavo materialnih modelov, ki se kasneje uporabljajo v simulacijah po metodi končnih elementov ali v analitičnih modelih za oceno celovitosti konstrukcij v skladu s standardom BS 7910. V naslednjem koraku so bili izvedeni preizkusi udarne žilavosti po Charpy metodi. Ti preizkusi so bili izvedeni na tritočkovnih upogibnih preizkušancih, ki so bili izrezani iz visoko in nizko trdnostnih delov zvara ter iz osnovnega materiala. Rezultati so pokazali, da zvarni material v povprečju izkazuje nekoliko nižjo udarno žilavost kot osnovni material. Izjema so bili preizkušanci, v katerih je razpoka rastla iz nizko trdnostnega področja v visoko trdnostno področje. Ti so pokazali višjo lomno žilavost kot osnovni material. Dejstvo, da je bila hitrost udarnega kladiva dokaj konstantna za vse izvedene udarne preizkuse ter da udarni preizkušanci z začetno razpoko v nizko trdnostnem področju absorbirajo večjo količino udarne energije, nakazuje na zmanjšano gonilno silo za razvoj razpoke. Ta ocena je kvalitativna in potrebuje kvantitativno potrditev z izvedbo lomno mehanskih preizkusov in izmerjeno lomno žilavostjo. Lomno mehanski preizkusi so bili izvedeni s preizkušanjem tritočkovnih upogibnih SE(B) preizkušancev z bočno zarezo in predstavljajo jedro te raziskave. SE(B) preizkušanci so imeli *zarezo izdelano iz smeri temena v centralni ravnini, glede na presek zvara. Obremenjeni so bili v kvazistatičnem režimu s konstantno hitrostjo obremenjevanja. Stabilna rast razpoke je bila ocenjena s pomočjo normalizacijske metode v skladu s standardom ASTM E1820. Ta metoda omogoča oceno rasti razpoke na osnovi izmerjene začetne in končne dolžine razpok na prelomnih površinah preizkušancev po opravljenih preizkusih. Pri tem je potrebno uporabiti pravilno kalibrirano korelacijsko funkcijo za oceno stabilnega prirastka. Izvajanje lomno mehanskih preizkusov na ta način je precej enostavnejše kot z uporabo klasičnih metod za merjenje stabilne rasti razpoke med preizkusom. Primera takšnih metod sta metoda delnega razbremenjevanja in metoda padca električnega potenciala. Prva zahteva številna delna razbremenjevanja SE(B) preizkušanca med izvajanjem lomno mehanskega preizkusa, pri drugi pa je potrebna draga in kompleksna oprema, ki vključuje napetostni izvor in ustrezne senzorje za merjenje padca električnega potenciala zaradi rasti razpoke v kovinskem preizkušancu. Nekatere študije, ki so omenjene v prvem in drugem poglavju te doktorske disertacije, so pokazale, da pri lomno mehanskem testiranju homogenih materialov daje normalizacijska metoda rezultate, ki se dobro ujemajo z rezultati metode delnega razbremenjevanja. Hkrati je bilo pokazano, da je možno normalizacijsko metodo uporabiti za testiranje zvarov, pri čemer se rezultati razlikujejo manj kot 10 % v primerjavi z metodo delnega razbremenjevanja. Vendar, normalizacijska metoda do danes še ni bila uporabljena na zvarih, izdelanih iz dveh dodajnih materialov, ki imajo izrazito heterogene mehanske lastnosti. V tem primeru je potrebno kalibrirati korekcijske faktorje η_{pl}, λ in γ_{pl} za pravilno oceno lomne žilavosti oz. J-integrala za zvare z izrazito heterogenimi mehanskimi lastnostmi. Omenjene faktorje je bilo potrebno kalibrirati tudi zaradi uporabe nestandardnih podpor preizkušanca med lomno mehanskim preizkusom. Te podpore so imele fiksne valje s premerom 25 mm. V nasprotju standard ASTM E1820 zahteva uporabo podpor z drsnimi valji, ki imajo premer 10 mm ali manj glede na dimenzije testiranih SE(B) preizkušancev.*

Četrto poglavje opisuje kalibracijo korekcijskih faktorjev η_{pl}, λ in γ_{pl} za izračun J-integrala. Kalibracija je bila narejena s parametričnimi simulacijami po metodi končnih elementov. Za ta namen so bili ustvarjeni ravninski numerični modeli, ki upoštevajo ravninsko deformacijsko stanje. Razlog za tako poenostavljene modele je ta, da se analitični preračuni J-integrala po ASTM E1820 nanašajo na ravninsko deformacijsko stanje, kar daje nekoliko bolj konservativne rezultate. V numeričnih modelih so bile kreirane stacionarne razpoke, z radijem konice 0.0025 mm. Okoli konice je bilo ustvarjenih približno 80 kontur, katerih velikost se je postopno večala.

v numeričnih modelih je bil uporabljen pristop majhnih deformacij, ki pospeši konvergiranje J-integrala po nastavljenih konturah, vendar daje nepravilne deformacije na konici razpoke. V splošnem se pristop majhnih deformacij priporoča, kadar je iz simulacije potrebno pridobiti zgolj J-integral. V kolikor je potrebno analizirati tudi deformacije in napetosti neposredno ob konici razpoke, se priporoča uporaba pristopa velikih deformacij. Materialni modeli so bili določeni na podlagi opravljenih miniaturnih nateznih preizkusov za TVP in na podlagi standardnih nateznih preizkusov za osnovni material in oba materiala zvara. Oblike zvarov so bile poenostavljene. Na podlagi pridobljenih numeričnih rezultatov so bili kalibrirani korekcijski faktorji η_{pl}, λ *in* γ_{pl}. *Hkrati je bila izvedena analiza vpetosti materiala pred konico razpoke, v smislu triaksialnosti napetostnega polja, ki temelji na razmerju hidrostatične napetosti in ekvivalentne von Misesove napetosti. Navedene napetosti so bile odčitane na ustrezni razdalji pred konico razpoke, na kateri pristop majhnih deformacij ni vplival na napetostno polje. Numerični modeli so bili verificirani na podlagi primerjave pridobljenih numeričnih rezultatov z rezultati drugih študij. Simulacije so bile izvedene za tri konfiguracije podpor in devet konfiguracij zvarov. Najprej je bil preučen vpliv podpor. Pri tem je bil modeliran SE(B) preizkušanec iz osnovnega materiala. Pridobljeni rezultati so pokazali, da fiksno vpetje valjev in povečanje premera valjev (kar ustreza dejanskim uporabljenim podporam) zniža preračunan J-integral do približno 12 %. To pomeni, da preračun J-integrala po standardu ASTM E1820 daje lomno žilavost, ki je precenjena do 12 %, v primeru uporabe opisanih nestandardnih podpor pri lomno mehanskem preizkusu. Hkrati je v tem koraku bila izvedena analiza konvergiranja J-integrala. Ta je pokazala, da se vrednosti J-integrala iz konture, oddaljene 0.5 mm od konice razpoke, in iz konture, oddaljene 2.0 mm od konice razpoke, razlikujejo manj kot 1.5 %. Zato je bila kontura, na razdalji 0.5 mm od konice razpoke, izbrana kot merodajna v vseh nadaljnjih simulacijah. Prednost manjše konture je tudi v tem, da je možno konico razpoke modelirati bližje k meji med materialnimi regijami v zvaru. V tem primeru se bo manjša kontura v celoti nahajala v eni materialni regiji, ki je lokalno homogena. Analize zvarov iz enega materiala in brez TVP so pokazale, da pride do plastične deformacije v osnovnem materialu, če ima material zvara višjo trdnost. To zniža vpetost materiala pred konico razpoke in posledično tudi gonilno silo za razvoj razpoke. Nasprotno je bilo opaženo pri materialu zvara z nižjo trdnostjo. V tem primeru osnovni material z višjo trdnostjo deluje kot pregrada, ki omeji razvoj plastične cone na material zvara. To zviša hidrostatični tlak in posledično tudi vpetost materiala pred konico razpoke. Obnašanje visoko trdnostnega zvara se v celoti spremeni, če je v numeričnem modelu upoštevano TVP z višjo trdnostjo. V tem primeru,*

TVP zadrži plastično deformacijo pretežno v zvaru, kar se opazi v povečanju triaksialnosti in gonilne sile za razvoj razpoke. Izračunan J-integral je, v primerjavi s standardno rešitvijo, ob upoštevanju TVP nižji za 8.3 % v primeru visoko trdnostnega zvara ter za 8.9 % v primeru nizko trdnostnega zvara. To pomeni, da je TVP potrebno upoštevati pri kalibraciji η_{pl}*,* λ *in* γ_{pl} *faktorjev v vseh nadaljnjih primerih. V naslednjem koraku so bili modelirani zvari, izdelani iz kombinacije visoko in nizko trdnostnih dodajnih materialov. V primeru, ko razpoka raste iz visoko trdnostnega materiala v nizko trdnostni material, je bilo opaženo povišanje gonilne sile za razvoj razpoke in vpetosti materiala, ko se je konica razpoke nahajala v bližini meje med obema materialoma. Zaradi kombinacije dveh različnih materialov v zvaru je preračunan J-integral višji do 17.2 % v primerjavi z osnovnim materialom. Nasprotno je bilo možno opaziti v primeru, ko je razpoka rastla iz nizko trdnostnega materiala v višje trdnostni material. V tem primeru je bilo opaženo zmanjšanje gonilne sile za razvoj razpoke in vpetosti materiala, ko se je konica razpoke nahajala v bližini meje med obema materialoma. Takšno obnašanje zvara je posledica visoko trdnostnega materiala, ki se nahaja pred konico razpoke. Ta nosi večino obremenitev, zato je nižje trdnostni material ob meji bistveno manj obremenjen. Hkrati je potrebno poudariti, da so se v tem primeru, pri dejanskih lomno mehanskih preizkusih, pojavili lokalni nestabilni lomi. Pri tem je imela razpoka tendenco do odklona smeri rasti okoli višje trdnostnega materiala. Ker ustvarjeni numerični modeli ne upoštevajo odklona smeri rasti razpoke, so v tem primeru kalibrirani* η_{pl}*,* λ *in* γ_{pl} *neprimerni za preračun J-integrala pri dejanskih lomno mehanskih preizkusih. V tem primeru se priporoča ocena lomne žilavosti v skladu s standardom ASTM E399, ki se nanaša na nestabilni lom.*

V petem poglavju doktorske disertacije so predstavljene izračunane J-R odpornostne krivulje z uporabo kalibriranih η_{pl}*,* λ *in* γ_{pl} *faktorjev. Vpliv konfiguracije zvarov in podpor je bil opisan v prejšnjem odstavku tega uvoda.*

APPLICATION OF NORMALIZATION METHOD TO FRACTURE TOUGHNESS TESTING OF WELDS WITH PRONOUNCED STRENGTH HETEROGENEITY

Keywords: weld, strength mismatch, fracture, normalization data reduction technique, plastic correction factors, test fixture, SE(B) specimen, J-R resistance curve

ABSTRACT

This doctoral dissertation presents the results of an extensive fracture testing programme of welds with pronounced strength heterogeneity. Purpose of this programme was to determine fracture toughness of heterogeneous welds that contain a midplane crack. Application of standardized fracture testing methods in heterogeneous welds might lead to overestimation or underestimation of fracture toughness and consequentially to inaccurate assessment of structural integrity. Reasons for that are variations in mechanical properties of different material regions in the weld which have a significant impact on development of deformation at the crack tip, and consequently on the crack driving force. Experimental procedures in scope of this research include fabrication of weld sample plates, that were welded with MAG process. The welds were fabricated using two different electrodes, one with higher and one with lower mechanical properties, with respect to base material S690QL in order to replicate extreme variations of mechanical properties in the weldment. Fabricated welds were then characterized in detail using metallography, three-point bend impact testing, indentation hardness measurements and tensile testing of flat miniature and round bar standard tensile specimens. Resistance of welds to stable tearing was investigated by fracture testing of square surface cracked SE(B) specimens containing a weld midplane notch. J-integral has been estimated from plastic work, using the normalization data reduction method that is included in standard ASTM E1820. The advantage of the normalization data reduction method is that no special equipment or complex testing method is needed to measure ductile crack growth during fracture testing. The ductile crack growth is determined directly from the load-displacement record, by applying appropriate calibration function and physical lengths of initial and final cracks that were measured post-mortem with the nine-point method. Several correction factors had to be calibrated in order to successfully implement the normalization data reduction method to *fracture testing of welds with pronounced strength heterogeneity. For that reason, parametric finite element analyses were conducted for several weld configurations. Finite element models incorporated plane strain conditions in order to provide calibrated factors that comply with plane strain equations included in ASTM E1820. Additionally, crack tip constraint has been extensively analysed and correlated with the plastic deformation fields. This clarified altered deformation behaviour of modelled welds in comparison with the base material and corresponding effect on fracture toughness. Finally, calibrated factors were applied to computation of J-integral from data that were measured during fracture testing. J-R resistance curves were constructed for the tested heterogeneous welds and compared to the ones of the base material. This directly showed the effect of variations of mechanical properties on the weld fracture behaviour.*

TABLE OF CONTENTS

SYMBOLS

a	Depth of the notch [mm]
A_0	Nominal cross-sectional area [mm^2]
a_0	Fatigue precrack length [mm]
a_b	Blunting corrected crack length [mm]
A_f	Final cross-sectional area [mm^2]
A_i	Actual cross-sectional area [mm^2]
a_{i-1}	Crack length [mm]
a_p	Final crack length [mm]
A_{pl}	Area under the plastic Load-CMOD curve [Nmm]
A_t	Elongation [%]
b	Remaining ligament length [mm]
B	Specimen thickness [mm]
B_N	Notch thickness [mm]
C	Compliance [mm/N]
CET	Carbon equivalent [%]
CVN	Impact toughness [J]
d_{cr}	Transition plate thickness [mm]
d_L	Load rollers diameters
d_P	Force increment [N]
d_S	Support rollers diameter
e	Engineering strain [mm/mm]
E	Elastic modulus [MPa]
e_f	Elongation at rupture [%]
e_Y	Engineering strain at yield onset [mm/mm]
F_2	seam factors for 2D type of heat dissipation [-]
F_3	seam factors for 3D type of heat dissipation [-]
G	Gauge length [mm]
h	Stress triaxiality [-]
H_D	Diffusible hydrogen content [ml/g]
H_W	Weld root width [mm]
I	Current [A]
J	J-integral [kJ/mm^2]

J'_{pl}	Normalized plastic component of the J-integral [-]
$J_{0.5}$	J-integral extracted from 0.5 mm [kJ/mm^2]
$J_{2.0}$	J-integral extracted from 2.0 mm contours [kJ/mm^2]
J_{el}	Elastic component of J-integral [kJ/mm^2]
J_{Ic}	Represents J-integral at crack initiation [kJ/mm^2]
J_{id}	Dynamic fracture toughness [kJ/m^2]
J_{pl}	Plastic component of J-integral [kJ/mm^2]
K	Strain hardening coefficient [-]
K_I	Stress intensity factor [MPa·m$^{1/2}$]
K_{Ic}	Critical stress intensity factor [MPa·m$^{1/2}$]
L	Length [mm]
L_0	Initial gauge length [mm]
L_f	Distance to fusion line in the weld root [mm]
L_W	Distance to weld root [mm]
M	Yield strength mismatching factor [-]
m	Mass [kg]
n	Strain hardening exponent [-]
P	Force [N]
P_{Gy}	General yielding force [N]
P_i	Applied load [N]
P_{max}	Maximal recorded load [N]
$P_{N,i}$	Normalized load [N/mm^2]
P_Y	Yield limit load [N]
Q	Heat input during welding [kJ/mm]
q	Reduction in cross-sectional area [%]
R	Stress ratio [-]
r	Distance ahead of the crack tip [mm]
r_p	Size of plastic zone ahead of the crack tip [mm]
S	Engineering stress [MPa]
s	Standard deviation
S_{UTS}	Engineering ultimate tensile strength [MPa]
S_{YS}	Engineering yield strength [MPa]
$S_{YS,BM}$	Engineering yield strength of base material [mm]

$S_{YS,WM}$	Yield strength of weld material [mm]
t	Time interval [s]
T_0	Plate temperature [°C]
t_0	Lower and upper limit of the time interval [s]
T_i	Interpass temperature [°C]
T_p	Preheating temperature [°C]
U	Voltage [V]
v	Welding speed [mm/s]
V'_{pl}	Normalized CMOD [-]
v_0	Initial impact velocity [m/s]
V_{el}	Elastic CMOD [mm]
V_i	Total CMOD [mm]
V_{pl}	Plastic CMOD [mm]
W	Specimen width [mm]
W_i	Energy to crack initiation [J]
W_p	Energy to crack propagation [J]
W_t	General energy to failure of specimens during impact loading [J]
$\bar{x}$	Mean value [-]
x_0	Reference value of the population [-]
x_i	Individual attribute value [-]
α	Coefficient of the Ramberg-Osgood material law
γ_{pl}	Crack growth correction factor [-]
Δa	Crack extension [mm]
ΔL	Change in gauge length [mm]
$\Delta t_{8/5}$	Cooling time from 800 °C to 500 °C [s]
ε	True strain [mm/mm]
ε_f	True strain at fracture [mm/mm]
ε_i	True strain [mm/mm]
ε_w	Thermal efficiency factor [-]
ε_Y	True strain at yielding onset [mm/mm]
η_{pl}	Correlation factor [-]
λ	Geometry factor [-]
v	Poisson's number [-]

ρ_0	radius of blunted crack tip [mm]
σ	True stress [MPa]
σ_{eq}	Von Mises equivalent stress [MPa]
σ_f	True stress at fracture [MPa]
σ_h	Hydrostatic stress [MPa],
σ_Y	Material true yield strength [MPa]

ACRONYMS

AWMTT	All weld metal tensile testing
BM	Base material (S690 QL)
C(T)	Compact tension specimen
CMOD	Crack mouth opening displacement
CTOD	Crack tip opening displacement
DIC	Digital image correlation
EDM	Electric discharge machining
FEA	Finite element analysis
HAZ	Heat affected zone
L	Longitudinal
LLD	Load line displacement
LOM	Light optical microscopy
MAG	Metal active gas welding
MTS	Miniature tensile specimen
NDRT	Normalization data reduction technique
OM	Overmatched weld material (MIG90)
PEEQ	Equivalent plastic strain
S	Short transverse
SD	Standard deviation
SE(B)	Single edge notched bend specimen
SE(T)	Single edge notched tension specimen
SIF	Stress intensity factor
T	Long transverse
UCM	Unloading Compliance Method
UM	Undermatched weld material (VAC65)

1 PROLOGUE TO THE DOCTORAL DISERTATION

1.1 Introduction

The prologue to the doctoral dissertation provides a brief description of the topic that has been researched in scope of this work. A corresponding hypothesis and goals of the doctoral dissertation will be presented as well. Finally, a structure of the doctoral dissertation will be established.

1.2 Description of topic

Welded joints often contain defects, which may be the result of non-metallic inclusions in the microstructure or the result of defects in the welding technology (pores, lack of fusion, cracks, poor alignment of plates, etc.). Defects in welds act as stress concentrators where cracks can initiate under imposed loads. In the absence of preventive measures, the crack can grow to a critical size, leading to fracture or collapse of the welded structure. In most cases, cracks grow when the welded structure is exposed to dynamic loads, which are lower than the design loads.

To ensure the safe operation of welded machine structures and machine structures in general, many procedures have been developed to assess the integrity of structures, which include methods for engineering critical assessment (ECA) of existing defects. Examples of such procedures are R6 (Revision 4), FITNET FFS (Fitness-For-Service) [1], [2], and EFAM (Engineering Flaw Assessment Method) [3]. The R6 procedure was developed as a procedure for the specific needs of the nuclear industry, while the other listed procedures were developed as general procedures. The R6 and FITNET procedures have also recently been included in the British standard BS 7910 [4], which is in general use for assessing the integrity of structures.

The evaluation of the integrity of the structure, in accordance with the mentioned procedures, is based on a comparison of the crack driving force with the fracture toughness of the material of the structure. Based on such comparison, it is possible to carry out an engineering critical assessment of the existing cracks or defects and to determine the type and extent of repairs. Critical engineering assessment generally allows for plastic deformation of the material due to stress concentration at the crack tip, which requires material fracture toughness values in the form of the J-integral parameter.

Basic ECA methods assume that the crack is located in homogeneous material, which corresponds to most cases. Based on this assumption, the crack driving force can be evaluated using analytical methods included in procedures for assessment of integrity of structures, and the fracture toughness of the material can be evaluated according to standardized procedures such as ASTM E399 [5], ASTM E1820 [6], BS 7448 [7]–[10] and ISO 12135 [11]. The assumption of homogeneous material properties becomes questionable for flaws in fusion welds, which typically comprise a wide variety of microstructures resulting from their complex thermal history. This variety may lead to strong local yield strength variations (e.g. changes up to 100 MPa have been observed within a distance of 5 mm [12]).

Variations in local mechanical properties of the weld joint affect the crack driving force [13] and constraint of the material at the crack tip [14], which directly affects the fracture toughness of welds. Several studies [15], [16] were recently carried out that were focused on determining the effect of the weld geometry and heterogeneous mechanical properties on the fracture toughness of the welded joint. Obtained results contributed to the development of procedures for ECA, which takes into account the differences in the average mechanical properties of the weld and the base material (mismatching of elastic and plastic material properties) and to a certain extent also the geometric properties of the weld joint. The developed ECA procedures are based on a simplified weld joint where weld and base material exhibit homogeneous mechanical properties, and the fusion lines are treated as straight boundaries. An example is the BS 7910 standard [4], which treats the weld as a homogeneous structure and instructs that the strength difference between the weld and the base material is taken into account when it is greater than 10%.

Idealized welds have been extensively analysed on the basis of parametrical finite element analyses [17] and fundamental plasticity studies involving slip line field theory [18]. Some studies considered more detailed models of welded joints in order to provide more accurate estimations of the crack driving force by assuming V-grooved welds [19], [20], or welds consisting of two different materials in the crack growth direction [13]. Research [21] showed that the heat-affected zone (HAZ) affects the deformation behaviour of the weld and, consequently the load-bearing capacity of the welded joint. Despite aforementioned research efforts, a unified approach for assessment of weld integrity that considers variations of local mechanical properties when the crack traverses different material regions in the weld as it grows, is not available to this date.

In addition to the crack driving force, the fracture toughness of weld is also needed in the critical engineering assessment. For the needs of industry, standards BS 7448-2 [8] and ISO 15653 [22] are used to assess the fracture toughness of weld joint materials. Both standards enable determination of fracture toughness in terms of the J-R or CTOD-R resistance curve, and critical values of K, J or CTOD at the crack growth onset. Here it is important to note, that ISO 15653 [22] is a cover standard, that relies on fracture testing procedures that are specified in ISO 12135 [11] standard. Both standards BS 7448-2 [8] and ISO 12135 [11], allow measurements of ductile crack growth with the partial unloading method or by the electric potential drop method. Both methods are relatively complex, and the potential drop method requires additional expensive laboratory equipment.

In general, it is possible to simplify the calculation of ductile crack growth using the normalization data reduction method (NDRM) that is included in the ASTM E1820 [6] standard for measurement of fracture toughness of homogeneous materials. The NDRM is based on the load separation method [23] and key curve method [23]. Instead of measuring the ductile crack growth during fracture testing, the NDRM estimates instantaneous crack length directly from the load-displacement data record. This is possible by applying an appropriate calibration function that considers physically measured lengths of the initial and final cracks. The NDRM was validated in scope of the test programs that were organized by the ASTM E08.08 working group with purpose to determine the J-R resistance curves for high-rate and quasi-static loading conditions of compact CT (Compact Tension) test specimens. Further investigations showed, that the NDRT can be used for fracture testing of single edge notched bending (SE(B)) specimens made of various metallic materials [24]. These researches also showed, that ductile crack growth estimated by the NDRT is in close agreement with measurements, that were done using the unloading compliance and direct current potential drop methods. Additional study showed, that the NDRT can be used for estimation of ductile crack growth in welds. Here, an average difference of less than 10% between the J-R resistance curves provided by the NDRT and unloading compliance method was reported. However, no research has been conducted to validate the use of a normalization method to determine the CTOD-R and J-R resistance curves of welds as the crack progresses from one region of the microstructure to another with different strengths.

Therefore, this research is an effort to apply the NDRM in fracture testing of welds with pronounced strength heterogeneity in order to assess the fracture toughness of such welds in terms of J-R resistance curves.

1.3 Hypothesis and goals

Hypothesis that is formed in scope of this thesis is the following; Using the NDRM, it is possible to determine the *J*-R tearing resistance curves for welds consisting of two different materials in the crack growth direction that differ in terms of microstructure and mechanical properties.

Resistance curves, such as *J*-R, are constructed by combining the computed *J*-integral with the estimated ductile crack growth, by using the NDRM. Implementation of such fracture test is significantly simpler and more suitable when measurement of the crack length by conventional methods is difficult (e.g. the use of 3D DIC measurement systems, testing at high loading rates, testing in aggressive liquids). Although the NDRM is often used to determine the *J*-R resistance curves of homogeneous materials, its application to welds with markedly heterogeneous mechanical properties is limited. Previously conducted researches have shown that it is possible to estimate the ductile crack growth using the NDRM, when the crack grows stably along the boundaries between areas of the weld joint with different mechanical properties [25], [26]. However, this requires correction of the plastic coefficients η_{pl} and γ_{pl}. Researches that would investigate whether the NDRM is appropriate to estimate ductile crack growth when the crack traverses the interface between two mismatched weld regions, have not been conducted up to this date. Therefore, the goals of this doctoral dissertation are as follows:

1) Perform fracture tests of SE(B) test specimens with heterogeneous welds, in which the crack traverses from the region with a lower strength to the region with higher strength and vice versa;
2) Determine the *J*-R resistance curves for ductile crack growth that was estimated with the NDRM and for ductile crack growth that was measured with conventional methods (unload compliance method or direct current potential drop method);
3) Calibrate the plastic parameters η_{pl} and γ_{pl} to accommodate effects of weld geometry and effect of strength mismatching of different weld regions in the analytical computation of the *J*-integral.

1.4 Structure of the doctoral dissertation

This thesis is organized into seven chapters, including introduction.

Chapter 1 gives a brief background on fracture testing of welded joints and influences of the weld strength heterogeneity on the *J*-integral. It details challenges that were recognized by researches and their approach towards finding a solution. Also, this chapter points out the importance of addressing the strength heterogeneity in fracture testing of welds.

Chapter 2 explains the background of fracture test procedures that are standardised and used in modern industry and community of researchers. Important concepts such as experimental determination of the *J*-integral with incremental equations and estimation of the ductile crack growth with NDRM are explained.

Chapter 3 employs the experimental procedures utilized in this work. This includes preparation of welded sample plates, extraction of specimens, metallography and characterization of microstructure, indentation hardness measurements and Charpy impact testing. Local and average mechanical properties of different weld regions were determined with tensile testing of non-standard miniature and standard round bar tensile specimens. Fracture testing of SE(B) specimens is presented in detail, as this forms the core of experimental work. Provisional *J*-R curves are presented in this chapter as η_{pl}, λ and γ_{pl} factors are yet to be calibrated.

Chapter 4 provides an overview of parametric finite element analysis to aid the interpretation of experimental results. Different single materials and double mismatched weld configurations were modelled and analysed. Insight in the relation between plastic deformation of the weld and material constraint at the crack tip is presented. Influence of weld material and HAZ yield strength mismatching on fracture behaviour of welds is investigated. Correspondingly, η_{pl}, λ and γ_{pl} factors, essential for analytical computation of the *J*-integral in fracture testing, are calibrated.

Chapter 5 presents results of fracture tests in terms of the *J*-R resistance curves and critical values of J_{Ic} at fracture onset. The *J*-R curves, computed with calibrated and standard η_{pl}, λ and γ_{pl} factors are compared, and the corresponding effect of yield strength mismatching on obtained results is discussed.

Chapter 6 gathers the outcomes of chapters 1 to 7 to provide a concise summary and key conclusions of this thesis.

1.5 Summary and Conclusions

The safety of welded structures must be ensured by the ECA procedures. The current editions of these procedures rely on the principle of the material homogeneity in the vicinity of the crack tip. The accuracy of the ECA becomes questionable when the crack is located in the welds that have heterogeneous structure and mechanical properties. In such particular cases the current ECA procedures treat welds as homogeneous sections of the structure. Additionally, they prescribe corrections for the equivalent mechanical properties of the homogenized weld or failure assessment diagrams (FAD), when the mismatching of the average yield strength of the weld material and the base material exceeds a certain level (e.g. 10 %, as defined in the BS 7910 [4]). On the other hand, several studies showed that the shape of the weld [19], [20], the heterogeneous structure of the weld [13] and the HAZ [21] have a significant impact on the driving force for the crack development in the weld.

Furthermore, ECA require fracture toughness of the weld as a reference parameter for the assessment of the weld integrity. Fracture toughness of the welds is normally determined in conformance with standards (BS 7448-2 [8] and ISO 15653 [22]) that incorporate methods of fracture toughness testing of homogeneous materials (e.g. ISO 12135 [11], ASTM E1820 [6]). Therefore, this work represents an attempt to calibrate the existing methods for fracture testing of homogeneous materials in such way, that the effect of the weld heterogeneity and shape on the fracture toughness of the weld will be considered. The selected testing method is the NDRM that is incorporated in the ASTM E1820 standard [6], as the NDRM proves to be robust enough to be used for fracture testing in aggressive environments and at different load rates.

2 FRACTURE TESTING OF WELDED JOINTS

2.1 Introduction

The previous chapter presented the background of the doctoral thesis. This chapter provides theoretical insight into the J-integral based fracture testing, the NDRM and the fracture testing of the single material welds and the double mismatched welds. The complete work in scope of this doctoral thesis is formed around the J-integral. The reason for that is that the J-integral enables more accurate assessment [27] of the fracture toughness of the tested material. As a result, the latest editions of the ASTM E1820 [6] standard provide methods that consider the J-integral as the main fracture toughness parameter, while the CTOD, is then derived on the basis of the computed J-integral.

2.2 J-integral Based Fracture Testing

Linear elastic fracture mechanics [28] cannot accurately characterize the fracture behaviour of material in presence of large-scale plasticity. Therefore, Rice [29] proposed a new fracture parameter that was called the *J*-integral and is defined as:

$$J = \oint_{\Gamma} \left(w dy - T_i \frac{\partial u_i}{\partial x} ds \right) \tag{2.1}$$

where Γ is an arbitrary curve around the crack tip as shown in Figure 2.1, w is the strain energy density, T_i presents the components of the traction vector, u_i stands for the components of the displacement vector, d_s is the length increment along the contour, while x and y are the coordinates in orthogonal coordinate system. Rice [29] also showed that the *J*-integral is independent of the path of integration around the crack tip for deformation plasticity.

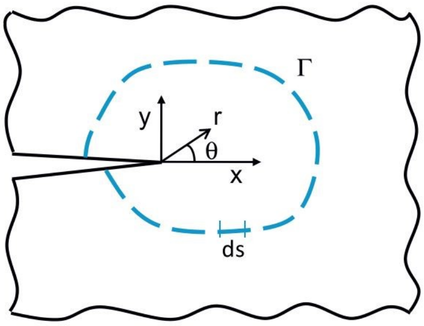

Figure 2.1 Illustration of an arbitrary contour around the crack tip that is used in the definition of the *J*-integral (source: [27]).

Researches conducted by Begley and Landes [30] and Landes and Begley [31] showed that the J-integral and specifically, the critical J_{Ic} at fracture onset, can be considered as a measurable material parameters for characterizing fracture toughness of ductile materials. However, experiments, needed to determine the J_{Ic} were complex. For example, Begley and Landes [30] tested a series of compact tension (C(T)) specimens with the same geometry but different crack sizes. From the measured load-displacement records, they determined the energy that was absorbed by the each tested specimen and then calculated the corresponding J-integral, using the following equation:

$$J = -\left(\frac{dU}{Bda}\right)_{\Delta} \tag{2.2}$$

where U is the strain energy stored in the body, a is crack length, B is the thickness of the cracked body and Δ follows the partial derivative convention indicating the displacement variable that is held constant during partial differentiation. Here, Equation (3.46) represents a relationship between the J-integral and the energy release rate or work done on a nonlinear elastic body, containing a crack per unit fracture surface area, expressed in displacement control conditions according to Rice [29].

The first major step forward in the J based fracture testing was the development of a method for estimating J as a function of crack length a at a point on the load-displacement record from a single specimen test. This was done by Rice et al. [32], who considered that strain energy U can be determined from the area under load-displacement curve, and J could be expressed according to Equation (2.3) for displacement control condition, and according to Equation (3.46) for load control conditions.

$$J = -\frac{1}{B}\int_0^{\Delta}\left(\frac{\partial P}{\partial a}\right)_{\Delta} d\Delta \tag{2.3}$$

$$J = \frac{1}{B}\int_0^{P}\left(\frac{\partial \Delta}{\partial a}\right)_{P} dP \tag{2.4}$$

where B is the thickness of the cracked body, P is applied load and Δ is measured displacement. In this case, Δ could be either load line displacement (LLD) or crack mouth opening displacement CMOD. From the Equation (2.3), Rice et al. [32] developed J estimation equations for a single edge notched three point bend SE(B) specimen:

$$J = \frac{2}{Bb}\int_0^{\Delta} P d\Delta = \frac{2A}{Bb} \tag{2.5}$$

where A is the total area under the load-displacement P-Δ curve and represents the energy absorbed by the specimen. B is the width of the specimen, and b is the ligament of the specimen, defined as difference $b=W-a$ between the specimen width W and crack length a. For SE(B) specimens with different sized cracks, Sumpter and Turner [33] proposed a general expression, where J was separated into an elastic component J_{el} and a plastic component J_{pl}:

$$J = J_{el} + J_{pl} = \frac{{K_I}^2(1-\nu^2)}{E} + \frac{\eta_{pl}}{bB}\int_0^{\Delta_{pl}} P d\Delta_{pl} \tag{2.6}$$

where K_I is mode I stress intensity factor, E is elastic modulus, ν is Poisson’s coefficient, b is the remaining ligament, B is specimen thickness, P is applied load, Δ_{pl} is the plastic component of the measured displacement and η_{pl} is a correlation factor, that is a function of the normalized crack length a/W. Considering that the absorbed plastic strain energy in a fracture specimen can be expressed as the area under a P-Δ_{pl} curve, then the second term in Equation (2.6) can be expressed as follows:

$$J_{pl} = \frac{\eta_{pl}}{bB}\int_0^{\Delta_{pl}} P d\Delta_{pl} = \frac{\eta_{pl} A_{pl}}{bB} \tag{2.7}$$

where A_{pl} is the area under the P-Δ_{pl} curve. The first term in Equation (2.6) equals the energy release rate, $G=J_{el}$ according to Irwin [34], and can be computed straightforwardly. Therefore, the determination of the plastic η_{pl} factor becomes essential in the experimental estimation of the J-integral. The early attempts to determine η_{pl} factor were based on plastic limit analysis. Clarke and Landes [35] obtained η_{pl} factors for C(T) specimens as:

$$\eta_{pl} = 2 + 0.522\left(\frac{b}{W}\right) \tag{2.8}$$

Additionally, Sumpter [36] obtained η_{pl} factor for SE(B) specimens in the following form:

$$\eta_{pl} = \begin{cases} 2, & a/W > 0.282 \\ 0.32 + 12\left(\frac{a}{W}\right) - 49.5\left(\frac{a}{W}\right)^2 + 99.8\left(\frac{a}{W}\right)^3 & a/W \leq 0.282 \end{cases} \tag{2.9}$$

More accurate values of η_{pl} can be determined with finite element analysis (FEA), as demonstrated by Kirk and Dodds [37] and Nevalainen and Dodds [38]. The use of η_{pl} factor significantly simplifies the analytical evaluation of the *J*-integral from experimental results. However, the Equation (2.6) and the Equation (2.7) are valid only for stationary cracks. Therefore, multiple specimens have to be tested, where loading is stopped and the cracks are marked, broken open and measured, in order to determine the *J*-integral and corresponding J_{Ic} for the tested material [39]. In order to determine the *J*-integral from a single specimen fracture test, the *J* estimation should consider the current crack length and the crack growth correction. An early attempt to develop incremental equations that would incorporate crack growth correction in *J* evaluation was made by Garwood et al. [40]. Later, Ernst et al. [41] developed a full set of incremental equations for the *J* estimation, based on the principle of load separation [42]. Since the *J*-integral was developed on the basis of the deformation theory of plasticity, it is independent of the loading path that leads to the current displacement Δ and crack length a, provided that *J*-controlled crack growth conditions are satisfied [43]. Accordingly, the *J*-integral is a unique function of two independent variables: LLD Δ and crack length *a*. Ernst et al. [41] derived the complete differential of J_{pl} as:

$$dJ_{pl,LLD} = \frac{\eta_{pl,LLD}P}{bB}d\Delta_{pl} - \frac{\gamma_{pl,LLD}}{b}J_{pl}da \tag{2.10}$$

where $\eta_{pl,LLD}$ is the LLD based correlation factor and $\gamma_{pl,LLD}$ is the LLD based crack growth correction factor, that is defined according to the following equation:

$$\gamma_{pl,LLD} = \eta_{pl,LLD} - 1 - \frac{b}{W}\frac{\eta'_{pl,LLD}}{\eta_{pl,LLD}} \tag{2.11}$$

where *b* is the remaining ligament, *W* is a specimen width, and $\eta'_{pl,LLD}$ is a partial differential with respect to *a/W*, i.e. $\eta'_{pl,LLD}=\partial\eta_{pl,LLD}/\partial(a/W)$. Integrating Equation (2.10), one has:

$$J_{pl} = \int_0^{\Delta_{pl}} \frac{\eta_{pl,LLD} P}{bB} d\Delta_{pl} - \int_{a_0}^{a} \frac{\gamma_{pl,LLD}}{b} J_{pl} da \tag{2.12}$$

where a_0 is the initial crack length and a is the current crack length. This equation is valid for any load path that leads to current values of a and Δ_{pl}, including the actual path for a growing crack. Figure 2.2 shows an example of true P-Δ for a growing crack and three additional deformation paths for original crack length a_0, and two arbitrary crack lengths a_{i-1} and a_i. Since the Equation (3.46) is valid for any loading path, leading to the current values of a_i and $\Delta_{pl,i}$, the integration path AC can be approximated with deformation segment AB, where crack length a_{i-1} is fixed, and deformation segment BC, where the displacement Δ_{pl} remains constant, but the crack length increases from a_{i-1} to a_i. Along the deformation segments AB and BC, the plastic component J_{pl} at the i-th step of crack growth is determined with the following incremental equation:

$$J_{pl,i} = \left(J_{pl,i-1} + \frac{\eta_{pl,LLD}^{i-1}}{b_i B} A_{pl,LLD}^{i,i-1} \right) \left(1 - \frac{\gamma_{pl,LLD}^{i-1}}{b_{i-1}} (a_i - a_{i-1}) \right) \tag{2.13}$$

where $J_{pl,i}$ and $J_{pl,i-1}$ are plastic components of J integral for increments i and i-1 respectively, a_i and a_{i-1} are crack lengths from increments i and i-, and $A_{pl,LLD}^{i,i-1}$ is the area under plastic load-LLD curve between increments i and i-1. The Equation (3.46) is LLD based incremental equation for estimation of J, and was included in earlier versions of the ASTM E1820 standard.

Kirk and Dodds [37] showed that the LLD based J estimation equation (3.46) gives accurate results for $a/W>0.3$, but inaccurate results for $a/W\leq0.3$. This is due to the fact that the LLD based $\eta_{pl,LLD}$, sensitive to the strain hardening exponent for SE(B) specimen with shallow cracks. In contrary, CMOD based $\eta_{pl,CMOD}$ is insensitive to the strain hardening for $a/W>0.05$.

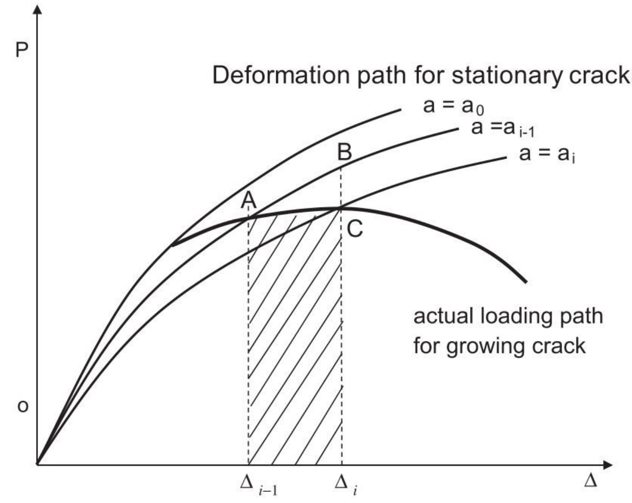

Figure 2.2 An actual load-displacement curve for a growing crack and three examples of the deformation paths for stationary cracks (source: [27])

In a recent study, Zhu and Joyce [44] developed a CMOD method for direct evaluation of the *J*-integral from a single fracture test. Here, the complete differential of the *J*-integral was obtained by defining the relation between LLD and CMOD:

$$\lambda = \frac{V_{pl}}{\Delta_{pl}} = \frac{A_{pl,CMOD}}{A_{pl,LLD}} = \frac{\eta_{pl,LLD}}{\eta_{pl,CMOD}} \tag{2.14}$$

where λ is geometry factor that gives ratio between plastic components of LLD Δ_{pl} and CMOD V_{pl}. Additionally, $A_{pl,CMOD}$ and $\eta_{pl,CMOD}$ are CMOD based area under plastic load-CMOD curve and a corresponding correlation factor, respectively. This enabled Zhu and Joyce [44] to derive the total differential of plastic *J*-integral:

$$dJ_{pl} = \frac{\eta_{pl,CMOD}P}{bB}dV_{pl} - \frac{\gamma_{pl,CMOD}}{b}J_{pl}da \tag{2.15}$$

where $\eta_{pl,CMOD}$ and $\gamma_{pl,CMOD}$ are CMOD based correlation and crack growth correction factors respectively, V_{pl} is the plastic component of CMOD, *B* is the thickness of the cracked body, *a* is the crack length and *b* is the remaining ligament. The crack growth correction factor is here defined as:

$$\gamma_{CMOD} = \lambda\eta_{pl,CMOD} - 1 - \frac{b}{W}\left(\frac{\lambda'}{\lambda} + \frac{\eta'_{pl,CMOD}}{\eta_{pl,CMOD}}\right) \tag{2.16}$$

where λ' and $\eta'_{pl,CMOD}$ are partial differentials of the geometry factor λ and the CMOD based correlation factor $\eta_{pl,CMOD}$, with respect to the normalized crack length a/W. By integrating te Equation (2.15) an expression for plastic component of the J-integral can be obtained:

$$J_{pl} = \int_0^{V_{pl}} \frac{\eta_{pl,CMOD}P}{bB} dV_{pl} - \int_{a_0}^{a} \frac{\gamma_{pl,CMOD}}{b} J_{pl} da \tag{2.17}$$

where a_0 and a are the initial and the current crack lengths. The Equation (2.17) is valid for any load path that leads to the current values of a and V_{pl}. CMOD based incremental equation was developed in a similar way than the LLD based Equation (2.13) and has the following form:

$$J_{pl,i} = \left(J_{pl,i-1} + \frac{\eta^i_{pl,CMOD}}{b_i B} A^{i.i-1}_{CMOD}\right)\left(1 - \frac{\gamma^i_{CMOD}}{b_i}(a_i - a_{i-1})\right) \tag{2.18}$$

where $A^{i,i-1}_{pl,CMOD}$ is the area under the plastic P-CMOD curve, that can be computed with a simple trapezoidal rule:

$$A^i_{pl,CMOD} = \frac{1}{2}(P_i + P_{i-1})(V_{pl,i} - V_{pl,i-1}) \tag{2.19}$$

where P_i and P_{i-1} are applied loads in increments i and $i-1$ respectively, while $V_{pl,i}$ and $V_{pl,i-1}$ are measured plastic CMOD components in increments i and $i-1$ respectively. Zhu and Joyce [44] proposed the following expressions for CMOD based $\eta_{pl,CMOD}$ and $\gamma_{pl,CMOD}$ factors:

$$\eta_{pl,CMOD} = 3.667 - 2.199\left(\frac{a}{W}\right) + 0.437\left(\frac{a}{W}\right)^2 \tag{2.20}$$

$$\gamma_{pl,CMOD} = 0.131 + 2.131\left(\frac{a}{W}\right) - 1.465\left(\frac{a}{W}\right)^2 \tag{2.21}$$

These two functions were obtained by curve fitting of the available, valid finite element results, such as; Wu et al. [45], Kirk and Dodds [37], Nevalainen and Dodds[38], Kim and Schwalbe

[46], Kim et al. [47] and Donato and Ruggieri [48]. Incremental Equation (2.18), is included in latest editions of ASTM E1820 [49] standard, where the total *J*-integral is computed as:

$$J_i = J_{el,i} + J_{pl,i} = \frac{{K_{I,i}}^2(1-\nu^2)}{E} + J_{pl,i} \tag{2.22}$$

Here, J_i, $J_{el,i}$ and $J_{pl,i}$ are total, elastic and plastic components of the *J*-integral in i-th increment, respectively. Furthermore, $K_{I,i}$ is the stress intensity factor for the crack opening mode I, while E and ν are elastic modulus and Poisson's coefficient, respectively. The $J_{pl,i}$ is the plastic component of the *J*-integral, computed according to the Equation (2.18).

This Chapter briefly outlined the background of incremental equations for the *J*-integral estimation in order to provide better understanding on how are $\eta_{pl,CMOD}$, λ_{CMOD} and γ_{plCMOD} factors included in the computation process. A comprehensive information on the development of *J*-based fracture testing procedures is available in an overview paper, prepared by Zhu and Joyce [27]. The remaining parts of this research will focus entirely on CMOD based determination of the *J*-integral for base material and welds. For that reason, $\eta_{pl,CMOD}$, λ_{CMOD} and γ_{plCMOD} factors will be henceforth denoted simply as η_{pl}, λ and γ_{pl} respectively, due to more convenient writing.

2.3 Normalization Data Reduction Technique

Conventional methods for measuring ductile crack growth during fracture testing [39], such as unloading compliance method and direct current potential drop method, are challenging to be implemented. This is especially true, if a fracture specimen is to be tested under severe test conditions, such as high load rate, high temperature, or aggressive environments. An alternative method, called NDRM, was developed to estimate crack growth directly from load-displacement (LLD or CMOD) data record. The NDRM is based on load separation [50], [51] and key curve-method [52]. Correspondingly, recorded load P is divided into two parts, the geometry function $G(a/W)$ that is related only to the specimen geometry and the crack length, and the plastic function $H(V_{pl}/W)$:

$$P = G\left(\frac{a}{W}\right) H\left(\frac{V_{pl}}{W}\right) \tag{2.23}$$

Load P_i, recorded during fracture test, is normalized with the geometry function G(a/W):

$$P_{N,i} = \frac{P_i}{G\left(\frac{a}{W}\right)} = \frac{P_i}{WB\left(\frac{W - a_{bi}}{W}\right)^{\eta_{pl}}} = H\left(\frac{V_{pl}}{W}\right) \tag{2.24}$$

where $P_{N,i}$ and P_i are normalized and recorded load, W and B are a specimen width and thickness, η_{pl} is a correlation factor that is CMOD based in this case, and a_{bi} is the blunt corrected crack length, given as:

$$a_{bi} = a_0 + \frac{J_i}{2\sigma_Y} \tag{2.25}$$

Here, a_0 is initial crack length, σ_Y is material yield strength and J_i is total J-integral computed with incremental equation (2.22), according to the standard ASTM E1820 [6] for SE(B) specimens, using the initial crack length a_0. In the second term of equation (2.22) $\gamma_{pl}=0$, as the crack is assumed to be stationary in the first computation iteration. Next, each corresponding measured plastic CMOD is normalized as:

$$V'_{pl,i} = \frac{V_{pl,i}}{W} = \frac{V_i - P_i C_i}{W} \tag{2.26}$$

where $V'_{pl,i}$ and $V_{pl,i}$ are normalized and measured CMOD, W is a specimen width and C_i is an initial compliance of a tested specimen. The final load-displacement pair P_i-$V_{pl,i}$ is normalized using the same equations, except that the final crack length a_p is used without blunting correction. The a_p is measured post-mortem on the fracture surface of a tested specimen, using the 9-point method according to the ASTM E1820 [6] or GKSS [53] procedure. Thereafter, a normalized data is plotted and a tangent line from the final P_i-$V_{pl,i}$ pair to the normalized curve must be drawn, as demonstrated in the Figure 2.3. The data to the right of the tangency point shall be excluded for the fitting procedure. The normalized data with plastic CMOD $V'_{pl,i}<0.001$ must be excluded as well. The remaining data, including the final P_i-$V_{pl,i}$ pair, is then used to fit the calibration function:

$$P_N = \frac{a + bV'_{pl} + cV'_{pl}{}^2}{d + V'_{pl}} \tag{2.27}$$

where a, b, c and d are the curve-fitting coefficients that are determined by the least squares regression method. The normalization function should fit selected data pairs (including the final data pair) with a maximum deviation less than 1% of the $P_{N,i}$ at the final load point.

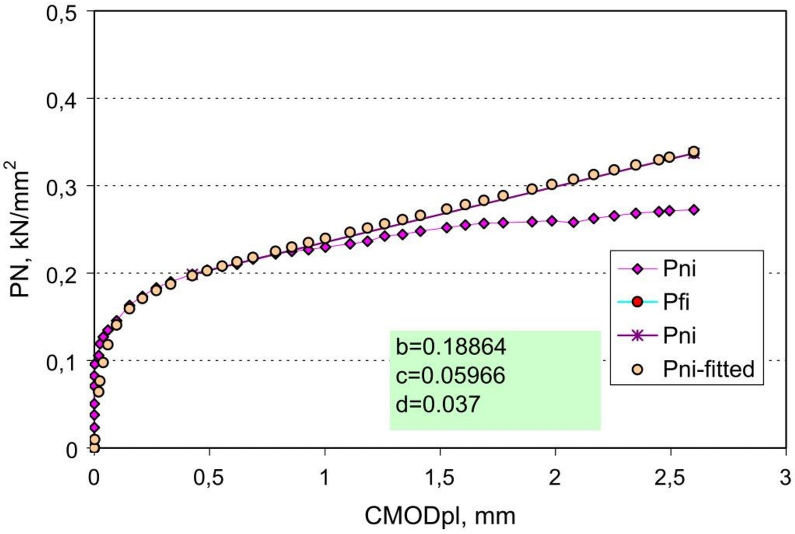

Figure 2.3 An example of the normalized load-CMOD curve with fitted calibration function (source: [54])

Finally, a normalized blunt corrected crack length a_{bi}/W should be exposed from the Equation (2.24) and substituted by a_i/W. The normalized crack length a_i/W can be then computed from each fitted $P_{N,i}$-$V'_{pl,i}$ data pair and the corresponding recorded load P_i during fracture testing.

Studies such as Dzugan and Viehrig [55], Zhu and Joyce [24] and Zhu et al. [56] investigated the application of NDRM to fracture testing of SE(B) specimens for different metallic materials. Published results confirmed that NDRM can be equivalent to the elastic unloading compliance method and the direct current potential drop method. A recent study by Tang et al. [57] showed that NDRM can be applied to welds as well. An average difference of less than 10% between the *J*-R resistance curves provided by the NDRM and the unloading compliance method was reported. Finally, it is important to note that several different forms of the normalization function were proposed in the past. A review of proposed normalization functions is given by Zhu and Joyce [27].

2.4 Fracture Testing of Welds

Experimental determination of the *J*-R curve for welded joints is based on testing of small, laboratory fracture specimens according to standardised procedures, specified by ISO 15653 [22] and BS 7448-2 [8]. The former is based on the *J*-evaluation method for homogeneous metallic materials, included in the ASTM E1820 [6] standard, that has been extended to weldments with yield strength mismatch ratio M in the range $0.5 \leq M \leq 1.25$. Here, M is defined as:

$$M = \frac{S_{YS,WM}}{S_{YS,BM}} \tag{2.28}$$

where $S_{YS,WM}$ and $S_{YS,BM}$ are engineering yield strengths of the weld and the base material respectively, and are determined by the tensile testing. The ISO 15653 assumes that Equation (2.20) is valid for M values in the range $0.5 \leq M \leq 1.25$. However, M values of weld joints used for various applications often exceed the limit of 1.25. It is necessary to adopt the appropriate η_{pl} and γ_{pl} equations in terms of the strength mismatch M and the normalized crack length a/W, in order to accurately evaluate the *J*-R curves for such joints. Several researchers provided η_{pl} and γ_{pl} solutions for the evaluation of J in fracture testing of the strength mismatched weld joints. Kim et al. [58] performed a detailed FEA to obtain η_{pl} of various specimens (including SE(B)) with $a/W=0.5$ from weld joints with strength mismatch M varying between 0.5 and 2.0. The obtained results demonstrated that values of η_{pl} decrease in case of undermatching welds ($M<1$) and increase in case of overmatching (OM) welds ($M>1$), relative to the evenmatching welds ($M=1$). Furthermore, it was shown that η_{pl} depends on the weld width. Reduction of the weld width results in further increase of η_{pl} values for undermatching (UM) welds, reaching a maximum value at geometry ratio $(W-a)/H_W=5$, where H_W is the weld width. The opposite was observed for OM welds, where reduction of the weld width resulted in further decrease of η_{pl} values, reaching the minimum value at geometry ratio $(W-a)/H_W=2$. However, such effect was observed only if the geometry ratio was $(W-a)/H_W \geq 2$. For very narrow welds with $(W-a)/H_W<2$, the effect of the weld geometry was negligible and computed values of η_{pl} were similar to the one for the base material. Eripret and Hornet [59] performed a parametric finite element study of SE(B) specimens from weld joints with mismatch levels $M=0.2$ and $M=2.0$ for a wide range of crack lengths ($0.1 \leq a/W \leq 0.7$). The results demonstrated that η_{pl} values increase across the entire range of the analysed crack lengths, by reducing the mismatch factor M. Similar observations were made by Donato et al. [60]. Their study showed that η_{pl} solutions for the analysed levels of M are in relatively close agreement if the crack is located at the central plane of a narrow weld with H_W=5 mm, and dispersed in a wider weld with H_W=20 mm (SE(B) specimens with B=25.4 mm and W=2B=50.8 mm). While aforementioned studies [58]–[60] incorporated 2D plane strain conditions in parametric FEM for SE(B) specimens having W/B=2 configuration, Mathias et al. [61] performed a parametric 3D FEA of SE(B) specimens for a wide range of crack lengths ($0.1 \leq a/W \leq 0.7$). Although, SE(B) samples were from X80 steel weld joint with M=1.18 (according to published yield stresses for base and weld material), η_{pl} solutions were developed for the homogeneous material with various yield strength levels and hardening properties. The results revealed that the produced η_{pl} solution for SE(B) specimens with W/B=2 is in close agreement with the one obtained by Donato [48], while the η_{pl} solution for SE(B) specimens with W/B=1 was considerably lower (approx. 11 % for shallow cracks and 25 % for deep cracks).

2.5 Double Mismatched Welds

Welded joints are considered as critical parts of a welded structure due to possible occurrence of defects, such as undercuts, pores or cracks. They represent heavily inhomogeneous material regions of structures that cause local crack driving force and a crack path deviation, as the crack propagates through weld regions with different strength. Several researches have investigated the influences of strength heterogeneity in welded joints on fracture behaviour using experimental and numerical methods [60], [62]–[64]. A comprehensive study focused on an experimental determination of the fracture toughness for welds with pronounced strength heterogeneity was conducted by Gubeljak [21], [65]. This study showed scatter and local instabilities in the measured crack tip opening displacement (CTOD), which indicated variations of the crack driving force, when a growing crack traverses different strength regions in the weld.

A particularly notable example of welds with pronounced strength heterogeneity are repair multi-pass welds in high loaded structures. Such welds are created when a part of the original weld with defect must be removed by growing and filled with UM weld material. If hidden defects, i.e. porosity, non-metallic inclusions or lack of fusion between weld layers, occur during repair welding, a crack is initiated in the UM weld material and propagates towards the OM part of the weld. The determination of fracture toughness for such double mismatched welds is demanding because near-tip crack driving force becomes different from the normally applied far-field crack driving force, if the material properties vary in the direction of a crack extension, as demonstrated by Kolednik [66]. Nevertheless, fracture toughness testing of SE(B) specimens with double mismatched welds was conducted by Gubeljak et al. [67]. Here, double mismatched welds were artificially fabricated on sample plates by filling a half of the groove with OM and a half of the groove with UM weld materials, as shown in the Figure 2.4. Corresponding results showed that unstable fracture occurred when the crack was transitioning from the UM to the OM weld material through the interface. This indicated increased crack driving force when the crack tip was located near the interface, which was confirmed by the special inhomogeneity term, defined as a ratio between the local and the far-field crack driving force. A similar study has been conducted by Predan et al. [68], where a crack that was traversing from the OM to the UM weld material was analysed through FEA and a corresponding fracture behaviour was determined with testing of SE(B) specimens. The results indicated reduced crack driving force when the crack tip was located near the interface between both weld materials. This effect was more detailly presented by Simha et al. [69]. Motivated by listed studies, Predan et al. [70] conducted the extensive FEA of configurational forces for double mismatched welds at various levels of elastic, yield strength and plastic hardening mismatching. The obtained results showed, that greater levels of mismatching further increased local crack driving force near the interface when the crack tip traversed from the OM to the UM weld material. In contrast, greater levels of mismatching caused reduced local crack driving force near the interface, when the crack traversed from the UM to the OM weld material.

The study of Predan et al. [70] was focused on cracks that were growing in the plane. Recently, Starčevič et al. [71] demonstrated through FEA that severe deviations of the crack grow path are expected when the crack grows from the UM towards the OM weld material. The reason for that is that the OM weld material ahead of the crack acts as a barrier. This can potentially cause additional complications when measuring ductile crack growth during the fracture testing. Although recent studies presented significant research efforts to determine fracture behaviour of double mismatched welds, a unified procedure for fracture testing of such welds has not been developed up to this date. Therefore, establishing such fracture procedure is the main objective of this thesis.

Material	E $[GPa]$	$R_{p0.2}$ $[MPa]$	R_m $[MPa]$	M $R_{p0.2,WM} / R_{p0.2,BM}$	Charpy Cv $[J/80\,mm^2]$
Over-match	184	648	744	1,19	>40 J at -60 °C
Base metal	203	545	648	-	>60 J at -60 °C
Under-match	208	469	590	0,86	>80 J at -60 °C

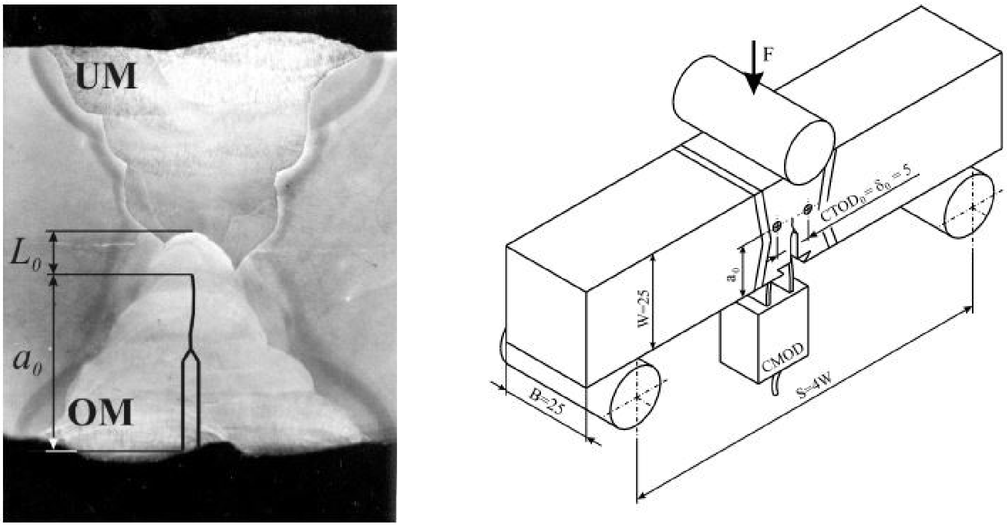

Figure 2.4 An example of fabricated double mismatched welds with corresponding mechanical properties of the BM, the OM weld and the UM weld materials. A configuration of the SE(B) specimen for fracture testing of such welds is shown as well (source: [67]).

2.6 Summary and conclusions

The ASTM E1820 [6] standard provides procedure for experimental determination of the *J*-integral. This is done by measuring the applied load and displacement (either LLD or CMOD) during the monotonous loading of the fracture specimen. The *J*-integral is divided to the elastic J_{el} and the plastic J_{pl} component according to Equation (2.6). The elastic component J_{el} is determined on the principles of linear elastic fracture mechanics, and is therefore dependent on the applied SIF K_I and the fracture specimen specific shape function *f(a/W)*. Moreover, the plastic component J_{pl} is determined on the basis of the computed area under plastic load-displacement record that is associated with the deformation energy. However, this computation process is not straightforward, but rather includes parameters η_{pl} and γ_{pl} that assure correction of the J_{pl} due to specimen configuration and the crack growth. According to Anderson [6], the J_{pl} can be computed for fracture specimens of various configurations if η_{pl} and γ_{pl} parameters are calibrated properly.

The aforementioned approach has been applied to the single material welds in scope of several researches. Researches, conducted by Kim et al. [58], Eripret and Horner [59] and Donato et al. [60] showed that the η_{pl} for the single material welds is under high influence of the width and the yield strength mismatch of the weld.

While the variations of the η_{pl} in single material welds have been investigated, the behaviour of the η_{pl} for the double mismatched welds is still unknown. Gubeljak et al. [67] performed experimental testing of such welds. The study showed onset of locally unstable fracture when the crack was transitioning from UM to OM weld material through the interface. Predan et al. [70] demonstrated through extensive FEA study that the crack driving force increases when the crack is traversing from the OM to UM weld material through the interface, and decreases when the crack traverses from UM to OM weld material through the interface. Here, the level of variation of the crack driving force, when the crack tip is located near the interface between two different weld materials, is determined by mismatch of their yield strengths. another study, conducted by Starčevič et al. [71] demonstrated through FEA that severe deviations of the crack grow path are expected when the crack grows from the UM towards the OM weld material.

The findings of the aforementioned researches motivated the author of this doctoral dissertation to conduct extensive fracture testing of the double mismatched welds, and to calibrate the corresponding η_{pl} and γ_{pl} parameters. The main goal of this work is to determine the fracture toughness and the crack driving force from the fracture test records.

3 MATERIALS AND TESTING

3.1 Introduction

The previous chapter provided an insight to fracture testing of the single material welds. A goal of this doctoral dissertation is to apply these methods to fracture testing of welds with pronounced strength heterogeneity. In order to do so, an extensive experimental work had to be conducted. The corresponding procedures and results are presented in this chapter. First of all, materials were selected and welded sample plates were fabricated. Next, heterogeneity of the fabricated welds was investigated with optical microscopy and microindentation hardness measurements. Furthermore, local and average material properties were determined by tensile testing of micro and all weld metal tensile specimens, respectively. Moreover, impact toughness of the welds was investigated with Charpy impact testing. Finally, fracture toughness of the fabricated welds was determined through fracture testing of standardized SE(B) specimens according to the ASTM E1820 standard. Obtained result of the fracture tests are provisional, as η_{pl} and γ_{pl} parameters must be calibrated. The corresponding calibration procedure is presented in Chapter 4, while the application of the calibrated η_{pl} and γ_{pl} parameters is presented in chapter 5.

3.2 Materials

3.2.1 Base Material and Weld Consumables

High strength low alloyed steel S690 QL (W.-Nr.: 1.8928) has been selected as the base material. This is a structural steel in quenched and tempered condition with fine-grained microstructure that is composed of ferrite, bainite and martensite. The principal advantage of the S690 QL steel is a good combination of the yield strength (> 690 MPa) and the ultimate tensile strength (770 - 940 MPa), a high strength to weight ratio and a good impact toughness (27 J at - 40 °C) [72]. As a result, the S690 QL steel is suitable for highly loaded constructions and components (e.g. cranes, heavy duty trucks, mobile cranes) where low weight is important. For requirements of this research, the S690 QL steel has been provided by Vítkovice Steel, a.s. in the form of 25 mm thick plate with dimensions 2000 x 1000 mm.

The weld consumables Mn4Ni2CrMo (with commercial designation MIG 90) and G4Si1 (with commercial designation VAC 65) have been selected in order to fabricate the OM, the UM and combined bi-material welds. The Mn4Ni2CrMo has higher yield strength (> 890 MPa) and ultimate tensile strength (940 - 1180 MPa) in comparison to the base material [73]. Although this weld consumable is suitable for welding of high-strength, heat treated, fine-grained construction steels with yield strength of > 890 MPa, it has been selected for the fabrication of the welds with pronounced yield strength overmatch (M ≈ 1.30). In contrast, the G4Si1 has lower yield strength (> 460 MPa) and ultimate tensile strength (530 - 680 MPa) in comparison to the base material and is suitable for welding of unalloyed construction steels with ultimate tensile strength of < 640 MPa [73]. Nonetheless, it has been selected for fabrication of the welds with pronounced yield strength undermatch (M ≈ 0.67). Both weld consumables were provided by Elektrode Jesenice, d.o.o. in the form of spooled welding wires with diameter of Ø1.2 mm, and are suitable for metal active gas (MAG) welding process. The corresponding chemical composition of the listed materials according to certificates, is presented in Table 3.1. The corresponding provisional mechanical properties, as certified, are presented in Table 3.2. Mismatching of weld consumables yield strength with respect to the base material has been evaluated with mismatching factor M that is defined with the Equation (2.28), where $R_{p0.2,WM}$ and $R_{p0.2,BM}$ were used for $S_{YS,\ WM}$ and $S_{YS,\ BM}$ (yield strengths of the base and the weld material are denoted as $R_{p0.2,WM}$ and $R_{p0.2,BM}$ according to the ISO standards, and $S_{YS,\ WM}$ and $S_{YS,\ BM}$ according to the ASTM standards, respectively). The estimated yield strength mismatching factors are reported in Table 3.2 as well.

Table 3.1 Provisional chemical composition of utilized material that was provided in the enclosed material certificates.

Material	Mass percent composition [%]											
	C	Si	Mn	P	S	Cr	Mo	Ni	Al	Ti	V	Cu
S690 QL	0.164	0.27	0.96	0.017	0.006	0.84	0.342	0.88	0.047	0.003	0.005	0.04
MIG 90	0.09	0.80	1.75	0.005	0.009	0.35	0.568	2.19	0.004	-	0.006	0.04
VAC 65	0.06	0.89	1.63	0.013	0.017	0.04	0.006	0.02	0.004	-	0.005	-

Table 3.2 Provisional mechanical properties of utilized material that were provided in the enclosed material certificates

Material	Yield strength $R_{p0.2}$ [Mpa]	Ultimate tensile strength R_m [Mpa]	Elongation A_t [%]	Inpact toughness CVN [J]	Estimated yield strength mismatch M [-]
S690 QL	719	797	16.7	178 (at -40 ºC)	-
MIG 90	937	999	16.0	62 (at -60 ºC)	1.303
VAC 65	504	598	24.0	95 (at -40 ºC)	0.701

3.2.2 Welded Sample Plates Configuration

Welded sample plates were fabricated, joining 25 mm thick HSLA steel S690 QL plates with 500 mm length and 200 mm width, that were cut from the delivered plate prior to the welding, using a CNC plasma cutting system. Parent plates were joined by MAG welding. Two types of welded sample plates were fabricated. For the first type, the weld groove had been machined to a double V configuration with a bevel angle of 60 ° and a root gap of 2 mm that is presented in Figure 3.1 a); a commonly used weld configuration in practice. Various specimens (SE(B), Charpy V-groove, miniature tensile) were later extracted from these sample plates in order to the characterize strength heterogeneity of the weld and its effect on fracture toughness of the weld.

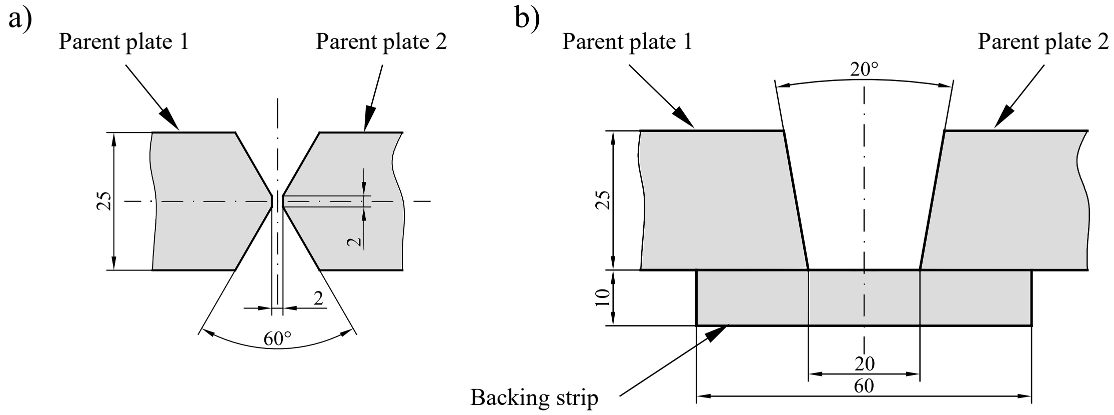

Figure 3.1 Utilized weld grooves in a) double V configuration and b) wide V configuration.

The first type of the welded sample plates proved to be inappropriate for extraction of round bar tensile specimens for all weld metal tensile testing (AWMTT) due to the narrow weld width. As a result, a second type of welded sample plates had been fabricated with the weld groove in a wide V configuration with a bevel angle of 20 ° and a weld root gap of 20 mm, as presented in Figure 3.1 b). In this case, a 10 mm thick backing strip had been attached to both parent plates to be joined beneath the weld groove in order to fabricate the weld. Such weld configuration meets requirements of standard ISO 15792-1 [74] for tensile testing of weld consumables and extraction of the corresponding AWMTT specimens.

3.2.3 Welding Parameters

MAG welding procedure has been used to fabricate welded sample plates. Welding parameters were adopted from a detailed study that was conducted by D. Arsić et al. [75]. Authors stated that using MAG welding procedure with specific heat input in range of Q = 11.20 ÷ 14.89 kJ/cm, preheating temperature T_p = 150 ÷ 200 °C and interpass temperature $T_i \leq 250$ °C, resulted in quality welds with low porosity and impact toughness, expressed in terms of absorbed impact energy in the range of 24.2 ÷ 45.5 J (for filler welds) at temperature 20 °C.

In scope of this research, trial welding has been performed prior to the welding of sample plates in order to verify welding parameters that were provided in D. Arsić et al. [75]. The trial welding demonstrated that welding voltage U=25.8 V, current I=230 A and speed v=25 cm/min, resulted in heat input during the welding Q=11.4 kJ/cm (Q=1.14 kJ/mm). Here, the heat input during the welding was computed according to the following equation:

$$Q = \frac{\epsilon_w \cdot U \cdot I \cdot 6}{v} \cdot 10^{-2} \tag{3.1}$$

where thermal efficiency factor ε_w=0.85 for the MAG welding.

Furthermore, cooling time from 800 °C to 500 °C $\Delta t_{8/5}$=5 ÷ 20 s is generally recommended for the S690 QL steel [76] in order to fabricate welds with optimal mechanical properties. A recent study, conducted by Chen et al. [77], confirms that yield strength of welded joint gradually declined as the cooling time $\Delta t_{8/5}$ was increased from 10 s to 60 s, while ultimate tensile strength remained unaffected for $\Delta t_{8/5}$<30 s. Although, the referred investigation was limited to welded sample plates of S690 QL steel with maximum thickness 16 mm, it provides a useful guideline for determining the optimal $\Delta t_{8/5}$. In this research, the cooling time $\Delta t_{8/5}$ was estimated using hand calculation procedure, given by DIN EN 1011-2:2005 standard [78]. Here, the type of heat dissipation (2D or 3D) had to be initially defined by using the following equation:

$$d_{er} = \sqrt{\frac{4300 - 4.3 \cdot T_0}{6700 - 5 \cdot T_0} \cdot \frac{Q \cdot F_2}{F_3} \cdot \left(\frac{1}{500 - T_0} + \frac{1}{800 - T_0}\right)} \tag{3.2}$$

where d_{cr} is transition plate thickness in [mm], Q=1.14 kJ/mm is heat input during the welding, T_0=180 °C is the plate temperature (preheat temperature in this case, T_0=T_p), while F_2=0.9 and

F_3=0.9 are seam factors for 2D and 3D type of heat dissipation, respectively, in single or double V butt joint. The comparison of computed transition plate thickness d_{cr}=18.1 mm with actual plate thickness d=25 mm indicates that heat dissipation is 3D as $d$cr<d. Therefore, the cooling time $\Delta t_{8/5}$ was evaluated by using the following equation for preheating temperature in the range T_p= 150 ÷ 200 °C:

$$\Delta t_{8/5} = (6700 - 5 \cdot T_0) \cdot Q \cdot \left(\frac{1}{500 - T_0} + \frac{1}{800 - T_0}\right) \cdot F_3 \tag{3.3}$$

where the evaluated cooling time $\Delta t_{8/5}$=8 ÷ 10 s, heat input during the welding Q=1.14 kJ/mm, temperature of the plate T_0=T_p=150 ÷ 200 °C and the seam factor F_3=0.9 for the double V butt joint. Considering the calculated cooling time $\Delta t_{8/5}$=8 ÷ 10 s and the fact that weld joint yield strength gradually declines for $\Delta t_{8/5}$>10 s, it was assumed that the welding parameters determined in trial welding should enable fabrication of a welded joint with optimal mechanical properties. Additionally, minimum required preheating temperature was verified by using hand calculation procedure, given by DIN EN 1011-2:2005 standard [78]. Here, carbon equivalent had to be calculated first by using the following equation:

$$CET = C + \frac{Mn + Mo}{10} + \frac{Cr + Cu}{20} + \frac{Ni}{40} \tag{3.4}$$

where C=0.164 %, Mn=0.95 %, Mo=0.339 %, Cr=0.80 %, Cu=0.03 % and Ni=0.76 % are mass percent compositions of Carbon, Nickel, Molybdenum, Chrome, Copper and Nickel respectively that are provided in Table 3.2. Carbon equivalent CET=0.36 % was computed by inserting listed mass percent compositions into Equation (3.4). Next, the minimum required preheating temperature was calculated using the following equation:

$$T_p = 697 \cdot CET + 160 \cdot tanh(d/35) + 62 \cdot HD^{0,35} + (53 \cdot CET - 32) \cdot Q - 328 \tag{3.5}$$

where CET=0.36 % is carbon equivalent, d=25 mm is combined thickness of the weld joint, HD=5 ml/100g is the diffusible hydrogen content, which was conservatively assumed from experience, and Q=1.14 kJ/mm is heat input during welding that was proofed by the trial welding. Minimum required preheating temperature T_p=116 °C was calculated by inserting aforementioned quantities in Equation (3.6). This result proves, that preheating temperature T_p

= 150 ÷ 200 °C suggested by D. Arsić et al. [75] meets minimum requirements given by the DIN EN 1011-2:2005 standard [78] and should help preventing hydrogen cracking. Finally, a set of welding parameters for welding of sample plates was formed and is here presented in Table 3.3. It is important to add, that the preheating temperature was set to the higher end of the suggested temperature range in order to avoid hydrogen cracking. Additionally, the cooling time $\Delta t_{8/5}$ was estimated by inserting the preheating temperature with other welding parameters, presented in Table 3.3, into equation (3.3). The estimated range of the cooling time is presented in Table 3.3, as well in order to provide confirmation that other welding parameters were properly set and would enable fabrication of quality welds with solid mechanical properties and a low rate of defects.

Table 3.3 Welding parameters that were implemented in welding of sample plates.

Voltage U [V]	Current I [A]	Welding speed v [mm/s]	Heat input Q [kJ/mm]	Preheating temperature T_p [°C]	Estimated cooling time $\Delta t_{8/5}$ [s]
25.8	230	25	1.14	180÷200	9.0÷9.7

3.2.4 Welding Process

Welding of sample plates has been conducted in the Laboratory for Welding at the Faculty of Mechanical Engineering in Maribor, Slovenia. A mixture of 82 % Ar and 18 % CO_2, provided by Messer with commercial designation Ferroline C18, has been used as a protective gas with a flow rate 14 l/min. MIG 90 and VAC 65 welding wires with diameter of Ø1.2 mm were used. A welding torch has been mounted to a carriage for submerged arc welding equipment, as shown in Figure 3.2 a). This ensured movement of the welding torch along the groove at a constant speed v=25 cm/min and at a constant distance, measured from the nozzle of the welding torch to the surface of the plates. Parent plates of S690 QL steel with thickness 25 mm were spot welded and preheated to T_p=180 ÷ 200 °C prior the welding, and were not fixed during the welding.

A special sequence of weld layers deposition has been implemented in order to avoid excessive bending of the sample plates due to residual stresses that were induced during the welding. At first, a weld root and two filling layers of the weld were deposited in one side of the weld groove. After that, the welding was stopped and the sample plate was let to cool down. Next, the weld root has been inspected for possible defects using penetrant method, as demonstrated in Figure 3.2 b). Detected defects were manually grinded out and results of the repair work were verified using the penetrant method. If no defects had been detected, then the sample plate was preheated and the welding continued by filling the other half of the weld groove with root layer and remaining filler layers. After that, the remaining filling layers were deposited in the weld groove on the side that was left partially filled. The interpass temperature has been carefully monitored using a thermocouple throughout the welding process. Deposition of a new weld layer had not been started until the interpass temperature reached the optimal range, T_i=180 ÷ 200 °C. An example of weld layers deposition sequence and a corresponding measured and computed welding parameters is provided in Table 3.4 for the OM weld, in Table 3.5 for the UM weld and in Table 3.6 for the bi-material, half OM and half UM weld. Finally, the fabricated welds were inspected using an x-ray method. The conducted inspection showed, that the fabricated welds did not contain any critical defect which could have significant effect on structural integrity and fracture toughness of the weld. Therefore, the fabricated welds were proved to be suitable for an extraction of various testing specimens in the following stages of the presented research.

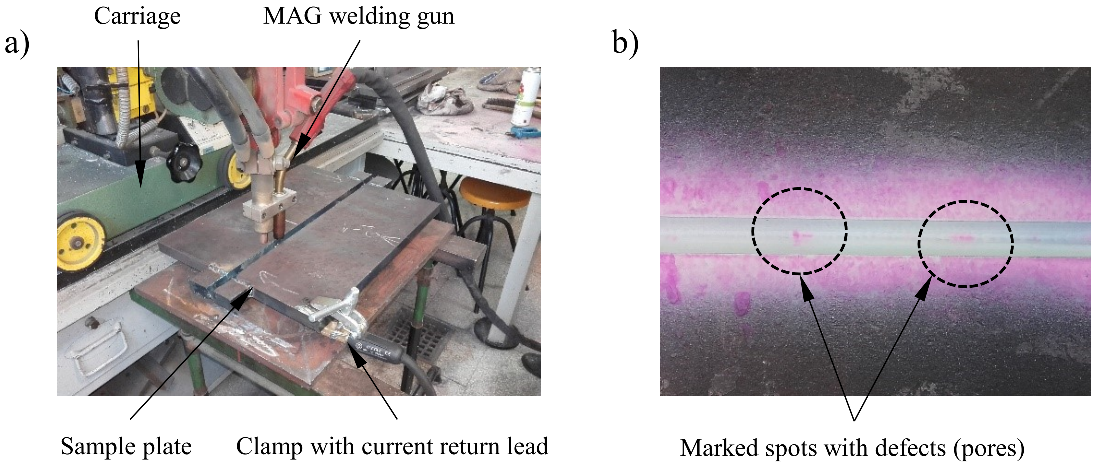

Figure 3.2 Important details in the welding process; a) setup of the welding equipment and b) detail of the deposited layer in the weld root, inspected with the penetrant method.

Table 3.4 The welding sequence with the corresponding welding parameters for the single material OM weld joint.

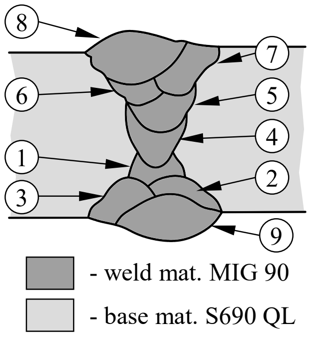

Weld layer	Voltage U [V]	Current I [A]	Welding speed v [mm/s]	Heat input Q [kJ/mm]	Plate temp. T_0 [°C]	Cooling time $\Delta t_{8/5}$ [s]
1	26.3	237.0	25.0	1.20	200	10.2
2	25.2	237.0	25.0	1.15	200	9.8
3	25.1	237.0	25.0	1.14	200	9.8
4	27.1	237.0	25.0	1.23	180	9.7
5	26.3	237.0	25.0	1.20	200	10.2
6	25.3	237.0	25.0	1.15	200	9.8
7	25.3	236.0	25.0	1.15	190	9.4
8	25.0	236.0	25.0	1.13	190	10.3
9	25.0	237.0	25.0	1.14	185	10.2

Table 3.5 The welding sequence with the corresponding welding parameters for the single material UM weld joint.

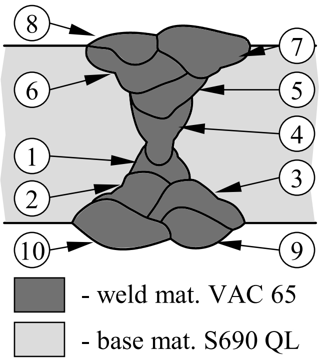

Weld layer	Voltage U [V]	Current I [A]	Welding speed v [mm/s]	Heat input Q [kJ/mm]	Plate temp. T_0 [°C]	Cooling time $\Delta t_{8/5}$ [s]
1	30.0	234.0	25.0	1.35	200	11.5
2	29.3	234.0	25.0	1.32	180	10.4
3	29.5	232.0	25.0	1.31	180	10.4
4	30.3	233.0	25.0	1.36	200	11.6
5	29.2	233.0	25.0	1.31	200	11.2
6	29.4	234.0	25.0	1.32	200	11.3
7	28.9	233.0	25.0	1.29	195	10.8
8	29.3	233.0	25.0	1.31	200	11.2
9	29.8	233.0	25.0	1.33	180	11.7
10	29.0	232.0	25.0	1.29	200	12.3

Table 3.6 the welding sequence with the corresponding welding parameters for the bi-material half OM and half UM weld joint.

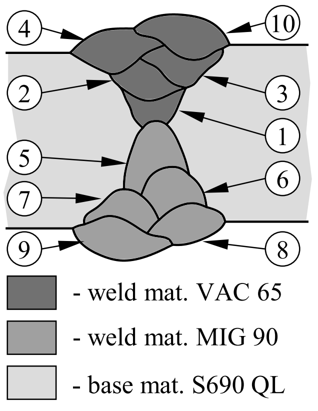

Weld layer	Voltage U [V]	Current I [A]	Welding speed v [mm/s]	Heat input Q [kJ/mm]	Plate temp. T_0 [°C]	Cooling time $\Delta t_{8/5}$ [s]
1	26.5	224	25	1.14	182	9.0
2	26.4	224	25	1.14	180	9.0
3	25.2	223	25	1.08	180	8.5
4	26.0	223	25	1.11	181	8.8
5	26.5	237	25	1.21	180	9.5
6	25.8	236	25	1.17	180	9.2
7	25.3	237	25	1.15	182	9.2
8	24.8	236	25	1.12	180	8.9
9	28.7	237	25	1.17	190	9.6
10	25.0	223	25	1.07	180	8.4

3.2.5 Metallographic Analysis

A metallographic inspection of the welded joints has been conducted in the Laboratory for Materials at the Faculty of Mechanical Engineering in Maribor, Slovenia. An expert opinion on composition of a microstructure has been provided by researchers at the Faculty of Technology and Metallurgy in Belgrade, Serbia.

The metallographic inspection was performed on macrograph samples that had been extracted from the welded plates by a saw cutting. These macrographs were then metallographically prepared and polished. Furthermore, macrographs were etched with a 2% solution of nitric acid and alcohol (i.e. Nital) in order to expose microconstituents. Next, the microstructure of prepared macrographs was inspected with light optical microscopy (LOM), at x500 and x1000 magnification. Only the observations made on the macrograph sample of the bi-material half OM and half UM weld (shown in Figure 3.3) will be presented here, as this macrograph includes all relevant types of the microstructures.

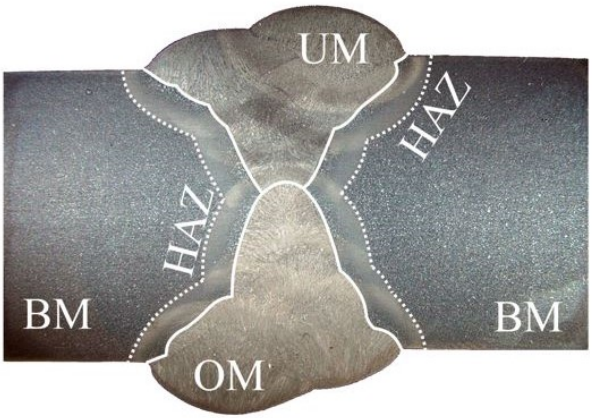

Nomenclature:
UM – undermatched weld mat. (VAC65)
OM – overmatched weld mat. (MIG 90)
HAZ – heat affected zone
BM – base material (S690 QL)

Figure 3.3 The macrograph of the bi-material half OM and half UM weld with a marked distinctive microstructure regions.

To begin with, the observed microstructure of the base material (presented in Figure 3.4 a) and Figure 3.4 b)) shows the presence of the Widmanstättenferrite (proeutectoid ferrite) in the form of side plates, nucleated at the austenite grain boundaries forming the lamellar microstructure, sparsely present and designated as the primary ferrite with the aligned second phase, i.e. upper bainite. Moreover, the presence of the martensitic phase is also observed.

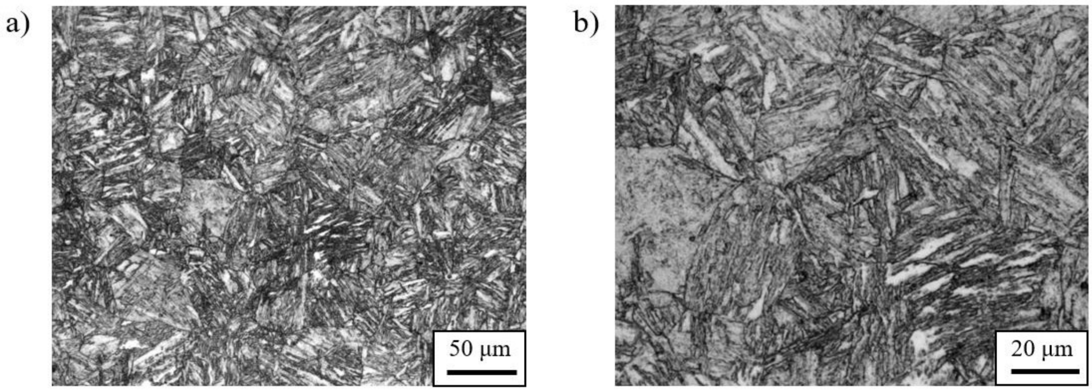

Figure 3.4 The microstructure of the base material (S690 QL) presented at a) 500x and b) 1000x magnifications.

Next, the microstructure of the UM weld material (presented in Figure 3.5 a) and Figure 3.5 b)) is a mixture of the coarse intragranular polygonal primary ferrite islands, present in the high extent, the sparse upper bainite and the pearlite with the interior of the grain transformed to a fine acicular ferrite.

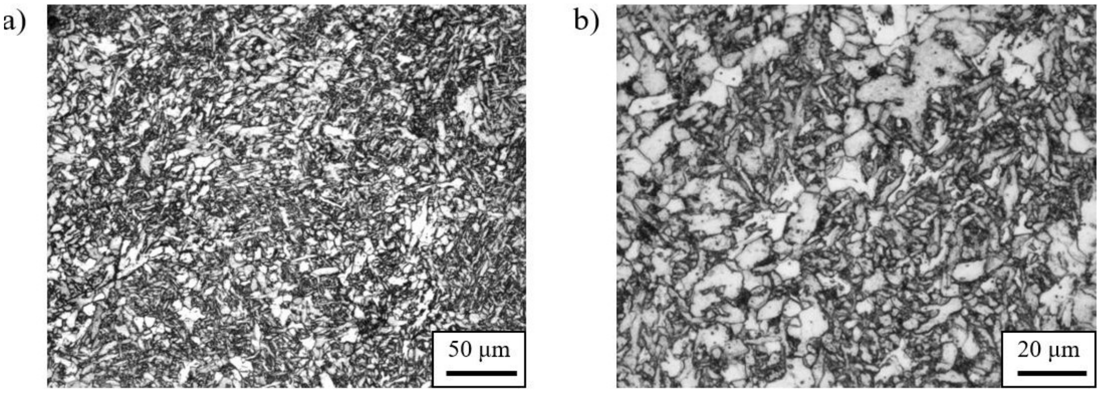

Figure 3.5 The microstructure of the UM weld material (VAC 65) presented at a) 500x and b) 1000x magnifications.

Moreover, the LOM micrographs of the OM weld material (presented in Figure 3.6 a) and Figure 3.6 b)) reveal the presence of the three microconstituents: ferrite, upper bainite and pearlite. On the LOM micrographs, ferrite can be recognized as white grains, while the presence of pearlite can be recognized as the black islands at the ferrite grains boundaries. The microstructure of the OM weld material is quite similar to the UM material microstructure, except that all present microconstituents are finer and ferrite is present in smaller extent than in the case of the UM weld material.

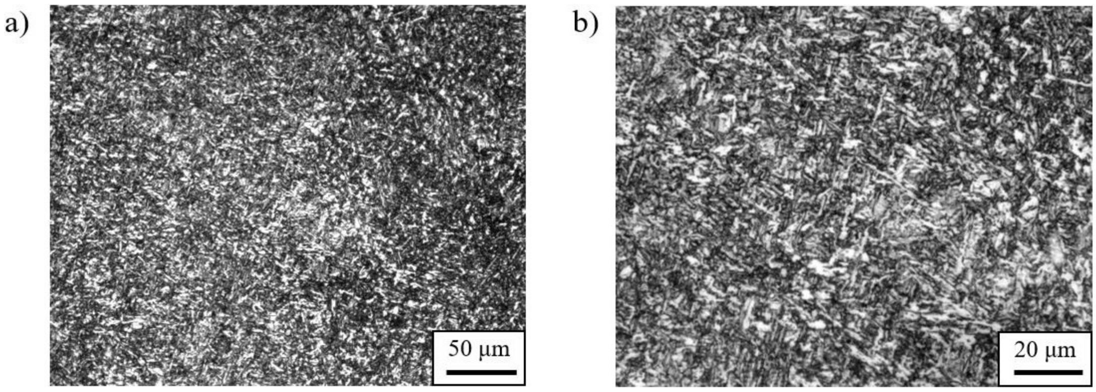

Figure 3.6 The microstructure of the OM weld material (MIG 90) presented at a) 500x and b) 1000x magnifications.

Finally, the heat affected zone (HAZ) has been inspected using LOM. Here, different microconstituents were observed in the HAZ near the UM and the OM weld materials. In the microstructure of the HAZ, present between the base material and the UM material (presented in Figure 3.7 a) and Figure 3.7 b)), the ferrite grains accompanied by pearlite and upper bainite are distinguished. The HAZ present between the base material and the OM material (presented in Figure 3.8 a) and Figure 3.8 b)) is characterized with the presence of upper bainite, as the major microconstituent, accompanied with sparse pearlite and rare ferrite islands.

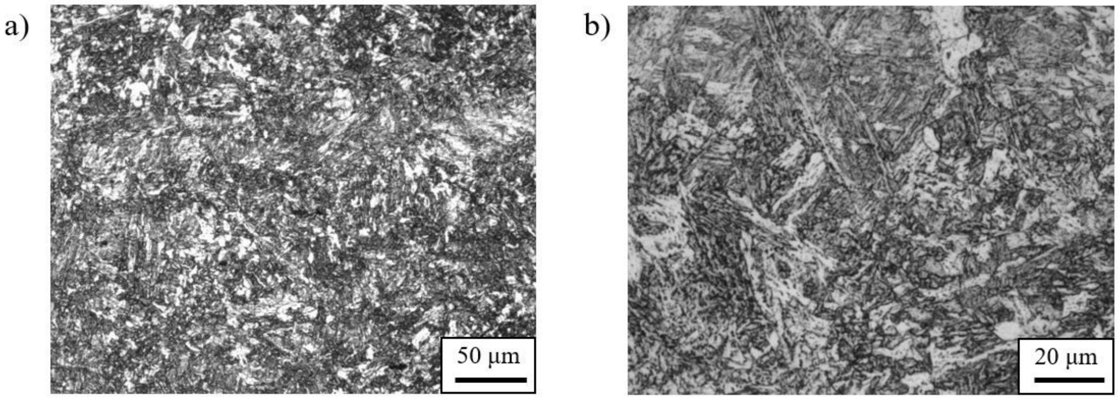

Figure 3.7 The microstructure of the HAZ between the base material (S690 QL) and the UM material (VAC65) presented at a) 500x and b)1000x magnifications.

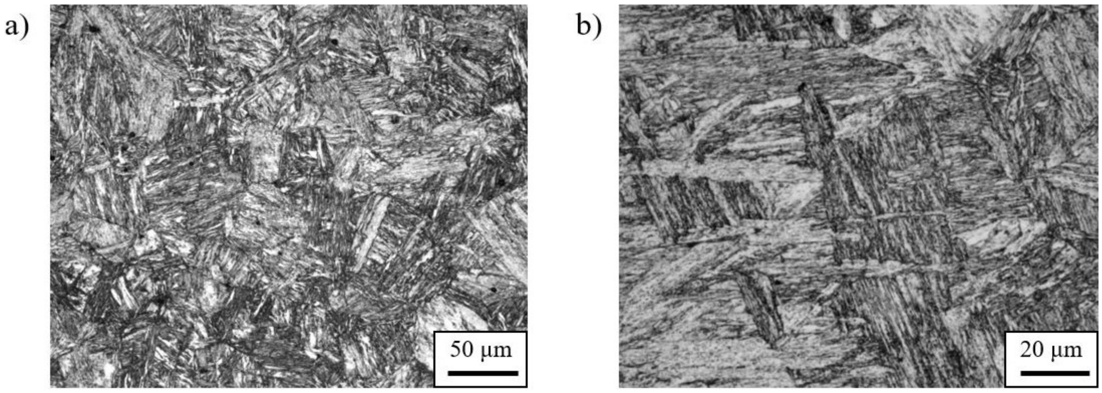

Figure 3.8 The microconstituents of the HAZ between the base material (S690 QL) and the OM material (MIG 90) presented at a) 500x and b) 1000x magnifications.

To conclude, the presented macrographs show differences in the microstructure of the distinctive material regions in the fabricated welds. It is therefore expected, that each material region would exhibit significantly different mechanical properties which can potentially have an effect on fracture toughness and integrity of the entire weld. For that reason, it is important to investigate variations in strength and other mechanical properties of each material region in the weld in a quantitative manner. Procedures of such investigation will be presented in the following chapter.

3.3 Weld Heterogeneity Characterization

3.3.1 Microindentation Hardness

Hardness traverses are an important indicator of material (in)homogeneity and can be correlated with mechanical properties of different parts of a weld. This has been demonstrated in a recent study, conducted by Hertelé et al. [79], where unique material models of different microstructures in a weld have been predicted on the basis of hardness maps. These material models were then assigned to individual finite elements in numerical model of SE(T) fracture specimen, containing a weld with a mid-plane crack. The purpose of such FEM was to evaluate a crack driving force in a single material weld with heterogeneous structure, due to complex thermal history. The listed work is an example of how measured hardness provides a clear insight in variations of strength in different weld regions. For that reason, hardness measurements have been implemented in this research. A detailed investigation of hardness has been made using hardness profiles, which provide insight in variations of material properties in different parts of a weld [80], [81].

Hardness measurements were conducted on the sample of the half OM and half UM weld in the Laboratory for Materials at the Faculty of Mechanical Engineering in Maribor. A special indentation machine with indentation load 0.1 kg has been used to measure microindentation hardness according to Vickers method. All performed measurements were in conformance with ASTM E384 standard [82]. The microindentations were made in equidistant points at interval length 0.5 mm that were aligned in three lines, crossing the entire weld, as shown in Figure 3.9.

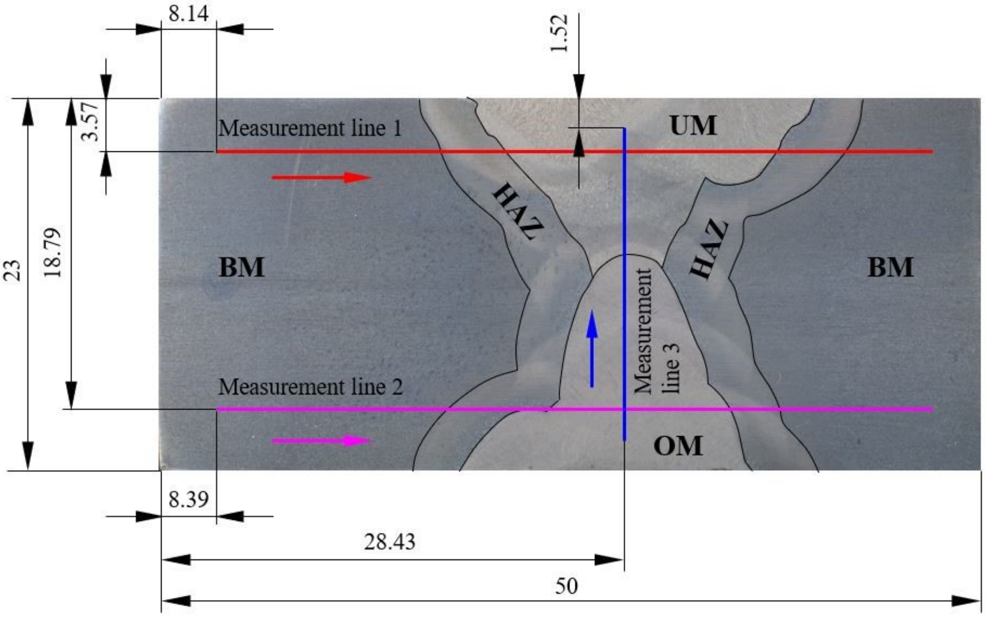

Measurment line	No. of microindentation points	Total line length
Measurement line 1	74	36.0 mm
Measurement line 2	76	36.1 mm
Measurement line 3	42	20.1 mm

Nomenclature:
UM – undermatched weld mat. (VAC65)
OM – overmatched weld mat. (MIG 90)
HAZ – heat affected zone
BM – base material (S690 QL)

Figure 3.9 The macrograph of the bi-material half OM and half UM weld with the marked microindentation hardness measurement lines and weld parts. The arrows indicate the direction of measurement progression.

Hardness profiles were then created by plotting measured hardness values in dependence of a position of the microindentation points along the measurement lines that are marked in Figure 3.9. The created hardness profiles are presented in Figure 3.10, Figure 3.11 and Figure 3.12 for the measurement lines 1, 2 and 3, respectively. It is important to note, that position of the microindentation points is given as a relative position with respect to the outmost left edge of the weld macrograph sample in case of the horizontal measurement lines 1 and 2, and as a relative position with respect to the bottom edge of the weld macrograph sample in case of vertical measurement line 3.

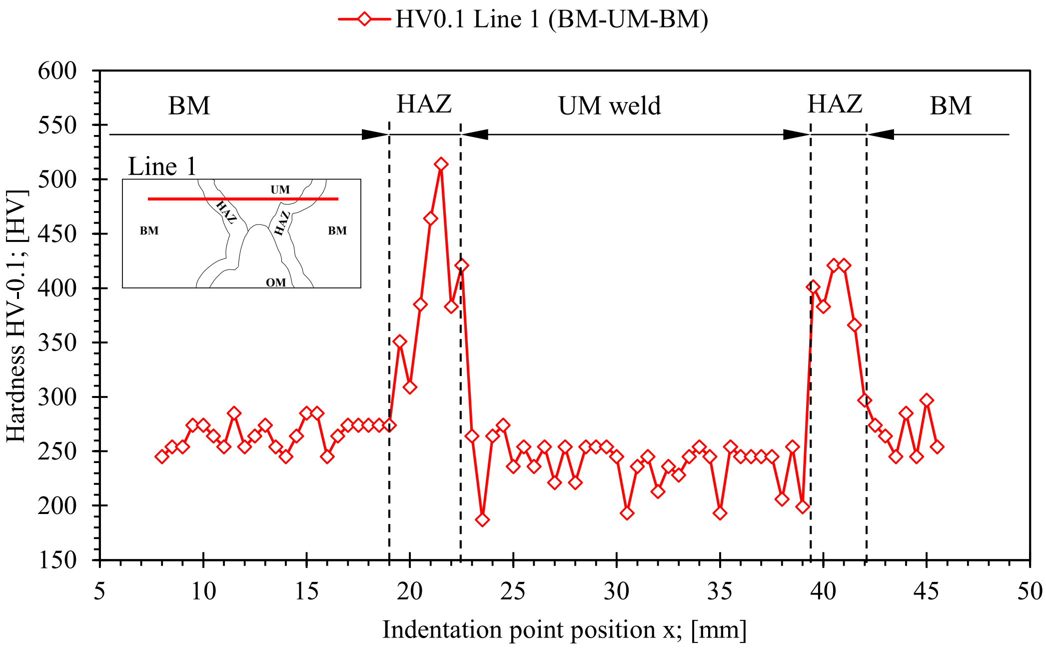

Figure 3.10 The microindentation hardness profile for measurement line 1 on the weld micrograph sample (marked in Figure 3.9).

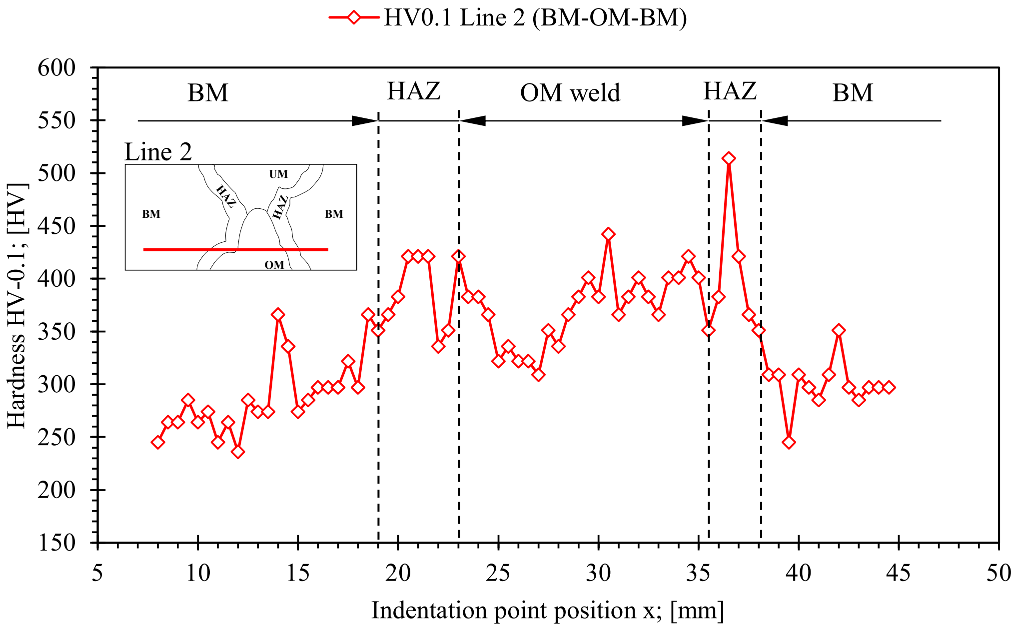

Figure 3.11 The microindentation hardness profile for measurement line 2 on the weld micrograph sample (marked in figure 3.9).

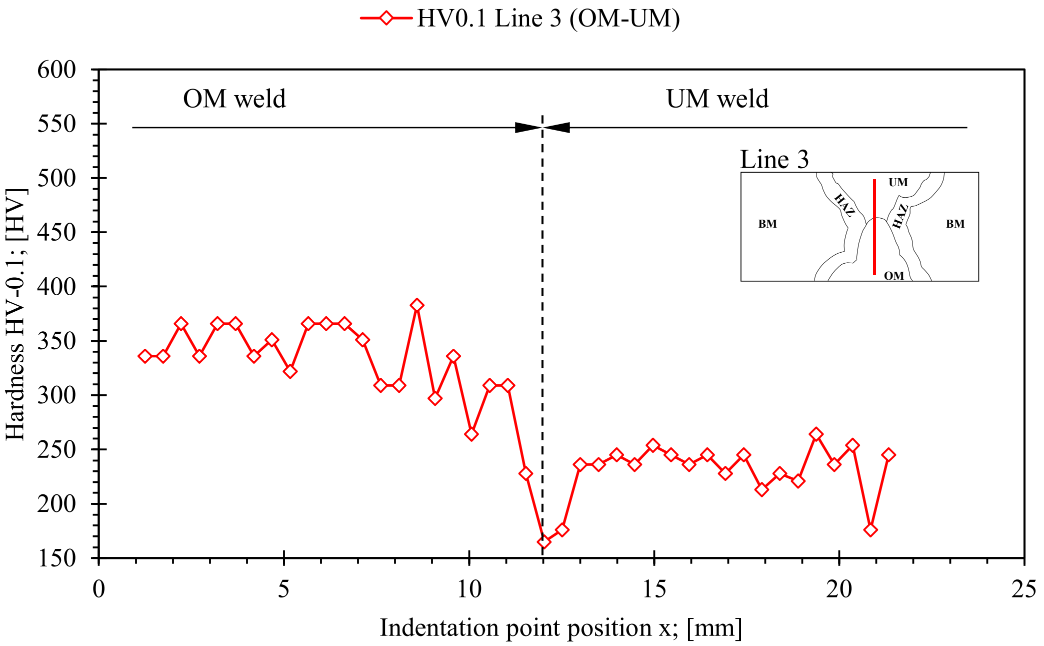

Figure 3.12 The microindentation hardness profile for measurement line 3 on the weld micrograph sample (marked in figure 3.9).

The following observations can be made on the basis of obtained hardness profiles. The average hardness of the base material with mixed ferrite and bainite microstructure is 280.9 HV. In comparison, the UM weld material has mainly ferritic microstructure with portion of sparse upper bainite and pearlite and exhibits slightly lower hardness 243.4 HV than the base material, as demonstrated in Figure 3.10. Furthermore, hardness profiles in Figure 3.10 and Figure 3.12 show fairly consistent hardness of the UM weld, with relatively low scatter, despite the complex thermal history due to the welding process. In contrary, the OM weld exhibits an average hardness 346.2 HV, which is 18.9 % higher in comparison to the base material and 29.7 % higher in comparison to the UM weld material. This can be contributed to a fine-grained ferrite microstructure with bainite and pearlite microconstituents. Finally, the highest recorded hardness can be observed in the HAZ as demonstrated in Figure 3.10 and Figure 3.11. Here, an average hardness 362.2 HV was recorded with the highest values, reaching 514 HV. Such significant increase in hardness is contributed to ferrite microstructure with upper bainite as the major microconstituent. This observation is comparable to the results of the study that was conducted by Pamnani et al.[83], where microstructures and hardness of the welded joints in high strength low alloyed steels of lower grade were thoroughly investigated.

In general, presented hardness profiles provide an insight in hardness variations in different parts of the half OM and half UM weld. However, a more comprehensive overview of variations in properties over weld cross section can be provided by a hardness map, as reported in several other studies [84]–[87]. For that reason, hardness mapping has been conducted in SOETE Laboratory at University of Ghent, Belgium. Here, hardness has been measured using an automated indentation device with indentation load 5 kg and pyramidal indenter. The hardness has been measured according to Vickers method, in conformance with ASTM E384 standard [82]. Around 1000 indentations were made in an array pattern over the entire weld macrograph sample, which was grinded and polished prior to the measurements. Hardness map was then obtained by interpolation of the measured hardness between neighbour points. The computed hardness map is here presented in Figure 3.13, and was published in scope of research conducted by Naib et al. [88].

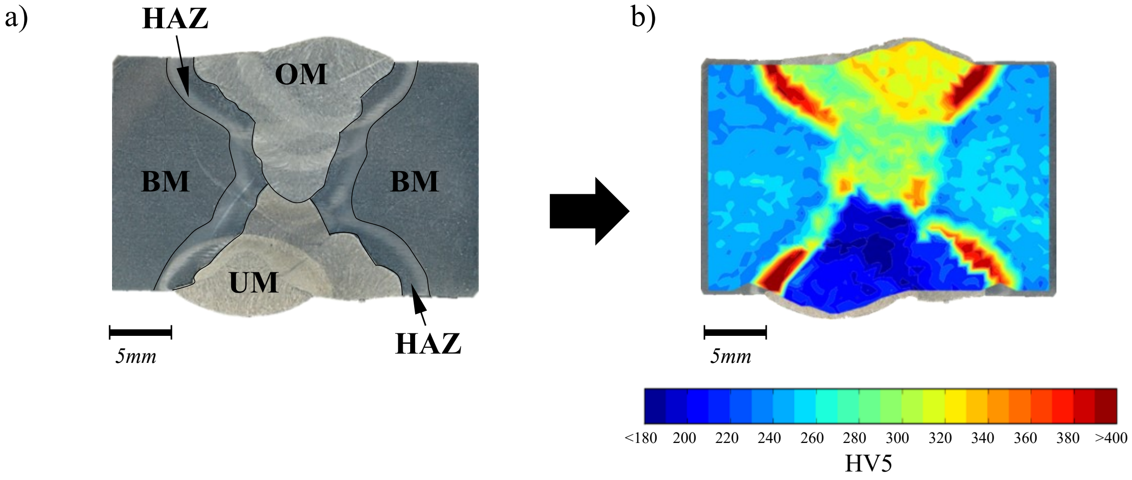

Figure 3.13 a) A weld section extracted from S690 test plate and b) hardness (HV5) contour plot obtained from the sample shown in a) with approximately 1000 indents (source: [17]).

Comparing Figure 3.10, Figure 3.11 and Figure 3.12with the hardness map that is shown in Figure 3.13 b) reveals that all measurements produced similar values of hardness. The hardness map indicates hardness of the base material in range 230 ÷ 260 HV. In comparison to the base material, the UM weld exhibits lower hardness in range 180 ÷ 220 HV, while the OM weld exhibits higher hardness in range 280 ÷ 350 HV. Again, the highest hardness >370 HV is observed in the HAZ. The presented hardness map also shows variations in hardness within the weld material. Here, peak hardness values occur in narrow bands at the interfaces between subsequent weld passes and correspond with the weld metal that was reheated (grain refined) after its deposition. Moreover, the hardness map reveals that maximum values of hardness in the HAZ can be observed near both weld faces, where final layers of the weld were deposited. The HAZ near the weld root underwent multiple reheating cycles during the weld layers deposition and thus subjecting the base material in that region to tempering heat treatment. Lacalle et al.[89] reported, that such heat treatment results in transformation of the typical structure of carbides into nodular clusters and thus severely reduces the hardness of the material.

3.3.2 Local Tensile Properties

The results of hardness measurements, presented in the previous chapter, provide a comprehensive insight in heterogeneity of the material in the weld joint. This was the main motivation to investigate local mechanical properties, as their variations have a significant impact on the crack driving force [79].

Local mechanical properties are normally characterized by tensile testing of micro tensile specimens [90]. Due to their small dimensions, such specimens are appropriate for testing specific microstructural regions in the bulk material [91]. Study conducted by Koçak [92] demonstrated that micro tensile specimens are suitable to determine variations in the stress-strain behaviour of various weld regions. These stress-strain relations are particularly useful for establishing constitutive material models of local material regions in various welds [12]. In conjunction with the corresponding hardness map of the weld cross section [88], these material models enable in depth analysis of the effect of the weld heterogeneous structure on the crack driving force, as it was recently demonstrated by Naib et al. [93].

The micro tensile specimens that were incorporated in this research, were oriented in longitudinal direction with respect to the weld and were stacked in two directions; i.) across the weld and ii.) through the thickness of the weld. The micro tensile specimens, extracted from the former stack direction were used for determining the material properties of the heat affected zone and variations of mechanical properties across the weld. And the micro tensile specimens extracted from the latter stack direction were used for determining the weld material properties in the narrow regions of deposited material and reheated material in the weld layers. The corresponding layout is shown in Figure 3.14 a). It is important to note that the micro tensile specimens were extracted from the part of the welded sample plate that was later used for the hardness measurements which are described in the previous chapter. This way, the hardness and the material tensile properties were obtained from the same part of the weld and could be correlated as described in the following chapter.

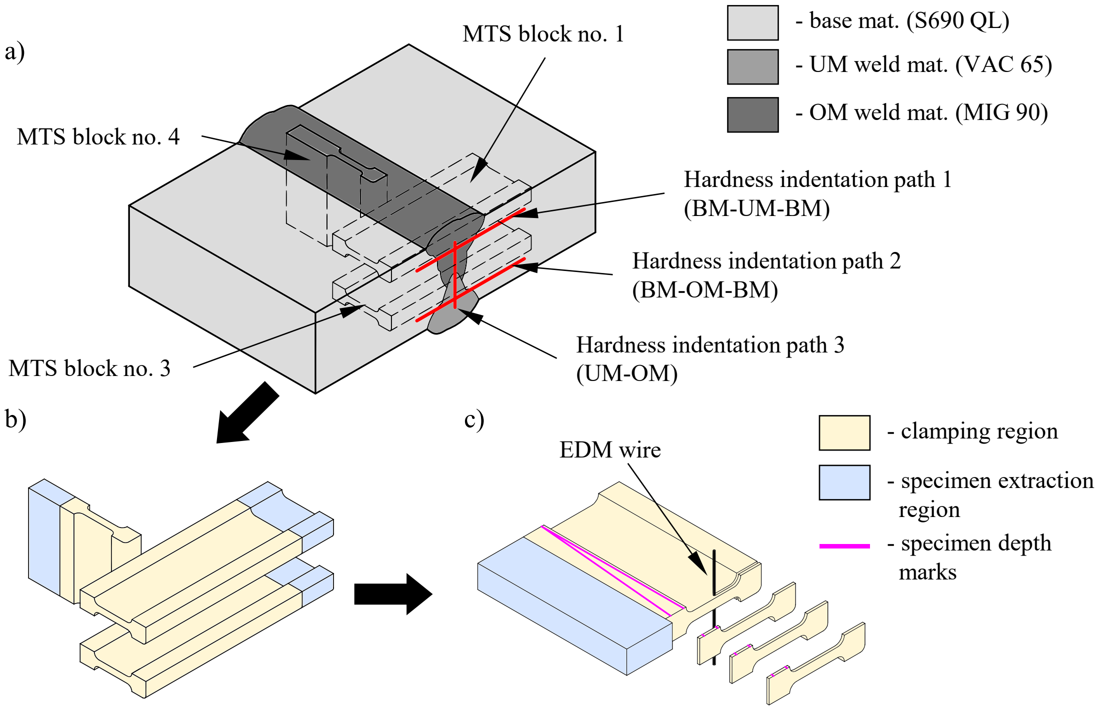

Figure 3.14 The process of the micro tensile specimens extraction; a) the part of a welded sample plate with a layout of the micro tensile specimens blocks and marked hardness measuring paths, b) extracted blocks and c) the cutting of the micro tensile specimens from the extracted blocks.

The micro tensile specimens were extracted by wire electrical discharge machining. The cutting operations were performed in two steps. In the first step, blocks of material were extracted from a part of the weld in stack directions of micro tensile specimens, as shown in Figure 3.14 b). In the second step, the flat micro tensile specimens were cut from the extracted blocks, as shown in Figure 3.14 c). A dog bone shape of the fabricated micro tensile specimens has been adopted from [21] and is shown in Figure 3.15. The shape of the micro tensile specimens is characterized by $a \times b = 2.0 \times 0.5$ mm prismatic cross-section, with area 1 mm^2 and a gauge length $G = 4 \times a = 8.0$ mm.

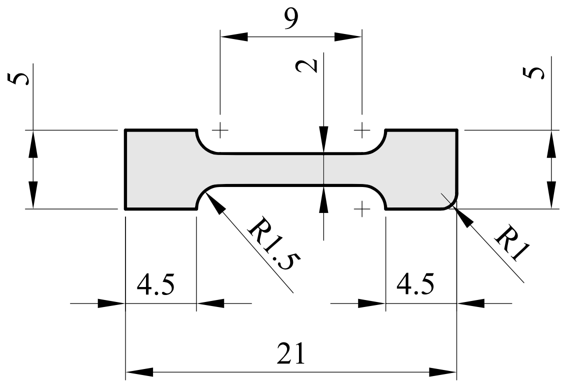

Specimen thickness: 0.5 mm

Figure 3.15 The geometry of the tested micro tensile specimens.

Micro-scale uniaxial tests were conducted in Laboratory for Machine Parts and Structures at Faculty of Mechanical Engineering in Maribor. Instron 1255 uniaxial testing machine has been used. A load cell with maximum capacity of 20 kN has been mounted in order to accurately measure the load, as shown in Figure 3.16 a). The micro-scale uniaxial tests are not yet standardized except for the specific requirements for testing foil materials given in ASTM E345-93 [94]. For that reason, tensile testing protocol that is given by ASTM E8/E8M-13a standard [95] has been followed. Small dimensions of the micro tensile specimens prevented tracking elongation during the test with a classical extensometer. Therefore, the elongation has been measured using GOM Aramis 3D Digital Image Correlation (DIC) system [96], as shown in Figure 3.16 b). The micro tensile specimens were loaded in displacement control with crosshead displacement rate 0.45 mm/min. Despite slightly elevated test speed, quasi-static conditions were established during the monotonous loading. In total, 122 micro tensile specimens were tested.

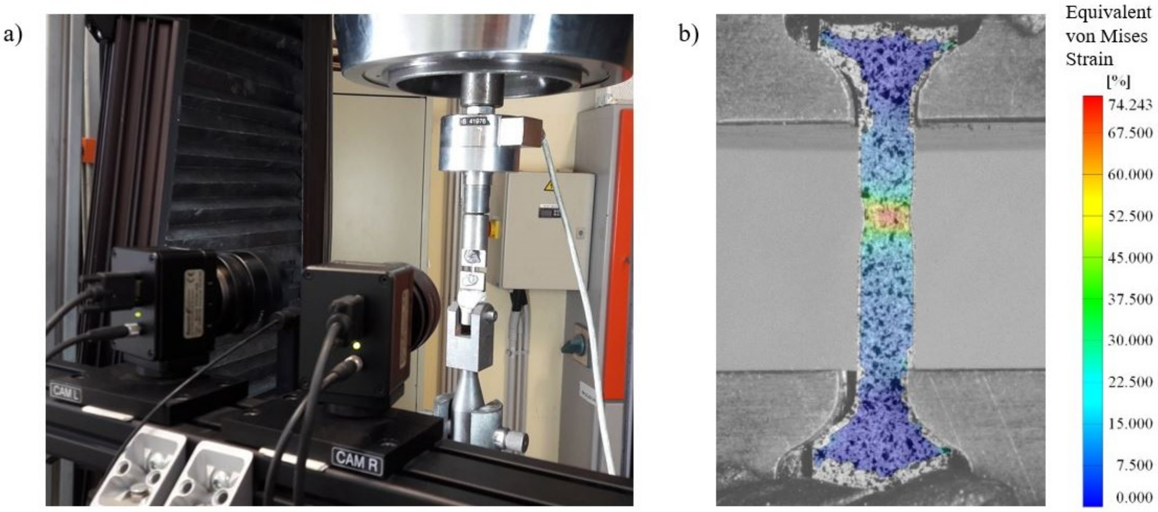

Figure 3.16 The micro-scale tensile testing; a) test setup with additional load cell and GOM Aramis 3D DIC system and b) post-test analysis of strain field on the surface of the micro tensile specimen.

Engineering stress-strain relationship (henceforth denoted as S-e curve) has been determined for each micro tensile specimen from the measured load-elongation history. Here, an engineering stress was computed using the following equation:

$$S = P/A_0 \tag{3.6}$$

where S is the engineering stress in [MPa], P is tensile load in [N] and A_0 is the initial cross-sectional area of the gage section in [mm^2]. The corresponding engineering strain was computed using the following equation:

$$e = \Delta L/L_0 \tag{3.7}$$

where e is an engineering strain in [mm/mm], L_0 is the initial gage length in [mm] and ΔL is the change in the gage length that is defined as difference between elongated gage length and the initial gage length (L–L_0) in [mm]. Elastic behavior of the material has been characterized with elastic modulus E that represents the slope of the initial proportional part of the S-e curve. the elastic modulus is defined according to the following equation:

$$E = S/e \tag{3.8}$$

where E is the elastic modulus in [MPa], S is engineering stress in [MPa], and e is engineering strain in [mm/mm]. According to ASTM E111-04 standard [97], all data points in proportional part of the *S-e* curve have been incorporated in linear relationship in Equation (3.8) by the least squares method.

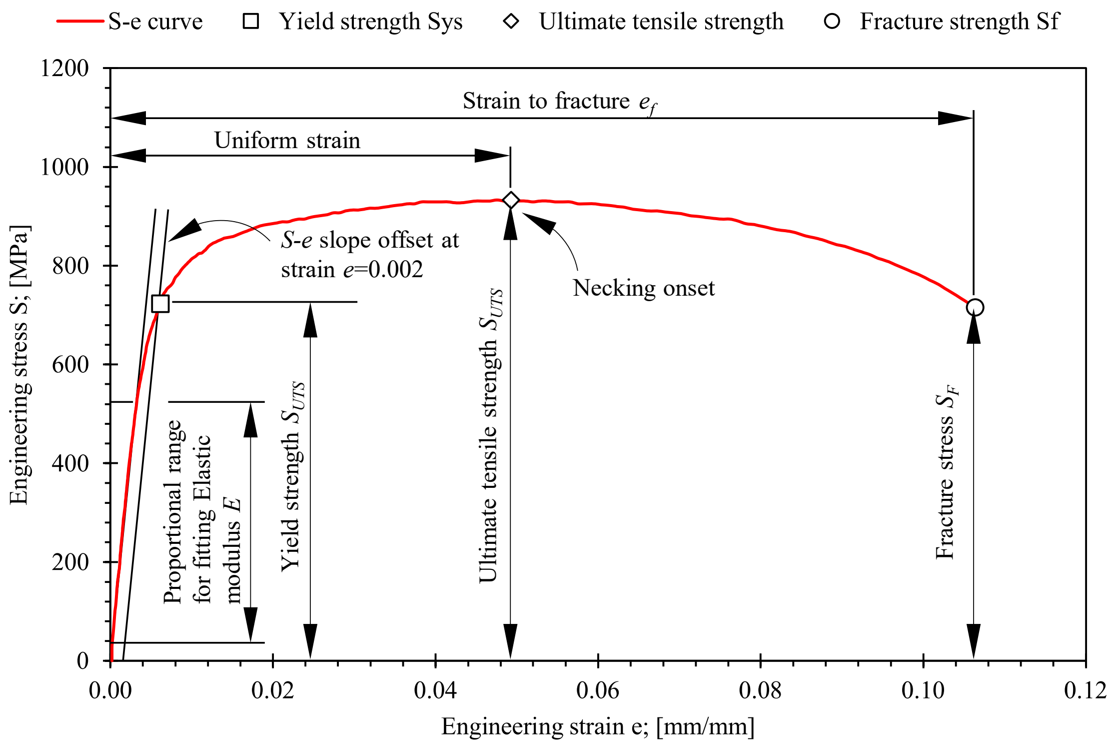

Figure 3.17 The example of *S-e* curve of the tested micro tensile specimen that was extracted from the reheated OM weld material. The characteristic parameters are marked.

In general, the obtained *S-e* curves exhibited a smooth onset of yielding, as demonstrated on the example of the reheated OM weld material *S-e* curve in Figure 3.17. Therefore, yield strength S_{YS} has been defined as the stress corresponding to the intersection of the *S-e* curve offset at 0.2 % strain, i.e. e=0.002 mm/mm. The ultimate tensile strength S_{UTS} has been defined as maximum load divided by nominal cross-sectional area according to the following equation:

$$S_{UTS} = P_{max}/A_0 \tag{3.9}$$

where S_{UTS} is the ultimate tensile strength in [MPa], P_{max} is maximum recorded load in [N] and A_0 is nominal cross-sectional area in [mm^2]. For ductile metals, the ultimate tensile strength is regarded as a measure of the maximum load that a metal can withstand under the very restrictive conditions of the uniaxial loading. It also represents the point of material instability during plastic deformation under the uniaxial loading that results in the specimen necking onset, which from herein develops continuously until the specimen rupture. The engineering strain at rupture has been used to characterize the ductility of the material. It is defined according to the following equation:

$$e_f = \frac{L_f - L_0}{L_0} \cdot 100\% \tag{3.10}$$

where e_f is elongation at rupture in [%], L_f is final length in [mm], and L_0 is the initial gage length in [mm]. Because an appreciable fraction of the plastic deformation is concentrated in the necked region of the tensile specimen, the value of e_f depends on the gage length L_0, over which the measurement was taken. The reduction in area does not suffer from this difficulty and it was therefore incorporated in this study as well. The reduction in area is defined as:

$$q = \frac{A_0 - A_f}{A_0} \cdot 100\% \tag{3.11}$$

where q is reduction in cross-sectional area in [%], while A_0 and A_f are the initial and the final cross-sectional area in [mm^2], respectively. Hardening behavior of the material due to plastic deformation has been characterized according to ASTM E646-07 standard [98]. First, the engineering S-e curves were converted to true stress-strain curves that are in this thesis denoted as σ-ε curves. This conversion has been done by using the principle of the constant volume and the principle of a homogeneous distribution of strain along the gage length of the tensile specimen [99]. Therefore, true stress was computed using the following equations:

$$\sigma = \frac{P}{A_0} \cdot (e + 1) = S \cdot (e + 1) \tag{3.12}$$

where σ is true stress in [MPa], S is the engineering strain defined as ratio of measured tensile force and initial cross-sectional area S=P/A_0 in [MPa], and e is the engineering strain in [mm/mm]. True strain was computed using the following equation:

$$\varepsilon = ln(e+1) = ln\frac{L}{L_0} \tag{3.13}$$

where ε and e are true and engineering strain in [mm/mm], respectively, and L and L_0 are the measured elongated and initial gage lengths in [mm]. It is important to note, that Equations (3.12) and (3.13) are valid only until the necking onset due to the subsequent material instability and the localized plastic deformation in the necked region in the gage section of the tensile specimen. For that reason, material behaviour beyond the maximum load (shown in Figure 3.18 a)) must be evaluated on the basis of true cross-sectional area, using Equations (3.14) and (3.15):

$$\sigma_i = \frac{P_i}{A_i} \tag{3.14}$$

$$\varepsilon_i = ln\frac{A_0}{A_i} = ln\frac{a_0 \cdot b_0}{a_i \cdot b_i} \tag{3.15}$$

where σ_i and ε_i are true stress in [MPa] and strain in [mm/mm], respectively, and P_i is actual measured tensile force in [N]. A_i and A_0 are the actual and the initial cross-sectional areas in [mm^2] that are expressed as products of true $A_i=a_i \cdot b_i$ and the initial $A_0=a_0 \cdot b_i$ cross-section width and thickness (for flat micro tensile specimens). The accurate measurements of a_i and b_i during tensile tests were not possible with the available equipment. Therefore, behaviour of the material after the maximum load was described with linear relationship between the points of maximum load and fracture (majority of materials express linear behaviour beyond the maximum load [99]). In case of the latter (shown in Figure 3.18 b)) true stress σ_f and strain ε_f at fracture were computed by substituting members a_i and b_i in Equations (3.14) and (3.15), with specimen's width a_f and thickness b_f at fracture. Both dimensions were measured post-test with high precision optical microscope. It is important to note, that simply measuring minimum thickness and width of the contracted cross-section does not suffice in this case as deformation of the cross-section is substantial with respect to its initial dimensions. To overcome this issue, five consecutive measurements of the width a_f and the thickness b_f of the cross-section were performed as shown in Figure 3.18 c).

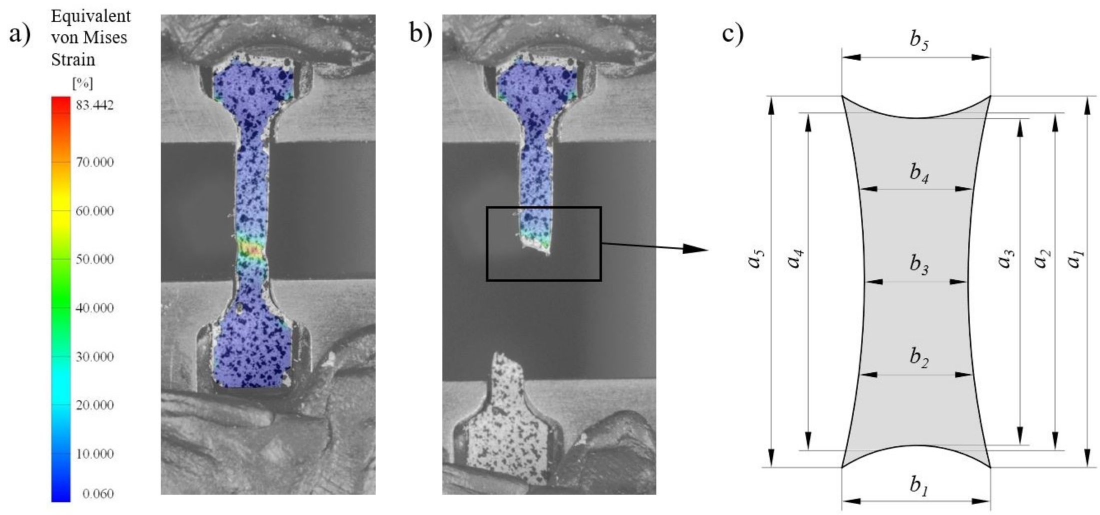

Figure 3.18 Important features of micro tensile testing; a) specimen necking beyond the maximum load, b) a fracture onset and b) the post-test measurement sequence of a specimen's cross-section (the width a_i and the thickness b_i).

The average width and thickness at fracture were then computed as the average values of five consecutive measurements:

$$a_f = \frac{\sum_{i=1}^{n} a_i}{n} \tag{3.16}$$

$$b_f = \frac{\sum_{i=1}^{n} b_i}{n} \tag{3.17}$$

where a_f and b_f are the specimen width and thickness at fracture, while a_i and b_i represent five consecutive measurements of the width and the thickness, respectively, as shown in Figure 3.18 c). Plastic behaviour of the material was described in terms of strain hardening by computing, strain hardening exponent n and coefficient K determined as per ASTM E646-07 standard [98]. Here, the strain hardening exponent was computed by using the following equation:

$$n = \frac{N \cdot \sum_{i=1}^{N}(\log \varepsilon_i \cdot \log \sigma_i) - (\sum_{i=1}^{N} \log \varepsilon_i) \cdot (\sum_{i=1}^{N} \log \sigma_i)}{N \cdot \sum_{i=1}^{N}(\log \varepsilon_i)^2 - \sum_{i=1}^{N}(\log \sigma_i)^2} \tag{3.18}$$

where n is unitless strain hardening exponent, σ_i is true stress in [MPa], ε_i is true strain in [mm/mm], and N is total number of (ε_i, σ_i) data pairs. The strain hardening coefficient was computed according to the following equation:

$$logK = \frac{\sum_{i=1}^{N}(\log \sigma_i) - n \cdot \sum_{i=1}^{N}(\log \sigma_i)}{N} \tag{3.19}$$

where *K* is unitless strain hardening coefficient, σ_i and ε_i are true stress and strain respectively, *N* is the total number of (ε_i, σ_i) data pairs, and *n* is strain hardening exponent, computed using Equation (3.19). It is important to note that the computed strain hardening exponent *n* and coefficient *K* should not be mistaken for exponent *n* and coefficient *α* of the Ramberg-Osgood material law [100], [101], as the latter are defined in a different way and have a different meaning.

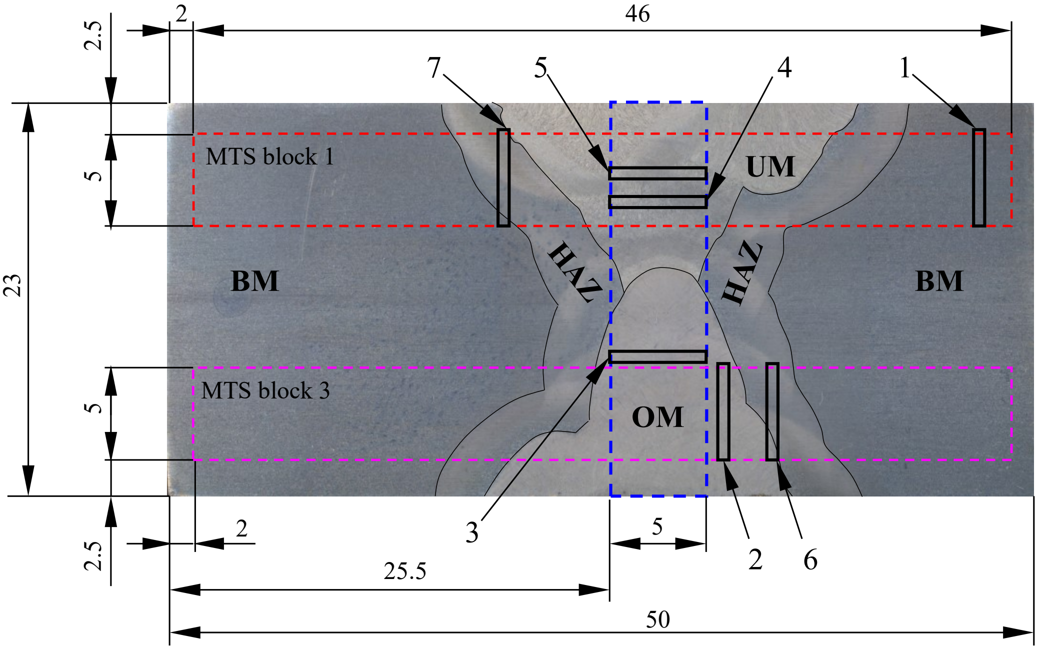

Marked micro tensile specimens:

1 - MTS-1-46 (base mat.)	2 – MTS-3-32 (OM, as welded)	3 – MTS-4-23 (OM, reheated)
4 – MTS-4-8 (UM, as welded)	5 – MTS-4-5 (UM, reheated)	6 – MTS-3-32 (HAZ, coarse)
7 – MTS-1-11 (HAZ, fine)		

Figure 3.19 Weld cross-section with marked positions of characteristic micro tensile specimens and corresponding extracted blocks.

Finally, a location of the gage section in the microstructure of the weld joint was investigated for each micro tensile specimen. First, a position of each specimen was compared to the weld macrograph photos and an initial assumption of the microstructure in the necked region was assessed. Then, the specimens were metallographically prepared, polished and etched with 2%

solution of nitric acid and alcohol, in order to expose microconstituents. A composition of microstructure in the gage section was investigated, using optical microscopy. Examples of the analysed micro tensile specimens that exhibited stress-strain behaviour closest to the average behaviour of all specimens with the same microstructural composition in the gage section are presented in this chapter. An approximate position of these micro tensile specimens in the weld joint is presented in Figure 3.19, while the corresponding microstructural compositions of the gage sections are presented in Figure 3.20 to Figure 3.26. The results for micro tensile testing are summarized in Table 3.7. The corresponding engineering stress-strain i.e. *S*-*e* curves are presented in Figure 3.27, while true stress-strain i.e. σ-ε curves are presented in Figure 3.28.

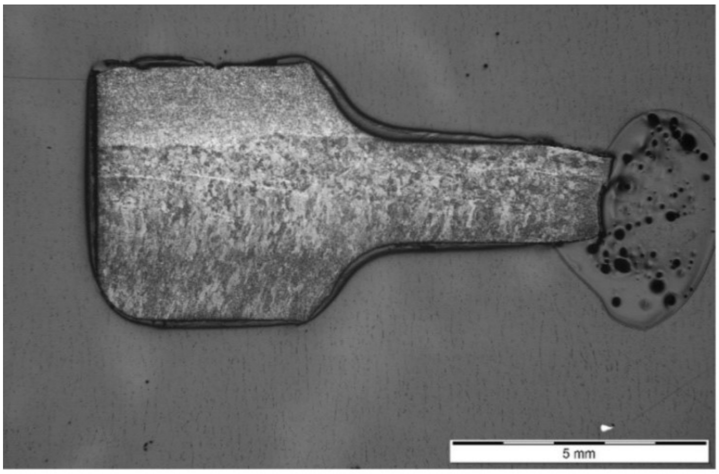

Specimen designation:
MTS-3-30

Material condition:
OM, as welded

Material data from tensile test:
SYS=754,3 MPa
SUTS=851,0 Mpa

Image magnification:
20x

Figure 3.20 The macrograph of micro the tensile specimen, extracted from the OM weld material in as welded condition.

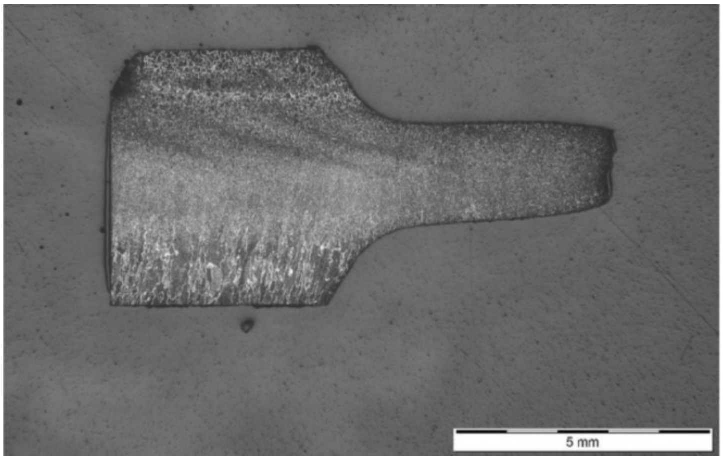

Specimen designation:
MTS-4-23

Material condition:
OM, reheated

Material data from tensile test:
SYS=749,9 MPa
SUTS=976,4 MPa

Image magnification:
20x

Figure 3.21 The macrograph of the micro tensile specimen, extracted from the OM weld material in reheated condition.

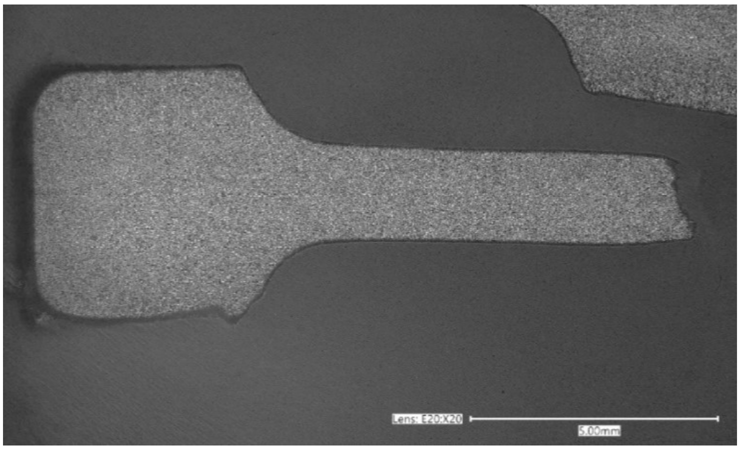

Specimen designation:
MTS-4-8

Material condition:
UM, as welded

Material data from tensile test:
SYS=508,2 MPa
SUTS=649,9 MPa

Image magnification:
20x

Remarks:
Image taken with different microscope.

Figure 3.22 The macrograph of the micro tensile specimen, extracted from the UM weld material in as welded condition.

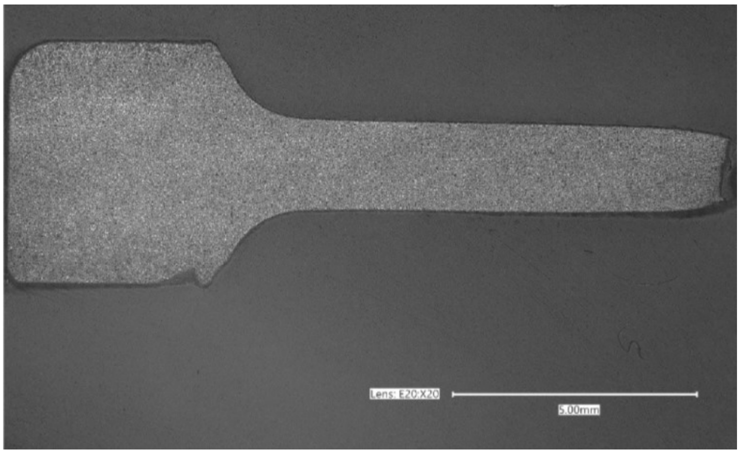

Specimen designation:
MTS-4-5

Material condition:
UM, reheated

Material data from tensile test:
SYS=430,4 MPa
SUTS=618,9 MPa

Image magnification:
20x

Remarks:
Image taken with different microscope.

Figure 3.23 The macrograph of the micro tensile specimen, extracted from the UM weld material in reheated condition.

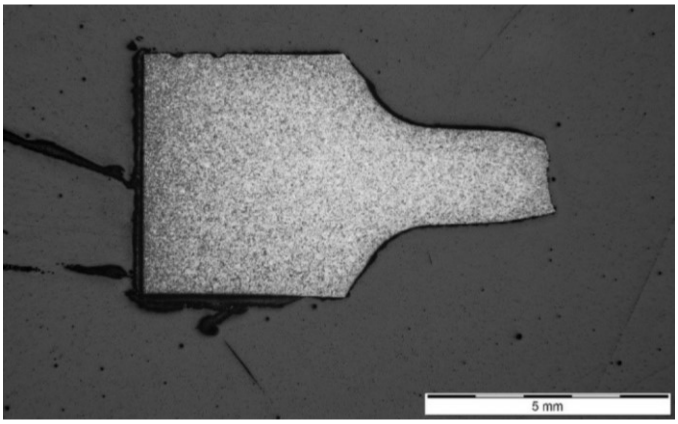

Specimen designation:
MTS-3-32

Material condition:
HAZ, coarse grained

Material data from tensile test:
SYS=864,3 MPa
SUTS=967,7 MPa

Image magnification:
20x

Figure 3.24 The macrograph of the micro tensile specimen, extracted from the coarse-grained part of the HAZ.

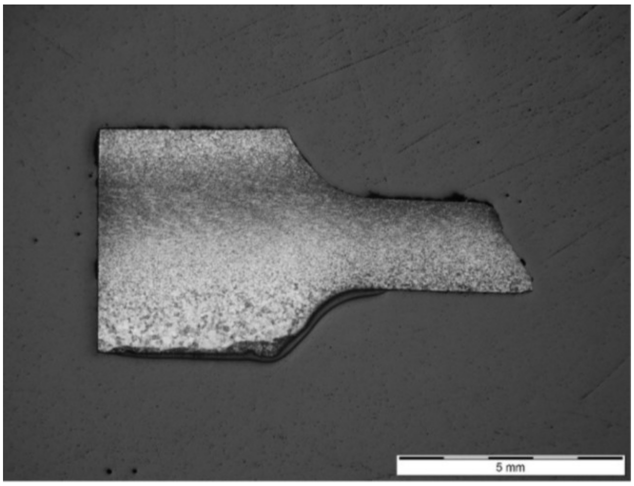

Specimen designation:
MTS-1-11

Material condition:
HAZ, fine grained

Material data from tensile test:
SYS=981,7 MPa
SUTS=1121,7 MPa

Image magnification:
20x

Remarks:
mixed microstructure from
coarse and fine grained HAZ

Figure 3.25 The macrograph of the micro tensile specimen, extracted from the fine-grained part of the HAZ.

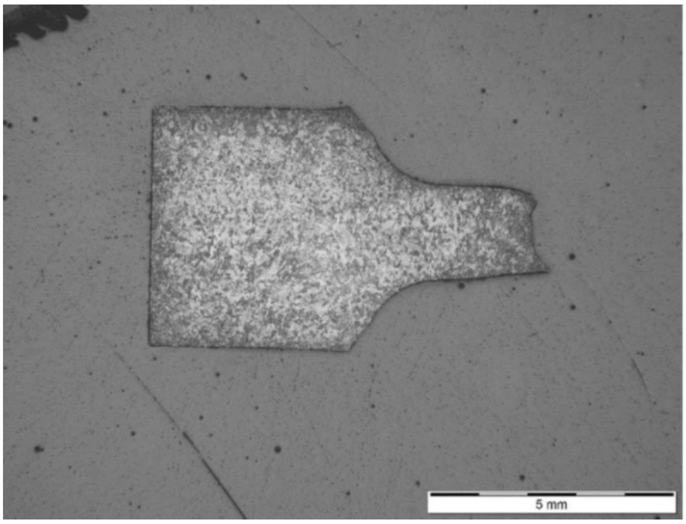

Specimen designation:
MTS-1-46

Material condition:
base material

Material data from tensile test:
SYS=642,0 MPa
SUTS=771,9 MPa

Image magnification:
20x

Remarks:
mixed microstructure from
coarse and fine grained HAZ

Figure 3.26 The macrograph of the micro tensile specimen, extracted from the base material.

Table 3.7 Overview of average results, obtained by tensile testing of micro tensile specimens.

Material	Elastic mod. E [MPa]	Yield strength S_{YS} [MPa]	Yield strength mismatch M [-]	Ultimate tensile strength S_{UTS} [MPa]	Elongation at rupture e_f [%]	Contraction at rupture q [%]	Hardening exponent n [-]	Hardening coefficient K [-]
OM as welded	208205	754.3	1.175	851.0	13.34	58.27	0.0737	20.839
OM as reheated	200167	749.9	1.168	874.8	7.48	55.81	0.1365	24.733
UM as welded	20888	447.5	0.697	632.8	18.50	62.48	0.1298	19.414
UM as reheated	200139	486.9	0.758	594.9	22.08	68.98	0.1567	19.547
HAZ coarse	26046	864.3	1.346	967.7	7.29	56.36	0.0693	22.272
HAZ fine	172954	974.3	1.518	1121.7	5.01	57.21	0.1169	25.866
Base material	199863	642.0	reference	771.9	11.75	60.10	0.0975	20.605

<u>Corresponding specimens:</u>

OM as welded – MTS-3-30
OM reheated – MTS-4-23
UM as welded – MTS-4-8
UM reheated – MTS-4-5
HAZ coarse – MTS-3-32
HAZ fine – MTS-1-11
Base material – MTS-1-46

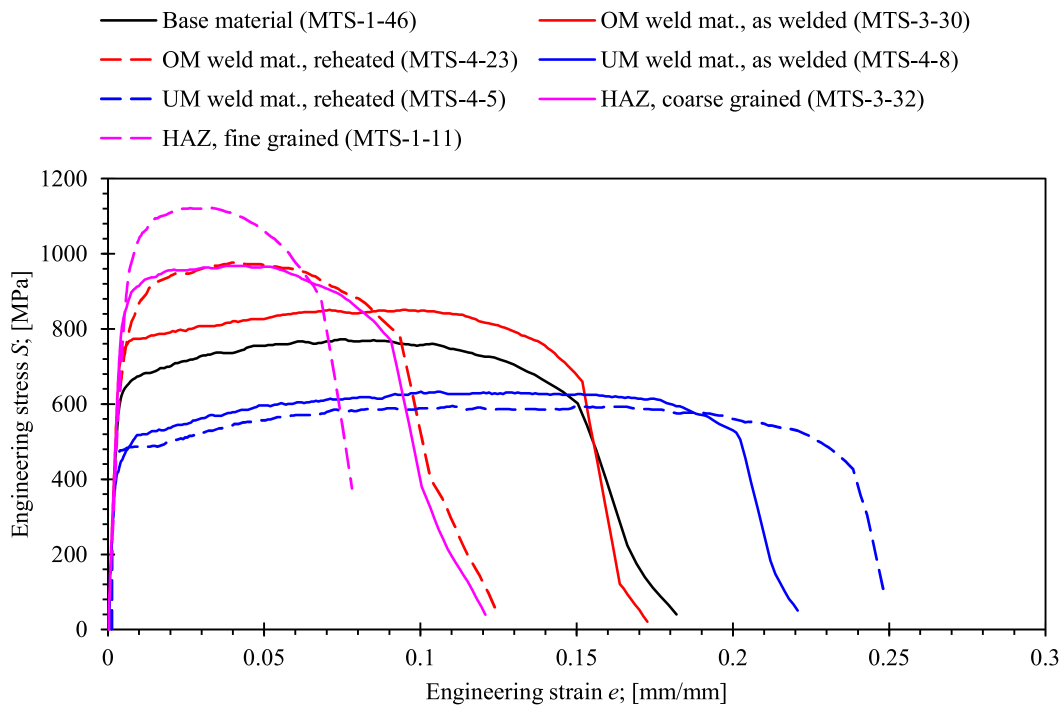

Figure 3.27 The engineering stress-strain (S-e) curves, obtained by micro tensile testing of specimens that are listed in Table 3.7.

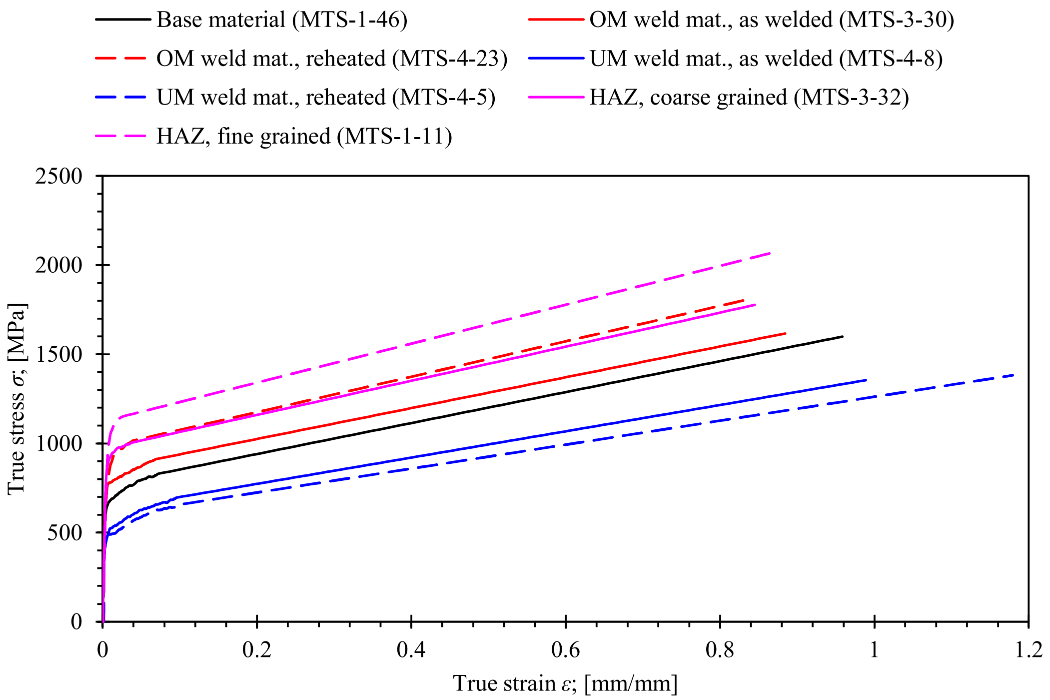

Figure 3.28 True stress-strain (σ-ε) curves, obtained by micro tensile testing of specimens that are listed in Table 3.7.

Figure 3.27 shows results of micro tensile tests in terms of engineering *S*-*e* curves. A significant difference between various parts of the weld can be observed. The fine-grained HAZ has the highest yield strength (S_{YS}=981.7 MPa) and ultimate tensile strength (S_{UTS}=1121.7 MPa), but low ductility (e_f=5.01 %, q=57.21 %). The opposite can be observed for the UM weld material in reheated condition. In this case, the material is highly ductile and has the highest total elongation (e_f=22.08 %) and contraction (q=68.98 %) at rupture but the lowest ultimate tensile strength (S_{UTS} =632.8 MPa) of all tested parts of the weld.

The comparison of results, listed in Table 3.7, and *S*-*e* curves, presented in Figure 3.27, show that, the OM weld material in as welded condition has 17 % higher yield strength and 10 % higher ultimate tensile strength in comparison to the base material. Both materials have a similar ductility with differences in total elongation and contraction at rupture within 10 % and 3 %, respectively. In contrary, the UM weld material in the as welded condition has 30 % lower yield strength and 18 % lower ultimate tensile strength in comparison to the base material. In terms of ductility, the UM weld material surpasses the base material with higher total elongation and contraction at rupture by 57 % and 4 %, respectively.

Moreover, the results in Table 3.7 and Figure 3.27 indicate that additional heat input has hardening effect on the OM weld material, where there is 3 % higher ultimate strength in reheated condition with respect to as welded condition. However, total elongation and contraction at rupture are reduced by 36 % and 7 %, respectively, indicating reduced ductility of the weld material in reheated condition.

The opposite effect was observed for the UM weld material. Yield strength is increased by 9%, but the ultimate tensile strength is reduced by 6 %, respectively in reheated condition, with respect to as welded condition. However, ductility is improved by 19 % regarding the total elongation, and 10 % regarding the contraction at rupture onset.

The HAZ show distinctive behaviour in their coarse-grained and fine-grained layers. The coarse columnar grains in the fusion zone are significantly larger than the grains in the remaining parts of the HAZ, and exhibit lower strength and hardness. This is a result of enhanced grain growth due to the high heat input during the welding process [32]. The fine-grained HAZ is a result of moderate heat input and short retention above the effective temperature of phase transformation. This results in finer grains that are primarily composed of ferrite and bainite with small parts of martensite. As a result, an increased hardness and material strength is expected in this part of the HAZ. The results of micro tensile tests in Figure 3.27 are in line with this theory and indicate that the coarse-grained HAZ has 35 % higher yield strength and 25 % higher ultimate tensile strength, with respect to the base material. However, ductility in terms of total elongation and contraction at rupture is reduced by 38 % and 6 %, respectively. Furthermore, stress-strain behaviour of the fine-grained heat affected zone shows the highest yield and ultimate tensile strengths of tested parts of the weld. The former is 14 % higher and the latter is 16 % higher in comparison to the coarse-grained HAZ. Furthermore, ductility of the fine-grained HAZ, in terms of total elongation at rupture, is further reduced by 31 % with respect to coarse-grained HAZ, while contraction is slightly lower, within 1.5 %.

3.3.3 Correlation of Local Hardness and Tensile Properties

A comprehensive overview of variations in mechanical properties over welded cross-section has been produced by comparing Vickers hardness (described in Chapter 3.3.1) with yield and ultimate tensile strength, obtained by micro tensile testing (described in Chapter 3.3.2). The purpose of this is to better understand mechanical properties of specific parts of the weld which could not be done with large scale testing (e.g. tensile testing of standard round bar specimens, extracted from the weld).

The overlay plots of hardness, yield strength and ultimate tensile strength versus distances along the weld section, were created. In general, the locations of indentation points (Figure 3.10 to Figure 3.12) and micro tensile specimens in the weld (Figure 3.19) do not match. Hardness at locations of micro tensile specimens has been computed using linear interpolation in order to compare it directly to the strength of the material. The obtained matching overlay plots are shown in Figure 3.29 for traverse across UM part of the weld, in Figure 3.30 for traverse across OM part of the weld, and in Figure 3.31 for traverse over the weld thickness.

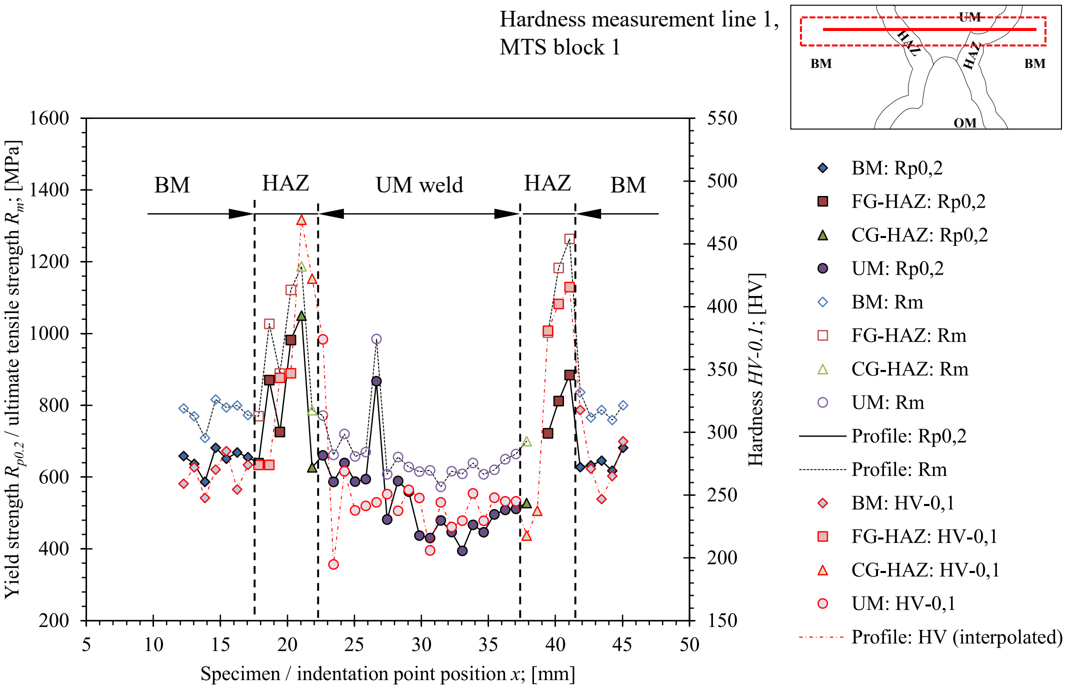

Figure 3.29 The overlay of the micro-indentation hardness, yield and ultimate tensile strength profiles for the UM part of the weld.

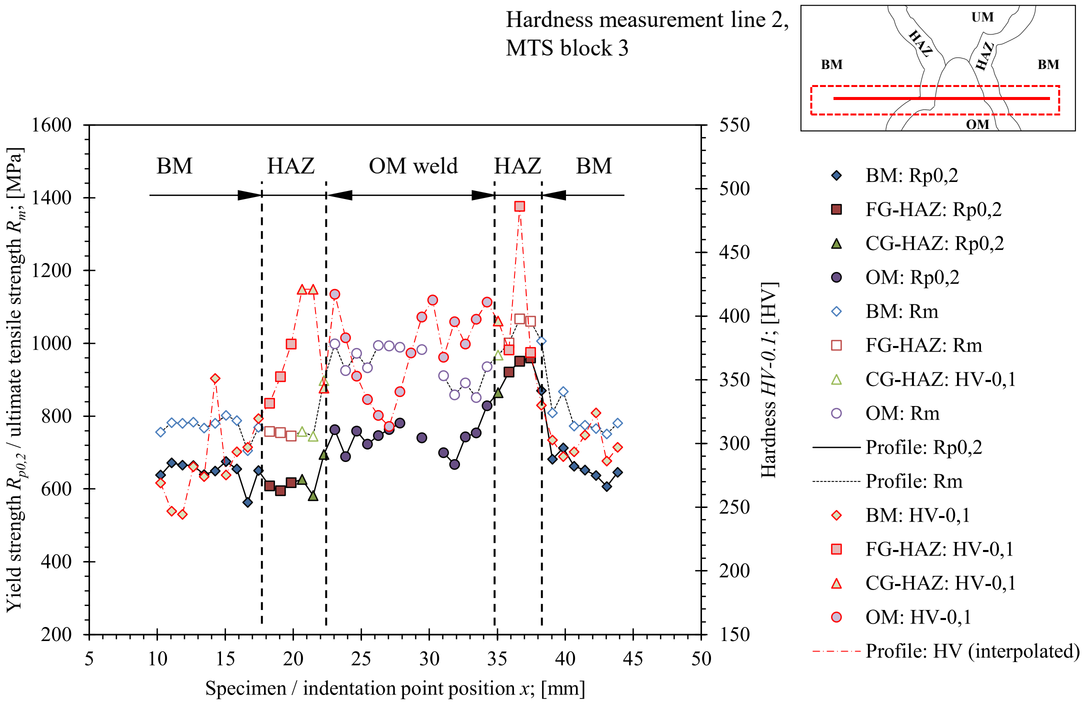

Figure 3.30 The overlay of the micro-indentation hardness, yield and ultimate tensile strength profiles for the OM part of the weld.

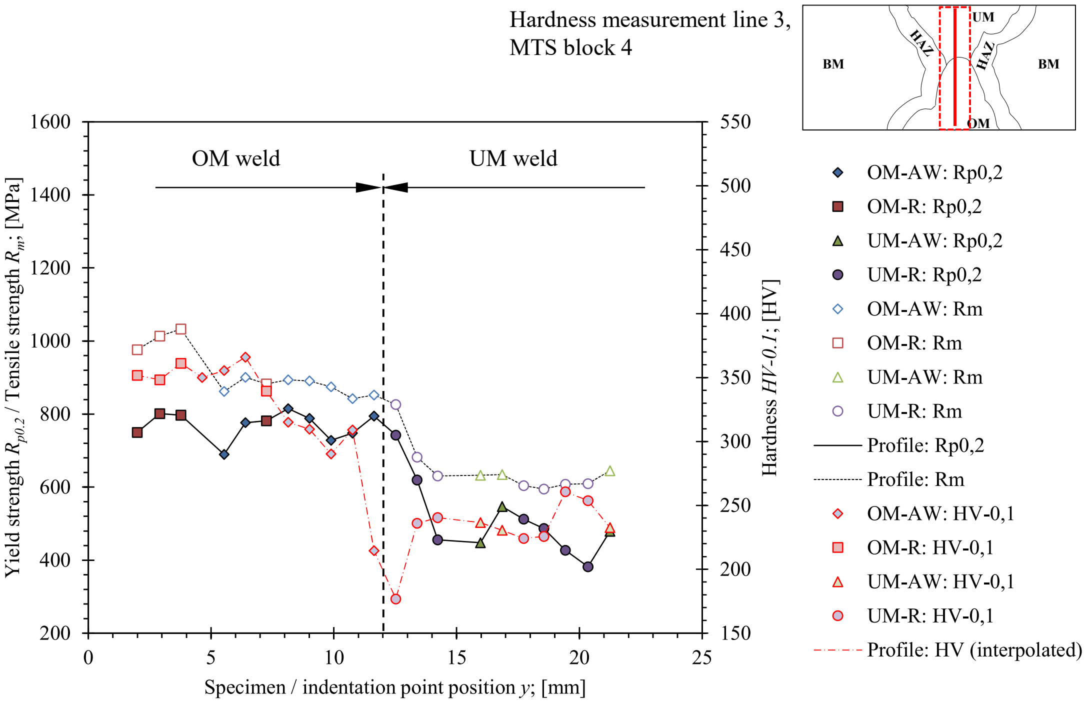

Figure 3.31 The overlay of the micro-indentation hardness, yield and ultimate tensile strength profiles along the weld thickness

In general, the strength corelates with the measured hardness. The overlay plots in Figure 3.29 and Figure 3.30 indicate that the entire weld is encased with the high strength layers of the HAZ. Variations in yield and ultimate tensile strengths in both, OM and UM parts of the weld are observed as well. Additionally, sudden changes in material properties can be observed in the transition from the OM to the UM part of the weld, as shown in Figure 3.31.

3.4 Determination of Global Material Properties

3.4.1 Tensile Testing

An average mechanical properties of the weld and the base material were investigated by tensile testing of standard round bar specimens with neck diameter of d=6 mm and gage length G=5×d=30 mm, as shown in Figure 3.32. The round bar AWMTT specimens were extracted from the qualification welds according to ISO 5792-1 [74], as described in Chapter 3.2.2. The groups of 3 specimens were extracted from base material and UM and OM weld materials, which constitutes 9 round bar tensile specimens in total. The tensile tests were conducted in the Laboratory for Machine Parts and Constructions in Maribor. INSTRON 1255 tensile and compression testing machine has been used. The specimens were loaded in displacement control with a crosshead displacement rate of 0.2 mm/min. Such rate of loading assured quasi-static conditions during monotonous loading, as specified in standard ASTM E8/E8M [95]. The elongation of specimens during testing has been measured with a dedicated extensometer, as shown in Figure 3.33. The same procedure, as described in Chapter 3.3.2, was used to post-process recorded load-elongation history. The summary of test results is presented in Table 3.8. Stress-strain behaviour in terms of engineering S-e and true σ-ε curves is shown in Figure 3.34 and Figure 3.35, respectively along with the results of micro tensile tests for a comparative purpose. Here, only curves closest to the average behaviour of each tested group of round bar tensile specimens are shown. The reason for that is to provide a clear overview of an average material behaviour under load for each part of the weld.

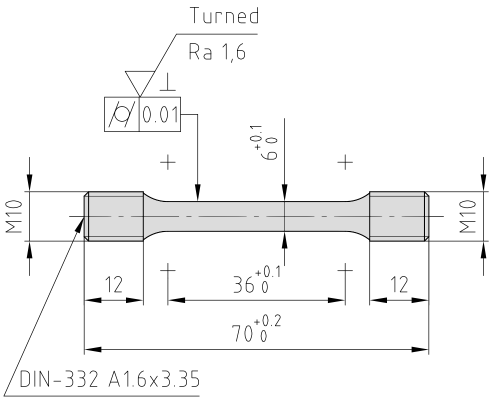

Figure 3.32 The geometry of tested round bar base material and AWMTT specimens.

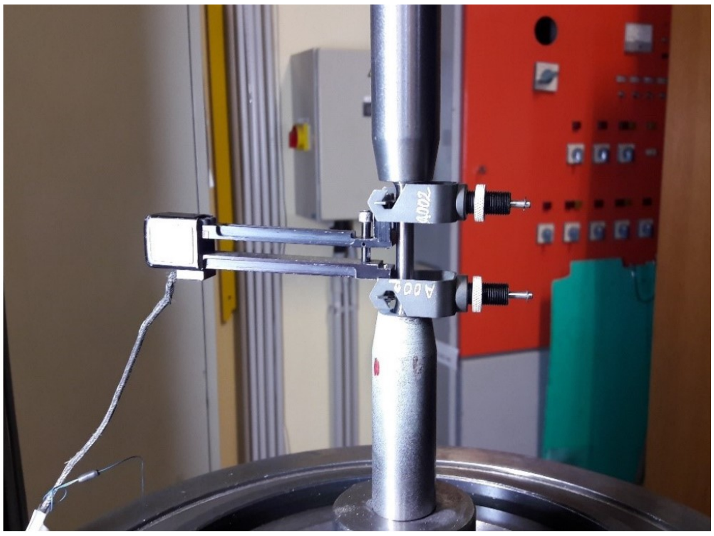

Figure 3.33 The Configuration of grips for tensile testing of round bar specimens. The dedicated extensometer is attached to the specimen for measuring elongation during loading

Table 3.8 The average results of the tensile testing of base material and AWMTT round bar tensile specimens.

Material	Elastic modules E [MPa]	Yield strength S_{YS} [MPa]	Yield strength mismatch M [-]	Ultimate tensile strength S_{UTS} [MPa]	Elongation at rupture e_f [%]	Contraction at rupture q [%]	Hardening exponent n [-]	Hardening coefficient K [-]
OM weld	215230	889.0	1.302	949.0	17.69	64.11	0.2123	24.493
UM weld	209879	532.1	0.779	587.4	22.52	66.27	0.1477	19.231
Base material	201109	682.8	Reference	791.3	21.85	75.23	0.0895	20.645

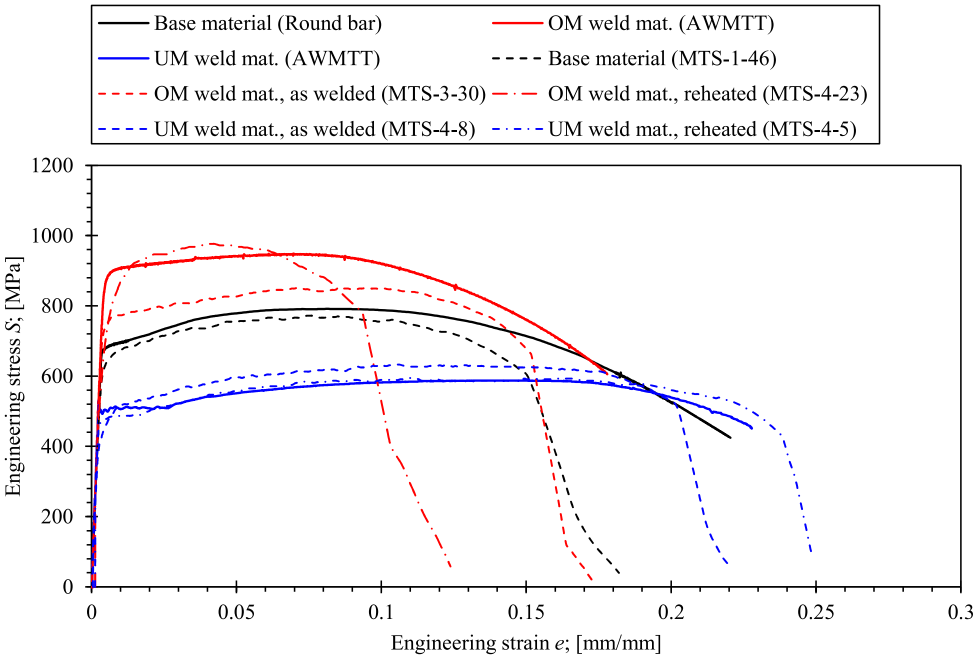

Figure 3.34 The engineering *S*-*e* relationships of different parts of weld, obtained by the tensile testing of round bar specimens.

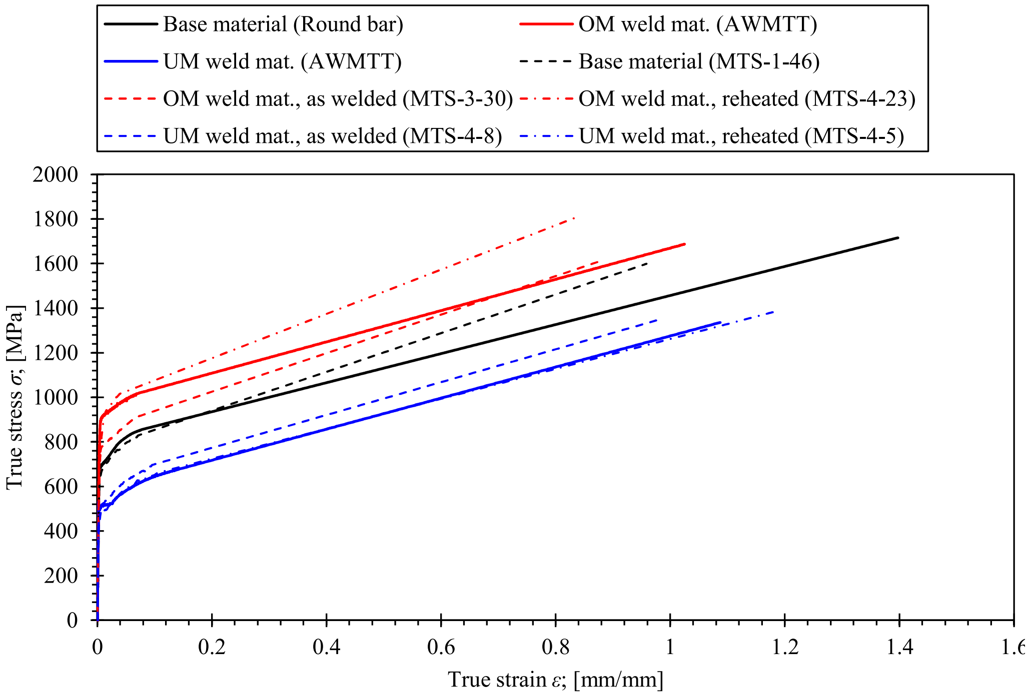

Figure 3.35 The true *σ*-*ε* relationships of different parts of the weld, converted from the *S*-*e* results of the round bar tensile testing.

In general, obtained *S*-*e* curves show a smooth onset of yielding. In this case, yield strength S_{YS} has been defined as stress corresponding to the intersection of the *S*-*e* curve offset at 0.2 % strain (i.e. e=0.002 mm/mm). However, the UM weld material exhibits discontinuous yielding with a Lüders plateau, as shown in Figure 3.34. Here, the yield strength has been defined as the upper yield strength S_{UYS}.

The comparison of the round bar AWMTT and miniature tensile tests in Figure 3.34 and Figure 3.35 shows very consistent behaviour of the UM weld material. In this case, *S*-*e* curves of the UM weld in as welded and reheated conditions follow average material behaviour that was determined by the AWMTT tensile test. A particularly good agreement between both kinds of tensile tests was observed in hardening behaviour of the UM material that is depicted with σ-ε curves. This indicates that the mechanical properties of the UM weld material are fairly consistent across the weld and are less susceptible to additional reheating of the material due to the deposition of multiple weld layers, as demonstrated in Figure 3.30 and Figure 3.31. The opposite was observed in case of the OM weld material. Here, *S*-*e* curves for as welded and reheated condition show deviations from the results of the AWMTT tensile test. The OM weld material in reheated condition shows similar yield strength and ultimate tensile strength, as in AWMTT tensile test, but ductility is severely reduced. The OM weld material in as welded condition has ductility that is comparable to AWMTT tensile test, but lower strength. Furthermore, σ-ε curves show increased local hardening of the OM weld in comparison to the average hardening behaviour that was determined by the AWMTT tensile test. This indicates that the OM weld material is more sensitive to additional reheating and therefore shows greater variations in terms of strength and ductility across the weld that is confirmed in overlay plot of hardness and strength properties in Figure 3.30 and Figure 3.31. Finally, the base material shows similar behaviour in miniature and AWMTT tensile tests. However, ductility is reduced in case of the former due to early onset of ductile fracture, that is recognized by the significant drop of the *S*-*e* curve before the final rupture of the miniature specimen. This earlier onset of ductile fracture is associated with reduced triaxiality of the stress field in the neck of the tensile specimen due to its smaller dimensions and flat geometry [102].

3.4.2 Charpy Impact Testing

Charpy impact tests [103], [104] provide a straightforward measure of the resistance of the tested material to brittle or fast fracture in the presence of a flaw or notch under fast loading conditions. The resistance of the material to fracture is here denoted as impact toughness and is quantified in terms of absorbed energy before the final fracture of the tested impact specimen. In the past, there were multiple attempts to correlate Charpy energy to the fracture toughness parameters, such as critical stress intensity factor K_{Ic} [105]–[107]. These correlations provide approximation of the fracture toughness at best, and are often unreliable or material specific. Structural integrity procedures, such as Fitness for Service [1] or BS 7910 [4] provide modules for the assessment of the fracture toughness from Charpy impact energy. However, such assessment is often highly conservative. The correlations between the fracture toughness and the Charpy impact energy are less reliable due to several differences between the Charpy impact test and fracture mechanics tests. Impact specimens contain blunt notch while fracture testing specimens have sharp fatigue cracks. Furthermore, sub-sized impact specimens have lower constraint, which has an effect on estimated fracture toughness [108]. In addition, impact specimens experience impact loading, while most fracture toughness tests are conducted under quasistatic conditions [28]. Despite the aforementioned specifics, Charpy impact test allows testing of specific regions in the weld due specimens' small dimensions [109], [110]. This is a simple test, that provides an approximate assessment of fracture behaviour for each part of the weld in a qualitative manner. Therefore, a programme of impact testing has been incorporated in this research.

Charpy impact tests were conducted in Laboratory for Welding at University of Maribor. The purpose was to test OM and UM weld materials and to investigate the influence of material heterogeneity on absorbed impact energy when a crack is propagating from the OM to the UM weld material and the opposite. 5 groups of 3 specimens were extracted from the weld root, pure OM weld material, pure UM weld material and the base material, as shown in Figure 3.36. This constitutes 15 notched Charpy specimens in total. In case of the former, double mismatched weld root (the combination of OM and UM weld material) was contained in the ligament of the notched Charpy specimens. The vertex of the fusion line located in the midplane. Here, 2 groups of these specimens were extracted. The first group had notches located in the OM weld material, while the second group had notches located in the UM weld material. This would result in crack initiation at the tip of the notch in the first weld material, and crack propagation through the fusion line to the other weld material, until the final fracture of the specimen during the impact loading.

The Charpy specimens were initially extracted as oversized rectangular bars with wire EDM. Sides of these bars were etched with 2% solution of nitric acid and alcohol in order to expose the weld. The position of the notch in the middle of the weld was then carefully marked as depicted in Figure 3.37. Finally, the Charpy impact specimens were machined with length L=55 mm, cross section $W \times b$=10×10 mm and V shaped notch with tip radius r=0.25±0.025 mm, as shown in Figure 3.38. The configurations of the extracted notched Charpy impact specimens with the notch located in the weld are presented in Figure 3.39.

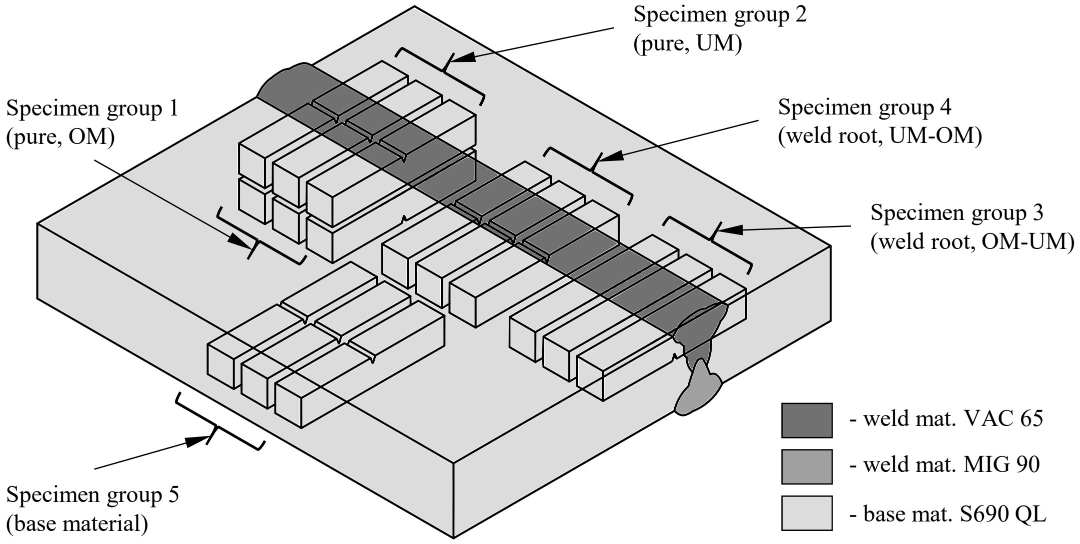

Figure 3.36 The layout of the extracted notched Charpy specimens.

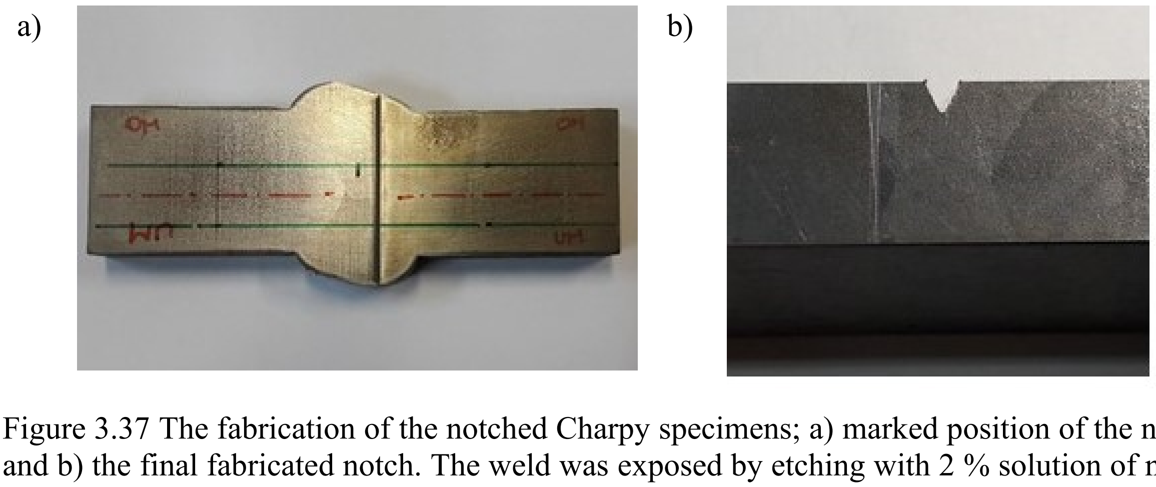

Figure 3.37 The fabrication of the notched Charpy specimens; a) marked position of the notch and b) the final fabricated notch. The weld was exposed by etching with 2 % solution of nitric acid and alcohol

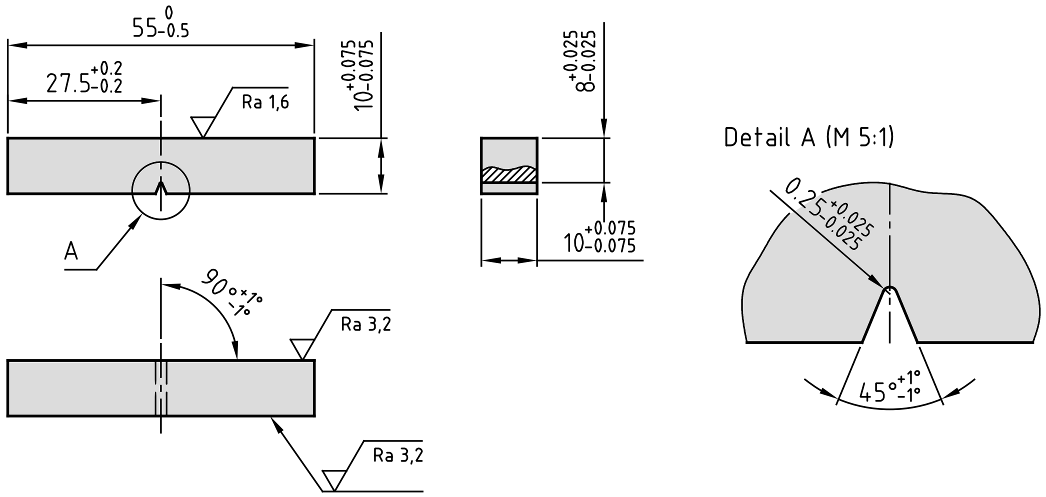

Figure 3.38 The geometry of the fabricated notched Charpy specimens.

a) Specimen group 1
(notch in OM weld material)

b) Specimen group 2
(notch in UM weld material)

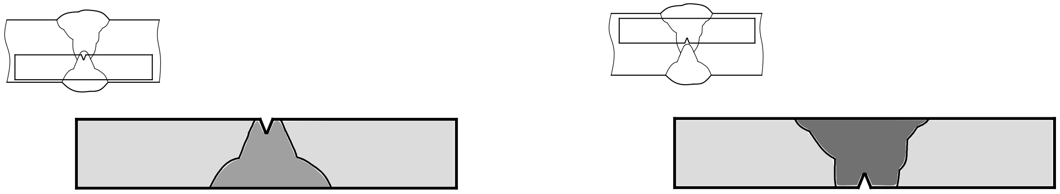

c) Specimen group 3
(notch in OM weld material, crack propagation to UM weld material)

d) Specimen group 4
(notch in UM weld material, crack propagation to OM weld material)

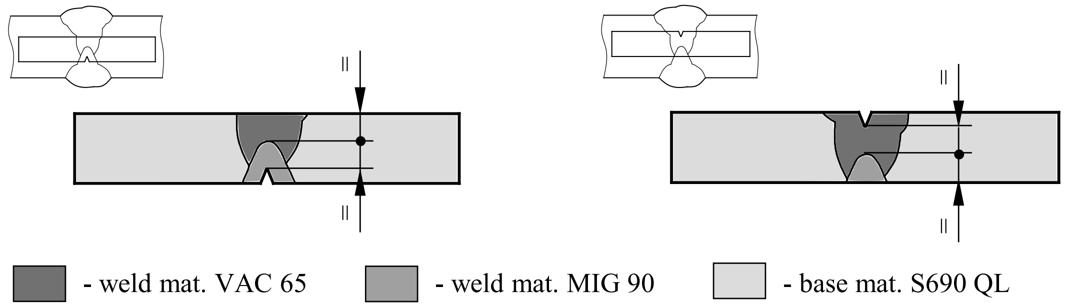

Figure 3.39 The configurations of the notched Charpy specimens that were extracted from a) the OM weld material, b) the UM weld material, c) the weld root with notch located in the OM weld material and d) the weld root with notch located in the UM weld material.

These tests were performed in conformance with ASTM E23 [111] standard. A pendulum device AMSLER RKP 300 with maximum capacity of 300 J has been used for impact testing of Charpy notched specimens in three-point bending. This pendulum device was equipped with sensors for high speed monitoring of the impact force during the testing and VUHICHARPY software [112], [113]. This software allows dividing the specimen fracture energy into components by means of transforming the load-time (*P-t*) recorded history into the load-displacement (*P-s*) data. To do this, changes in the velocity of the striker *v(t)* during the impact loading of the specimens are determined using double successive integration according to the recommendations given in [114]:

$$v(t) = v_0 - \frac{1}{m} \int_{t_0}^{t} P(t)\, dt \tag{3.20}$$

where *m* is the known mass of the striker in [kg], v_0 is the initial impact velocity in [m/s], *v*(t) is a variation of the striker velocity in the process of impact loading in [m/s], t_0 and t are lower and upper limit of the time interval in [s] and *P*(t) is a function of the impact force in dependence of time in [N]. Then, the dependence of the hammer displacement *s* on the duration of loading *t* is determined as follows:

$$s(t) = \int_{t_0}^{t} v(t)\, dt \tag{3.21}$$

where *s(*t) is a variation of the striker displacement in dependence of time in [m], *v*(t) is variation of striker velocity in [m/s] and t_0 and *t* are lower and upper limit of time interval in [s]. Furthermore, general energy to completely break the specimens *W* during the impact loading was considered as the sum of energies required for crack initiation W_i and propagation W_p:

$$W_t = W_i + W_p \tag{3.22}$$

where W_t, W_i and W_p are total energy to completely break the specimens, energy to crack initiation and energy to crack propagation, respectively in [J]. Here, the energy to completely break the specimens is determined as the area under the complete *P-s* curve. Energy to initiate the crack is determined as the area under the *P-s* curve up to the point of ductile crack initiation

P_i. Energy to crack propagate the crack is determined as $W_p=W_t-W_i$, which is the difference between the total energy to completely break the specimens and energy to initiate the crack. The dynamic fracture toughness of tested specimens was estimated according to the following formula [115]:

$$J_{id} = \frac{2W_i}{B(W-a)} \tag{3.23}$$

where J_{id} is dynamic fracture toughness, expressed in terms of the energy in [J/m^2], W_i is energy to initiate the crack in [J], B and W are specimen thickness and width in [mm], respectively, while a is the depth of the notch in [mm]. The J_{id} was then converted to [kJ/m^2] for a better comparison of results of quasi-static fracture tests, which are in detail described in Chapter 3.5.

The obtained results are presented in Table 3.9 along with computed mean values and standard deviation (SD) of the sample data. The computed load-displacement (P-s) data is presented in Figure 3.40. Here, the only data corresponding to the specimens that exhibited impact behaviour closest to the average in each tested group is presented. The presented load-displacement (P-s) data indicates ductile failure of the tested specimens. It is assumed that only stable crack propagation occurred during the impact loading as no sudden drops of the load P are observed. In this case, standards for impact testing with instrumented pendulum device, such as ISO 14556 [114] and ASTM E2298 [116], do not provide a method for evaluation of the point on P-s data that corresponds to crack initiation.

To identify the point of ductile crack initiation from the experimental results in form of P-s data, Kobayashi [117] proposed a method that is based on principle of the compliance changing rate. The changing rate of the compliance of loaded Charpy specimen in three-point bend can be calculated from the following expression:

$$\frac{\Delta C}{C} = \frac{C - C_{el}}{C_{el}} \tag{3.24}$$

where C is the secant compliance in [mm/N] and C_{el} is the initial elastic compliance of the loaded Charpy specimen in [mm/N]. Aforementioned compliance factors are defined as follows:

$$C = \frac{ds}{dP} \tag{3.25}$$

$$C_{el} = \frac{s_{el}}{P_{el}} \tag{3.26}$$

where ds and dP are displacement increment in [mm] and force increment in [N], respectively, while S_{el} and P_{el} are displacement increment in [mm] and force increment in [N] for the initial linear elastic part of the P-s data. Basically, C_{el} represents reciprocal value of the slope defined in the initial linear elastic part of the P-s data. Furthermore, C represents reciprocal value of the slope of the secant line that is defined through the initial point and an arbitrary point on the P-s data set. The corresponding visual presentation on the definition of C and C_{el} compliance factors is shown in Figure 3.41. Considering that displacement of the striker gives good prediction of bending deflection of the Charpy specimen, then the ductile crack initiation can be determined by a calculation and plotting of the $\Delta C/C$ against the displacement of the striker. The corresponding point of ductile crack initiation is then identified as a sudden transition point on the secant compliance gradient as shown in Figure 3.41. This method has been proved to be valid by a comprehensive research that was conducted by N. D. Alexopoulos et al. [118]. The corresponding results showed that the onset of the ductile crack initiation occurs prior the maximum force in P-s data. This fact has been recently endorsed in study of Jia et al. [119] that is based on corellation of experimental results that were obtained by impact testing and numerical results that were obtained through extensive FEA programme.

The presented method [117] has been used in this research to determine the ductile crack initiation from the P-s record. Remaining characteristic points on the P-s data, such as general yield force P_{Gy} and maximum force P_m, have been identified according to standard ASTM E2298 [116]. The energy inputs to rupture W_t, ductile crack initiation W_i and propagation W_p were determined as the area under P-s curve up to final fracture, ductile crack initiation force P_i and up to maximum recorded force P_m, respectively. Finally, fracture surfaces of the tested Charpy specimens were visually inspected with the optical microscope. The corresponding photos of the fracture surfaces are shown in Figure 3.42. The inspection confirmed that all specimens exhibited ductile fracture.

Table 3.9 The results of the Charpy impact testing.

Material	Specimen designation	Energy of rapture W_t [J]	Energy of crack initiation W_i [J]	Energy of crack propagation W_p [J]	General yielding force P_{Gy} [N]	Maximum force P_m [N]	Dynamic fracture toughness J_{id} [kJ/m^2]
OM weld (Group 1)	CVN-31-TS	102.78	27.85	74.93	12023	23082	687.77
	CVN-32-TS	09.15	22.16	87.02	12362	23516	556.34
	CVN-33-TS	101.49	21.80	79.69	12839	23516	540.71
	Mean val.	104.49	23.39	80.54	12408	13209	594.94
	SD	4.10	3.40	6.09	410	267	80.77
UM weld (Group 2)	CVN-37-TS	124.16	34.83	89.33	12170	21661	868.22
	CVN-38-TS	127.50	23.68	103.82	12174	20823	593.94
	CVN-39-TS	124.66	17.85	106.81	12160	21050	451.37
	Mean val.	125.44	25.45	99.99	12168	21068	637.84
	SD	1.80	8.63	9.35	7	254	211.87
OM-UM notch in OM (Group 3)	CVN-43-TS	125.98	19.98	106.01	12161	19713	507.24
	CVN-44-TS	117.89	23.72	94.17	12379	19494	597.81
	CVN-45-TS	110.75	28.35	82.40	12094	20135	710.10
	Mean val.	118.21	24.01	94.20	12201	19781	605.05
	SD	7.62	4.20	11.81	155	325	101.62
UM-OM notch in UM (Group 4)	CVN-46-TS	133.09	28.50	104.59	11957	21339	721.19
	CVN-50-TS	143.77	31.00	112.77	12362	22529	780.06
	CVN-51-TS	141.33	40.47	100.86	12270	22597	1002.27
	Mean val.	139.40	33.32	106.07	12196	22155	834.51
	SD	6.31	6.31	6.09	212	707	148.24
BM (Group 5)	CVN-01-TS	169.42	35.11	134.31	12753	23831	879.43
	CVN-02-TS	155.54	25.22	130.32	12726	24283	639.06
	CVN-03-TS	171.32	25.00	146.32	13194	24511	637.23
	Mean val.	165.43	28.46	136.98	12891	24208	719.57
	SD	8.61	5.77	8.33	263	346	139.31

General definitions [120]:

Mean value: $\tilde{x} = \frac{1}{n}\sum_{i=1}^{n} x_i$ Standard deviation: $s = \sqrt{\frac{1}{n-1}\left(\sum_{i=1}^{n} x_i^2 - x_0 \sum_{i=1}^{n} x_i\right)}$

where n is number of attribute values in the random sample, x_i is individual attribute value (i.e. W_t for each tested specimen), x_0 is reference value of the population, $\tilde{x}$ is mean value and s is standard deviation

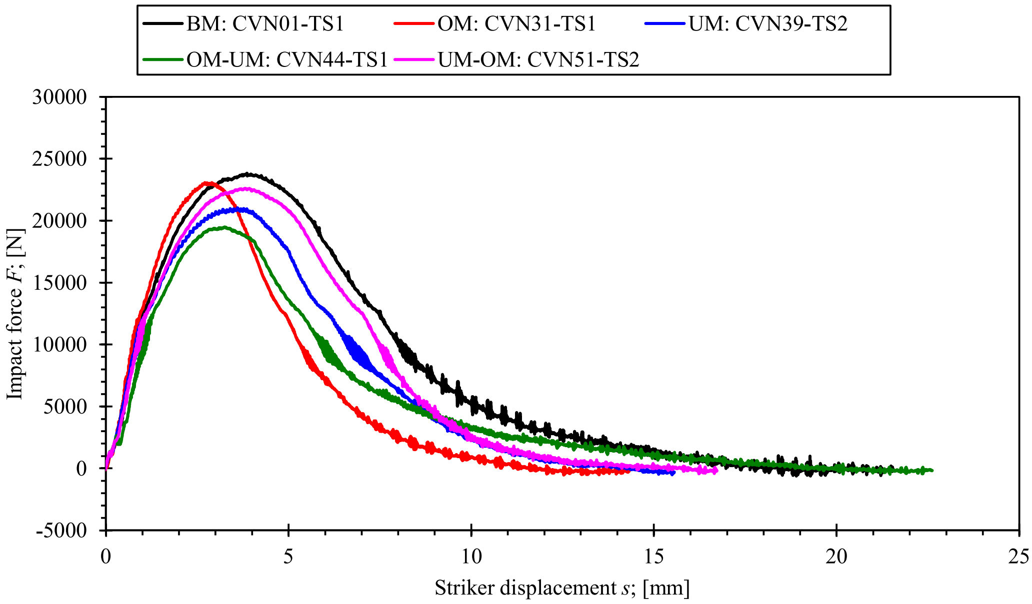

Figure 3.40 The review of computed *P*-*s* data for the Charpy impact testing. Only data closest to the average of each tested group of specimens is plotted.

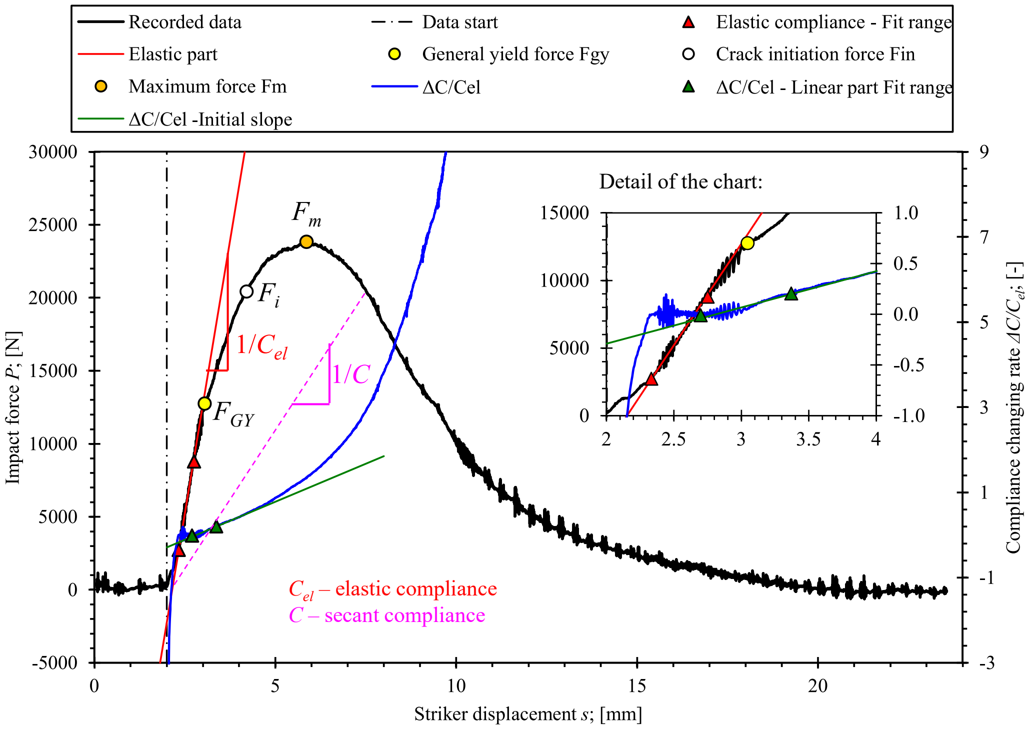

Figure 3.41 The overview of identified characteristic points on the *P*-*s* data and the definitions of the corresponding elastic and secant compliances. Here, P-s data for base material CVN01-TS Charpy specimen are used as an example.

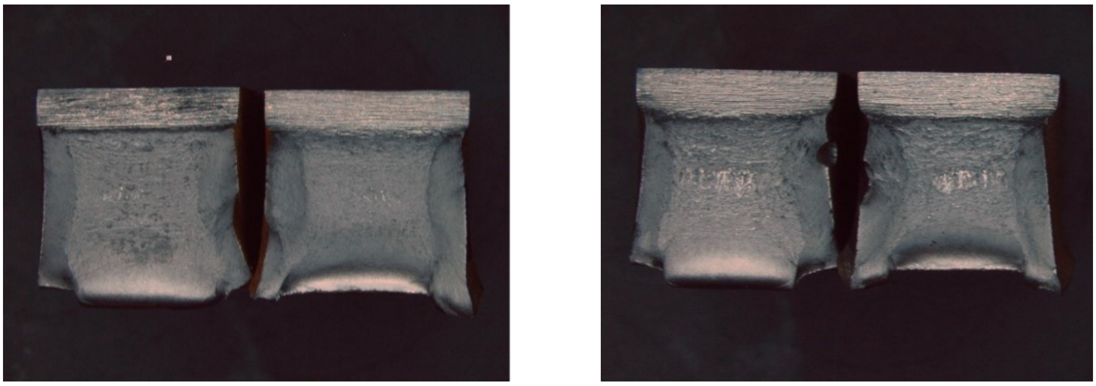

a) OM weld – specimen CVN31-TS

b) UM weld – specimen CVN39-TS

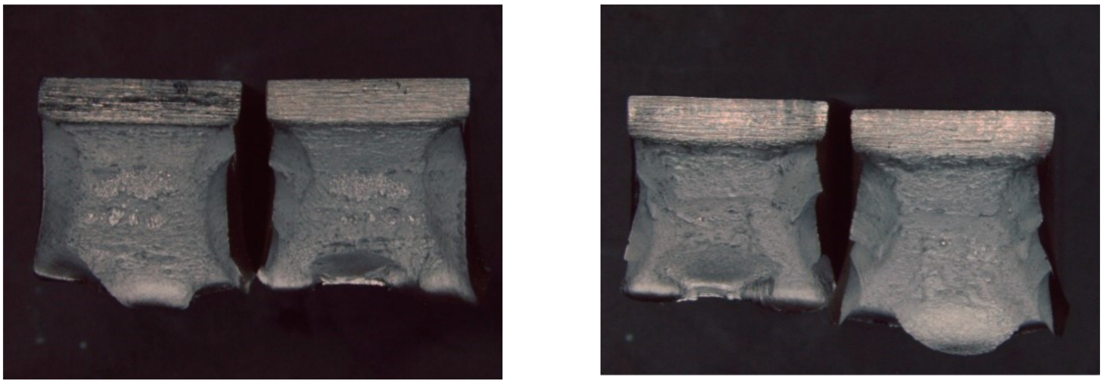

c) OM-UM weld – specimen CVN44-TS

d) UM-OM weld – specimen CVN51-TS

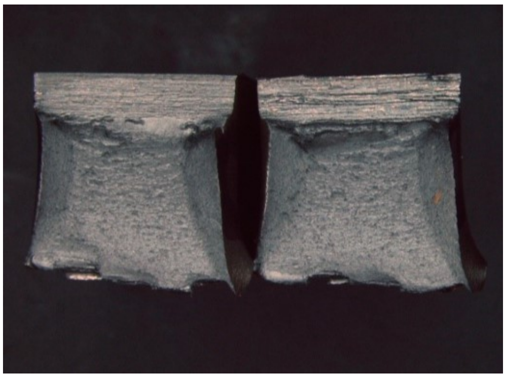

e) Base material – specimen CVN1-TS

Figure 3.42 Visual inspection of fracture surfaces of the tested Charpy specimens for a) the OM weld, b) the UM weld, c) the OM-UM weld, d) the UM-OM weld and e) the base material.

The double mismatched weld configurations show improved fracture behaviour in comparison to the pure OM and UM welds. Here, double mismatched OM-UM weld configuration, in comparison to the OM weld, shows increased $\overline{W}_t$ by 13.2 % while $\overline{J}_{id}$ is relatively comparable to the relative difference within 2 %. Furthermore, the double mismatched UM-OM weld configuration, in comparison to the UM weld, shows increased $\overline{W}_t$ by 11.1 % and increased $\overline{J}_{id}$ by 30.8 %. Additionally, the highest required energy for the ductile crack initiation $\overline{W}_i$ =33.32 J and corresponding dynamic fracture toughness $\overline{J}_{id}$ = 834.51 kJ/m^2 were observed for the UM-OM double mismatched weld with the crack in the UM weld material.

Furthermore, the pure OM and UM welds exhibit lower amount of required energy $\overline{W}_i$ of ductile crack initiation and corresponding dynamic fracture toughness $\overline{J}_{id}$ in comparison with the base material. However, fracture toughness can be potentially improved with the double mismatched weld configuration. Here, the OM-UM weld configuration (notch located in the OM weld material) exhibits a fracture toughness that is comparable to the base material. The UM-OM weld configuration show even increased fracture toughness in comparison to the base material.

3.5 Fracture Toughness Testing

3.5.1 Fracture Specimen Configuration

A fracture testing programme has been conducted in scope of this research with a purpose to investigate fracture behaviour of the welds under high constraint conditions at the crack tip (which is often preferred as it adds conservatism to the structural integrity assessment that adopts the measured fracture toughness value). For that reason, single edge notched bend (SE(B)) specimens [28], [39] were extracted from the welded sample plates that were mentioned in Chapter 3.2.2. The SE(B) specimens were extracted from the OM weld, UM weld and double mismatched OM-UM weld, where one group of specimens had a notch in the OM weld material while the other had a notch in the UM weld material. Additionally, one group of the specimens has been extracted from the base material as a reference. In total, 5 groups of 3 SE(B) specimens were extracted, which constitutes 15 specimens. The layout of the extracted specimens is shown in Figure 3.43.

The extracted SE(B) specimens had a squared cross section with a width and a thickness W=B=20 mm and the corresponding ratio W/B=1. The SE(B) specimens of such shape closely match plane strain conditions due to higher crack tip constraint [38] and are recommended by Toyoda et al. [121] for fracture testing of welds. Moreover, squared cross section SE(B) specimens are included in standards ISO 15653 [22] and BS 7448-2 [8] for fracture testing of welds and in ASTM E1820 [6], BS 7448-4 [10] and ISO 12135 [11] for fracture testing of metallic materials. the extracted SE(B) specimens were surface notched with a notch aligned with the midplane of the weld which resembles longitudinal cracks in the weld [63] (TS orientation according to ASTM E1820 [6]). Here, proper alignment of the notch was achieved by exposing the weld with etching of extracted oversized bars, using 2% solution of nitric acid and alcohol, as shown in Figure 3.44. The oversized bars were then milled to final dimensions that are shown in Figure 3.45. Finally, the notches with thickness less than 0.3 mm were fabricated with wire EDM. The depth of the notch was adjusted in such way, that fatigue precrack length was a_0=10 mm (a_0/W=0.5) for the base material and the single material OM and UM welds. In case of the double mismatched UM-OM welds the notch was adjusted in such way that the distance between the precrack front and fusion line in the weld was 1÷2 mm. The fabricated configurations of the SE(B) specimens are shown in Figure 3.46.

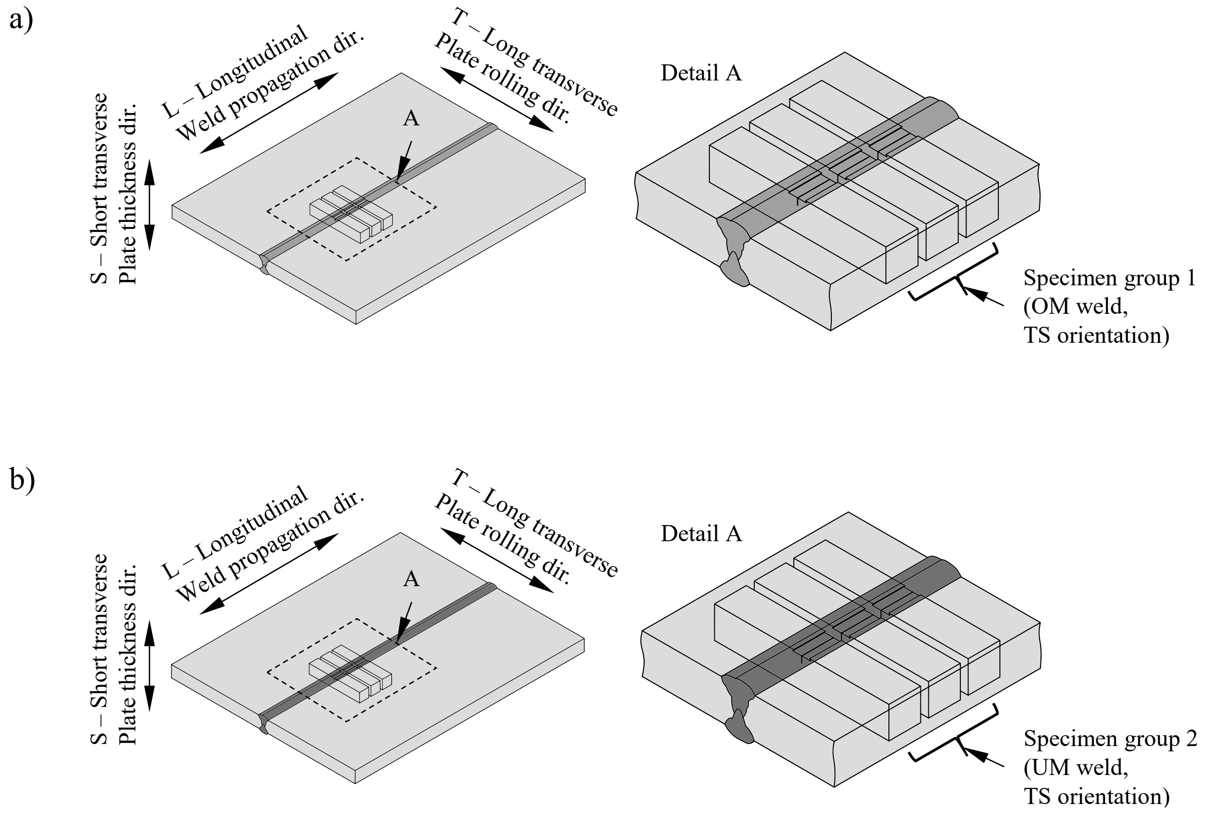

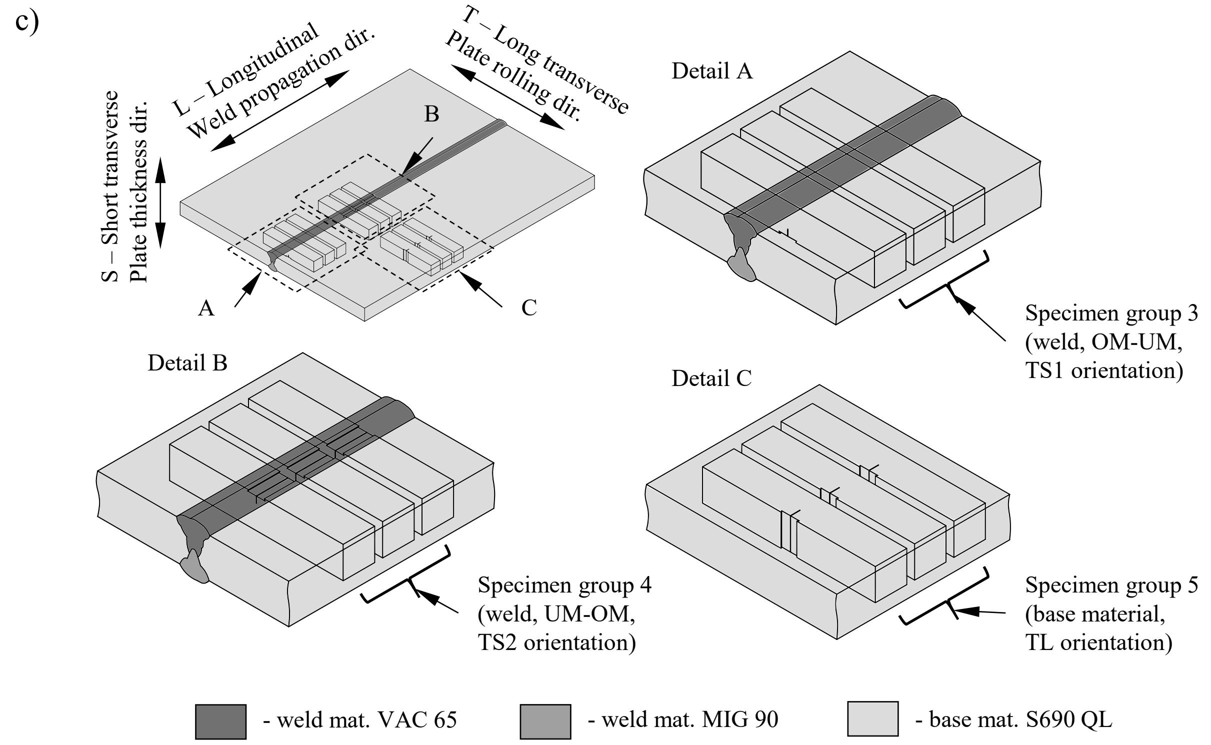

Figure 3.43 The layout of the SE(B) specimens in the sample plates that contained a) the OM weld, b) the UM weld and c) the double mismatched OM-UM weld.

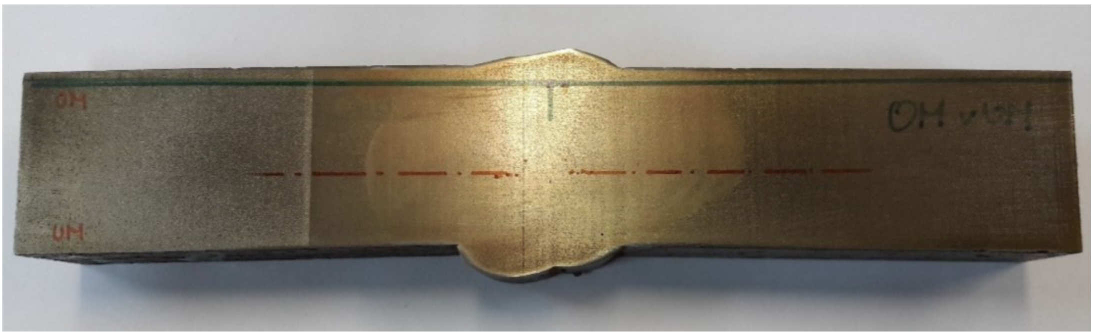

Figure 3.44 The example of marked position of the notch in the double mismatched OM-UM weld before fabrication of the SE(B) specimen. the weld has been exposed by etching with 2 % solution of nitric acid and alcohol.

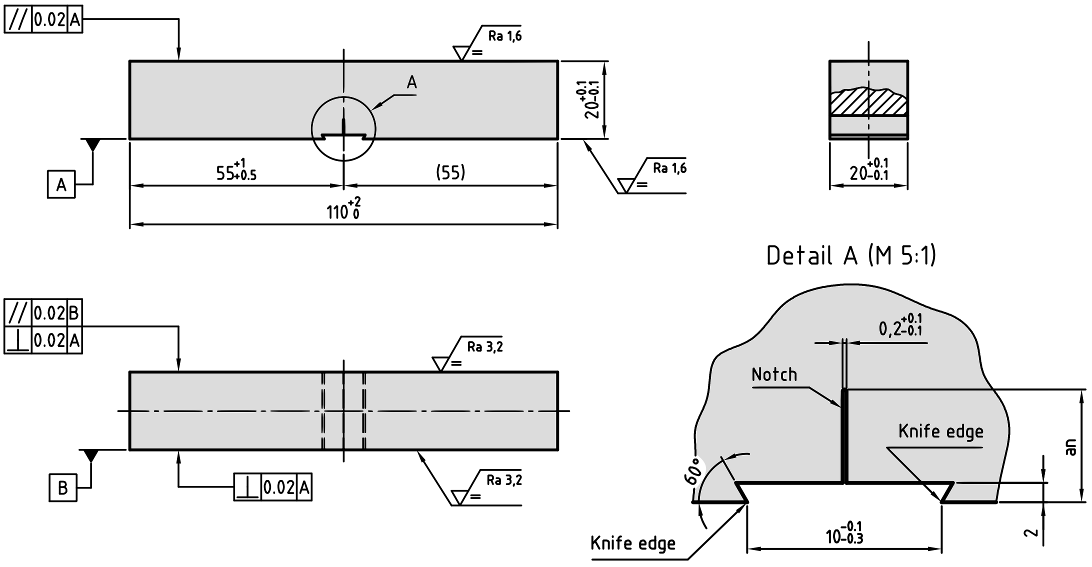

Material configuration	a_n [mm]	a_n/W [-]
Base material, OM weld, UM weld	5.0	0.25
OM-UM weld (notch in OM weld material)	5.0 ÷ 7.0	0.25 ÷ 0.35
UM-OM weld (notch in UM weld material)	3.0 ÷ 6.5	0.15 ÷ 0.33

Figure 3.45 The geometry of the fabricated SE(B) specimens.

The surface cracked configuration of the SE(B) specimens allows testing of a specific region of the weld as crack can be placed in a particular microstructure. Here, the aim of the fracture testing programme was to study the ductile crack growth from one weld material to the other weld material and identify the effect of material heterogeneity on the fracture behaviour of the weld. In order to achieve a stable crack growth during the fracture testing, side grooves were not fabricated. The personnel in SOETE laboratory reported significant instable fracture occurrences during the fracture testing of welds with side grooved single edge notched tension (SE(T)) specimens [122], [123], which was attributed to a high level of stress triaxiality induced by the combined presence of a material property change and side grooves (especially traversing from the UM into the OM weld material). Omitting the side grooves causes a state of low stress triaxiality near the outer surfaces of fracture specimen, which results in increased material yielding (and increased size of plastic zone) that can potentially reduce the stable crack growth rate. For that reason, fracture specimen is potentially subjected to crack tunnelling and shear lip formation. The research conducted by de Andrade and Donato [124] showed that crack tunnelling effects the crack length estimation for the SE(B) specimens when unloading compliance method is used. Deviation of 8 % in the crack size estimation has been reported. The main reason for that is altered compliance of the SE(B) specimen due to present shear lips. However, experience in Laboratory of Machine Parts and Structures indicates that minimal crack tunnelling is acceptable if crack size is estimated with the NDRM [125]. The NDRM incorporates a model for the crack size estimation that is calibrated to the measured lengths of an initial and a final crack. Furthermore, the NDRM is not dependent on measured compliances in intermediate unloading and reloading sequences during the fracture testing.

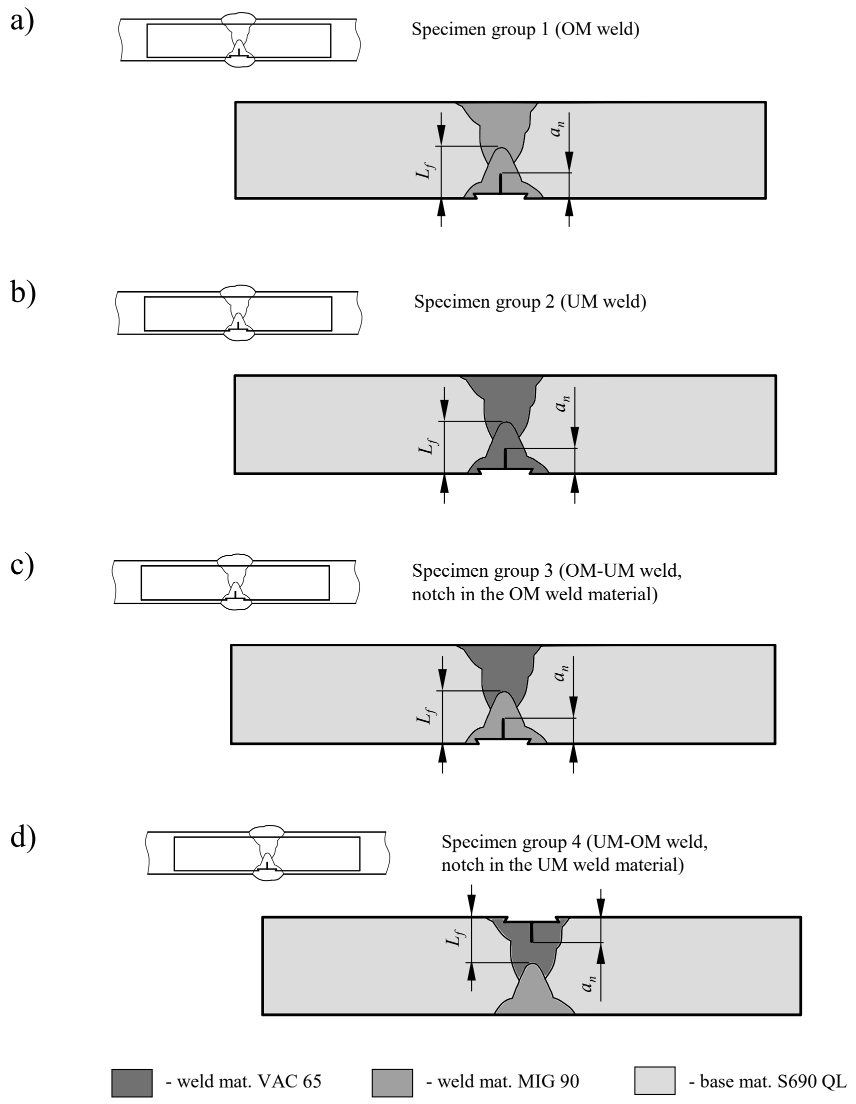

Figure 3.46 The configurations of the SE(B) specimens that were extracted from a) the OM weld material, b) the UM weld material, c) the OM-UM weld with a notch located in the OM weld material and d) the UM-OM weld with a notch located in the UM weld material.

3.5.2 Fatigue Precracking

According to standards ISO 15653 [22] and BS 7448-2 [8], it is advisable to reduce residual stresses prior to the fracture testing, as they have an effect on the crack driving force and the crack tip constraint [126]–[129], which can potentially lead to reduction of the weld toughness [126], [127]. Additionally, residual stresses normally show an inhomogeneous pattern across the weld section and can influence the fatigue crack growth, such that the precrack front will develop an uneven shape [62]. This also impacts the estimation of the fracture toughness, as existing solutions for the crack tip parameters *K*, *J*-integral or CTOD are developed for the assumption of a straight crack front in 2D geometry [27]. Residual stresses can be relieved by post-welding heat treatment. However, heat treatment can have an effect on microstructure of the weld and, due to this, on the fracture toughness of the weld. For that reason, a heat treatment should not be used for fracture testing unless the welds in the component to be assessed are treated in the same way. Instead, mechanical methods were proposed for modification of residual stress field in order to avoid the aforementioned issues. The corresponding guides are presented in standards for fracture testing of welds, such as ISO 15653 [22] and BS 7448-2 [8]. Mechanical methods for residual stress relieve are illustrated in Figure 3.47, while critical discussion is provided in [62], [130], [131].

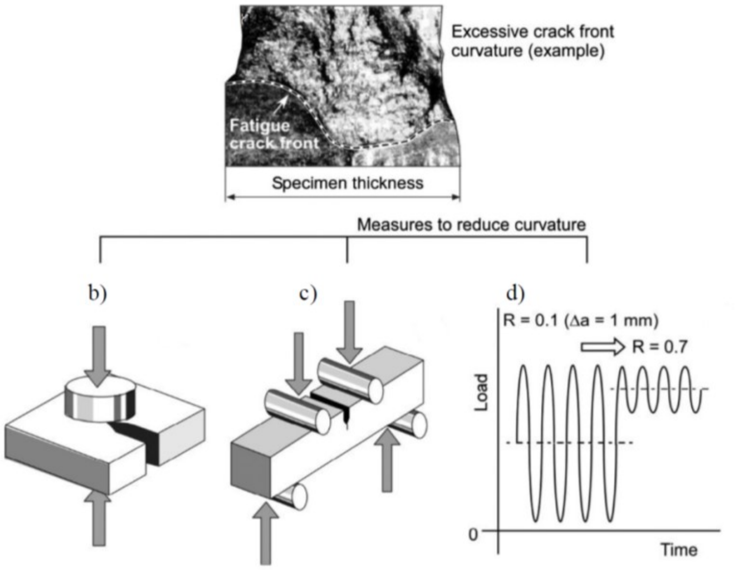

Figure 3.47 The mechanical methods for reduction and redistribution of the residual stresses in fracture test specimens prior to and during precracking; a) The example of excessive crack front curvature due to welding residual stresses, b) the local compression method, c) the reverse bending method and d) the stepwide high *R* ratio method (source: [72]).

A brief description of mechanical methods for reduction of residual stresses is recapped from BS 7448-2 [8]. The local compression method involves pressing the hardened steel plates on both side surfaces of the specimen across 88 ÷ 92 % of the ligament ($W–a_n$) ahead of the crack tip, such that a plastic strain of 1 % of the specimen thickness is generated. In the reverse bending method a fracture specimen is loaded to compress the machined notch before conventional fatigue precracking. The aim is to deform plastically the material at the notch root and produce a uniform tensile residual stress there. Finally, the stepwise high R ratio method introduces fatigue precracking procedure that consists of two steps, each at different fatigue ratios. For the first step, the stress ratio R=0.1 is used until the fatigue precrack has grown to a length approx. 1 mm. In the second step, the stress ratio is increased to R=0.7 until the desired length of the fatigue precrack is achieved.

According to Gubeljak et al. [130] the local compression method is unproductive for obtaining a uniform fatigue precracking front profiles of welds which have deposed UM material in the weld root. It is believed that reason for that is highly uneven residual stress field due to increase of the magnitude of the transverse residual stresses in the OM weld material and decrease in the UM welds as reported by Dong and Zhang [132]. The local compression method would therefore need individual modification compared to the standard [8], [22] in order to reduce stresses in a double mismatched weld. On the other hand, review of Zerbst et al. [62] showed that the reverse bending method is relatively inefficient in both, the reduction of residual stresses and generation of the straight crack front. Remarks regarding lesser effectiveness of the reverse bending method are provided in standards [8], [22] as well. Therefore, it seems that the stepwise high R ratio method is the only one appropriate for straightening the crack front. However, Zerbst et al. [62] provided list of references which reported that even after fatigue precracking with R=0.7, non-uniform residual stresses still remained ahead of the crack tip. Presented limitations make the application of mechanical methods for residual stress reduction to double mismatched welds relatively difficult. In contrast, residual stresses have important role in small-scale and contained yielding, since beyond that stress relief occurs due to plastic deformation. [62]. Furthermore, in GKSS procedure [131] the authors reported their experience that pre-treatment is often unnecessary for the surface notched SE(B) specimens with W/B=1, as straight crack front can be obtained with normal pre-cracking procedure.

Considering the listed limitations of residual stress reduction methods and the advantages of surface notched SE(B) specimens with W/B=1, a decision was made to introduce sharp cracks with normal precracking procedure. Therefore, the SE(B) specimens in this study were precracked with load ratio R=0.1 and applied maximum P to elastic modulus ratio $K_{max}/E \leq 1.5\times 10^{-4}$ m$^{1/2}$. This precracking protocol meets the requirements of the GKSS procedure [131], which are more strict than the ones included in standards ASTM E1820 [6], BS 7448-2 [8], ISO 12135 [11] and ISO 15653 [22]. The fatigue precracks were grown until distance between the precrack tips on side surfaces of the SE(B) specimens, and fusion line separating the OM and the UM weld materials was 1÷2 mm, as shown in Figure 3.48. For the single material welds and the base material, fatigue crack was grown until the length a_0=10 mm (i.e. a_0/W=0.5) was reached.

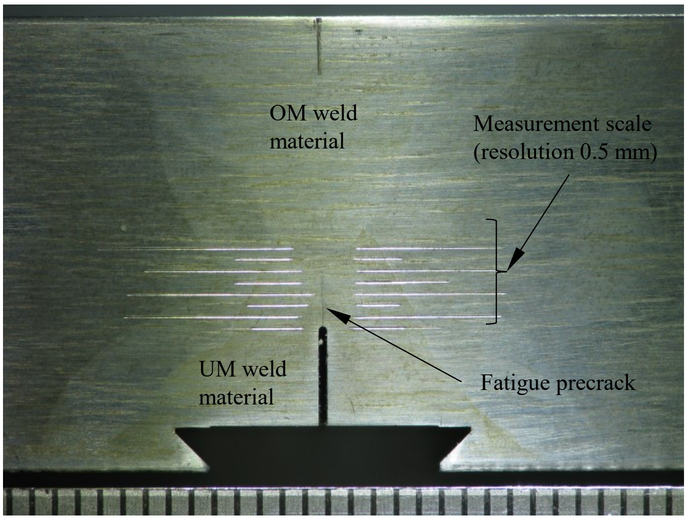

Figure 3.48 The view of the etched side surface of the SE(B) specimen. The OM-UM welded joint with fatigue precrack in the UM weld material is clearly visible. The measurement scale with resolution of 0.5 mm was marked on the side surface in order to monitor fatigue precrack length during precracking procedure.

3.5.3 Fracture Testing

The fracture testing of the welds and the base material has been performed by the single specimen test method that is in conformance with ASTM E1820 standard [6]. This standard governs procedures for fracture testing of metallic materials only. Therefore, additional requirements for the welded SE(B) specimen preparation and testing that are given in standards ISO 15653 [22] and BS 7448-2 [8], were considered when testing welds.

The fracture tests were performed on a multipurpose testing machine INSTRON 1255 under crosshead displacement control with displacement rate 1 mm/min and at room temperature. A fixture system with fixed support and load rollers with diameter of 25 mm with span width S=4*W*=80 mm (Figure 3.49 a) and b)) was used as standard fixture system that allow outwards displacement of the rollers [6], [8], [11], [22], [39] was not available. Such type of fixtures is appropriate for fatigue precracking, but it may have an effect on fracture behaviour of the SE(B) specimen. Therefore, the existing solution for calculation of *K*, *J* and CTOD in ASTM E1820 standard had to be calibrated. The calibration procedure will be presented in Chapter 4, while results in terms of the *J*-integral resistance curves (i.e. *J*-R curves) will be presented in Chapter 5.

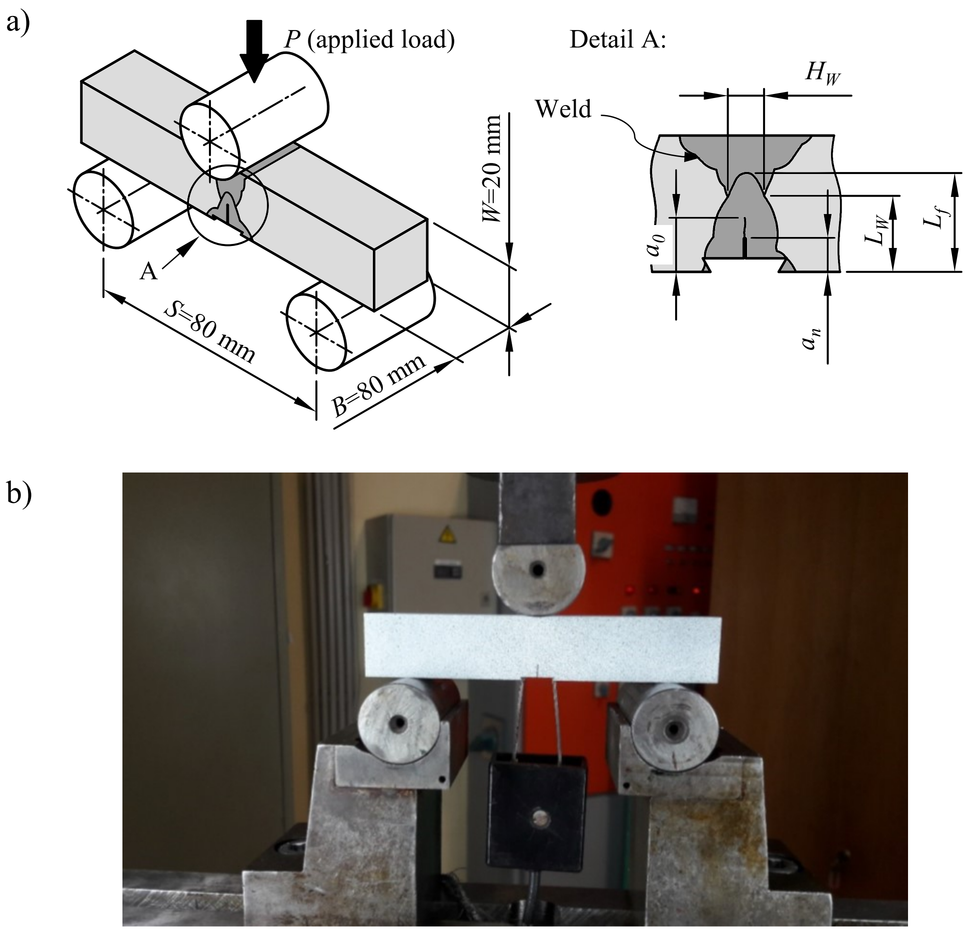

Figure 3.49 The setup of the fixture system for fracture testing of the SE(B) specimens; a) the corresponding characteristic dimensions and b) the actual fixture setup. Note the mounted clip gauge and applied speckle pattern for DIC measurements.

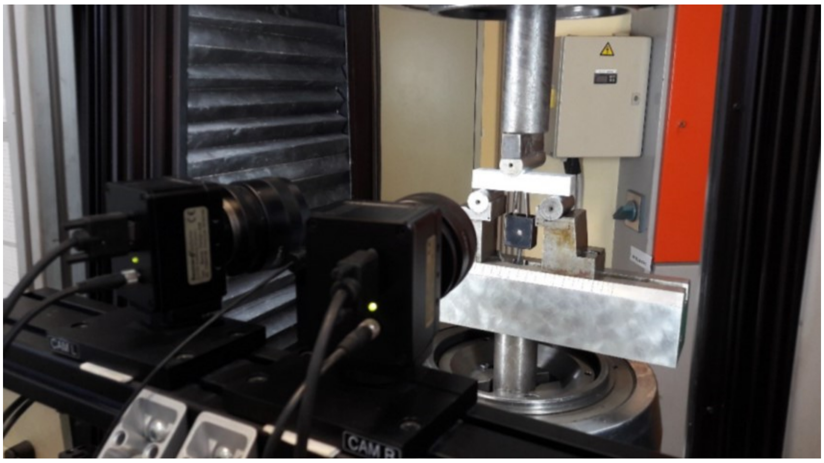

Figure 3.50 The GOM Aramis 3D DIC system setup for measuring displacements and strain field on the side surface of the tested SE(B) specimen.

The CMOD was measured with a dedicated clip gauge mounted onto the specimen surface. Displacements and strain fields on the side surface of the tested SE(B) specimens were monitored with GOM Aramis 3D DIC system [96], as shown in Figure 3.50. These measurements enabled a detailed analysis of plastic zone development on the side surface of the actual SE(B) specimen. Moreover, measured displacements field enabled direct extraction of the crack tip opening displacement (CTOD) in terms of CTOD-δ_5 parameter [131], [133].

3.5.4 Measurements of Fatigue Precrack and Final Crack Lengths

After the completed tests, the SE(B) specimens were fatigue cracked in order to mark the stable crack growth. Fatigue precrack a_0 and final crack a_p lengths were measured on the broken surfaces with an optical microscope, using the nine-point method, as specified in GKSS procedure [131]. This method suggests measuring the length of the desired crack front (either a_0 or a_p) should be measured at nine equally spaced points extending to $0.01B$ of the side surfaces of the SE(B) specimen, as shown in Figure 3.51. The corresponding crack length was then computed according to the following Equation:

$$a = \frac{1}{8}\left(\frac{a_1 + a_9}{2} + \sum_{i=2}^{8} a_i\right) \tag{3.27}$$

where a_1, a_9 and a_i are crack lengths in [mm] along the lines 1, 9 and the remaining lines 2-8, respectively. The a denotes the fatigue precrack length a_0 or the final crack length a_p in [mm]. The criteria for maximum allowed crack curvature was adopted from the ISO 15653 standard [22], which suggest that neither of the 9 measured crack lengths should deviate from the average crack length by more than 20 % of a_0 (the same criteria is recommended in BS 7448-2 standard [8] as well). For a comparison, standard ASTM E1820 [6] suggests that the nine equally spaced measuring points should be extending to $0.005W$ of the side surfaces, and that neither of the nine measured crack lengths should deviate from the average crack length by more than $0.05B$. These criteria is adjusted for fracture testing of homogeneous metallic materials (i.e. base material). Additionally, the final crack length at the outermost measurement points 1 and 9 could not be measured as these points would fall out of the cracked surface due to local contraction of the cross-section ahead of the fatigue precrack. Therefore, the adoption of the crack length measurement procedure from the GKSS procedure [131] and crack front straightness criteria from ISO 15653 standard [22] seemed reasonable.

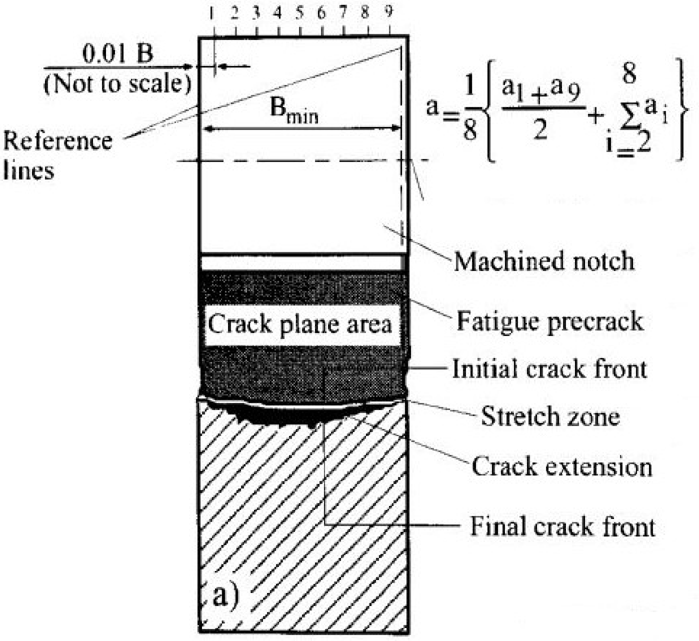

Figure 3.51 The principle of the crack length measurement that was adopted from the GKSS procedure (source: [131]).

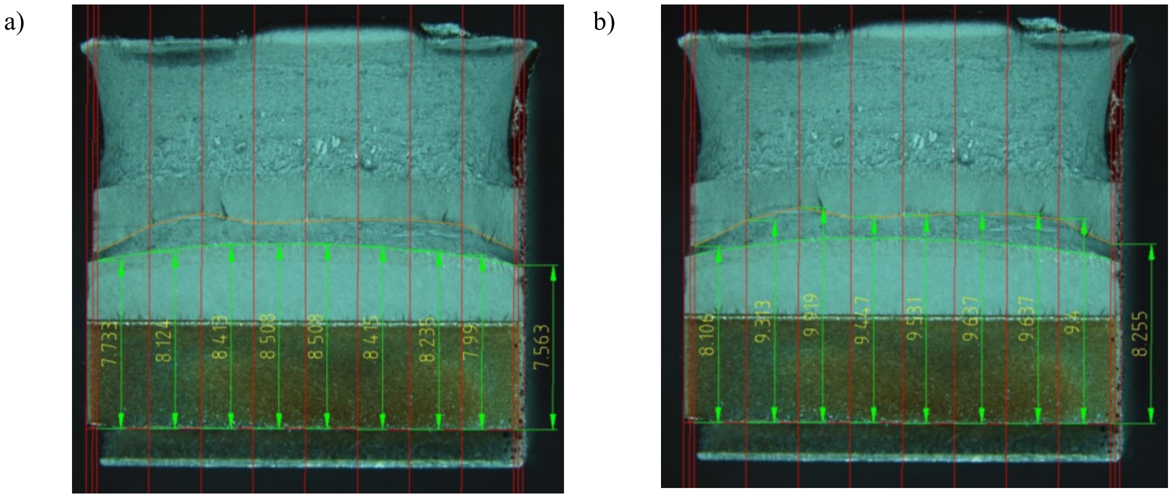

Figure 3.52 The example of the actual measurements of a) the fatigue precrack and b) the final crack lengths on one of the tested SE(B) specimens.

The measured fatigue precrack and the final crack lengths are listed in Table 3.10 for the tested SE(B) specimens. These measurements were used for calibration of mathematical model for an estimation of the stable crack growth Δ*a* according to the NDRM.

3.5.5 Results of Fracture Tests

The tested samples are listed in Table 3.10. Here, the corresponding measured crack lengths and the provisional results are listed as well. It is important to note, that the provisional fracture toughness in terms of the *J*-integral and K_{JIc} were obtained by using incremental equations and factors η_{pl} and γ_{pl} that are provided by the ASTM E1820 [6] standard for the single specimen test method. Fracture toughness was computed from the recorded *P*-CMOD history. Here, *P*-CMOD charts were separated to elastic and plastic components according to the following equation:

$$V_{pl,i} = V_i - V_{el,i} = V_i - C \cdot P_i \tag{3.28}$$

where V_i, $V_{el,i}$ and $V_{pl,i}$ denote total, elastic and plastic CMOD in [mm]. The *C* represents the initial compliance in [mm/N] that is determined from the linear part of *P*-CMOD record as ratio $\Delta V/\Delta P$. From here, the *J*-integral is computed as a sum of elastic $J_{el,i}$ and plastic $J_{pl,i}$ components:

$$J_i = J_{el,i} + J_{pl,i} \tag{3.29}$$

The elastic component $J_{el,i}$ is computed as follows:

$$J_{el,i} = \frac{(K_i)^2(1-\nu^2)}{E} \tag{3.30}$$

where K_i is stress intensity factor in [MPa·mm$^{1/2}$], ν is dimensionless Poisson's number and E is elastic modulus of material at the vicinity of the crack front in [MPa]. The K_i is here computed according to the following equation:

$$K_i = \left(\frac{P_i S}{(BB_N)^{1/2} W^{3/2}}\right) f(a_i/W) \tag{3.31}$$

where P_i is applied load in [N], S is span width between the centres of the support rollers in [mm], B and B_N are specimen thickness and notch thickness in [mm], respectively. The width of the specimen is presented by W in [mm] and f(a_i/W) is a shape function of normalized crack length a_i/W that is defined as follows:

$$f\left(\frac{a_i}{W}\right) = \frac{3\left(\frac{a_i}{W}\right)^{1/2}\left[1.99 - \left(\frac{a_i}{W}\right)\left(1-\frac{a_i}{W}\right)\left(2.15 - 3.93\left(\frac{a_i}{W}\right) + 2.7\left(\frac{a_i}{W}\right)^2\right)\right]}{2\left(1-2\frac{a_i}{W}\right)\left(1-\frac{a_i}{W}\right)^{3/2}} \tag{3.32}$$

Next, the plastic component of the J-integral $J_{pl,i}$ is computed according to the following equation:

$$J_{pl,i} = \left[J_{pl,i-1} + \left(\frac{\eta_{pl,i-1}}{b_{i-1}}\right)\left(\frac{A_{pl,i} - A_{pl,i-1}}{B_N}\right)\right]\left[1 - \gamma_{pl,i-1}\left(\frac{a_i - a_{i-1}}{b_{i-1}}\right)\right] \tag{3.33}$$

where $J_{pl,i}$, $J_{pl,i-1}$ are the plastic components of the J-integral in [kJ/mm^2], $A_{pl,i}$, $A_{pl,i-1}$ are areas under the P-CMOD$_{\mathrm{pl}}$ curve in [Nmm], a_{i-1} is crack length in [mm], b_{i-1} is the length of the remaining ligament, B_N is the notch thickness in [mm], $\eta_{pl,i-1}$ is a dimensionless correlation correction factor and $\gamma_{pl,i-1}$ is a dimensionless crack growth correction factor. Both factors are expressed with functions that are crack length dependent and are given in Equations (3.34) and (3.35).

$$\eta_{pl,i-1} = 3.667 - 2.199\left(\frac{a_{i-1}}{W}\right) + 0.437\left(\frac{a_{i-1}}{W}\right)^2 \tag{3.34}$$

$$\gamma_{pl,i-1} = 0.131 + 2.131\left(\frac{a_{i-1}}{W}\right) - 1.465\left(\frac{a_{i-1}}{W}\right)^2 \tag{3.35}$$

Note that in incremental equations indices *i* and *i-1* denote whether the quantity is computed in the current i-th step or is adopted from the preceding step. Furthermore, the NDRM in the first computation iteration assumes that the crack is stationary, i.e. $a_i=a_{i-1}=a_0$. Therefore, the second member in Equation (3.33) equals 1.

From here, the stable crack extension is estimated using the NDRM. First, the *P*-CMOD curve is converted into normalized $P_{N,i}$-$V'_{pl,i}$ curve. Here, the applied load P_i is normalised using Equation (3.36).

$$P_{N,i} = \frac{P_i}{WB\left(1 - a_{b,i}/W\right)^{\eta_{pl,i}}} \tag{3.36}$$

where P_i is applied load in [N], $P_{N,i}$ is normalized load in [N/mm^2], *W* is specimen width in [mm], *B* is specimen thickness in [mm], and $a_{b,i}$ is blunting corrected crack length in [mm] that is defined with Equation (3.37).

$$a_{b,i} = a_0 + \frac{J_i}{2\sigma_Y} \tag{3.37}$$

where a_0 is the fatigue precrack length in [mm], J_i is the *J*-integral in [kJ/mm^2] that is computed according to Equations (3.29), (3.30) and (3.33). The entire recorded load history was normalized using Equations (3.36) and (3.37) with the exception of the last recorded point, where $a_{b,i}$ in Equation (3.36) was substituted with the final physical crack length a_p. Moreover, the measured CMOD was normalized using the following equation:

$$v'_{pl,i} = \frac{v_{pl,i}}{W} \tag{3.38}$$

where $v'_{pl,i}$ is normalized CMOD without units, $v_{pl,i}$ is the measured CMOD in [mm] and W is specimen width in [mm]. Next, a line was constructed from the final data point tangent to the $P_{N,i}$-$v'_{pl,i}$ curve as shown in Figure 3.53.

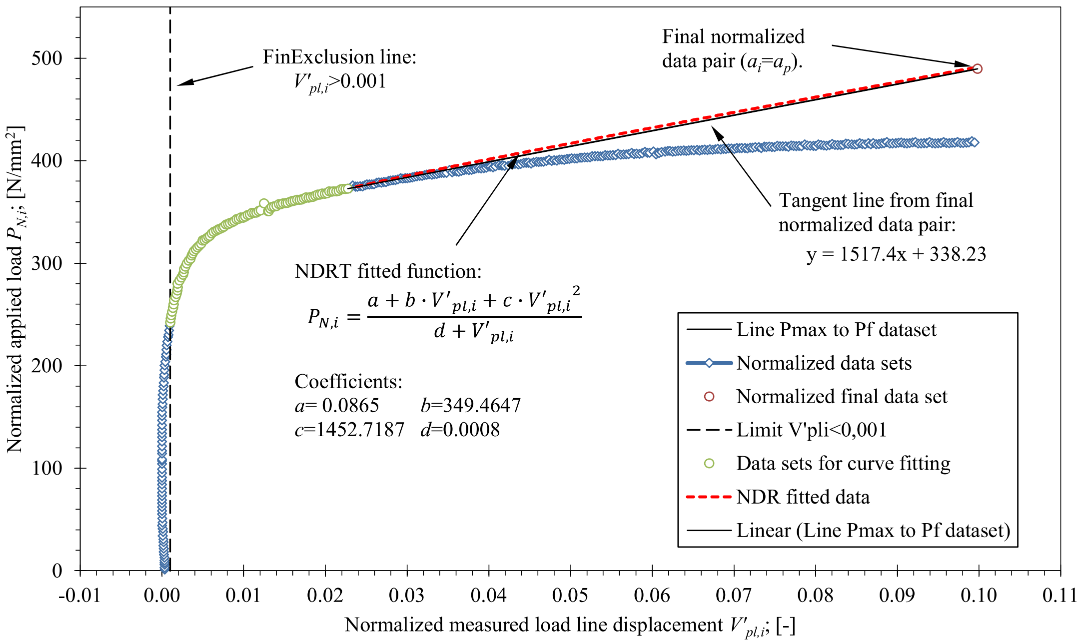

Figure 3.53 The normalized $P'_{n,i}$- $v'_{pl,i}$ curve with the constructed tangent line from the final data pair, marked data sets that were used for the curve fitting and the fitted normalization function. The presented curve corresponds to the experimental results of the double mismatched welded SE(B) specimen, designated as SE(B)-60, with the notch located in the OM weld material.

Data points on the normalized $P_{N,i}$-$v'_{pl,i}$ curve with $v'_{pl,i}$>0.001 up to the tangent point and the final data point were used to fit the following normalization function by the least squares regression method [134]:

$$P_{N,i} = \frac{a + bv'_{pl,i} + cv'_{pl,i}}{d + v'_{pl,i}} \tag{3.39}$$

where $P_{N,i}$ and $v'_{pl,i}$ are normalized applied load in [N/mm^2] and unitless normalized CMOD, respectively. Fitting coefficients a, b, c and d were adjusted through solving an optimization task in Microsoft Excel software, using GRG nonlinear solver [135]. The sum of the squares of the distances of selected data points from the function (3.39) was set as an objective in the optimization task with the goal to minimize it. Specific constraints in the optimization task were not specified. The quality of the fitted function was evaluated with computed corresponding probability value that has to be $P<0.05$, meaning that there is a 95% probability that the optimized function (3.39) accurately describes the selected datapoints. Additionally, the maximum deviation between the function (3.39) and the final data point must be less than 1%, as specified in ASTM E1820 standard [6]. Next, the crack length was computed by exposing the term a_i/W from Equation (3.39) and inserting the new $P_{N,i}$ values into derived equation. No crack length correction was needed, as measured $P_{N,i}$ and function (3.39) were already within ±0.1 % due to advanced fitting procedure.

The *J*-integral was finally computed by inserting the new a_i values into Equations from (3.28) to (3.35), and using the same corresponding procedure, as described earlier. However, the correction factors $\eta_{pl,i-1}$ and $\gamma_{pl,i-1}$, computed with Equations (3.34) and (3.35), respectively, were computed for each data point. Moreover, Equation (3.33) contained all terms in order to compute the $J_{pl,i}$ that takes crack growth correction into account. A plot of the *J*-integral values in dependence of the crack growth Δa was then created in order to produce the *J*-integral resistance *J-R* curve, as specified in ASTM E1820 standard [6]. Here, a critical value at crack initiation J_{Ic} was identified as a value of the *J*-integral corresponding to the intersection of the *J-R* curve offset at Δa=0.2 mm crack length that is parallel with the construction line that is defined with the following Equation:

$$J = 2\sigma_Y \Delta a \tag{3.40}$$

where J is the *J*-integral in [kJ/mm^2], σ_Y is material true yield strength in [MPa] and Δa is crack extension in [mm]. Furthermore, a SIF K_{Jc} corresponding to the J_{Ic} was computed using the following relationship:

$$K_{JIc} = \sqrt{\frac{EJ_{Ic}}{1-\nu^2}} \tag{3.41}$$

where E is elastic modulus in [MPa], ν is Poisson's coefficient, while J_{Ic} and K_{JIc} represent the *J*-integral in [kJ/mm^2] and SIF in [MPam$^{1/2}$] at the crack initiation, respectively.The results and the *J-R* curves that were obtained with post-processing of the experimental results are presented in Table 3.10 and Figure 3.56, respectively. The recorded *P*-CMOD histories are shown in Figure 3.55. It is important to note, that specimens SE(B)-29 and SE(B)-09 were tested according to the unloading compliance method (UCM), defined by ASTM E1820 [6] standard. Therefore, the unloading sequences are visible in the *P*-CMOD records. These unloading sequences were not considered when the fracture toughness of the tested SE(B) specimens was computed according to the NDRM. The comparison of the NDRM and the UCM will be discussed in Chapter 3.5.7. To continue, DIC recordings are presented in terms of equivalent von Mises strain fields on the side surfaces of the SE(B) specimens, as shown in Figure 3.57. Here, the strain fields at 95 % and 100 % of yield limit load P_Y are presented. The yield limit load was determined as a load that represents attainment of net section yielding, i.e. each point in the ligament ahead of the crack is supposed to have just reached the yield condition [80]. Therefore, the recorded strain fields were inspected for strains exceeding the true strain ε_Y that corresponds to the true yield strength. Such strains represent plastic deformation of the material and are in Figure 3.57 marked with magenta colour. For each SE(B) specimen, the first recorded DIC frame, that showed a band of plastic strain connecting the crack tip and top surface of the specimen, was marked, and a corresponding measured load was identified as P_Y. Such inspection was based on the ε_Y values that are listed in Table 3.11 for each material, obtained from results of MTS and round bar tensile testing, described in Chapters 3.3.2 and 3.4.1, respectively. It is important to note, that development of relatively asymmetrical plastic zone was observed in majority of the tested SE(B) specimens. This can be related to asymmetrical weld shape, misalignment of the SE(B) specimens on the fixtures within the specified tolerances and varying accuracy of the DIC system across the surface of the specimen due to the alignment of the cameras.

P-CMOD records in Figure 3.55e) show several locally instable fractures, i.e. “pop-ins”, during monotonous loading of the base material SE(B) specimens. However, these locally unstable fractures were identified as insignificant according to the criteria in ASTM E1820 standard [6]. Therefore, no special measures were considered when estimating the ductile crack growth with NDRM and evaluating the corresponding *J*-integral. The reason for occurrence of these locally instable fractures are segregations at mid thickness of the plate. Further details are discussed in Chapter 3.5.6. Additionally, multiple locally instable fractures were observed in fracture testing of the double mismatched welds with crack in the UM weld material. These fracture instabilities were identified as significant according to the criteria in ASTM E1820 standard [6]. In this case, fracture should be treated as unstable and fracture toughness must be evaluated in terms of SIF K_Q according to ASTM E399 standard [5], despite the SE(B) specimen having smaller dimensions as required; $(W\text{-}a \geq 2.\ K_{Ic}/\sigma_{YS})^2$. For that reason, the computed SIF is identified as K_Q instead of K_{Ic}, which represents critical SIF in mode I of crack opening for predominantly plane strain conditions.

The procedure for evaluation of K_Q requires plotting the P-CMOD record and computing the slope of the initial linear part of the curve. Then, a 95 % secant line is to be constructed with a slope equal to 95% of the initial elastic loading slope. A load P_5 is here defined as intersection of the P-CMOD record and the 95 % secant line, as demonstrated in Figure 3.54. For this type of the P-CMOD record, P_5 is considered as P_Q [5]. Finally, a SIF at fracture onset was computed according to an Equation that is similar to Equation (3.31) where terms K_i, P_i are replaced with K_Q and P_Q, respectively, while incremental crack length a_i is replaced with the fatigue precrack length a_0. For comparative reasons, the corresponding J_Q was computed from K_Q using Equation (3.40).

The comparison of experimental results in Table 3.10 indicates that single material welds have lower fracture toughness in comparison to the base material. Here, the OM welds exhibit average J_C=185 kJ/m^2, which is 52 % less than the base material that has J_C=388 kJ/m^2, while the UM welds exhibit average J_C=358 kJ/m^2, which is 8% less than the base material. Both, the OM and the UM weld, exhibit higher load bearing capacity than the base material as demonstrated in Figure 3.55 a), Figure 3.55 b) and Figure 3.55 c). However, it is important to note, that the fatigue precracks in the base material SE(B) specimens were longer by approx. 1.5 mm and 2 mm than precraks in the OM and the UM welds, respectively. Additionally, the analysis of DIC recordings showed that equivalent von Mises stress field on the side surfaces of the OM and the UM welds is altered due to the weld configuration. The OM weld shows plastic zone at the crack tip being forced towards the HAZ and the base material, as shown in Figure 3.57 a). On contrary, the UM weld show plastic zone being confined in the weld material between layers of the hardened HAZ, as demonstrated in Figure 3.57 b). Here, an extensive plastic deformation of the weld was observed at the plastic limit load.

Table 3.10 The results of the three-point bend fracture testing with the corresponding measured fatigue precrack and the final crack lengths.

Material	Specimen designation	Fatigue precrack length a_0 [mm]	Final crack length a_p [mm]	Crack growth Δa [mm]	Distance of fusion line $L_f$$^{(1}$ [mm]	Critical J-integral J_{Ic} (J_Q) [kJ/m^2]	Critical SIF K_{Jc}(K_Q) [MPam$^{1/2}$]
OM weld, TS orientation (group 1)	SE(B)-37	8.44	11.34	2.90	6.39	158	203
	SE(B)-38	8.58	9.89	1.31	5.71	193	224
	SE(B)-39	8.85	10.96	2.12	11.82	204	230
	Mean val.	8.62	10.73	2.11	7.97	185	219
	SD	0.21	0.75	0.80	3.35	24	14
UM weld, TS orientation (group 2)	SE(B)-40	9.02	9.99	0.98	4.98	336	293
	SE(B)-41	8.99	10.16	1.17	8.91	445	338
	SE(B)-42	9.23	10.36	1.14	10.37	293	274
	Mean val.	9.08	10.18	1.10	8.09	358	302
	SD	0.13	0.19	0.10	2.79	78	33
OM-UM TS1 orientation, notch in OM (group 3)	SE(B)-26	9.3	10.79	1.50	10.00	287	273
	SE(B)-60	10.30	11.46	1.16	10.50	441	338
	SE(B)-58	10.37	11.25	0.88	11.65	366	308
	Mean val.	9.99	11.17	1.18	10.72	365	307
	SD	0.60	0.34	0.31	0.85	77	33
UM-OM TS2 orientation, notch in UM (group 4)	SE(B)-09	6.07	7.73	1.67	7.20	612(6$^{(3}$)	396(38$^{(2}$)
	SE(B)-10	8.27	9.75	1.48	8.70	341(9$^{(3}$)	296(48$^{(2}$)
	SE(B)-52	9.58	10.88	1.30	8.82	312(8$^{(3}$)	283(45$^{(2}$)
	Mean val.	7.97	9.45	1.48	8.82	422(8)	325(44)
	SD	1.60	1.60	0.18	1.68	165(2)	62(5)
BM L orientation (group 5)	SE(B)-01	10.67	11.72	1.05	n.a.	293	253
	SE(B)-02	10.65	11.78	1.14	n.a.	451	314
	SE(B)-03	10.27	11.08	0.81	n.a.	421	303
	Mean val.	10.53	11.53	1.00	n.a.	388	290
	SD	0.23	0.39	0.17	n.a.	84	33

Remarks:

1) – Distance to fusion line in the weld root L_f as defined in Figure 3.49 a).

2) – Evaluated K_Q according to ASTM E399 [5] standard due to severe fracture i.e. pop-in

3) – Evaluated value of J-integral from K_Q

General definitions [120]:

Mean value: $\tilde{x} = \frac{1}{n}\sum_{i=1}^{n} x_i$ Standard deviation: $s = \sqrt{\frac{1}{n-1}\left(\sum_{i=1}^{n} x_i^2 - x_0 \sum_{i=1}^{n} x_i\right)}$

where n is number of attribute values in the random sample, x_i is individual attribute value (i.e. W_t for each tested specimen), x_0 is reference value of the population, $\tilde{x}$ is mean value and s is standard deviation

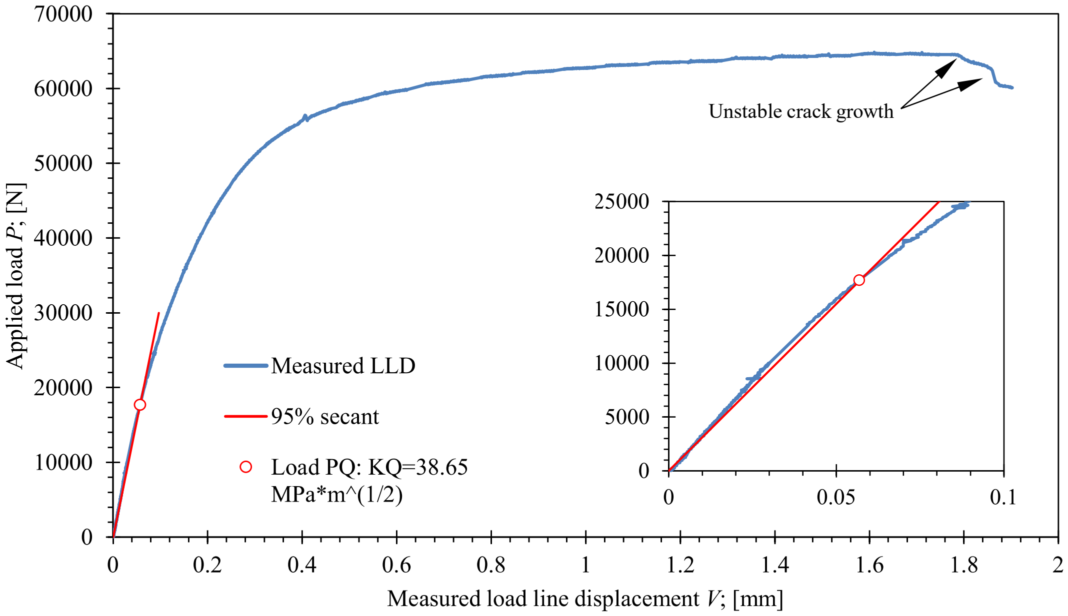

Figure 3.54 The P-CMOD record for the tested SE(B)-09 specimen with marked load P_Q. Marked unstable crack growth onsets were typical for the double mismatched UM-OM weld with notch and the fatigue precrack in the UM weld material.

In comparison to the single material welds, the double mismatched welds exhibit altered fracture properties and increased bearing capacity. Especially the UM-OM welds with notch and fatigue precrack located in the UM weld material showed distinctive behaviour under monotonous loading. The double mismatched welds show higher bearing capacity than the OM and the UM welds, as shown in Figure 3.55. The OM-UM welds with notch and fatigue precrack in the UM weld material show not only improved load bearing capacity in comparison to the OM welds, but severe scatter as well. In relation to that, the data in Table 3.10 shows the increased distance to the fusion line L_f (see Figure 3.49 a) for definition), and hereby the increased portion of the UM material in the weld, which leads to a reduction of the load bearing capacity of the weld. Furthermore, severe locally instable fractures were observed that are related to the crack path deviation, as elaborated in Chapter 3.5.6. The corresponding P-CMOD records were postprocessed according to ASTM E399 standard [5]. For a comparative reason, J-R curves were developed as well, according to procedure in ASMT E1820 standard [6], neglecting the influence of locally unstable fractures. The obtained results are polarizing. The ASTM E399 [5] standard gives highly conservative estimation of K_Q that considers load state prior to development of significant plastic zone. Here, the estimated $\overline{K}_Q$=44 MPam$^{1/2}$ is 80 % lower than the $\overline{K}_{JIc}$=219 MPam$^{1/2}$ that was measured for the OM weld. On the other hand, occurrence of locally unstable fractures might influence the precision of the J_{IC} derived from J-R curves, but to an unknown extend, as such type of fracture was observed on all SE(B) specimens from the UM-OM weld. Therefore, a reference test with only ductile crack extension was not produced. Regardless of that, the estimated $\bar{K}_{JIc}$=325 MPam$^{1/2}$ and the corresponding $\bar{J}_{Ic}$=422 kJ/m^2 for the UM-OM weld are 33 % and 56 % higher than the measured $\bar{K}_{JIc}$=219 MPam$^{1/2}$ and the corresponding $\bar{J}_{Ic}$=185 kJ/m^2 for the OM weld, respectively. Such large discrepancy in produced results between ASTM E399 [5] and ASTM E1820 [6] standards calls for modification of the existing methods, to take into account large ductile deformation preceding the locally unstable fracture.

The analysis of DIC records for the UM-OM weld show that plastic zone initially develops within the UM weld material ahead of the crack tip. Due to the layers of hardened HAZ with higher yield and ultimate tensile strengths than the UM weld material, the plastic zone is predominantly limited mainly to the UM weld material. With progressive loading, bands of plastic deformation are forced to spread around the OM weld material in parts of the HAZ with lower strength and the base material. The double mismatched OM-UM welds show similar fracture toughness in terms of $\bar{J}_{Ic}$ (average J_{Ic}) as the UM welds with relative deviation within 2%. However, the OM-UM welds show noticeable scatter in P-CMOD records and J-R curves. Again, this is associated with the ratio of the OM and the UM material in the weld. It seems that increasing the L_f and consequentially the portion of the OM weld material leads to decreased bearing capacity and increased fracture toughness. Analysis of the DIC records for the OM-UM welds show that plastic zone initially develops in the OM weld material ahead of the crack tip, as shown in Figure 3.57 c). With progressive loading the plastic zone spreads in the UM weld material, where it is again confined between layers of the hardened HAZ.

It is important to emphasize, that the results presented in this chapter are not final. Configuration of the material surrounding the crack has a major impact on development of the strain fields and fracture behaviour of the SE(B) specimens under monotonous loading. Therefore, it is important to calibrate the correlation factor η_{pl} and the crack growth correction factor γ_{pl}, given with Equation (3.34) and Equation (3.35), respectively, in order to incorporate the aforementioned effect in calculation of the J-integral. Calibration of these factors will be discussed in Chapter 4. Corrected results of fracture testing will be presented in Chapter 5.

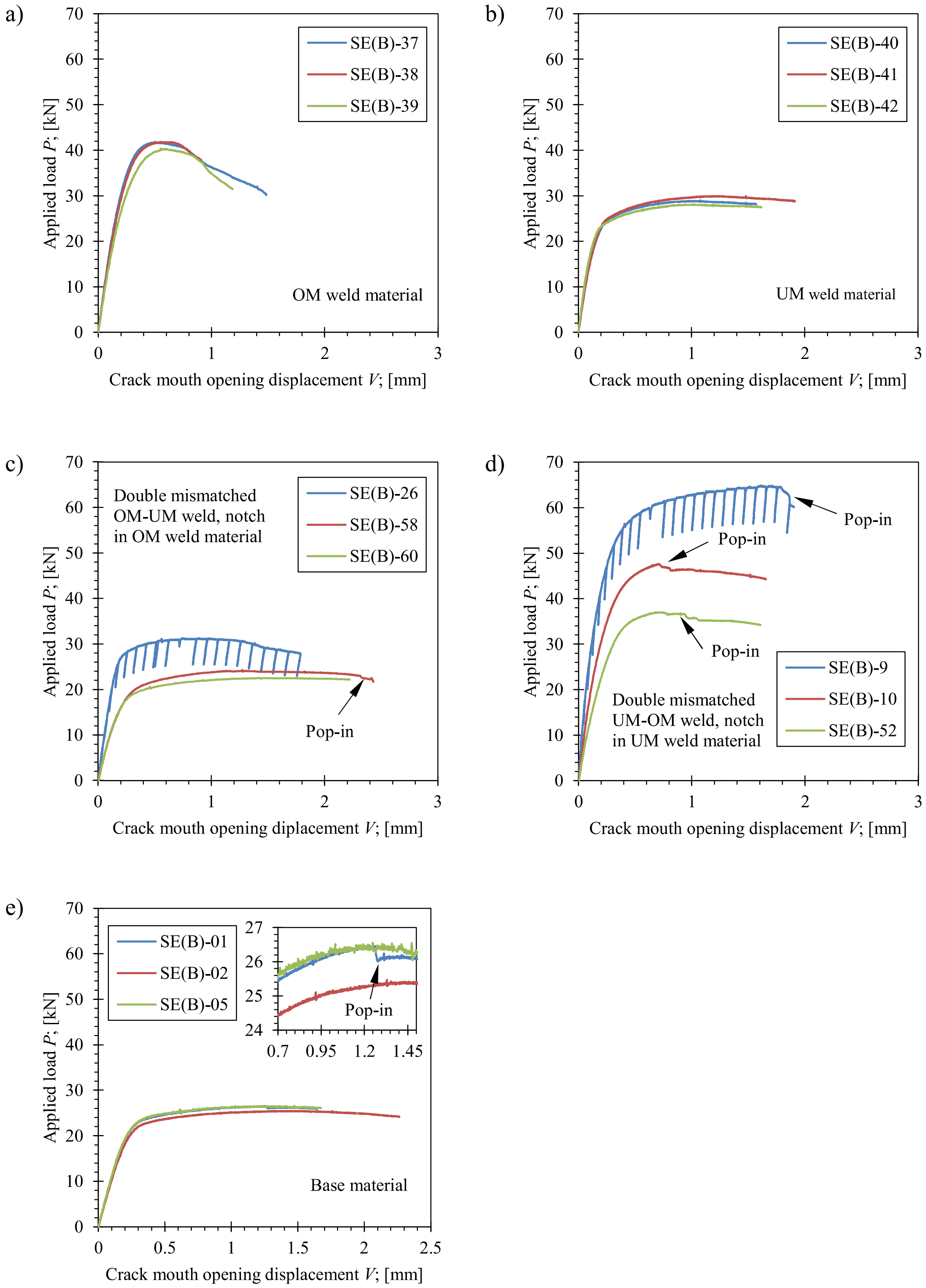

Figure 3.55 The results of fracture testing in form of the recorded P-CMOD history for a) the OM weld, b) the UM weld, c) the double mismatched OM-UM weld, d) the double mismatched UM-OM weld and e) the base material. Unstable crack propagations, i.e. pop-ins, are marked in the presented charts.

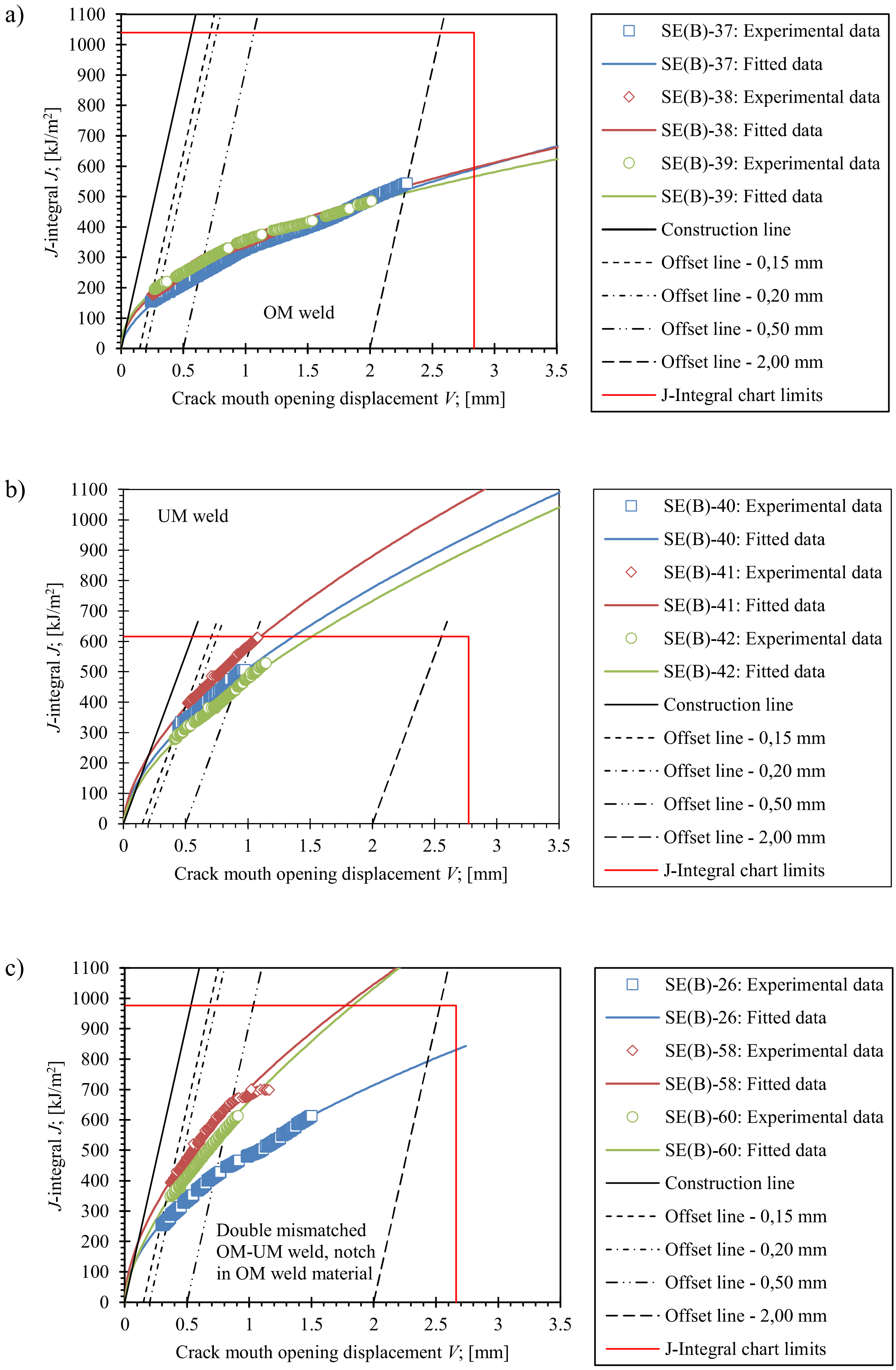
a)
1100
1000
900
800
700
600
500
400
300
200
100
0
J-integral J; [kJ/m²]
0
0.5
1
1.5
2
2.5
3
3.5
Crack mouth opening displacement V; [mm]
OM weld
SE(B)-37: Experimental data
SE(B)-37: Fitted data
SE(B)-38: Experimental data
SE(B)-38: Fitted data
SE(B)-39: Experimental data
SE(B)-39: Fitted data
Construction line
Offset line - 0,15 mm
Offset line - 0,20 mm
Offset line - 0,50 mm
Offset line - 2,00 mm
J-Integral chart limits
b)
UM weld
SE(B)-40: Experimental data
SE(B)-40: Fitted data
SE(B)-41: Experimental data
SE(B)-41: Fitted data
SE(B)-42: Experimental data
SE(B)-42: Fitted data
Construction line
Offset line - 0,15 mm
Offset line - 0,20 mm
Offset line - 0,50 mm
Offset line - 2,00 mm
J-Integral chart limits
c)
Double mismatched OM-UM weld, notch in OM weld material
SE(B)-26: Experimental data
SE(B)-26: Fitted data
SE(B)-58: Experimental data
SE(B)-58: Fitted data
SE(B)-60: Experimental data
SE(B)-60: Fitted data
Construction line
Offset line - 0,15 mm
Offset line - 0,20 mm
Offset line - 0,50 mm
Offset line - 2,00 mm
J-Integral chart limits

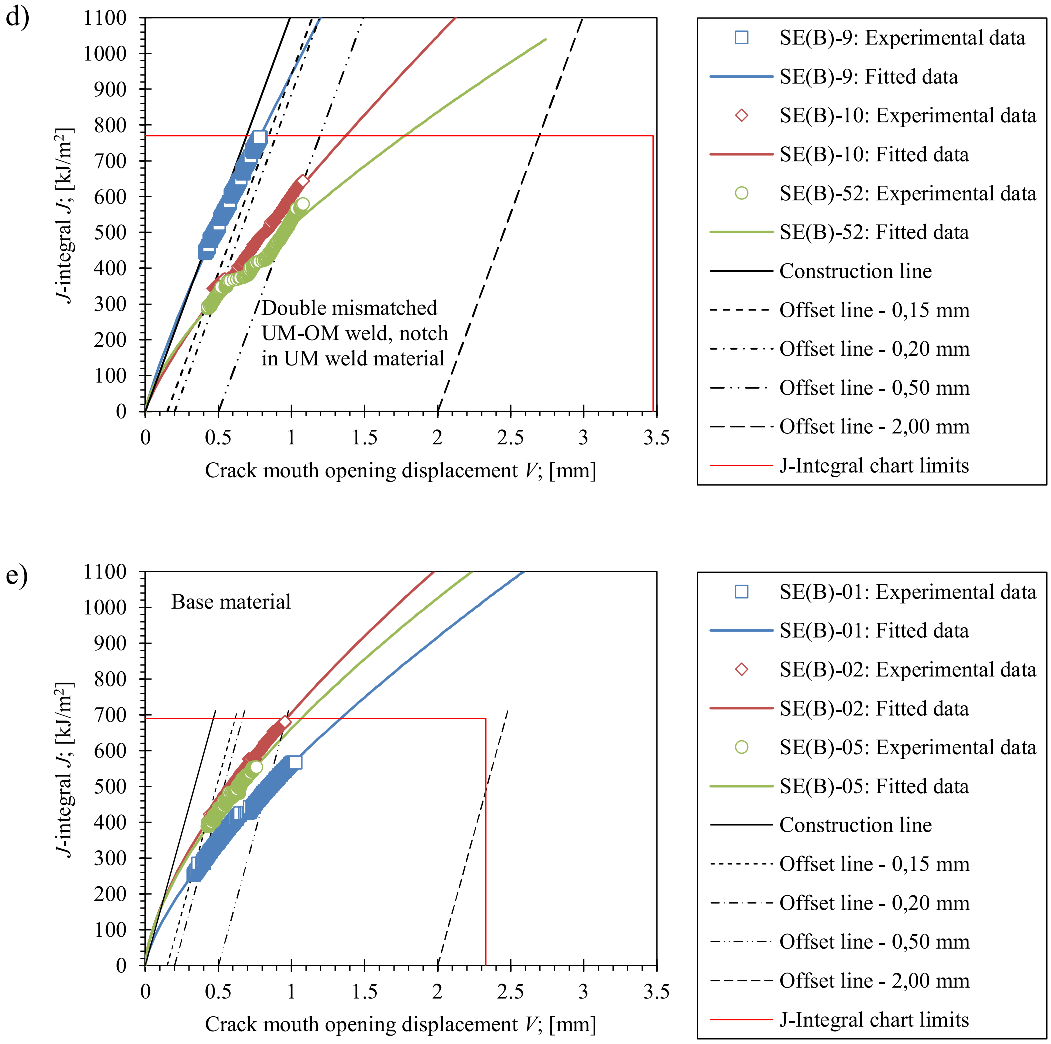

Figure 3.56 The fracture behaviour of the tested SE(B) specimens expressed in terms of *J*-R curves for a) the OM weld, b) the UM weld, c) the double mismatched OM-UM weld, d) the double mismatched UM-OM weld and e) the base material.

Table 3.11 The material yield properties used for the DIC analysis of strain fields.

Material	Type of tensile test	Engineering yield strength S_Y [MPa]	Engineering strain at yield onset e_Y [mm/mm]	True yield strength σ_Y [MPa]	True strain at yield onset ε_Y [mm/mm]
OM weld (average)	AWMTT (1	889.0	6.060 e^{-3}	894.4	6.050 e^{-3}
UM weld (average)	AWMTT (1	532.1	2.635 e^{-3}	533.5	2.631 e^{-3}
Base material (average)	Round bar, tensile (1	682.8	5.790 e^{-3}	686.7	5.770 e^{-3}
HAZ (average)	MTS (2	974.3	7.360 e^{-3}	981.5	7.330 e^{-3}

Remarks:

1) – See Chapter 3.3.1 for detailed information about corresponding standard round bar tensile tests.

2) – See Chapter 3.3.2 for detailed information about corresponding miniature tensile tests.

a) OM weld – specimen SE(B)-38

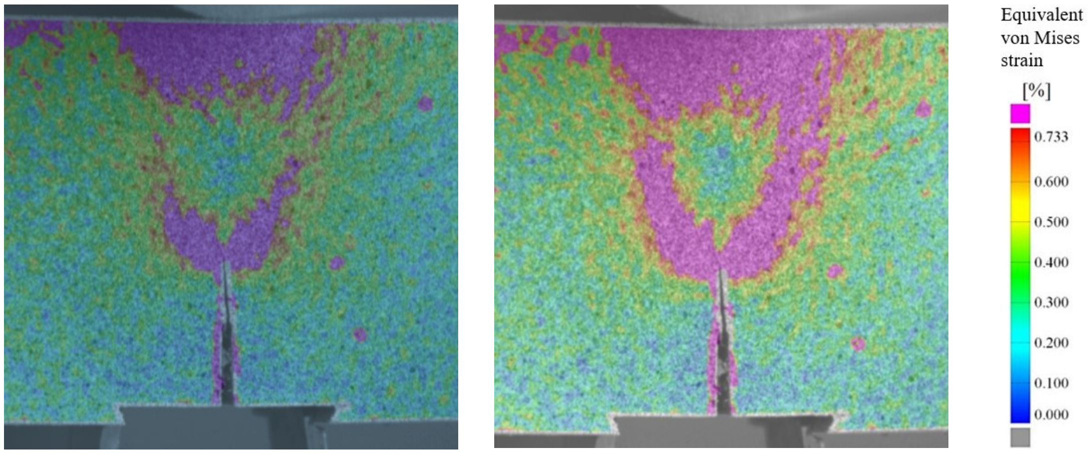

P=38.427 kN (0.948F_Y) *F_Y=40.527 kN*

b) UM weld – specimen SE(B)-40

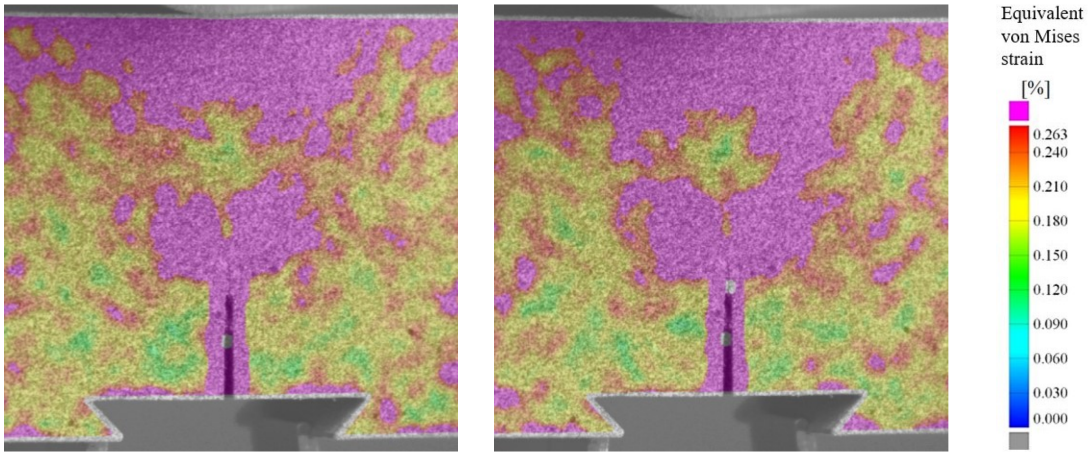

F=20.214 kN (0.952F_Y) *F_Y=21.240 kN*

c) OM-UM weld – specimen SE(B)-26

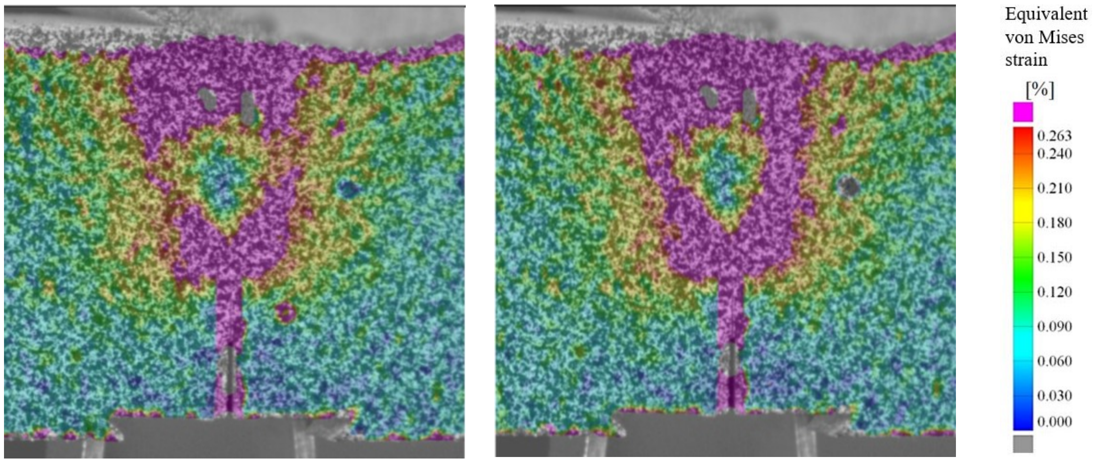

F=21.143 kN (0.948F_Y) *F_Y=22.314 kN*

d) UM-OM weld – specimen SE(B)-09

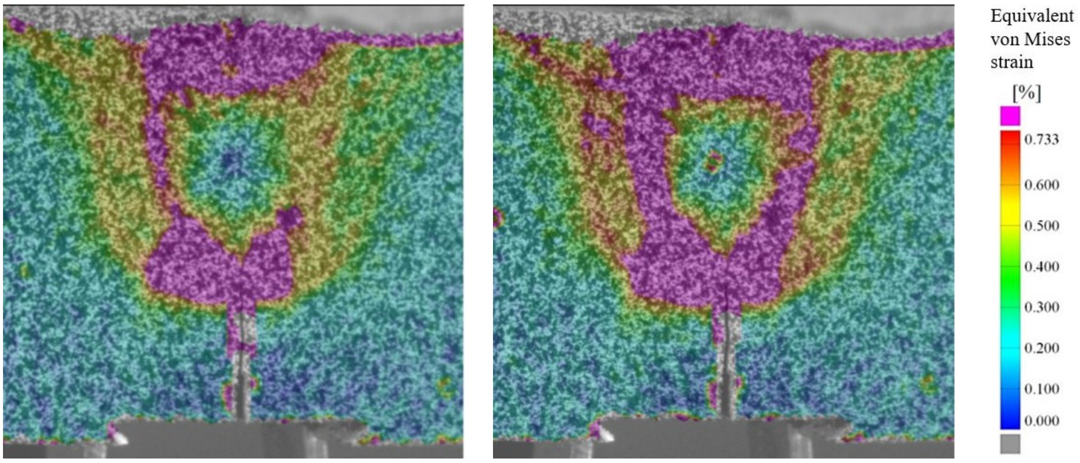

F=40.674 kN (0.936F_Y) *F_Y=43.457 kN*

e) Base material – specimen SE(B)-2

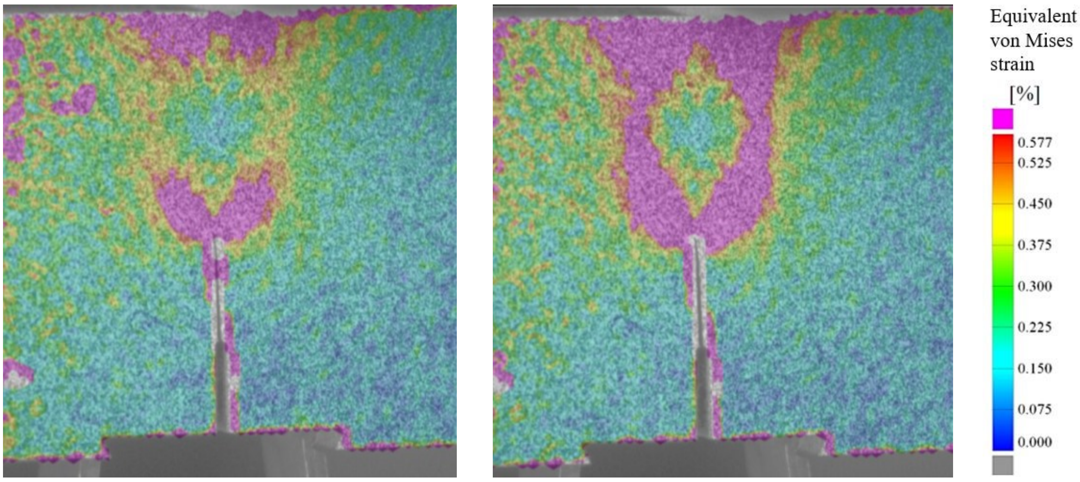

F=21.532 kN (0.950F_Y) *F_Y=22.655 kN*

Figure 3.57 The analysis of equivalent von Mises strain field on side surface of the SE(B) specimens from a) the OM weld, b) the UM weld, c) the double mismatched OM-UM weld, d) the double mismatched UM-OM weld and e) the base material.

3.5.6 Location of Fatigue Precrack and Final Crack Fronts with Respect to the Fusion Line in the Welds

Metallographic investigation has been conducted after the fracture testing, as specified in ISO 15653 [22] and BS 7448-2 [8] standards. Broken surface cracked SE(B) specimens were cut to sections using a horizontal straight cutting bandsaw. Configuration of the extracted sections is shown in Figure 3.58. Specific dimensions of cuts are not given as they were adjusted for each SE(B) specimen. However, it is important to note, that central longitudinal cut was offset by the width of the cut (approx. 3 mm), so that the inspected sections would contain maximum length of the fatigue precrack a_0 and the final physical crack a_p. The surfaces of the sections that should be examined were then polished and etched with 2% solution of nitric acid and alcohol (i.e. Nital) in order to expose microconstituents. Finally, the prepared surfaces were inspected using optical microscopy (Keyence VHX 7000) with magnifications up to 200x. The obtained images are presented and correlated with the fracture surfaces in Figure 3.59.

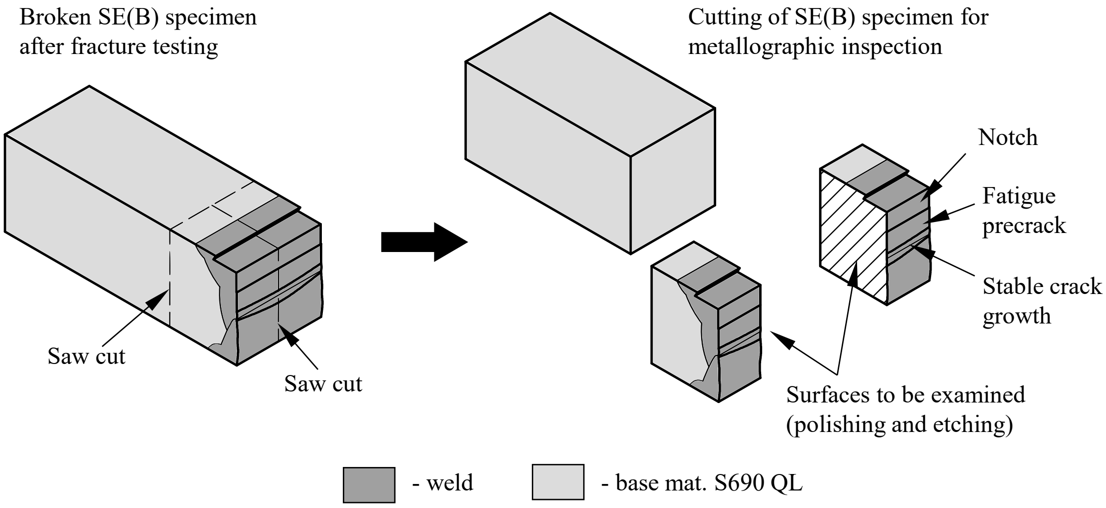

Figure 3.58 Post-test sectioning of the surface notched SE(B) specimen

Figure 3.59 a) and Figure 3.59 b) show the fracture surfaces and the corresponding microstructure of the OM and the UM weld respectively. Relatively straight and planar fatigue precracks were produced in both cases. Slight tunnelling of the final cracks can be observed. Despite that, all measurements of a_p were within the required specifications for the crack front straightness, that are given in ISO 15653 standard [22]. On the visible surfaces of the OM weld (Figure 3.59 a)), tip of the final crack is located on the fusion line between the layers of reheated and as welded material. Slight path deviations of the ductile crack extension were observed ahead of the reheated weld material layer. This is attributed to a sudden change in material toughness and therefore, stress triaxiality.

Similar observations, as in case of the OM and the UM welds, can be made on the OM-UM double mismatched weld with the notch and fatigue precrack in the UM weld material. Here, the cracks were planar with relatively straight fronts as shown in Figure 3.59 c). Other peculiarities were not observed. The most distinctive cracking was observed in the case of the double mismatched OM-UM weld with the crack traversing from the UM weld material towards the OM weld material. Here, the fatigue precrack is planar with relatively straight front, but a direction of the ductile crack growth shows severe deviations. The latter occurred when the crack reached vicinity of the fusion line between the OM and the UM weld materials. The absence of side notches allowed the ductile crack to spread towards the base material. Considering the hardness map presented in Figure 3.13 b), the HAZ normally shows increased hardness and toughness in comparison to the other material regions. However, the HAZ near the weld root has lower hardness, thus enabling the crack to traverse to the base material. Unstable fractures that were observed in the *P*-CMOD records were related to these severe crack path deviations. Similar behaviour of such welds was observed by Naib et al. [123] when conducting fracture testing of single edge notched tensile (SE(T)) specimens that enable predominantly low constraint conditions.

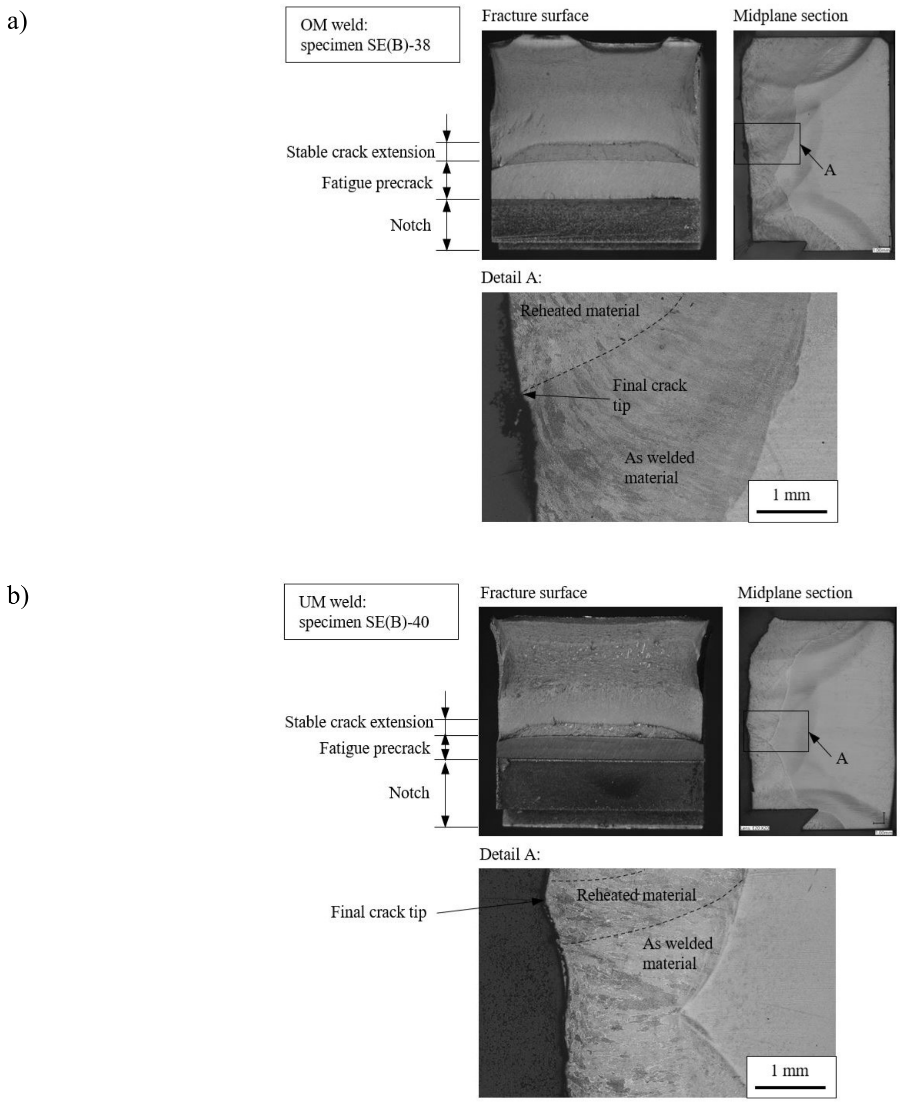

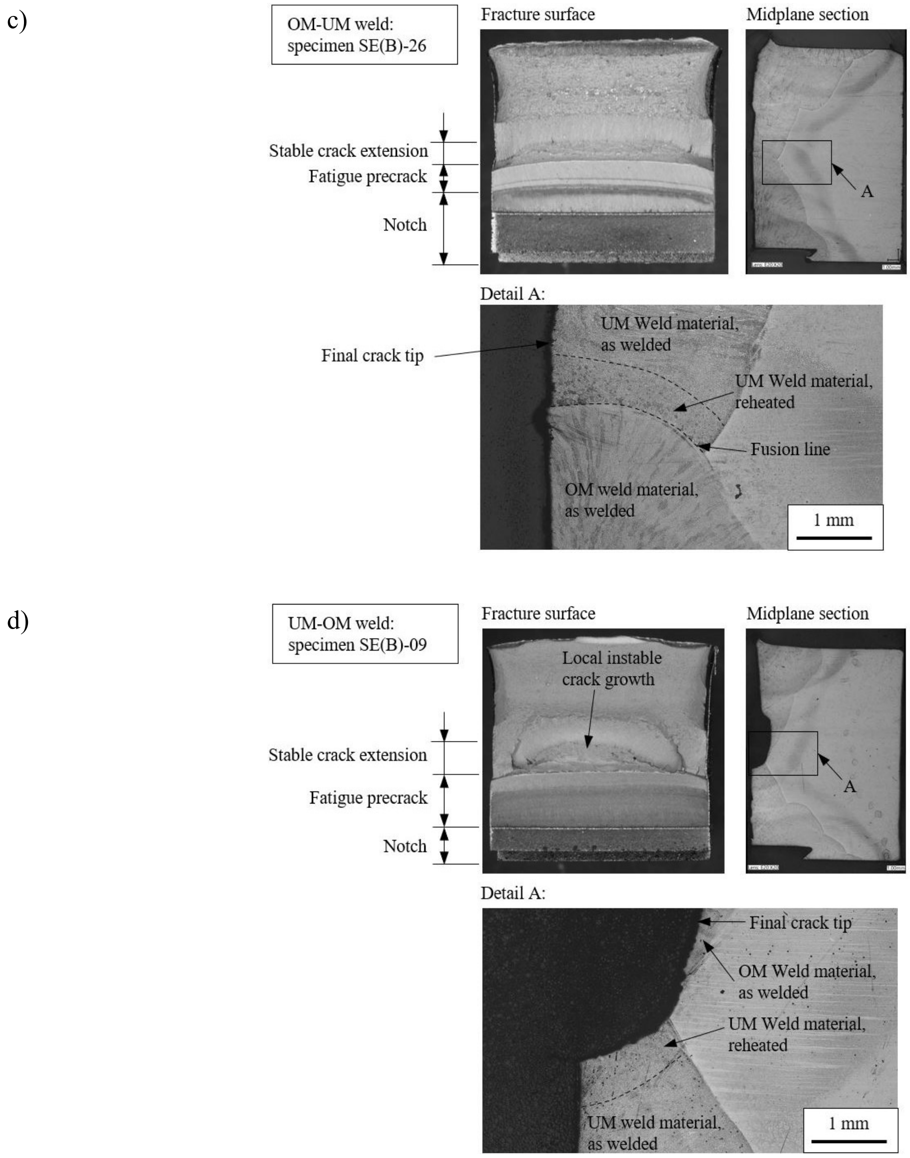

Figure 3.59 Post-test metallographic analysis of the sectioned SE(B) specimens from a) the OM weld, b) the UM weld, c) the double mismatched OM-UM weld and d) the double mismatched UM-OM weld.

3.5.7 Verification of the Results

The results, obtained with the NDRM were compared to the results, obtained with the UCM. This is mandatory, as the NDRM estimates the amount of the stable crack growth Δa during the test. On the other hand, the UCM provides a procedure, that enables indirect measurement of the stable crack growth on the basis of SE(B) specimen compliance. Both methods are included in the ASTM E1820 [6] standard.

The UCM method governs that the fracture specimen has to be partially unloaded at regular intervals during the fracture test. An example of such unloading (and reloading) phases are the *P*-CMOD records, obtained by fracture testing of specimens SE(B)-09 and SE(B)-26, as shown in Figure 3.60. Here, the compliance is computed for each unloading sequence as a reciprocal value of the average slope, determined by the least squares method.

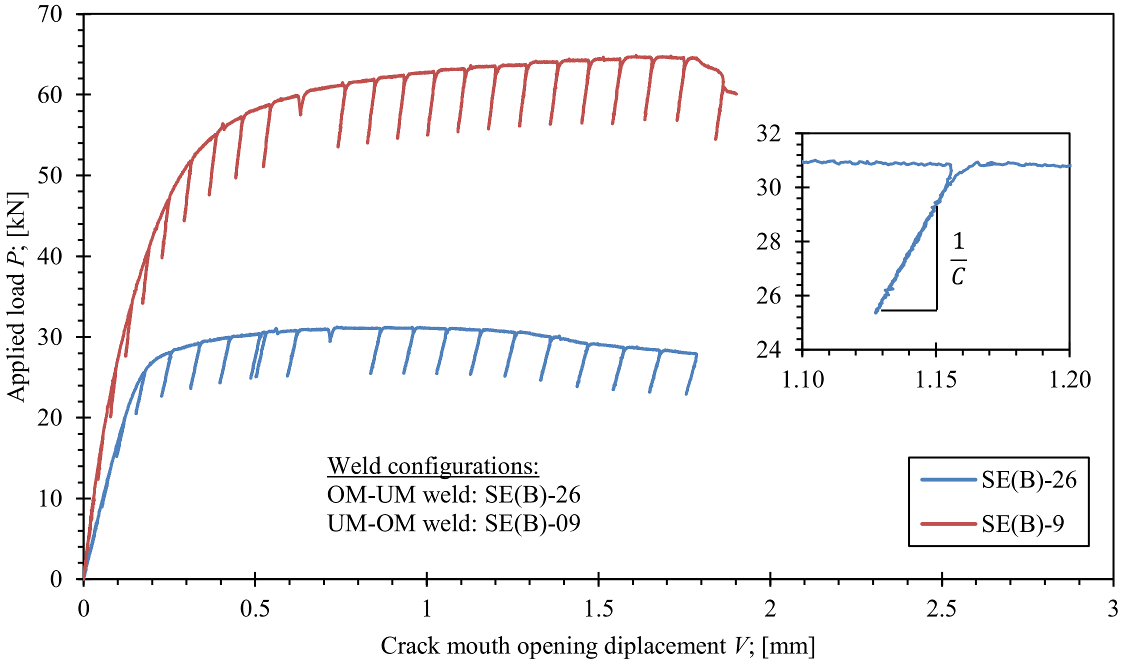

Figure 3.60 The *P*-CMOD records for the tested specimens SE(B)-26 and SE(B)-09 with the visible unloading phases.

The crack size is then determined on the basis of the computed compliances by using the following polynomial function:

$$\frac{a_i}{W} = 0.999748 - 3.9504u + 2.9821u^2 - 3.21408u^3 + 51.51564u^4 - 113.031u^5 \tag{3.42}$$

where the variable u is defined with the following expression:

$$u = \frac{1}{\left(\frac{B_e W E C_i}{0.25S}\right)^{1/2} + 1} \tag{3.43}$$

Here, W is the specimen width in [mm], E is the elastic modulus in [MPa], S is the span width in [mm] that is characteristic dimension for the SE(B) fracture specimen, and C_i is the unloading compliance of the i-th unloading phase. Moreover, B_e is the equivalent specimen thickness in [mm] that is defined according to the following equation:

$$B_e = B - (B - B_N)^2/B \tag{3.44}$$

where B and B_N are expressed in [mm] and represent normal specimen thickness and thickness of the specimen between the notches, respectively. From here on, the J-integral is computed according to the procedure, presented in Chapter 3.5.5, using the equations from (3.29) to (3.35). The only addition to this procedure is the correction of the initial measured crack length a_0. This is done by selecting the J_i-a_i data points, determined before the specimen reached the maximum force for the test. Then, the following equation should be fitted to the selected Ji-ai datapoints by the least squares method:

$$a_i = a_{0q} + \frac{J_i}{2S_Y} + B{J_i}^2 + C{J_i}^3 \tag{3.45}$$

where a_i and J_i are the crack length in [mm] and the J-integral in [J/mm^2] for the i-th J_i-a_i datapoint, respectively. The a_{0q} is the initial crack corrected length in [mm] (determined by the least squares method), S_Y is the engineering yield strength in [MPa], while B and C are dimensionless fitting coefficients. The new corrected ductile crack growth for the J-R curve is then determined as:

$$\Delta a_i = a_i - a_{0q} \tag{3.46}$$

The obtained J-R curves, using the UCM, are presented in Figure 3.61 and Figure 3.62 for the SE(B)-09 (the UM-OM weld) and SE(B)-26 (the OM-UM weld) specimens, respectively. Here, the J-R curves for the NDRM are plotted as a reference. Furthermore, the results of the fracture tests are presented in the Table 3.12.

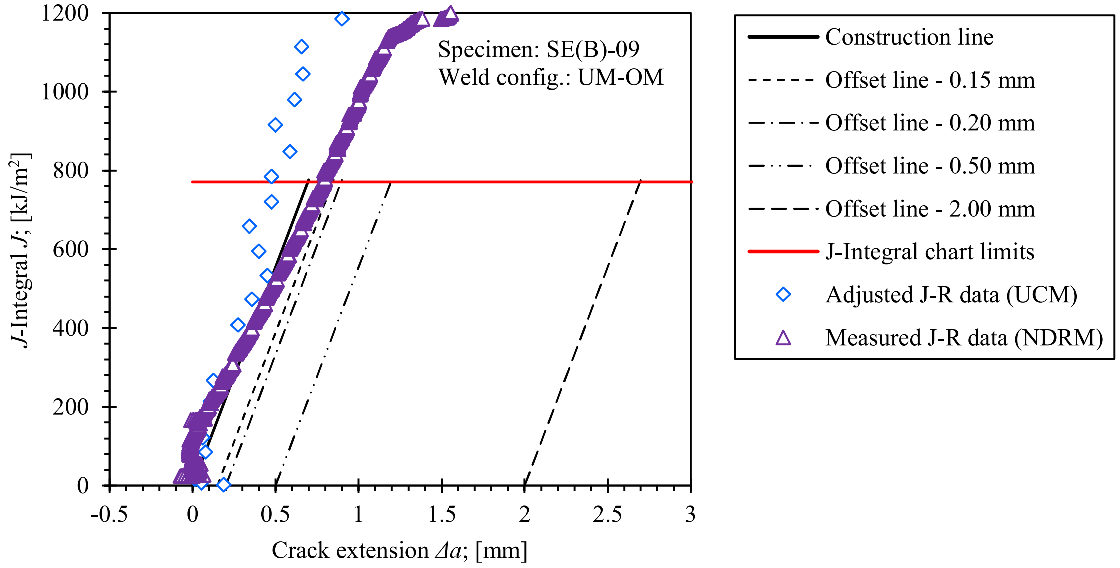

Figure 3.61 The obtained *J*-R resistance curves for the fracture test of the SE(B)-09 specimen (UM-OM weld), using the UCM. The *J*-R curve, obtained with the NDRM is plotted as a reference.

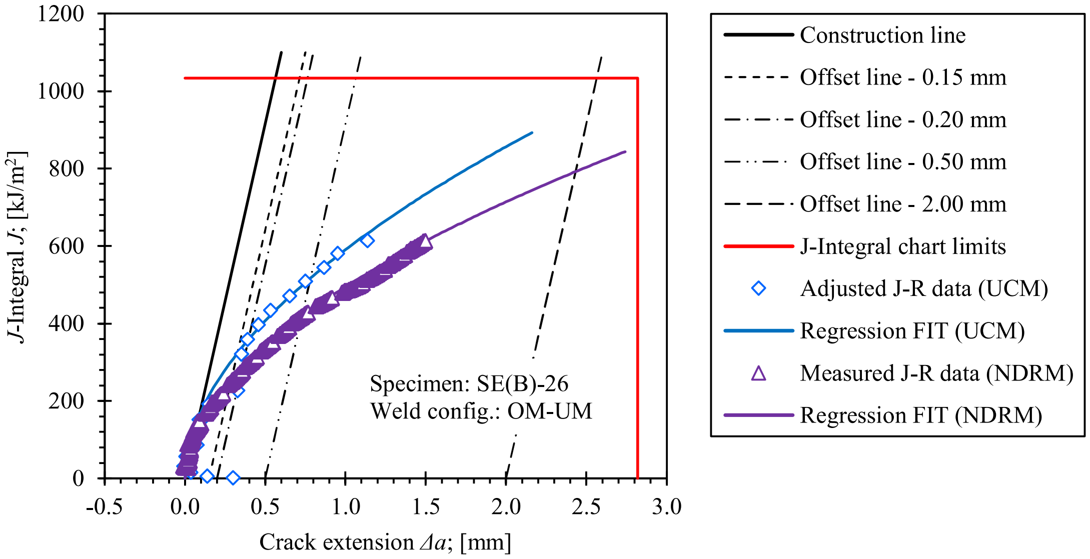

Figure 3.62 The obtained *J*-R resistance curves for the fracture test of the SE(B)-26 specimen (OM-UM weld), using the UCM. The *J*-R curve, obtained with the NDRM is plotted as a reference.

Table 3.12 Results for fracture tests of the SE(B)-09 and SE(B)-26 specimens.

Specimen	SE(B)-09		SE(B)-26	
Test method	NDRM	UCM	NDRM	UCM
Measured fatigue precrack length a_0; [mm]	6.07		9.30	
Measured final crack length a_p; [mm]	7.73		10.79	
Distance to fusion line L_f; [mm]	7.20		10.00	
Estimated ductile crack growth Δa; [mm]	1.67	0.90	1.50	1.14
Estimated final crack length $a_0+\Delta a$; [mm]	7.73	6.97	10.79	10.44
Critical J-integral J_{Ic}; [kJ/m^2]	612	n.a.	287	359
Critical SIF K_{JIc}; [MPam$^{1/2}$]	396	n.a.	273	305

The obtained J-R curves indicate good agreement between the NDRM and the UCM for small ductile crack growth, that is $\Delta a<0.5$ for the SE(B)-09 specimen and $\Delta a<0.4$ for the SE(B)-26 specimen. For larger ductile crack growth Δa, the J-R curves, obtained with the UCM deviate from the one, obtained with the NDRM. Such deviation is attributed to the effect of the interface between the OM and the UM weld material on the crack behaviour of the fracture specimens. Furthermore, the fractured surfaces in Figure 3.59 c) and Figure 3.59 d) for the SE(B)-26 and SE(B)-09 specimens, respectively, show curved final crack front that is within the tolerances according to the ISO standard but according to the ASTM E1820 [6] standard. The latter imposes strict tolerances for the crack front straightness in order to avoid the effect of the crack tunnelling on the results, obtained by the UCM. Considering that the tested SE(B) specimens did not have side grooves, it is assumed that deviation of the UCM J-R curves from the NDRM J-R curves can be attributed to the crack tunnelling effect [124] as well. Additionally, Figure 3.59 d) shows sever crack path deviation at the interface between the UM and the OM weld materials. Such deviation of the crack path has a significant impact on the stiffness of the SE(B) specimen, which causes further deviations of the UCM J-R curve from the NDRM J-R curve. In cases of the both test SE(B) specimens, the UCM failed to accurately predict the total ductile crack growth Δa and the final crack length, as shown in Table 3.12. For that reason, the obtained UCM J-R curves had higher inclination and therefore, provide higher fracture toughness than the NDRM, as demonstrated for the SE(B)-26 specimen in the Table 3.12. In extreme cases, such is the SE(B)-09 specimen, the UCM failed to provide data Ji-ai, that would lie within the 0.15 mm and 2.0 mm offset (i.e. exclusion) lines. Here, the fracture toughness was not computed, as the J-R curve could not be constructed. Based on that, it was concluded that the

UCM failed to provide accurate results for large Δa due to the crack tunnelling and crack path deviation effects.

3.6 Summary and conclusions

The S690 QL sample plates with thickness of 25 mm were welded, using the MAG welding process. Two different weld consumables were used for fabrication of the double mismatched welds. The first one, Mn4Ni2CrMo (with commercial designation MIG 90) with the mismatch factor $M \approx 1.3$ was used for fabrication of the OM part of the weld. The second one, G4Si1 (with commercial designation VAC 65) with the mismatch factor $M \approx 0.67$) was used for fabrication of the UM part of the weld. The corresponding welding parameters were adopted from Arsić et al. [75]. Two types of sample plates were welded. The first one had a double V configuration of the weld groove, while the second had a wide V configuration that is in conformance with the ISO 15792-1 [74] standard. In case of the former, single material and double mismatched welds were fabricated, and the plates were used for extraction of weld micrographs, and micro tensile, Charpy and SE(B) specimens. In case of the latter, only single material welds were fabricated, from which the AWMTT specimens were extracted. Finally, an X-ray inspection confirmed low quantity of defects in the final welds.

Optical microscopy of the macrograph, extracted from the double mismatched weld, showed that the microstructure of the base material consists mainly of ferrite and upper bainite. A presence of martensite was observed as well. Furthermore, the UM weld material has mainly ferritic microstructure with the presence of upper bainite and pearlite. Similarly, the OM weld material exhibited similar microstructure, composed of ferrite, upper bainite and pearlite. The most notable difference between microstructures of the both weld materials was the size of grains. Finally, inspection of the HAZ showed different microstructures in the vicinity of the OM and the UM weld materials. Near the UM weld material, the HAZ has a microstructure, consisting primarily of ferrite which is accompanied by pearlite and upper bainite. In contrary, the HAZ near the OM weld material has a microstructure that consists primarily of upper bainite that is accompanied by sparse pearlite and rare ferrite islands.

The optical microscopy exposed heterogeneous structure of the weld joint. Based on that, it was assumed that the fabricated weld joints should have highly heterogeneous properties. This assumption was endorsed by the microindentation hardness measurements on the micrograph of the double mismatched weld. The obtained results showed high variations in the measured hardness between the weld regions. In terms of the measure hardness, the inspected weld regions are arranged in the following descending order; the HAZ, the OM weld material, the base material and the UM weld material. The results also showed variation of hardness within individual weld passes due to complex thermal history, which additionally demonstrates heterogeneity of the weld joint.

Local mechanical properties were determined by tensile testing of micro specimens. Such specimens enabled to test specific regions of the weld joint due to their small dimensions. The obtained results in terms of yield strength and ultimate tensile strength are shown in Figure 3.29, Figure 3.30 and Figure 3.31 for various specimen stack orientations. The obtained results show variations of the yield and ultimate tensile strengths across the weld joint. This is an important observation as variations of the material properties within the weld can have an effect on the fracture behaviour of the weld joint and on crack propagation within the weld, as it was demonstrated through FEA by Starčevič et al. [71]. Moreover, the obtained yield and ultimate tensile strengths show a good correlation with the measured microindentation hardness.

The average mechanical properties of the OM weld, the UM weld and the base material were determined by tensile testing of AWMTT specimens, that were extracted from the wide V weld joints. Tensile tests were performed in conformance with ASTM E8/E8M [95] standard. Comparison of the obtained results with the results of tensile testing of micro specimens showed a good agreement of the engineering stress-strain curves. Based on that, it can be concluded, that the stress strain curves for the AWMTT are appropriate for establishment of the material model for the homogenized weld regions in the FEM. Furthermore, the average yield strength mismatching factors were determined for the UM (M=0.779) and the OM (M=1.302) weld materials.

The impact toughness of the welds was determined by impact testing of Charpy specimens according to the ASTM E23 [111]. Different groups of Charpy specimens were extracted from the double mismatched welds in such way that the cracking of the specimens could develop entirely in the OM or in the UM weld material and through interface from the OM to UM weld material and from the UM to the OM weld material. The obtained results showed that the fabricated welds have lower energy of rupture than the base material (mean Wt=165.43 J). The OM weld (mean Wt=104.49 J) has lower impact toughness than the UM weld (mean Wt=125.44 J) material. The most important finding is that the combination of the OM and the UM weld materials can increase the impact toughness of the weld joint in comparison to the single material weld joints. When the crack in the Charpy specimen traversed from the OM to the UM weld material, the mean impact toughness was W_t=118.21 J, which is 13 % higher than in the OM weld. Furthermore, when the crack in the Charpy specimen traversed form the UM to the OM weld material, the mean impact toughness was Wt=139.40 J, which is 11 % higher than in the UM weld.

The fracture toughness testing of the welds was conducted according to the ASTM E1820 [6] standard. Different groups of SE(B) specimens were extracted from the sample plates with the single material and the double mismatched welds in a double V configuration. Extracted SE(B) specimens were surface cracked and had a rectangular cross-section with dimensions $B \times W$=20×20 mm. The extracted specimens allowed fracture testing of the OM, the UM and the double mismatched welds, as described in Chapter 3.5.1. In case of the latter, one group of the SE(B) specimens was notched in the OM part of the weld, while the other group was notched in the UM part of the weld. This enabled the crack to traverse through the interface in the weld root from the OM to the UM part of the weld in case of the former, and from the UM to the OM part of the weld in case of the latter. No special method for modification of the residual stresses was applied prior to the fracture testing, as relatively straight fatigue precrack front were obtained with the conventional preecracking method. In the fracture testing, SE(B) specimens were monotonously loaded, while load and CMOD were continuously recorded throughout the entire test. Additionally, strain fields at the surface of the tested SE(B) specimens were recorded with the DIC system. The load-CMOD, i.e. P-CMOD, records indicated that the maximum load bearing capacity of the double mismatched welds is different in comparison to the single material welds, as shown Figure 3.55. SE(B) specimens from the double mismatched weld, with the notch in the OM part of the weld, showed the lowest load bearing capacity of all tested weld. In contrary, SE(B) specimens from the double mismatched weld, with the notch in the UM part of the weld, showed the highest load bearing capacity. However, a significant scatter of P-CMOD records, and presence of locally unstable fractures was detected. After the fracture tests were completed, SE(B) specimens were broken open and metalographic samples were extracted, as demonstrated in Figure 3.58. The surfaces on the metallographic samples that were aligned with the midplane of the SE(B) specimens were polished and etched, and were then visually inspected using the light optical microscope. The inspection showed that severe crack path deviations occurred in the SE(B) specimens from the double mismatched weld, with the notch and the fatigue precrack in the UM part of the weld. Here, the crack deviated severely near the interface between the UM and OM parts of the weld, and then propagated around the OM part of the weld at the interface with the HAZ. Such severe crack path deviations were associated with the locally unstable fractures that were recognized in the P-CMOD records. Because these locally unstable fractures were recognised as “significant” according to the ASTM E1820 [6] standard, the provisional fracture toughness in terms of SIF K_I had to be computed according to the ASTM E399 [5] standard. The resistance to stable tearing in terms of the J-integral resistance *J*-R curves was not computed for the tested SE(B) specimens, as correction factors ηpl and γpl had to be calibrated. The corresponding calibration procedure is described in Chapter 4, while computation and analysis of the J-R curves is described in Chapter 5.

The DIC records were inspected and the strain fields were obtained, as shown in Figure 3.57. In case of the OM welds, the obtained strain fields showed that the plastic deformation bands located in the OM weld material along the interface with the HAZ. Similarly, the obtained strain fields from the DIC inspection of the UM welds showed that the plastic deformation is completely contained within the UM weld. This is due to the HAZ that has higher yield strength than the UM weld material. Moreover, large areas of the UM weld were plastically deformed. I comparison to the single material welds, the double mismatched welds further alter the plastic deformation bands. For example, the double mismatched welds with the notch and the precrack in the UM part of the weld show that the plastic deformation is initially developed in the UM part of the weld. The plastic deformation band then propagate around the OM part of the weld at the interface with the HAZ. This is due to the OM weld material with higher yield strength being located ahead of the crack tip. Opposite was observed in case of the double mismatched welds with the notch and the precrack in the OM part of the weld. Here, the narrow plastic zone was formed ahead of the crack tip. From there on, the plastic deformation bands had rapidly developed within the narrow region of the UM part of the weld. This shows how significantly the strain field is modified if the configuration of the weld changes.

Finally, the J-R curves, obtained with the NDRM were compared with the J-R curves that were obtained with the UCM. The comparison showed, that the NDRM and the UCM J-R curves are in good agreement for the small Δa< approx.0.4 mm. However, at larger Δa the UCM fails to provide accurate results due to the crack tunnelling effect and the crack path deviation.

4 CALIBRATION OF CORRECTION PARAMETERS BY FINITE ELEMENT METHOD FOR FRACTURE TOUGHNESS CALCULATION

4.1 Introduction

The experimental results, presented in the previous chapter, showed that the fabricated welds have highly heterogeneous structure. This has an effect on behaviour of the SE(B) specimens under monotonous loading. Furthermore, different configurations of the single material and the double mismatched welds have a significant impact on development of the strain field and the corresponding bands of plastic deformation in the vicinity of the crack tip. Due to that, it is clear that the standard correction coefficients η_{pl} and γ_{pl} for the homogeneous materials will not be suitable for computation of the J-integral for the welded SE(B) specimens. Furthermore, design of the fixtures, used for the fracture testing of the SE(B) specimens, is not in accordance with the requirements of the ASTM E1820 standard. This this can impact the results of the fracture testing as well. Due to the aforementioned reasons, it is clear that the correction coefficients η_{pl} and γ_{pl} must be calibrated. The calibration procedure that is based on the FEA is presented in this chapter.

4.2 Overview of Methods for Calibration of *J*-integral Correction Factors

4.2.1 Calibration of η Factor

Evaluation of *J*-R resistance curves from load-displacement records using the NDRM (outlined in Chapter 3.5.5) requires specification of several parameters that define *J*, Δa and the η_{pl} correlation factor. It is important to note, that ASTM E1820 standard [6] recognizes two different types of the η_{pl} that are adjusted for computation of J_{pl} on the basis of measured LLD or CMOD. Kirk and Dodds [37] showed through detailed FEA that CMOD-based η_{pl} is insensitive to the strain hardening exponent *n* of the material. This is especially beneficial for fracture testing of welds which have a heterogeneous structure and therefore highly variable mechanical properties across different material regions. Moreover, LLD was not measured during the fracture testing (described in Chapter 3.5.3) as this would require a complex and expensive LLD dedicated gauge [83]. Therefore, a calibration process in scope of this research is focused on CMOD-based η_{pl} factor.

Two FEA based methods for calibration of the η_{pl} were considered in this research. The first method was originally published by Donato and Ruggieri [136] (henceforth denoted as the exclusion method). Their solution for the η_{pl} presented a baseline upon which Zhu et al. [49] fitted Equation (3.34) that is up to this date included in ASTM E1820 standard [6]. Moreover, this method has been incorporated in the recent studies that focused on calibration of η_{pl} factor for dissimilar welds [64], [137], [138], i.e. welds that joined plates of different metals.

The procedure for calibration of η_{pl} for SE(B) specimens according to the exclusion method [136] consists of the following operations. First, load P_i, *J*-integral J_i and CMOD V_i must be extracted from computational results of individual SE(B) specimen for each analysis increment *i*. Next, the computed *P*-CMOD history should be split into elastic and plastic components, using Equation (3.28). The corresponding area $A_{\mathrm{pl,i}}$ under P_i-$V_{pl,\mathrm{i}}$ curve is here computed using the following trapezoidal rule:

$$A_{pl,i} = A_{pl,i-1} + (P_i + P_{i-1})\big(V_{pl,i} - V_{pl,i-1}\big)/2 \tag{4.1}$$

Next, the elastic component of the *J*-integral $J_{el,i}$ should be computed on the basis of the computational results, using Equations (3.30), (3.31) and (3.32). The corresponding plastic component of the *J*-integral should be determined, using the relationship $J_{pl,i}=J_i-J_{pl,I}$, where J_i is total *J*-integral extracted from the computational results. In the next step, $\eta_{pl,i}$ is computed for each analysis increment *i* using Equation (4.2), where *B* and *b* are the SE(B) specimen thickness and remaining ligament in the same units as used in the FEM.

$$\eta_{pl,i} = \frac{J_{pl,i}Bb}{A_{pl,i}} \tag{4.2}$$

Equation (4.2) provides highly variable $\eta_{pl,i}$ values at low deformation level, as demonstrated in Figure 4.1. These values that meet condition (4.3) should be excluded from computation of average η_{pl}.

$$A_{pl,i} \le 0.1\big(A_{el,i} + A_{pl,1}\big) \tag{4.3}$$

Here, $A_{el,i}+A_{pl,i}$ is the area under the complete *P*-CMOD curve. Finally, the η_{pl} factor for the analysed SE(B) specimen should be computed as the average of the remaining $\eta_{pl,i}$ values.

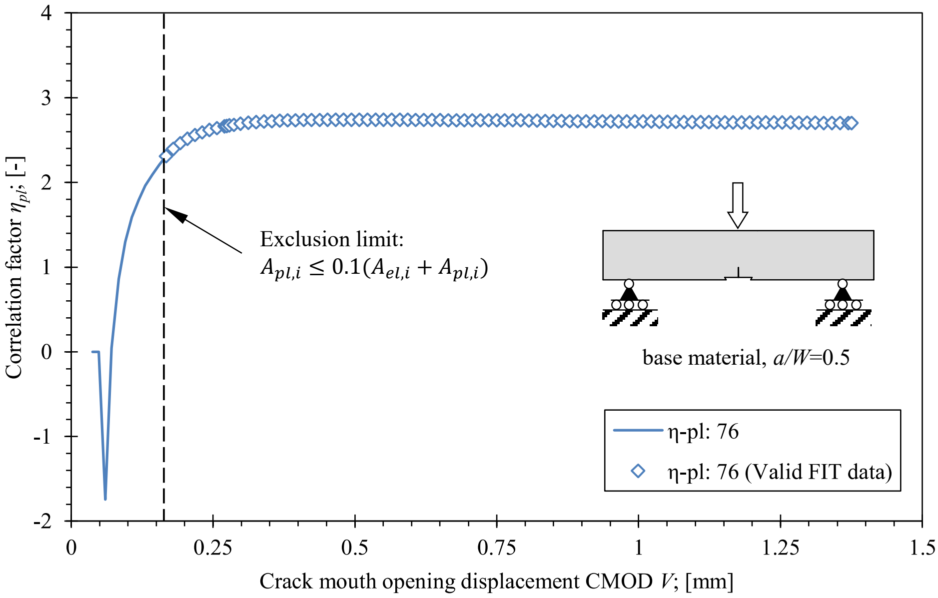

Figure 4.1 The definition of the η_{pl} factor according to Donato and Ruggieri [136]. Presented example is for the FEM of the base material SE(B) specimen with *a/W*=0.5 and standard system of support rollers. Additional information regarding the FEM is available in Chapter 4.2.2.

The second method has been originally published by Donato et al.[60] (henceforth denoted as slope method). This method is appropriate for calibration of η_{pl} factor for fracture specimens of various shapes [139] such as C(T), SE(B) and SE(T). Furthermore, it has proven to provide accurate η_{pl} factors for welds under high constraint [140] and low constraint [61] conditions.

Initial steps in the procedure for calibration of η_{pl} for SE(B) specimens according to the slope method [60] are similar to the exclusion method [136]. Again, quantities such as load P_i, J-integral J_i and CMOD V_i should be extracted from computational results and the corresponding plastic J-integral $J_{pl,i}$, and area $A_{pl,i}$ under P_i-$V_{pl,i}$ plot should be computed as described earlier. However, the main difference between both methods is the way of how the η_{pl} is determined. According to the slope method [60], the η_{pl} is based on normalized values of the plastic J-integral $J'_{pl,i}$ and area $A'_{pl,i}$ under P_i-$V_{pl,i}$ plot. Therefore, the normalized $A'_{pl,i}$ should be computed using the equation (4.4), where B and b are the SE(B) specimen thickness and remaining ligament in the same units as used in FEA, while σ_{YS} is the material yield strength in coherent units.

$$A'_{pl,i} = \frac{A_{pl,i}}{b^2 B \sigma_{YS}} \tag{4.4}$$

Next, the normalized plastic component $J'_{pl,i}$ of the J-integral should be computed by using equation (4.5), where $J_{pl,i}$ and σ_{YS} are plastic component of the J-integral and the material yield strength in coherent units.

$$J'_{pl,i} = \frac{J_{pl,i}}{\sigma_{YS}} \tag{4.5}$$

Finally, a plot of $J'_{pl,i}$ in dependence of $A'_{pl,i}$ should be created. The η_{pl} factor for the analysed SE(B) specimen should be computed as the slope of the $J'_{pl,i}(A'_{pl,i})$ plot by linear regression method, as shown in Figure 4.2. In order to obtain function $\eta_{p}l(a/W)$, either of the presented methods should be repeated to postprocess results for multiple FEA of the SE(B) specimens with different lengths of stationary cracks a/W. Next, the obtained η_{pl} values should be plotted in dependence of the normalized crack length a/W. A polynomial function $\eta_{pl}(a/W)$ should then be fitted using the least squares method. A spreadsheet software, e.g. Microsoft Excel, or any other program language e.g. Python, can be used to perform the function fitting. Both presented methods for calibration of η_{pl} were incorporated in this study. The corresponding results will be compared and discussed in detail in Chapter 4.3.3.

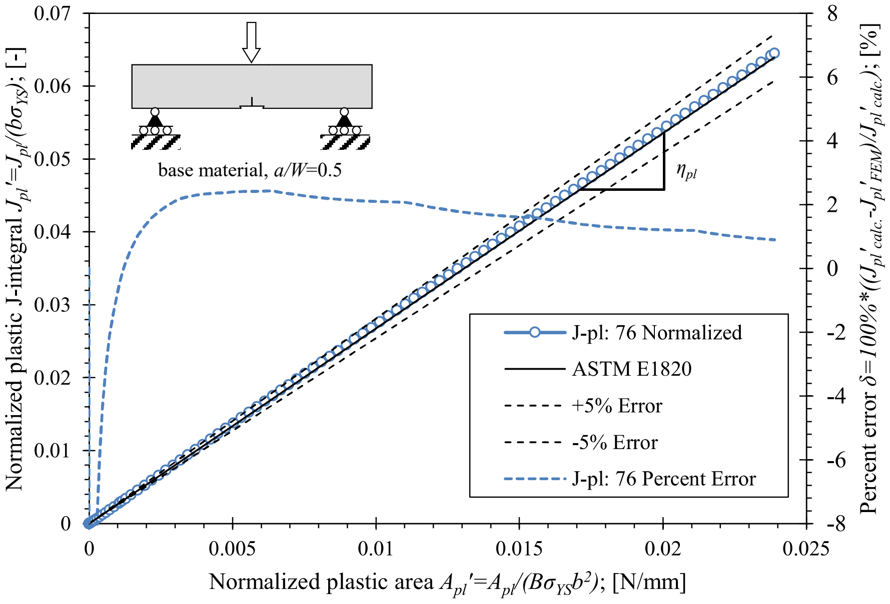

Figure 4.2 The definition of η_{pl} factor according to Donato et al.[60]. The presented example is for the FEM of the base material SE(B) specimen with a/W=0.5 and standard system of support rollers. The analytical solution provided by ASTM E1820 standard [60] is plotted as a reference. Additional information regarding the FEM is available in Chapter 4.2.2.

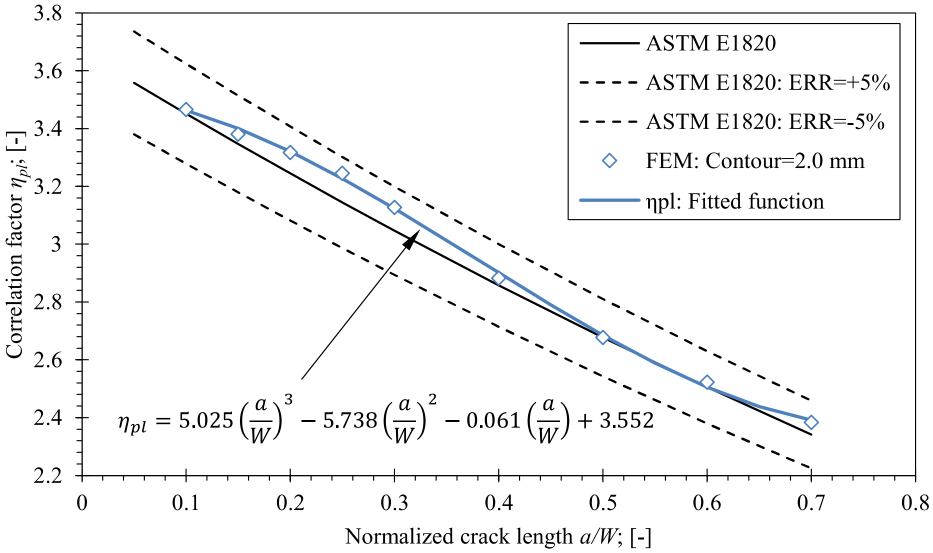

Figure 4.3 The example of fitted η_{pl} function for the base material SE(B) samples with standard configuration of support rollers. Additional information is available in Chapter 4.2.2.

4.2.2 Calibration of γ

The incremental procedure for evaluation of material fracture behaviour from a single specimen test, as specified in the ASTM E1820 standard [6], requires correction factor γ_{pl} in order to compensate stable crack growth and produce accurate *J*-integral. LLD-based crack growth correction factor γ_{pl} was initially developed by Ernst et al. [41] and represented a baseline solution that was later adjusted by Zhu et al. [49] in order to accommodate CMOD as a displacement. Both LLD-based and CMOD-based solutions are up to this date included in ASTM E1820 standard [6].

This research focuses on CMOD-based estimation of the *J*-integral. The calibration procedure is therefore formed around the CMOD-based definition of γ_{pl} crack growth correction factor [85] that is given with the following equation:

$$\gamma_{pl} = \lambda\eta_{pl} - 1 - \frac{b}{W}\left(\frac{\lambda'}{\lambda} + \frac{\eta'_{pl}}{\eta_{pl}}\right) \tag{4.6}$$

where *b* is the ligament length in [mm], *W* is the specimen width in [mm], while $\eta_{pl,i}$ and $\eta'_{pl,i}$ are the dimensionless CMOD-based correlation factor and a corresponding derivative. The dimensionless factor λ_i is here defined as the ratio of plastic CMOD $V_{pl,i}$ and LLD $\Delta_{pl,i}$, as given in Equation (4.7), where λ'_i is a corresponding derivative.

$$\lambda = \frac{V_{pl}}{\Delta_{pl}} \tag{4.7}$$

Equations (4.6) and (4.7) are used to post-process the results of FEA, conducted for series of the multiple SE(B) specimens with stationary cracks of variable lengths *a/W*. Shape factor λ must be obtained for each analysed SE(B) specimen according to the procedure, described next.

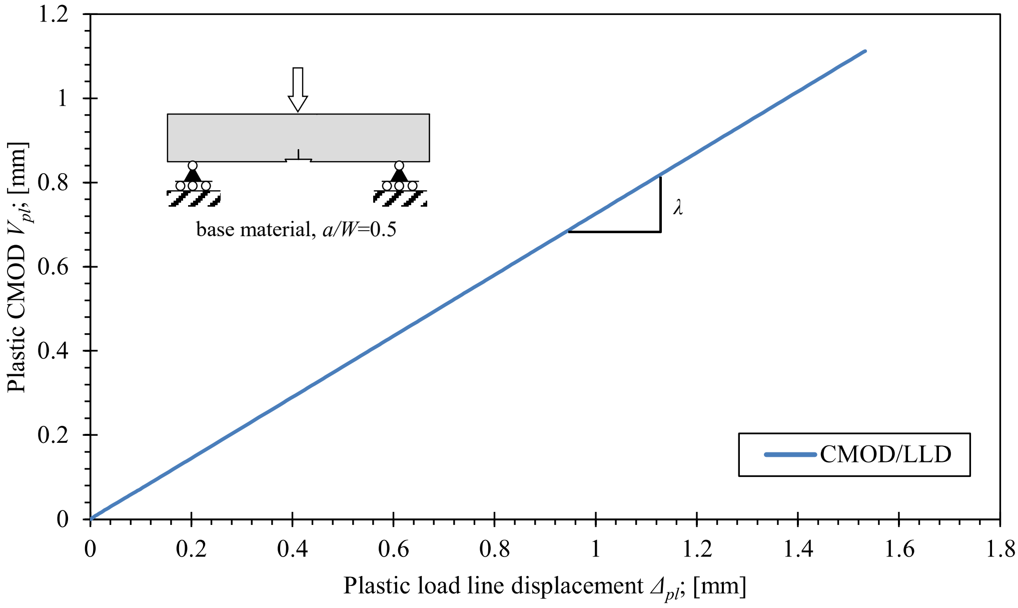

Figure 4.4 The definition of λ factor according to Zhu et al. [49]. The presented example is for FEM of the base material SE(B) specimen with *a/W*=0.5 and standard system of support rollers.

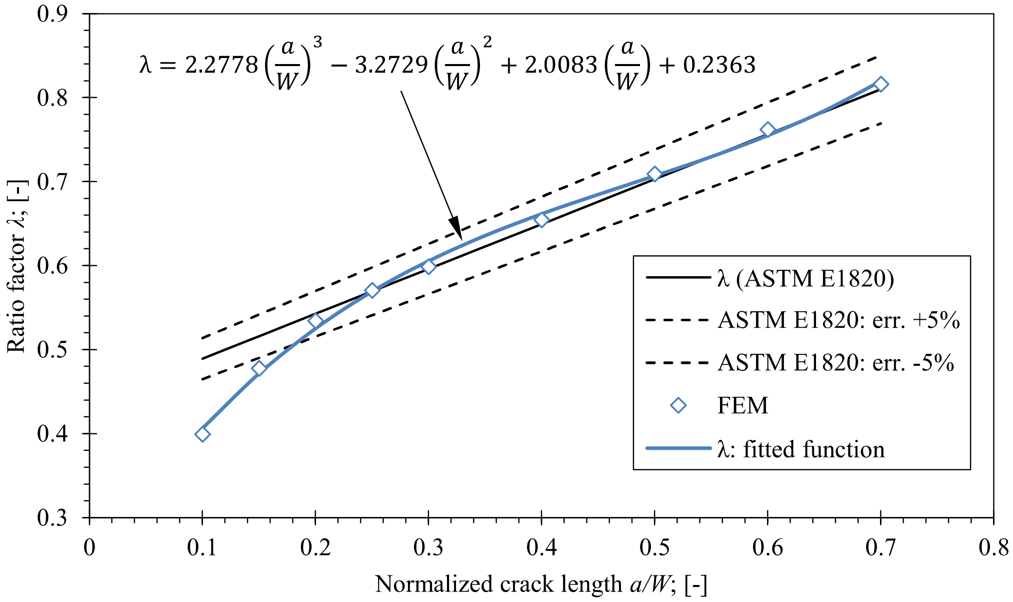

Figure 4.5 The example of fitted λ function for the base material SE(B) samples with standard configuration of support rollers. Additional information is available in Chapter 4.2.2.

First, LLD Δ_i and CMOD V_i should be extracted from the computational results of the analysed SE(B) specimen for each analysis increment i. The corresponding plastic components of LLD $\Delta_{pl,i}$ and CMOD $V_{pl,}i$ should be computed, using Equation (3.28). It must be noted, that Equation (3.28) can be applied to LLD as well, by substituting the CMOD components V_i, $V_{el,i}$ and $V_{pl,}i$ with the LLD components Δ_i, $\Delta_{el,i}$ and $\Delta_{pl,i}$, respectively. Next, a plot of plastic CMOD $V_{pl,i}$ in dependence of plastic LLD $\Delta_{pl,i}$ should be created. The corresponding average λ factor for the analysed SE(B) specimen is then computed as the slope of the $\Delta_{pl,i}(V_{pl,i})$ plot by linear regression method as demonstrated in Figure 4.4.

In order to obtain function $\lambda(a/W)$, the aforementioned procedure should be used in postprocessing of the computational results for series of the analysed SE(B) specimens with variable lengths of stationary cracks a/W. The obtained λ values should be plotted in dependence of the normalized crack length a/W, as demonstrated in Figure 4.5. Finally, function $\lambda(a/W)$ should be fitted using the least squares method.

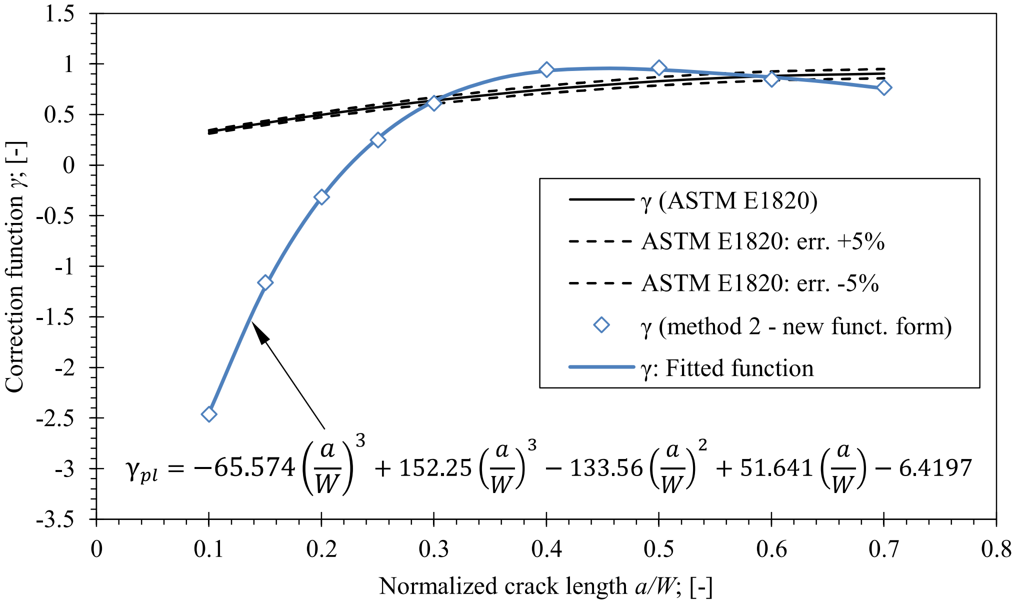

Figure 4.6 The example of fitted γ function for the base material SE(B) samples with standard configuration of support rollers. Additional information is available in Chapter 4.2.2.

The final step in post-processing of the computational results involves calibration of the crack growth correction factor γ_{pl}. The latter can be determined as a function $\gamma(a/W)$ on the basis of precedingly calibrated $\eta_{pl}(a/W)$ and $\lambda(a/W)$ functions. In order to do so, the corresponding derivatives of $\eta_{pl}(a/W)$ and $\lambda(a/W)$ functions should be computed, using Equation (4.8) and Equation (4.9).

$$\lambda'(a/W) = \frac{d\lambda(a/W)}{d(a/W)} \tag{4.8}$$

$$\eta'_{pl}(a/W) = \frac{d\eta_{pl}(a/W)}{d(a/W)} \tag{4.9}$$

Next, the computed values of $\eta_{pl}(a/W)$, $\eta'_{pl}(a/W)$, $\lambda(a/W)$ and $\lambda'(a/W)$ functions for the analysed SE(B) specimens with given crack lengths a/W should be substituted in Equation (4.6), and the corresponding crack growth correction factor γ_{pl} should be computed. Finally, a plot of γ_{pl} in dependence of the normalized crack length a/W should be constructed. The corresponding polynomial function $\gamma_{pl}(a/W)$ is then determined by a least squares method. The presented procedure for the calibration of factor γ_{pl} has been incorporated in this research and was used for various weld configurations, as it will be discussed in continuation of Chapter 4.

4.3 Finite Element Models

4.3.1 Weld Idealization

Ideally, the heterogeneous structure of the weld with the corresponding variations in material mechanical properties should be modelled in the FEM in order to obtain accurate stress and strain fields in the vicinity of the crack that is located in the weld. A good example is a recent study conducted by Starčevič et al. [71]. The focus of that study was to simulate the effect of local variations in mechanical properties on crack propagation in a double mismatched OM-UM weld. The study produced numerical results in terms of *P*-CMOD records that were comparable to experimental results with minor deviations. Another example is a study conducted by Naib et al. [93] where local mechanical properties were established on the basis of measured hardness map, and were prescribed to individual finite elements in FEM of mismatched welds. The goal of that study was to accurately predict yield limit load of welded joint with a crack under tensile load. Both examples confirmed that the fracture behaviour of mismatched welds can be accurately predicted. However, mathematical formulation of the *J*-integral assumes that a crack is located in homogeneous material with fixed, unique material properties [28], [23]. In order to obtain a valid solution for *J*-integral, a decision was made to simplify and homogenize modelled welds.

Current fracture assessment procedures adopt an idealized weld geometry with straight fusion lines to represent more complex weld configurations found in engineering applications. A systematic methodology for a simplification of an actual V-groove weld with a centreline crack has been proposed by Hertelé et al. [79], [141]. This methodology has been developed for SE(T) specimens and is based on the analysis of slip-line patterns. Research conducted by Souza et al. [142] showed that the weld simplification methodology proposed by Hertelé [79] is adequate for V-grooved welds with straight fusion lines for various weld strength mismatch levels.

However, the proposed methodology fails to produce accurate results in the presence of high levels of weld strength undermatch, as the deformation pattern near the crack tip changes significantly. Considering this, the double-V weld was in the scope of this research simplified to have bi-linear fusion lines, as shown in Figure 4.7, rather than a square weld cross section geometry consisting of perfectly straight fusion lines.

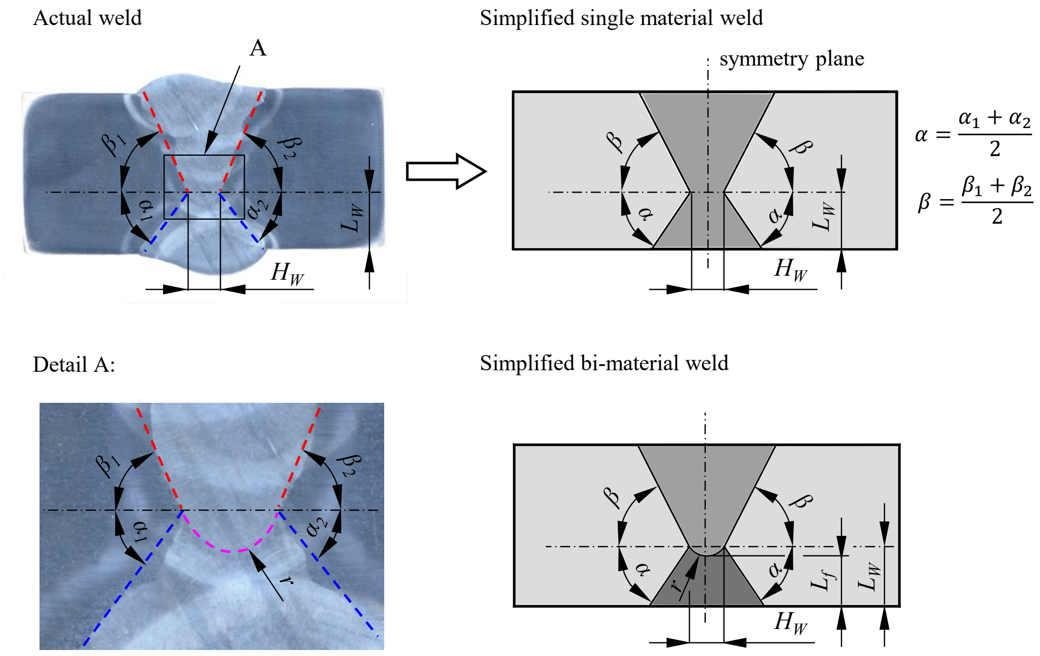
Actual weld

Simplified single material weld

Detail A:

Simplified bi-material weld

Figure 4.7 The approach to derive a simplified weld from an irregularly shaped actual weld.

Table 4.1 Computed dimensions of simplified welds.

Weld	Angle α α [°]	Angle β β [°]	Weld root width H_W [mm]	Distance to weld root L_W [mm]	Distance to fusion line L_f [mm]	Fusion line radius r [mm]
OM	48.3	62.7	5.17	7.2	n.a.	n.a.
UM	42.9	51.7	3.47	8.3	n.a.	n.a.
OM-UM	48.7	58.2	3.30	14.38	15.07	2.30
UM-OM	48.7	58.2	3.30	10.62	9.93	2.30

The geometry of the OM and the UM welds was modelled symmetrically with respect to the central vertical plane of the SE(B) specimen. The simplification of the double-V weld geometry has been done through post-processing of digital macrographs of actual welds using the following procedure. First, four distinctive fusion lines were recognized with respect to the position of the weld root; upper right, upper left, lower right and lower left fusion line. Points were then marked along each of the four fusion lines and coordinates of the marked points were extracted. Next, straight fusion lines were fitted to the extracted coordinates using linear regression. The average slopes of upper and lower fusion lines have been computed in order to create an asymmetrical simplified geometry of the weld. The width of the weld root has been measured so to accurately adjust the minimum width of the idealized weld in the FEM. Finally, the side surfaces of the actual SE(B) specimens have been etched and the vertical position of the weld root was measured prior to fracture testing. The position of the weld root was later transferred to the idealized weld in the FEM. This way, an idealized weld for each parametric FEM series was adjusted to match a corresponding SE(B) specimen that underwent fracture testing. The simplified weld geometry is shown in Figure 4.7, while the corresponding dimensions are presented in Table 4.1.

4.3.2 Configuration of Finite Element Models

A detailed nonlinear FEA has been performed using ABAQUS 2018 with the purpose to calibrate the correlation factor η_{pl}, the shape factor λ and the crack growth correction factor γ_{pl}. Plane strain FEM have been created for a wide range of SE(B) specimens with width W=20 mm, width to thickness ratio W/B=1, and span length S=4W=80 mm. The main motivation to create the plane strain FEM is that the standardised procedures for evaluation of fracture toughness [6], [8], [11], [22] are based on an assumption that fracture specimens are predominantly in plane strain condition during testing. A recent study conducted by Petti et al. [97] proved that 3D FEM provide accurate estimation of the aforementioned factors for *J*-integral calculation. However, considering that measured fracture toughness is size dependent [42], additional care should be taken when transferring fracture test results to structural integrity assessment process, if fracture test specimen size does not match a thickness of the structural component [4], [3].

The analysis matrix shown in Table 4.2 includes SE(B) specimens with a/W=0.1÷0.7 in various material configurations and in combination with three different fixture setups. Simplified welds in analysed FEM were configured to match characteristic dimensions (L_f, L_W, H_W) of welds in actual tested SE(B) specimens. The details of each FEM configuration will be discussed in the following chapters, while the common features will be discussed in the continuation of this chapter.

Table 4.2 The analysis matrix with FEM series distinctive features.

FEM series	FEM configuration	Diameters of fixture rollers and corresponding degrees of freedom	Modelled normalized a/W crack lengths
1A-BM	base material, small strain approach	d_S=10 mm, free in horizontal plane d_L=8 mm, applied displacement in vertical plane	0.1, 0.15, 0.2, 0.25, 0.3, 0.4, 0.5, 0.6, 0.7
1B-BM	base material, small strain approach	d_S=10 mm, free in horizontal plane d_L=25 mm, applied displacement in vertical plane	0.1, 0.15, 0.2, 0.25, 0.3, 0.4, 0.5, 0.6, 0.7
1C-BM	base material, small strain approach	d_S=25 mm, fixed d_L=25 mm, applied displacement in vertical plane	0.1, 0.15, 0.2, 0.25, 0.3, 0.4, 0.5, 0.6, 0.7
2A-OM	OM weld M=1.302, L_f/W=0.36, small strain approach	d_S=25 mm, fixed d_L=25 mm, applied displacement in vertical plane	0.1, 0.15, 0.2, 0.25, 0.3, 0.36, 0.4, 0.5, 0.6, 0.7
2B-UM	UM weld M=0.779, L_f/W=0.415, small strain approach	d_S=25 mm, fixed d_L=25 mm, applied displacement in vertical plane	0.1, 0.15, 0.2, 0.25, 0.3, 0.415, 0.5, 0.6, 0.7
3A-OM	OM weld M=1.5, L_f/W=0.36, small strain approach	d_S=25 mm, fixed d_L=25 mm, applied displacement in vertical plane	0.1, 0.15, 0.2, 0.25, 0.3, 0.36, 0.4, 0.5, 0.6, 0.7
3B-UM	UM weld M=0.5, L_f/W=0.415, small strain approach	d_S=25 mm, fixed d_L=25 mm, applied displacement in vertical plane	0.1, 0.15, 0.2, 0.25, 0.3, 0.415, 0.5, 0.6, 0.7
4A-OM	OM weld M=1.302, HAZ, L_f/W=0.36, small strain approach	d_S=25 mm, fixed d_L=25 mm, applied displacement in vertical plane	0.1, 0.15, 0.2, 0.25, 0.3, 0.36, 0.4, 0.5, 0.6, 0.7
4B-UM	UM weld M=0.779, HAZ, L_f/W=0.415, small strain approach	d_S=25 mm, fixed d_L=25 mm, applied displacement in vertical plane	0.1, 0.15, 0.2, 0.25, 0.3, 0.415, 0.5, 0.6, 0.7
5A-OM	OM weld M=1.302, HAZ, L_f/W=0.39, small strain approach	d_S=25 mm, fixed d_L=25 mm, applied displacement in vertical plane	0.1, 0.15, 0.2, 0.25, 0.3, 0.39, 0.5, 0.6, 0.7
5B-OM	OM weld M=1.302, HAZ, L_f/W=0.652, small strain approach	d_S=25 mm, fixed d_L=25 mm, applied displacement in vertical plane	0.1, 0.15, 0.2, 0.25, 0.3, 0.4, 0.5, 0.6, 0.652, 0.7
5C-UM	UM weld M=0.779, HAZ, L_f/W=0.440, small strain approach	d_S=25 mm, fixed d_L=25 mm, applied displacement in vertical plane	0.1, 0.15, 0.2, 0.25, 0.3, 0.4, 0.44, 0.5, 0.6, 0.7
5D-UM	UM weld M=0.779, HAZ, L_f/W=0.469, small strain approach	d_S=25 mm, fixed d_L=25 mm, applied displacement in vertical plane	0.1, 0.15, 0.2, 0.25, 0.3, 0.4, 0.469, 0.5, 0.6, 0.7
6A-OM-UM	OM-UM weld, crack in OM, M_{OM}=0.779, M_{UM}=1.302, HAZ, L_f/W=0.5, small strain approach	d_S=25 mm, fixed d_L=25 mm, applied displacement in vertical plane	0.1, 0.15, 0.2, 0.25, 0.3, 0.4, 0.471, 0.526, 0.6, 0.7
6B-UM-OM	UM-OM weld, crack in UM, M_{UM}=1.302, M_{OM}=0.779, HAZ, L_f/W=0.435, small strain approach	d_S=25 mm, fixed d_L=25 mm, applied displacement in vertical plane	0.1, 0.15, 0.2, 0.25, 0.3, 0.35, 0.409, 0.464, 0.5, 0.6, 0.7

7A-OM-UM	OM-UM weld, crack in OM, M_{OM}=0.779, M_{UM}=1.302, HAZ, L_f/W=0.525, small strain approach	d_S=25 mm, fixed d_L=25 mm, applied displacement in vertical plane	0.1, 0.15, 0.2, 0.25, 0.3, 0.4, 0.497, 0.551, 0.6, 0.7
7B-OM-UM	OM-UM weld, crack in OM, M_{OM}=0.779, M_{UM}=1.302, HAZ, L_f/W=0.583, small strain approach	d_S=25 mm, fixed d_L=25 mm, applied displacement in vertical plane	0.1, 0.15, 0.2, 0.25, 0.3, 0.4, 0.5, 0.554, 0.609, 0.6, 0.65, 0.7
7C-UM-OM	UM-OM weld, crack in UM, M_{UM}=1.302, M_{OM}=0.779, HAZ, L_f/W=0.360, small strain approach	d_S=25 mm, fixed d_L=25 mm, applied displacement in vertical plane	0.1, 0.15, 0.2, 0.25, 0.3, 0.334, 0.389, 0.5, 0.6, 0.7
7D-UM-OM	UM-OM weld, crack in UM, M_{UM}=1.302, M_{OM}=0.779, HAZ, L_f/W=0.528, small strain approach	d_S=25 mm, fixed d_L=25 mm, applied displacement in vertical plane	0.1, 0.15, 0.2, 0.25, 0.3, 0.35, 0.4, 0.501, 0.557, 0.6, 0.7

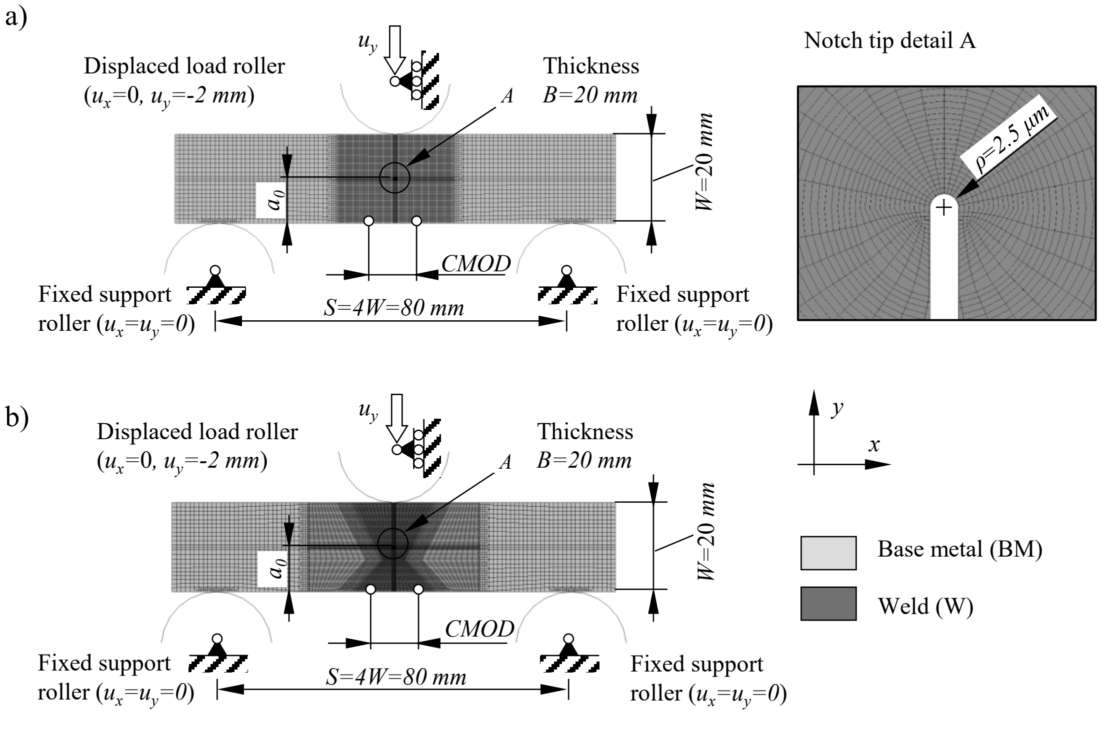

Figure 4.8 The examples of FEM of the SE(B) specimens; a) containing only the base material and b) containing the weld.

Figure 4.8 shows examples of plane strain FEM for SE(B) specimens with a/W=0.5 consisting of the base material and containing a welded joint (similar geometry for all weld configurations). All other models have similar features. A conventional mesh configuration, having a focused ring of finite elements surrounding a stationary crack with a blunted tip was used [23], [143]. According to SIMULIA documentation [144] and educational material [145], the J contour integral should be accurately evaluated if radius of blunted crack tip is $\rho_0 \approx 10^{-3} r_p$. Here, r_p is the size of the plastic zone ahead of the crack tip that is determined according to Irwin [28] as:

$$r_p = \frac{1}{2\pi}\left(\frac{K_I}{\sigma_{YS}}\right)^2 \tag{4.10}$$

where K_I is SIF that is obtained by post-processing of recorded P-CMOD curves (Chapter 3.4.5, Figure 3.54) using 95% secant method, as specified in ASTM E399 [5]. It is important to note that the K_I in Equation (4.10) is not a fracture toughness parameter but rather SIF, proportional to the applied remote stress. The size of plastic zone has been estimated for each tested material, using Equation (4.10). The results presented in Table 4.3 suggest that the average crack tip radius $\rho_0 \approx 1.5$ µm could be modelled in all FEM in order to minimize the influence of the geometry and the mesh on the computed results. However, blunt crack tip radius $\rho_0 = 2.5$ µm was implemented in analysed FEM, as published studies [28], [60] reported that such stationary crack configuration produces sufficiently accurate results.

Table 4.3 The computed plastic zone sizes for the materials in FEM that contain crack.

Material	Stress intensity factor according to 95 % secant method K_I [MPam$^{1/2}$]	Plastic zone size r_p [mm]
Base material (S690 QL)	69	1.6×10^{-3}
OM weld material (Mn4Ni2CrMo)	65	0.9×10^{-3}
UM weld material (G4Si1)	61	2.1×10^{-3}

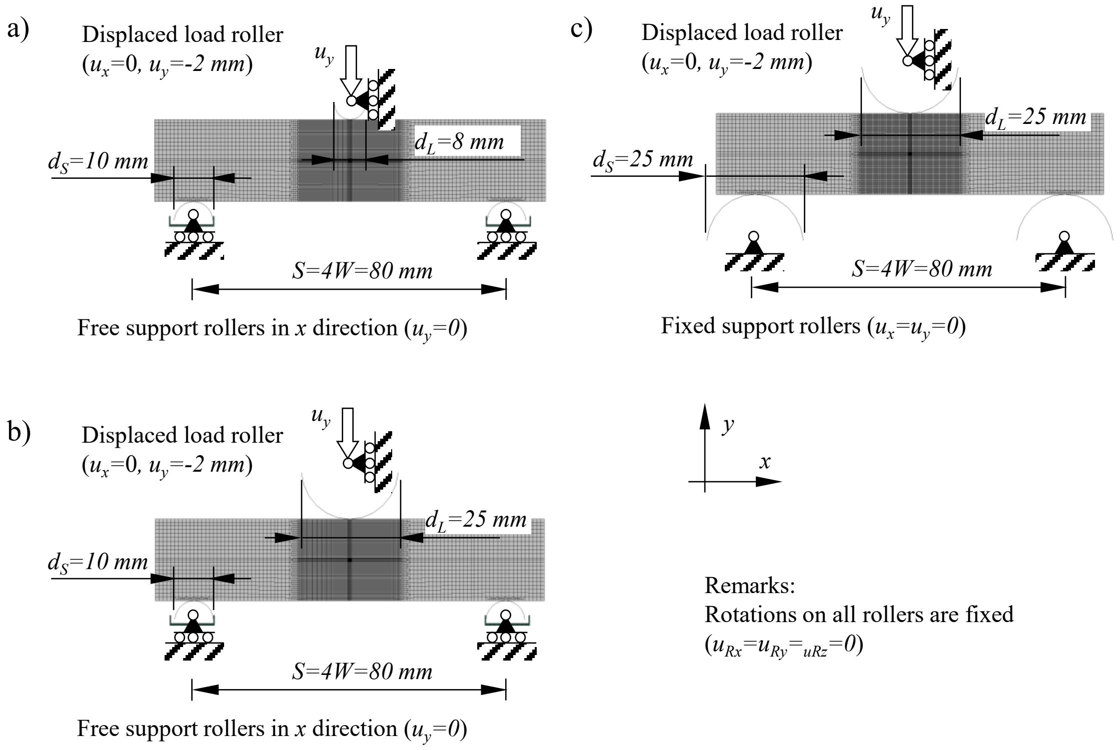

Figure 4.9 The overview of the investigated fixture setups; a) replica of standardised rollers according to ASTM E1820 standard, b) control setup of rollers and c) replica of the actual fixture setup, used in fracture testing.

The support and load rollers have been modelled as analytical rigid wire parts in the 2D plane strain FEM. Boundary conditions have been prescribed in reference points at the centre of each roller. Parametric studies included three different setups of support and load rollers, which are shown in Table 4.9. The first setup, which replicated the standard setup according to ASTM E1820 [6], included support and load rollers with diameters of d_L=10 mm and d_S=8 mm, respectively. The support rollers are free to move in the horizontal direction and are fixed in the vertical direction. The second setup served as a control to investigate the influence of load roller diameter on the computed *J*-integral values. It included the same support rollers as the previous setup, but the load roller diameter was increased to d_L=25 mm. The third setup replicated the actual setup of support and load rollers, used in fracture testing of SE(B) specimens. All rollers had diameter d_L=d_S=25 mm and support rollers were fixed in all directions. In all FEM, the load was introduced in displacement control with a prescribed displacement of magnitude 2 mm to the load roller. The rotations of the rollers were fixed in all three setups. Contacts have been established between rigid rollers and the deformable SE(B) specimen with a prescribed coefficient of friction μ=0.1.

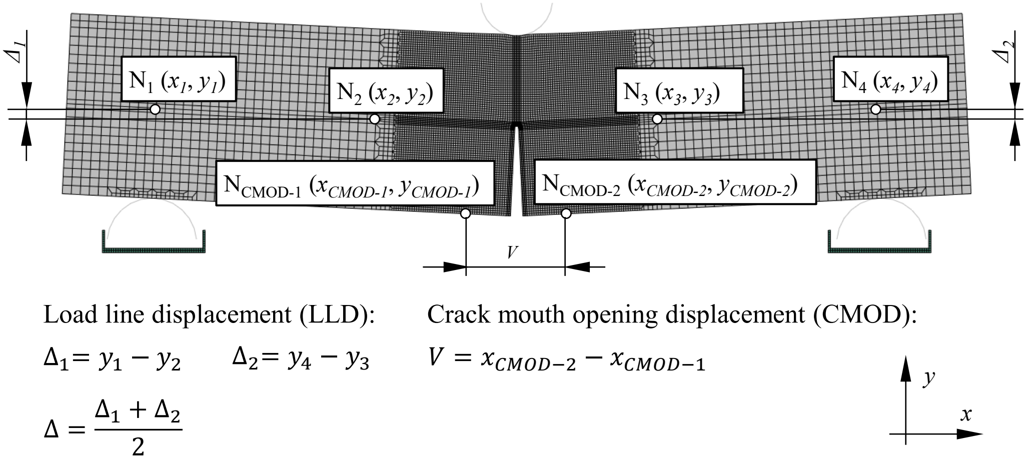

Load line displacement (LLD):

$\Delta_1 = y_1 - y_2$ $\quad \Delta_2 = y_4 - y_3$

$$\Delta = \frac{\Delta_1 + \Delta_2}{2}$$

Crack mouth opening displacement (CMOD):

$V = x_{CMOD-2} - x_{CMOD-1}$

Figure 4.10 The definition of the measured LLD and CMOD in the finite element model. Nodes with the corresponding coordinates are marked. LLD of the specimen is computed as the average of LLD *Δ1* and *Δ2*. Such definition of LLD excludes displacements due to indentation of displacement and support rollers.

The elastic-plastic material model, which adopts J_2 flow theory with conventional von Mises plasticity, has been used to describe the material behaviour under imposed loads. The regions of the base material and the weld material (OM and UM) were homogenized in order to simplify FEM, and enable computation of contour integral i.e. *J*-integral. For that reason, material models of the base, the OM weld and the UM weld materials have been determined on the basis of the experimental stress–strain curves, obtained through round bar specimens tensile testing, described in Chapter 3.3.1. Such stress-strain relationships from large scale tensile tests represent an average material behaviour. In contrary, material model of the HAZ was determined from tensile testing of MTS, as described in Chapter 3.2.2. The stress-strain relationship obtained by testing of MTS-1-11 was assumed to represent the average behaviour of the HAZ. Plastic properties of the listed materials have been implemented in the FEM in form of true plastic stress-strain curves which consisted of up to 24 data points. The corresponding elastic and plastic properties of the implemented material models are shown in Table 4.4. Finally, small strain assumptions have been implemented in order to enhance the *J*-integral convergence [102].

Table 4.4 The elastic and plastic properties of the material models, implemented in FEM.

Elastic properties		
Material	Elastic modulus E [MPa]	Poisson's coefficient v [-]
BM - S690 QL	201108.6	0.3
OM - MIG 90 (OM=1.302)	215299.6	0.3
UM - VAC 65 (M=0.779)	209879.3	0.3
HAZ (average CH & FG)	204916.0	0.3

Plastic properties

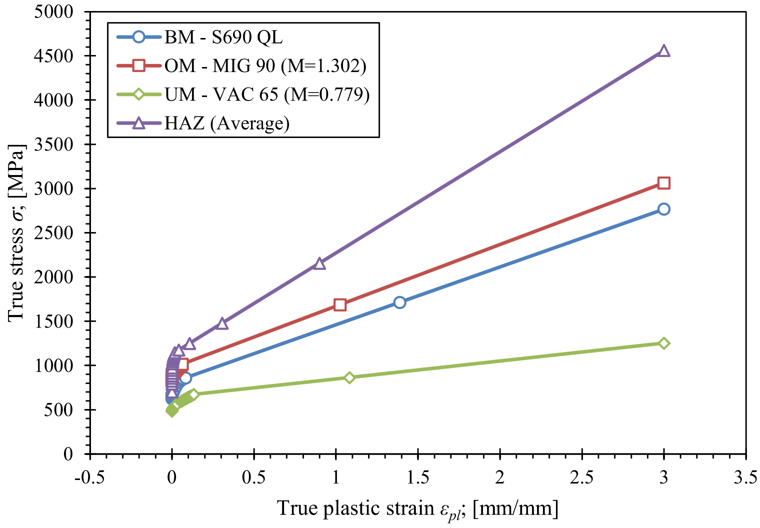

4.3.3 Verification of the Finite Element Models

The FEM series 1A-BM of the base material SE(B) specimen, with standard fixture setup, has been verified through analysis of the *J*-integral convergence and through comparison of the η_{pl} factor with the results of other verified published studies. The *J*-integral convergence analysis has been conducted for FEM of the SE(B) specimen with the crack length a/W=0.5. The model was computed twice; first, with small strain approach, and then with large strain approach. In both cases, the *J*-integral was extracted from consecutive contours, and plotted in dependence of contour distance y from the crack tip. The plots $J(y)$ are shown in Figure 4.11 for various load levels. The comparison of the results shows that the *J*-integral converges sooner when the small strain approach is incorporated in the FEM. Moreover, the *J*-integral convergence rate noticeably decreases as applied load increases. This is especially notable when the applied load is greater than the yield limit load F/F_Y>1. Furthermore, the FEM fails to accurately replicate large displacements at the crack tip in case of small strain approach as shown in Figure 4.12. This is the reason for the corresponding inconsistent values of the *J*-integral at $y<0.1$ mm, as demonstrated in Figure 4.11 a), Figure 4.11 b) and Figure 4.11 c). Therefore, it can be concluded that the small strain approach is suitable for FEA when the *J*-integral is main interest [102], but not when stresses and strains at the crack tip or crack tip opening displacements (CTOD) are investigated. The advantage of small strain approach is that accurate *J*-integral can be extracted from relatively small contour. This is beneficial in case of the double mismatched welds, as the crack tip can be modelled closer to the fusion line between the OM and the UM weld materials. Therefore, the small strain approach was incorporated in all further developed FEM for computation of the *J*-integral.

Figure 4.11 a), Figure 4.11 b) and Figure 4.11 c) demonstrate that the fully converged *J*-integral can be obtained from contour at 2.0 mm ahead of the crack tip (henceforth referred as 2.0 mm contour), if small strain approach is implemented in the FEM. In this case, relatively accurate *J*-integral can be obtained even from contour 0.5 mm ahead of the crack tip (henceforth referred as 0.5 mm contour). The relative difference in the *J*-integral between 0.5 mm and 2.0 mm contours is less than 2%, as demonstrated in Figure 4.11 d). Due to more convenient terminology, the *J*-integral, extracted from 0.5 mm and 2.0 mm contours will be henceforth denoted as $J_{0.5}$ and $J_{2.0}$, respectively.

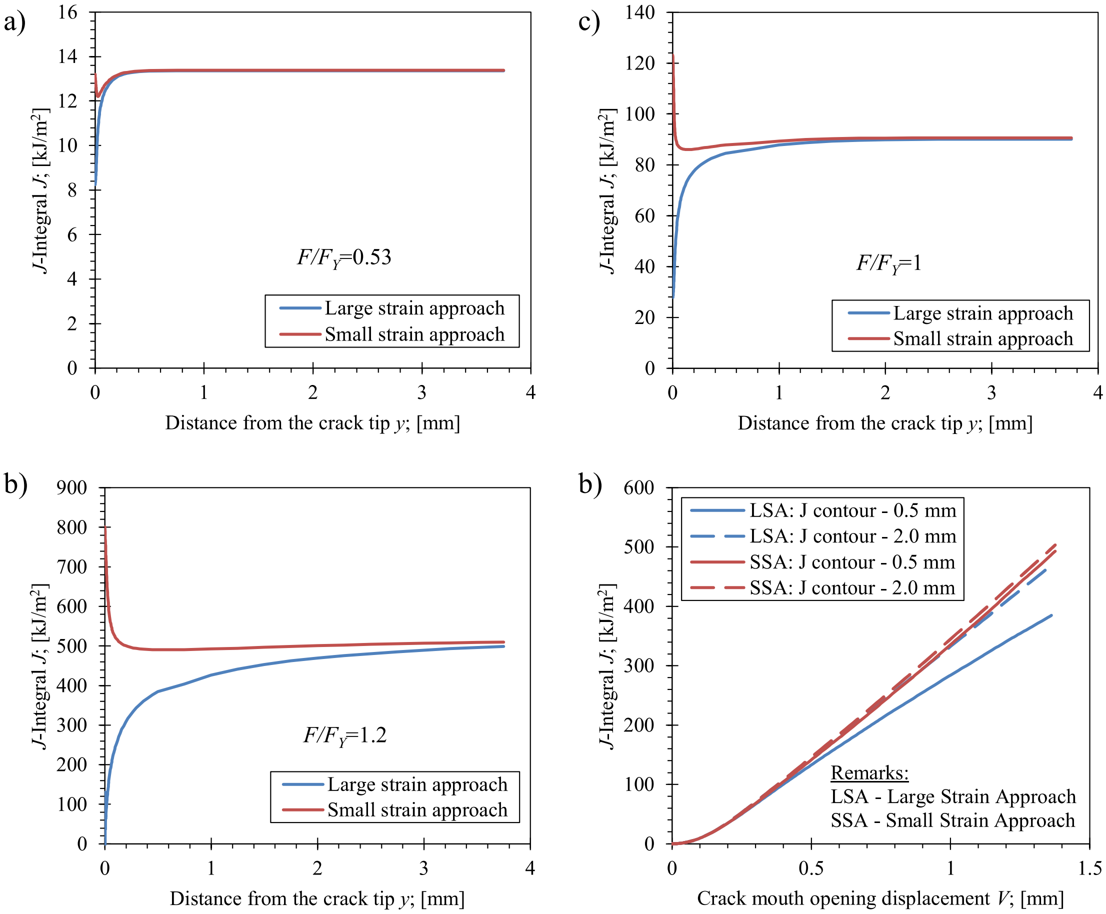

Figure 4.11 The *J*-integral convergence for the FEM with the small strain approach and the large strain approach at load levels a) F/F_Y=0.53, b) F/F_Y=1, c) F/F_Y=1.2 and d) the comparison of the obtained J-integral values for 0.5 mm and 2.0 mm contours for monotonically loaded SE(B) specimen with a/W=0.5.

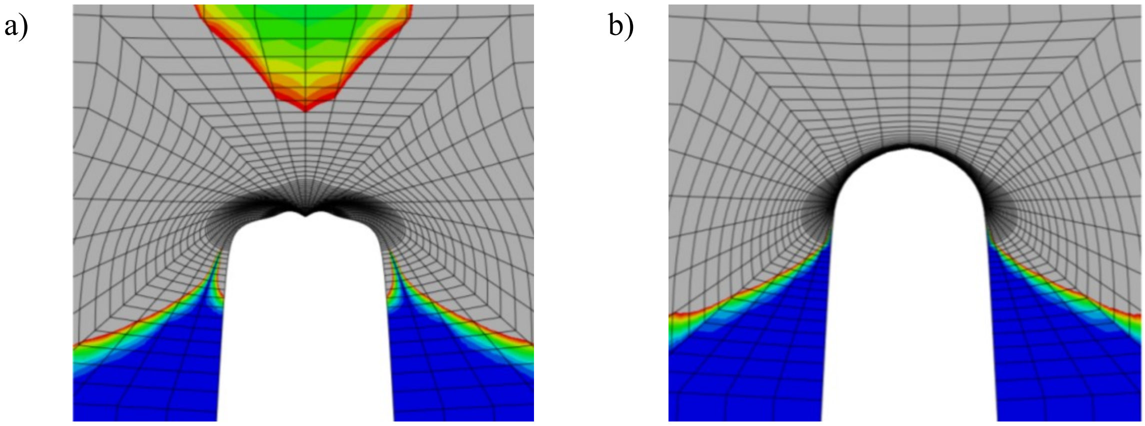

Figure 4.12 The deformed shape of the crack tip at F/F_Y=1.2 with a) the small strain approach and b) the large strain approach. The presented results were obtained with analysis of the SE(B) specimen with a/W=0.5.

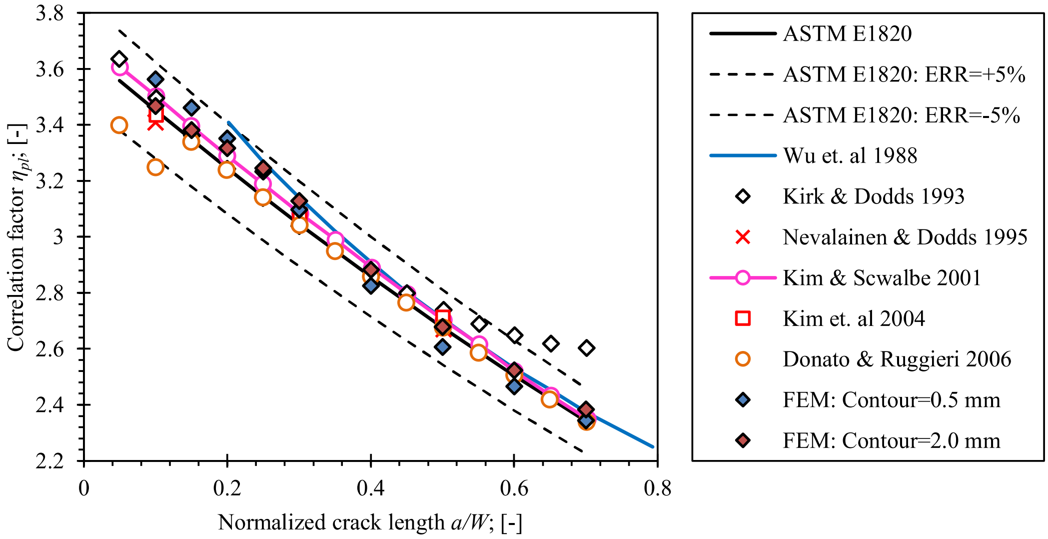

Figure 4.13 The comparison of η_{pl} values obtained from the created FEM series 1A-BM (Table 4.2), with the values published in literature and standard ASTM E1820 [60].

In order to verify the created FEM, models with small strain approach in series 1A-BM were computed and η_{pl} functions were calibrated using the slope method [89] on the basis of the *J*-integral, that was obtained from 0.5 mm and 2.0 mm contours, as described in Chapter 4.2.1. The calibrated η_{pl} functions were then compared to solutions that were published by Wu et al. [45], Kirk and Dodds [37], Nevalainen and Dodds [38], Kim and Schwalbe [46], Kim et al. [47], Donato and Ruggieri [136] and Zhu et al. [49], as shown in Figure 4.13.

The comparison of the results in Figure 4.13 shows that the calibrated η_{pl} values for 0.5 mm and 2.0 mm contours closely match the existing solutions. The former showed slightly increased deviations for cracks with normalized length $a/W<0.3$ and $a/W>0.5$, while the latter showed excellent agreement along the entire normalized crack length range $0.1<a/W<0.7$. This is due to the fact that the convergence of *J*-values improves with increasingly distant contours from the crack tip. The relative deviation from η_{pl} values included in ASTM E1820 standard [6] is less than 5% in both cases. Additionally, it is important to emphasize that the calibrated η_{pl} values according to the slope method [60] in scope of this research do not exhibit increased variation for cracks with normalized length $a/W<0.2$, as is the case for the solution obtained by Donato and Ruggieri [136].

To further investigate the aforementioned variations, η_{pl} factor has been recomputed from results of FEA using the exclusion method, proposed by Donato and Ruggieri [136]. The computed values of η_{pl} using the slope method and the exclusion method were plotted in dependence of the normalized crack length, and compared to the solution published by Donato and Ruggieri [136], as shown in Figure 4.14. The comparison of η_{pl} values in Figure 4.14 indicates that the reason for variations are differences in the methods for η_{pl} computation. The slope method [89] values are consistent with ASTM E1820 [6] across the entire range of the crack lengths $0.1 \le a/W \le 0.7$ and with solution of Donato and Ruggieri [60] in range of crack lengths $0.2 \le a/W \le 0.7$. The exclusion method [84] produces variations of η_{pl} for short cracks with $a/W < 0.2$ due to variable exclusion criteria. Furthermore, the exclusion criteria failed to completely isolate plateau in $\eta_{pl}(a/W)$ chart for short cracks, as demonstrated in Figure 4.14 b) and Figure 4.14 c). This is the main reason of observed variations of η_{pl} for short cracks. Therefore, the slope method [89] has been selected for the computation of η_{pl} in subsequent FEM. Based on the above stated arguments, it is assumed that the created FEM has passed the verification process and produces results that are in line with the solutions from the published researches and standard ASTM E1820 [6].

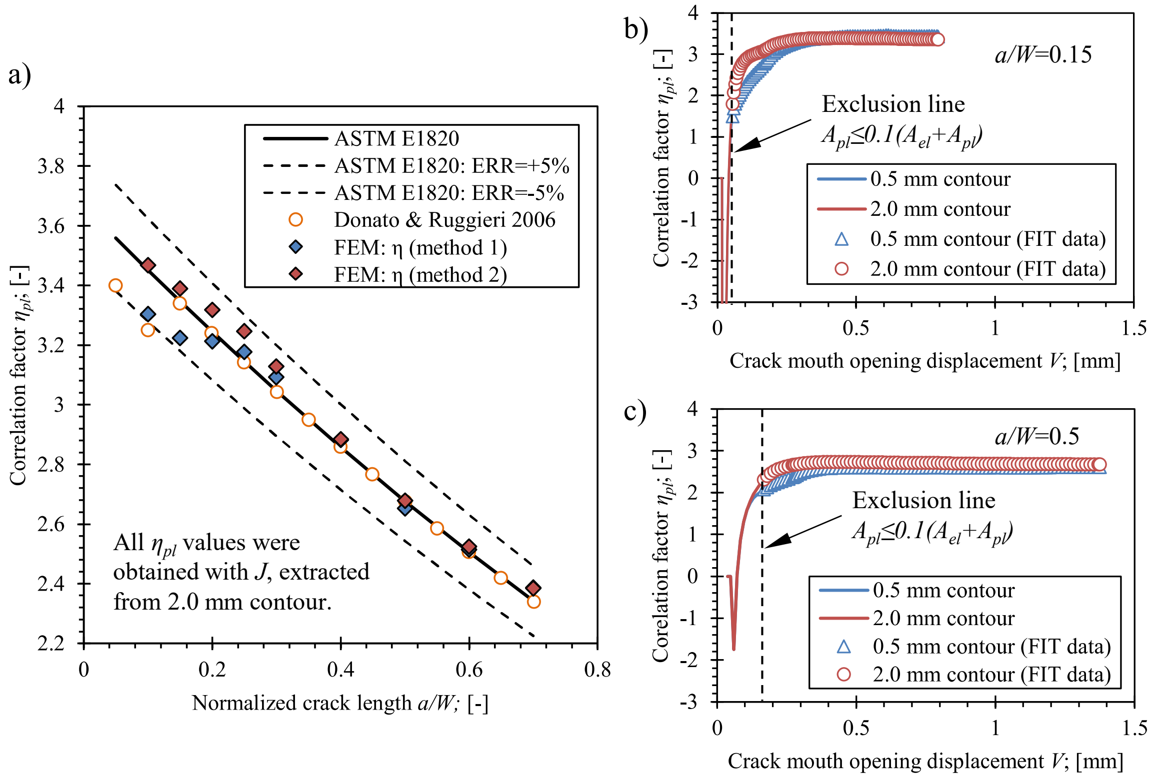

Figure 4.14 The comparison of a) calibrated η_{pl} factors by the slope method (denoted as method 1) and the exclusion method (denoted as method 2) with the existing solutions. Variations of exclusion criterion in the computation of η_{pl} according to the exclusion method are demonstrated for SE(B) specimens with crack length b) a/W=0.15 and c) a/W=0.5.

4.3.4 Crack tip Constraint

To further investigate the influence of the weld material in the double mismatched weld on its fracture behaviour, this study evaluates fracture behaviour by implementing a second fracture parameter, quantifying the constraint effect. Several frameworks, such as *J-T*, *J-Q* and *J-h* methods, are available to characterize the constraint level. The *J-T* and *J-Q* analysis, based on *T* stress [146] and Q-constraint respectively, have been implemented by Burstow et al. [147]–[149] in the investigation of fracture behaviour of mismatched welded joints with a through thickness crack oriented in direction of the weld axis. The results showed that *T*-stress failed to accurately reproduce the complex stress fields due to material mismatching. While *T*-stress had a similar effect on the constraint level in overmatched weld material as in homogeneous base material, stress fields became independent of *T*-stress in undermatched weld at higher loads. In case of the latter, the shape and elevation of the stress field were controlled entirely by the base material stress distribution. Such behaviour was attributed to the plastic zone being forced to expand in the weld material due to higher yield stress of the base material, preventing the *T*-stress from controlling the shape of the plastic zone [109]. Burstow made similar observations in case of *Q*-constraint; crack tip constraint can be characterized by *Q* parameter for ductile fracture of overmatched weld but not for undermatched welded joints due to complex stress field further ahead of crack tip [109]. Moreover, both, *T*-stress and *Q*-constraint, are suited for quantifying the in-plane constraint effect [47], [150] but may not be adequate to characterize the out-of-plane constraint effect, which is known to have a significant impact on fracture behaviour of material [151]. A better parameter to quantify the out-of-plane constraint effect is the stress triaxiality h [152]. Recently Verstraete et al. [153] successfully applied stress triaxiality in scope of constraint analysis of mismatched girth welded joints. The author motivates that stress triaxiality is equivalent to Q_m which is a modified *Q*-constraint parameter based on hydrostatic stress, though the stress triaxiality is assumed to have higher physical relevance in case of ductile failure. In scope of this research, stress triaxiality was computed according to the following equations [47], [152]:

$$h = \frac{\sigma_h}{\sigma_{eq}} = \frac{\frac{1}{3}\left(\sigma_{xx} + \sigma_{yy} + \sigma_{zz}\right)}{\sigma_{eq}} \tag{4.11}$$

$$\sigma_{eq} = \frac{1}{\sqrt{2}}\Big[\left(\sigma_{xx} - \sigma_{yy}\right)^2 + (\sigma_{xx} - \sigma_{zz})^2 + \left(\sigma_{yy} - \sigma_{zz}\right)^2 + 6\left(\sigma_{xy}^2 + \sigma_{yz}^2 + \sigma_{zx}^2\right)\Big]^{1/2} \tag{4.12}$$

where σ_h is hydrostatic stress in [MPa], σ_{eq} is Von Mises equivalent stress in [MPa], and variables σ_{xx}, σ_{yy}, σ_{zz}, σ_{xy}, σ_{yz} and σ_{zx} are components of stress tensor with respect to x, y and z axes of Cartesian coordinate system in [MPa]. The latter were extracted from the FEM by interpolation of nodal values along the ligament $b=W-a_0$ at angle $\theta=0$ ° and distance r ahead of the crack tip, as shown in Figure 4.15. The last was defined according to the following equation:

$$r = J/\sigma_Y \tag{4.13}$$

where J is total J-integral extracted from the FEM in [J/mm^2], and σ_Y is yield strength of the material at the vicinity of the crack tip in [MPa]. The distance r is selected with the intention to obtain h reasonably close to the crack tip, while avoiding the finite strain region adjacent to the crack tip [154]. At distances $r<J/\sigma_Y$, small strain theory breaks down due to blunting of the crack tip and the HRR field is no longer valid [152].

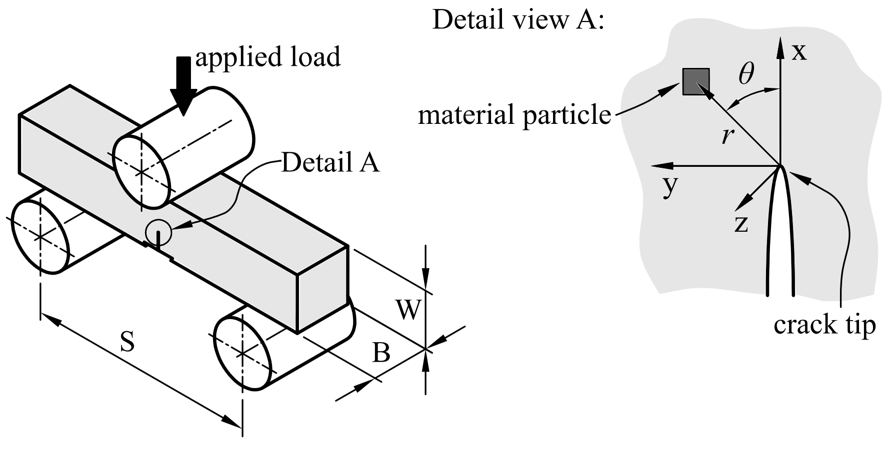

Figure 4.15 The definition of coordinate system ahead of the crack tip. The z direction is normal to the page.

4.4 Influence of the Fixture Setup on Fracture Behaviour of the Base Material

Special attention had to be devoted to the influence of the fixture setup on the calibrated η_{pl}, λ and γ_{pl} factors, because the non-standard fixtures were used for fracture testing of the SE(B) specimens, as described in Chapter 3.5.3. Following the FEM verification, the remaining configurations of fixture setups 1B-BM (standard setup of the support rollers, including oversized load roller with diameter d_S=25 mm) and 1C-BM (fixed oversized rollers with diameter d_S=d_L=25 mm) were included in the investigation. The former fixture setup is shown in Figure 4.9 b) while the latter is shown in Figure 4.9 c) and represents the actual setup of rollers, used in fracture testing of the SE(B) specimens (Chapter 3.5.3). Values of η_{pl}, computed from the J-integral that was extracted from 0.5 mm and 2.0 mm contours, are presented in Figure 4.16. Here, the influence of the boundary conditions, that is, roller setup, on η_{pl} can be recognized.

If the standard diameter of the load roller d_L=10 mm (FEM series 1A-BM), is increased to d_L=25 mm (FEM series 1B-BM), then the η_{pl} decreases at maximum 3.1% with respect to the standard solution (ASTM E1820 [6]), and 5.4% with respect to the baseline solution 1A-BM, when $J_{2.0}$ from the 2.0 mm contour is considered. However, both stated solutions seem to be in close agreement when the normalized crack length is $a_0/W \geq 0.6$.

The η_{pl} further decreases at maximum by 12.0% with respect to the standard solution (ASTM E1820 [6]), and by 13.3% with respect to the reference solution 1A-BM in case of the fixed load and support rollers with diameters d_S=d_L=25 mm, implemented in the FEM series 1C-BM. The comparison of both solutions is based on the $J_{2.0}$ from the 2.0 mm contour.

The η_{pl} values computed on the basis of $J_{0.5}$, extracted from the 0.5 mm contour, deviate from the values computed on the basis of $J_{2.0}$ that was obtained from 2.0 mm contour due to the J-integral not being fully converged. The former values deviate from the latter by 2.9%, 3.6% and 2.6 %, at most for the FEM series 1A-BM, 1B-BM and 1C-BM, respectively. Eventually, η_{pl} functions were developed by polynomial least squares curve fitting of the computational results, as described in Chapter 4.2.1. The proposed solutions are presented in Table 4.5 and Table 4.6 for 0.5 mm and 2.0 mm contours, respectively.

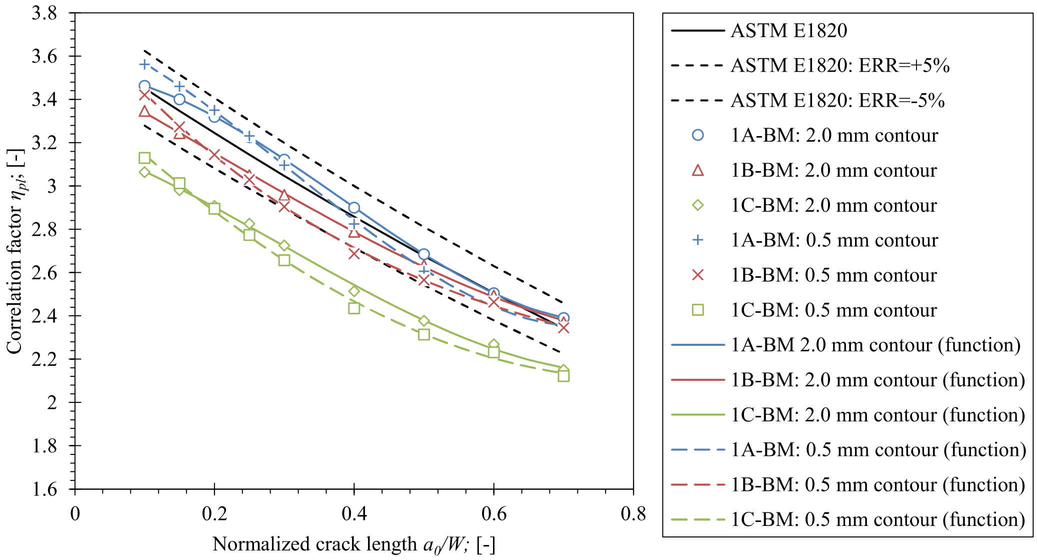

Figure 4.16 The comparison of the calibrated η_{pl} factors for the SE(B) base material specimens, obtained with the slope method, and standard solution according to ASTM E1820. The calibrated η_{pl} values correspond to the fixture setups, presented in Figure 4.9.

Table 4.5 The proposed η_{pl} functions for the SE(B) base material specimens, valid for the *J*-integral, extracted from 0.5 mm contour.

FEM series	η_{pl} functions for 0.5 mm contour in range $0.1 \le a_0/W \le 0.7$	R^2 [-]
1A-BM	$\eta_{pl} = 4.711\left(\frac{a}{W}\right)^3 - 4.339\left(\frac{a}{W}\right)^2 - 1.236\left(\frac{a}{W}\right) + 3.729$	0.999
1B-BM	$\eta_{pl} = -1.121\left(\frac{a}{W}\right)^3 + 3.300\left(\frac{a}{W}\right)^2 - 3.789\left(\frac{a}{W}\right) + 3.774$	0.999
1C-BM	$\eta_{pl} = 0.296\left(\frac{a}{W}\right)^3 + 1.556\left(\frac{a}{W}\right)^2 - 3.094\left(\frac{a}{W}\right) + 3.437$	0.998

Table 4.6 The proposed η_{pl} functions for the SE(B) base material specimens, valid for the *J*-integral, extracted from 2.0 mm contour.

FEM series	η_{pl} functions for 2.0 mm contour in range $0.1 \le a_0/W \le 0.7$	R^2 [-]
1A-BM	$\eta_{pl} = 5.025\left(\frac{a}{W}\right)^3 - 5.738\left(\frac{a}{W}\right)^2 - 0.061\left(\frac{a}{W}\right) + 3.552$	0.999
1B-BM	$\eta_{pl} = 1.226\left(\frac{a}{W}\right)^3 - 0.684\left(\frac{a}{W}\right)^2 - 1.751\left(\frac{a}{W}\right) + 3.519$	0.998
1C-BM	$\eta_{pl} = 2.483\left(\frac{a}{W}\right)^3 - 2.181\left(\frac{a}{W}\right)^2 - 1.183\left(\frac{a}{W}\right) + 3.206$	0.998

Furthermore, the corresponding shape factor λ has been determined on the basis of LLD and CMOD according to the procedure, described in Chapter 4.2.2. The obtained results are presented in Figure 4.17, which shows λ values, computed for the FEM series 1A-BM (standard roller setup) that are in close agreement with the solution included in ASTM E1820 standard [6] for $a/W \geq 0.25$. In case of shallower cracks with $a/W<0.25$, the computed results deviate from the standard solution. The reason this deviation is that Zhu et al. [49] produced the solution for λ by curve fitting of the existing results in the range $0.25 \leq a/W \leq 0.7$. The λ increases by 8.1% at maximum with respect to the reference solution for the FEM series 1A-BM, if the load roller diameter is increased from d_L=8 mm to d_L=25 mm (FEM series 1B-BM).

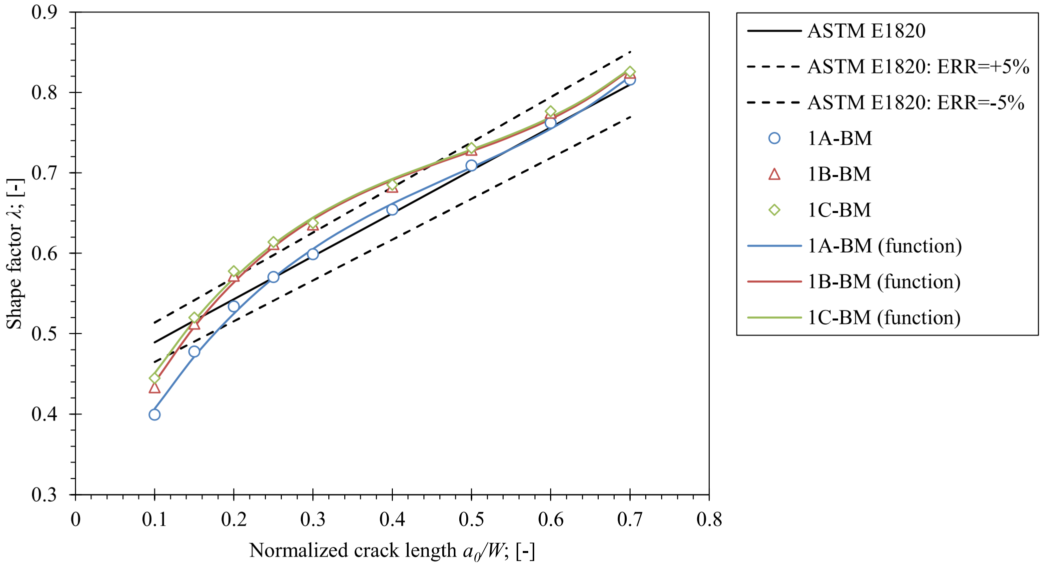

Figure 4.17 The comparison of the calibrated λ factors for the SE(B) base material specimens with standard solution according to ASTM E1820. The calibrated λ values correspond to the fixture setups, presented in Figure 4.9.

Table 4.7 The proposed λ solutions for the SE(B) base material specimens.

FEM series	λ functions in range $0.1 \leq a_0/W \leq 0.7$	R^2 [-]
1A-BM	$\lambda = 2.278\left(\frac{a}{W}\right)^3 - 3.273\left(\frac{a}{W}\right)^2 + 2.008\left(\frac{a}{W}\right) + 0.236$	0.998
1B-BM	$\lambda = 2.806\left(\frac{a}{W}\right)^3 - 4.001\left(\frac{a}{W}\right)^2 + 2.249\left(\frac{a}{W}\right) + 0.252$	0.998
1C-BM	$\lambda = 2.603\left(\frac{a}{W}\right)^3 - 3.707\left(\frac{a}{W}\right)^2 + 2.113\left(\frac{a}{W}\right) + 0.274$	0.997

Increasing the support rollers diameter from d_S=10 mm to d_S=25 mm and constraining their degrees of freedom has little effect on the λ values in case of the FEM series 1C-BM. The corresponding computed values of λ deviate 11.5 %, at maximum with respect to the reference solution for the FEM series 1A-BM. This shows that λ factor is predominantly dependent on the diameter of the load roller d_L. The calibrated λ functions were developed by polynomial curve fitting of the computed results, using the least squares method. The proposed solutions are presented in Table 4.7.

The crack growth correction factor γ has been determined from the calibrated solutions for η_{pl} and λ functions and their corresponding derivatives, determined according to the procedure that is described in Chapter 4.2.2. The obtained results are presented in Figure 4.18, where the following observations can be made.

The solutions obtained from the FEM series 1C-BM and 1A-BM deviate from the standard solution (ASTM E1820 [6]) by a factor of 6.1 to 7.7 at most respectively, where $J_{2.0}$ was evaluated from the 2.0 mm contour. Furthermore, the solutions obtained from the FEM series 1C-BM and 1A-BM, based on the $J_{0.5}$, evaluated from the 0.5 mm contour, deviated from the standard solution (ASTM E1820 [6]) by a factor of 7.2 to 8.4 at most. The solutions obtained from the FEM series 1B-BM deviated from the standard solution (ASTM E1820 [6]) within the specified ranges. Revision of post-processing procedures revealed that such deviations are due to the combination of η_{pl}, η_{pl}', λ and λ' values in Equation (4.6). The calibrated γ functions are presented in Table 4.8 and Table 4.9 for the J evaluated from 0.5 mm and 2.0 mm contours.

Final conclusion in the analysis of the fixture setups is that fixture setup has significant effect on η_{pl}, λ and γ_{pl} functions. Therefore, the solution for FEM series 1C-BM has been selected for computation of the crack driving force in terms of the *J*-integral for the SE(B) base material specimens that were tested, using the fixed oversized load and support rollers setup. Additionally, this solution has been selected as a reference, to which solutions, calibrated for the welded SE(B) specimens, can be compared. The corresponding effect on estimated fracture behaviour of the SE(B) specimens in terms of *J-R* resistance curves will be discussed in the following chapters.

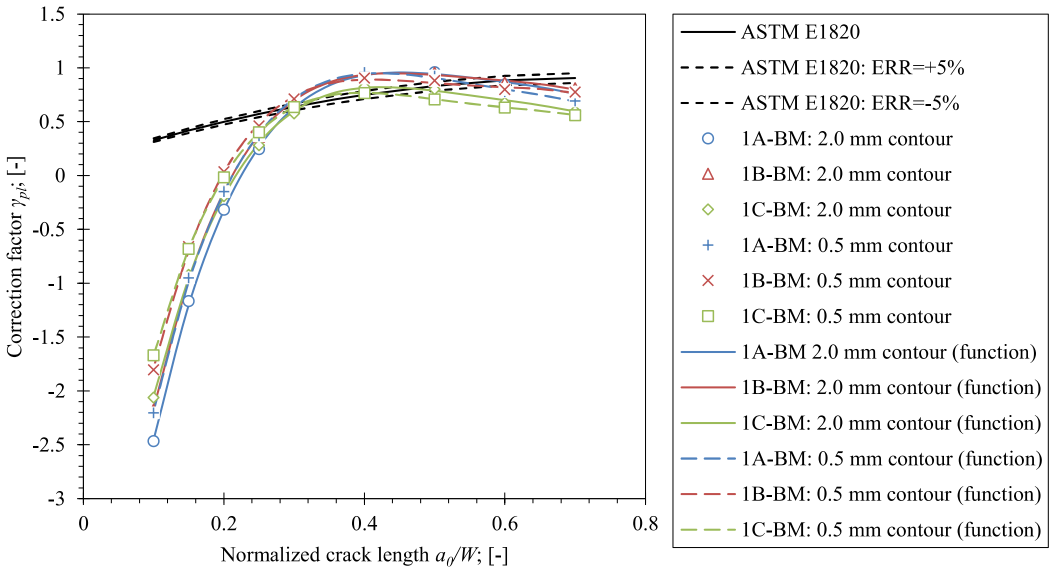

Figure 4.18 The comparison of the calibrated γ factors for the SE(B) base material specimens and standard solution according to ASTM E1820. The calibrated γ_{pl} values correspond to the fixture setups, presented in Figure 4.9.

Table 4.8 The proposed γ_{pl} functions for SE(B) base material specimens, valid for the *J*-integral, extracted from 0.5 mm contour.

FEM series	γ_{pl} functions for 0.5 mm contour in range $0.1 \le a_0/W \le 0.7$	R^2 [-]
1A-BM	$\gamma_{pl} = -65.073\left(\frac{a}{W}\right)^4 + 152.019\left(\frac{a}{W}\right)^3 - 132.906\left(\frac{a}{W}\right)^2 + 50.489\left(\frac{a}{W}\right) - 6.048$	1.000
1B-BM	$\gamma_{pl} = -77.924\left(\frac{a}{W}\right)^4 + 170.124\left(\frac{a}{W}\right)^3 - 137.863\left(\frac{a}{W}\right)^2 + 48.739\left(\frac{a}{W}\right) - 5.440$	0.999
1C-BM	$\gamma_{pl} = -63.999\left(\frac{a}{W}\right)^4 + 144.314\left(\frac{a}{W}\right)^3 - 120.653\left(\frac{a}{W}\right)^2 + 43.576\left(\frac{a}{W}\right) - 4.955$	0.999

Table 4.9 The proposed γ_{pl} functions for SE(B) base material specimens, valid for the *J*-integral, extracted from 0.5 mm contour.

FEM series	γ_{pl} functions for 2.0 mm contour in range $0.1 \le a_0/W \le 0.7$	R^2 [-]
1A-BM	$\gamma_{pl} = -65.574\left(\frac{a}{W}\right)^4 + 152.247\left(\frac{a}{W}\right)^3 - 133.564\left(\frac{a}{W}\right)^2 + 51.641\left(\frac{a}{W}\right) - 6.420$	1.000
1B-BM	$\gamma_{pl} = -73.362\left(\frac{a}{W}\right)^4 + 164.154\left(\frac{a}{W}\right)^3 - 137.889\left(\frac{a}{W}\right)^2 + 51.007\left(\frac{a}{W}\right) - 6.032$	1.000
1C-BM	$\gamma_{pl} = -60.373\left(\frac{a}{W}\right)^4 + 139.811\left(\frac{a}{W}\right)^3 - 121.465\left(\frac{a}{W}\right)^2 + 46.027\left(\frac{a}{W}\right) - 5.563$	1.000

4.5 Fracture behaviour of the Single mismatched welds

Single mismatched welds were analysed using FEM in the configuration that is presented in Figure 4.19. The FEM series 2A-OM, and 2B-UM were analysed in order to investigate fracture behaviour of modelled welds that have average material properties, corresponding to the actual welds. The elastic-plastic material models, presented in Table 4.4, were implemented in the FEM in order to describe behaviour of the base material and the weld material (OM and UM) under imposed load.

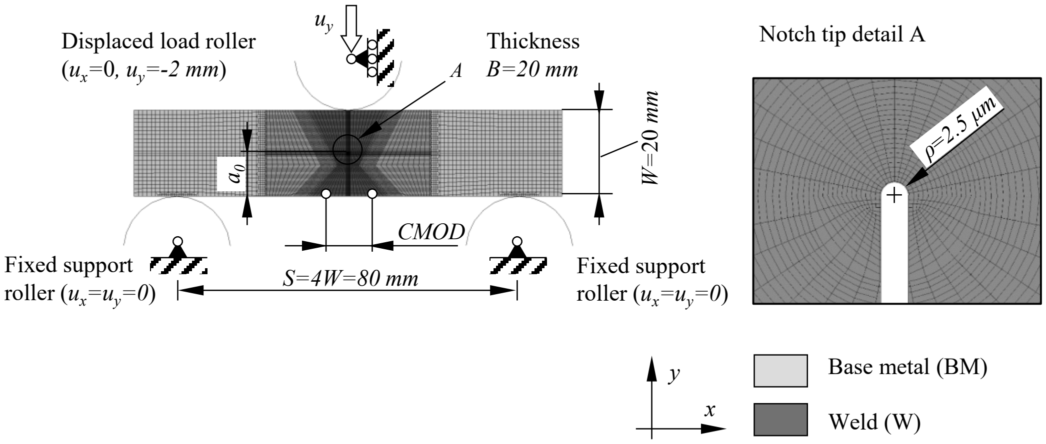

Figure 4.19 The configuration of the FEM for analysis of the single mismatched welds.

The FEM had fixed rollers with diameters d_S=d_L=25 mm. Load was prescribed as displacement of the load roller. The HAZ was not modelled in this iteration. The remaining features of the FEM were the same, as discussed in Chapter 4.3.2. *J*-integral was extracted from 0.5 mm contour only. This compact contour can be entirely located in the weld material when the crack tip is located in a narrow weld root, thus meeting the requirements of material homogeneity for computation of the *J* contour integral. One disadvantage is that values of $J_{0.5}$ are not fully converged at a distance 0.5 mm ahead of the crack tip. However, they deviate less than 3.2% in comparison to the $J_{2.0}$ values, obtained from the 2.0 mm contour, as reported in previous Chapter 4.4. Such deviation is considered acceptable for the following. The calibrated η_{pl} values were computed, using the slope method [89], as described in Chapter 4.2.1. The obtained results are presented in Figure 4.20 that shows significant decrease of the η_{pl} when the crack length *a/W* is similar to the distance to the weld root L_W/W=0.36 in case of the OM weld material. In contrary, values of η_{pl} increase significantly when the crack length a/W is similar to the distance to the weld root L_W/W=0.415 in case of the UM weld material.

The aforementioned behaviour of η_{pl} can be explained through analysis of equivalent plastic strain fields and corresponding plots of the crack driving force (J-integral) in dependence of stress triaxiality h, extracted at distance $r=J/\sigma_Y$ ahead of the crack tip. The former show development of plastic zone for SE(B) specimens with various crack lengths in the OM and the UM weld as, illustrated in Figure 4.21 and Figure 4.22, respectively. The latter gives an indication of the crack tip constraint and is shown in Figure 4.23.

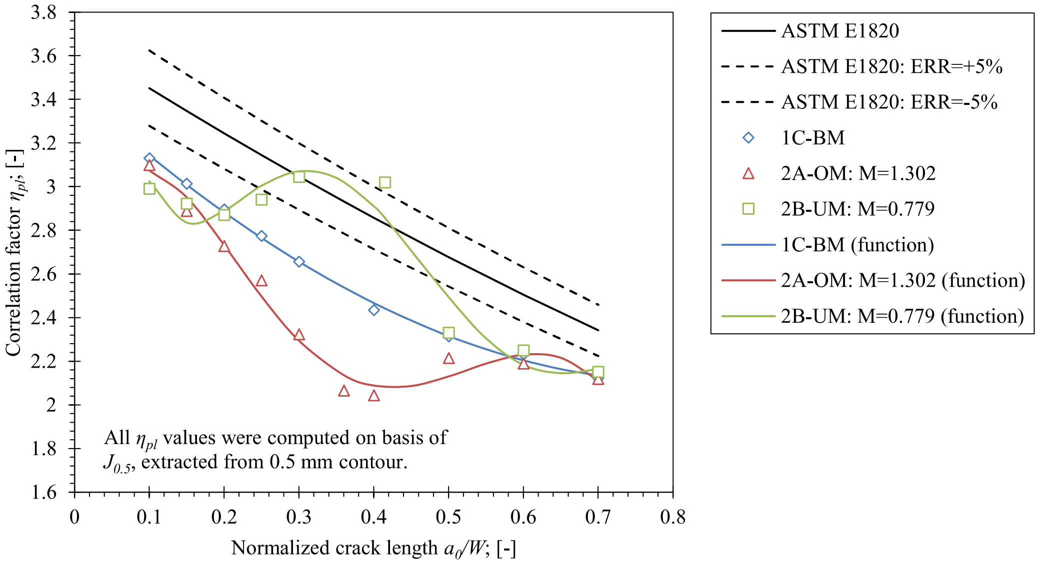

Figure 4.20 The comparison of the calibrated η_{pl} factors for welded SE(B) specimens, obtained with the slope method, and standard solution according to ASTM E1820. The results for the base material (series 1C-BM) are plotted for a reference.

Table 4.10 The proposed η_{pl} functions for the welded OM and UM SE(B) specimens, valid for the J-integral, extracted from 0.5 mm contour.

FEM series	η_{pl} functions for 0.5 mm contour in range $0.1 \le a_0/W \le 0.7$	R^2 [-]
2A-OM	$\eta_{pl} = 92.933\left(\frac{a}{W}\right)^5 - 269.918\left(\frac{a}{W}\right)^4 + 264.133\left(\frac{a}{W}\right)^3 - 104.146\left(\frac{a}{W}\right)^2 + 13.094\left(\frac{a}{W}\right) + 2.569$	0.979
2B-UM	$\eta_{pl} = -380.531\left(\frac{a}{W}\right)^5 + 877.582\left(\frac{a}{W}\right)^4 - 739.216\left(\frac{a}{W}\right)^3 + 274.115\left(\frac{a}{W}\right)^2 - 43.820\left(\frac{a}{W}\right) + 5.321$	0.934

When the crack is shallower than the distance to the weld root, i.e. $a/W<L_W/W=0.36$ for the OM weld, a plastic zone spreads into the base material with lower yield strength (σ_{YS}=686.7 MPa) than the weld (σ_{YS}=894.4 MPa), as demonstrated in Figure 4.21 a) Figure 4.21 b) and Figure 4.21 c). At the same time, the computed stress triaxiality h for the OM weld is lower than the one of the base material, as shown in Figure 4.23 a), Figure 4.23 b) and Figure 4.23 c). This is understood as, for the OM welds, the plastic zone originating from the crack tip develops relatively easy into the adjacent base material with lower yield strength. Hence, the lower crack driving force, which corresponds to the lower values of η_{pl} with respect to the base material for $a_0/W\leq 0.36$, as demonstrated in Figure 4.20. The reduction of η_{pl} due to the weld overmatching was also confirmed in other researches, such as Kim et al. [58], Donato and Ruggieri [60], Zhou et al. [155] and Zerbst [63], while the corresponding reduction of the crack tip constraint, i.e. stress triaxiality, was confirmed by Verstraete et al. [153] as well.

Such behaviour is observed until the crack length is similar as the distance to the weld root, as demonstrated in Figure 4.21 b). Here, the weld is narrowest and therefore, the plastic zone is obstructed by smaller amount of the OM weld material before it reaches softer base material. This results in reduced stress triaxiality, as shown in Figure 4.23 b), and reduced η_{pl} values, as shown in Figure 4.20. Moreover, the minimum η_{pl} is observed for the OM weld, when the crack tip is located in the weld root. The presented observation is in line with researches, conducted by Zhou et al. [155] and Zerbst [63]. Once the crack extends beyond the weld root, i.e. $a/W>L_W/W$, the plastic zone begins to develop entirely in the OM weld material with higher yield strength, as shown in Figure 4.21 c) and Figure 4.21 d). This results in a rapid rise of the stress triaxiality for deeper cracks in the OM weld material to a similar level that was observed in the base material, as shown in Figure 4.23 e) and Figure 4.23 f). Correspondingly, the rise of η_{pl} can be observed as well, where values for the cracks with $a/W\geq 0.5$ are similar to the one for the base material, as demonstrated in Figure 4.20.

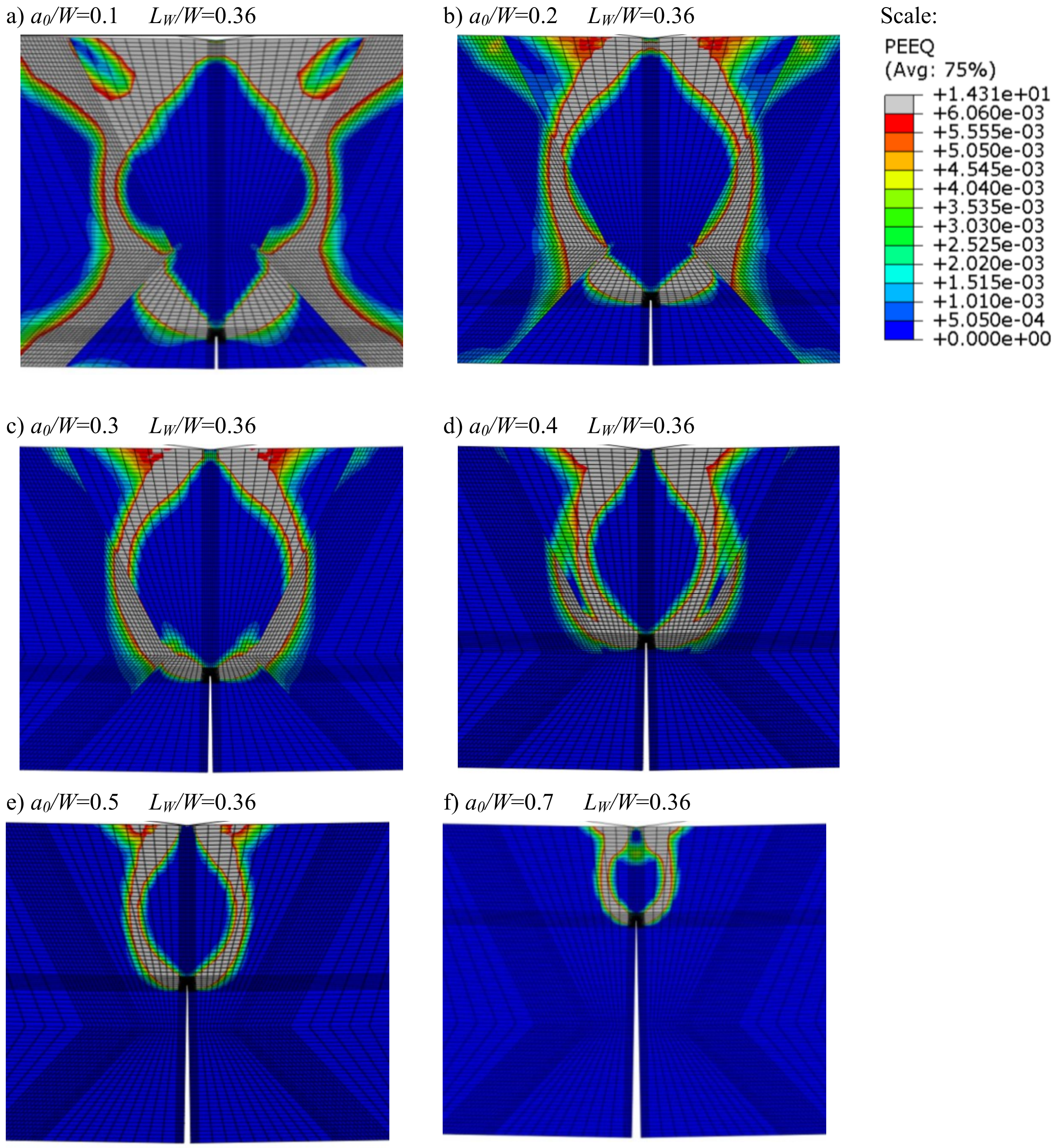

a) $a_0/W=0.1$ $L_W/W=0.36$

b) $a_0/W=0.2$ $L_W/W=0.36$

c) $a_0/W=0.3$ $L_W/W=0.36$

d) $a_0/W=0.4$ $L_W/W=0.36$

e) $a_0/W=0.5$ $L_W/W=0.36$

f) $a_0/W=0.7$ $L_W/W=0.36$

Figure 4.21 the plastic zone for the modelled SE(B) specimens with the OM weld and the crack lengths a) $a_0/W=0.1$, b) $a_0/W=0.2$, c) $a_0/W=0.3$, d) $a_0/W=0.4$, e) $a_0/W=0.5$ and f) $a_0/W=0.7$. The equivalent plastic strain (PEEQ) fields were obtained at the yield limit load $F/F_Y=1$ from the results of the FEM series 2A-OM.

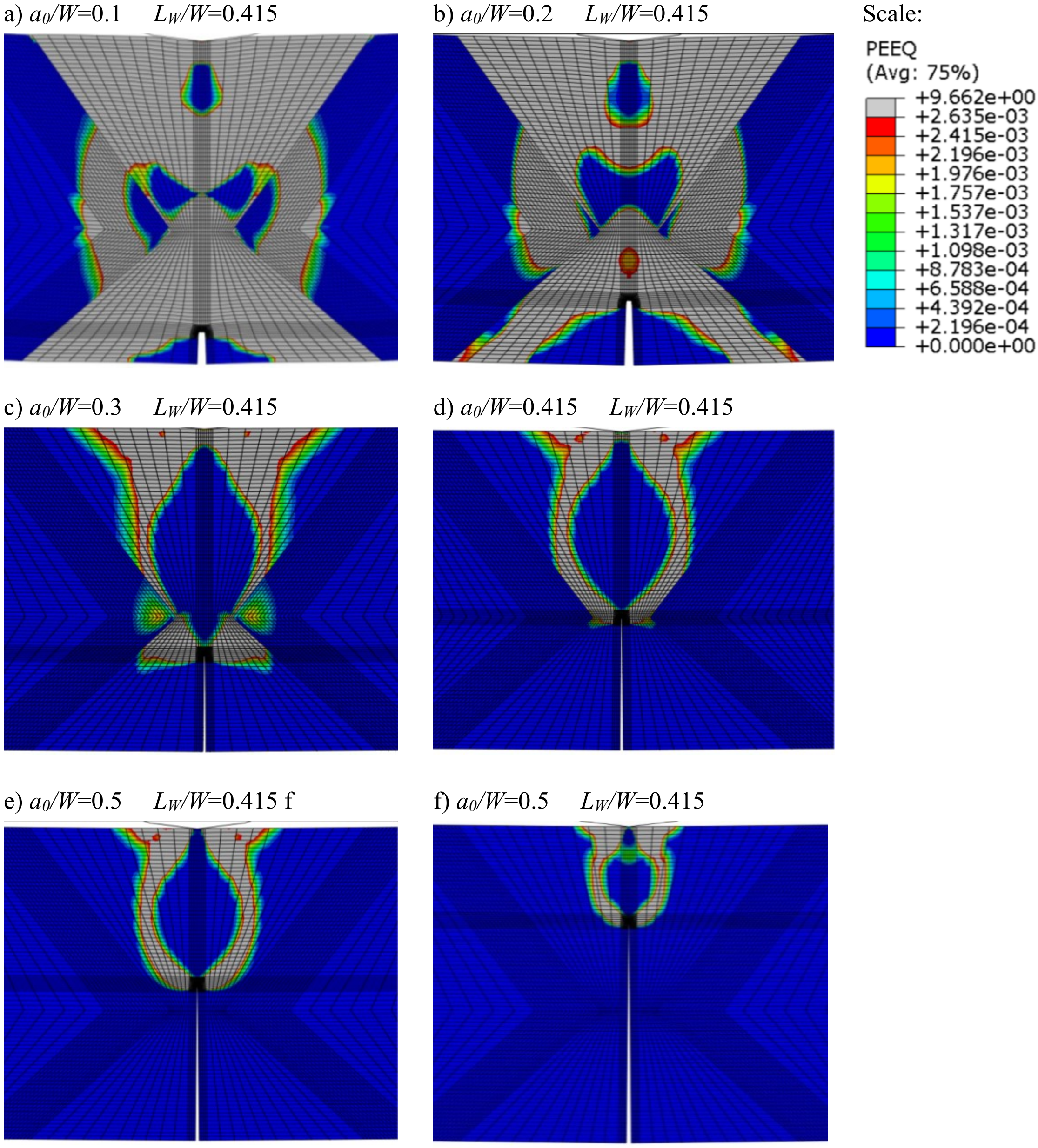

a) a_0/W=0.1 L_W/W=0.415

b) a_0/W=0.2 L_W/W=0.415

c) a_0/W=0.3 L_W/W=0.415

d) a_0/W=0.415 L_W/W=0.415

e) a_0/W=0.5 L_W/W=0.415 f

f) a_0/W=0.5 L_W/W=0.415

Figure 4.22 The plastic zone for the modelled SE(B) specimens with the UM weld and the crack lengths a) a_0/W=0.1, b) a_0/W=0.2, c) a_0/W=0.3, d) a_0/W=0.415 e) a_0/W=0.5 and f) a_0/W=0.7. The equivalent plastic strain (PEEQ) fields were obtained at the yield limit load F/F_Y=1 from the results of the FEM series 2B-UM.

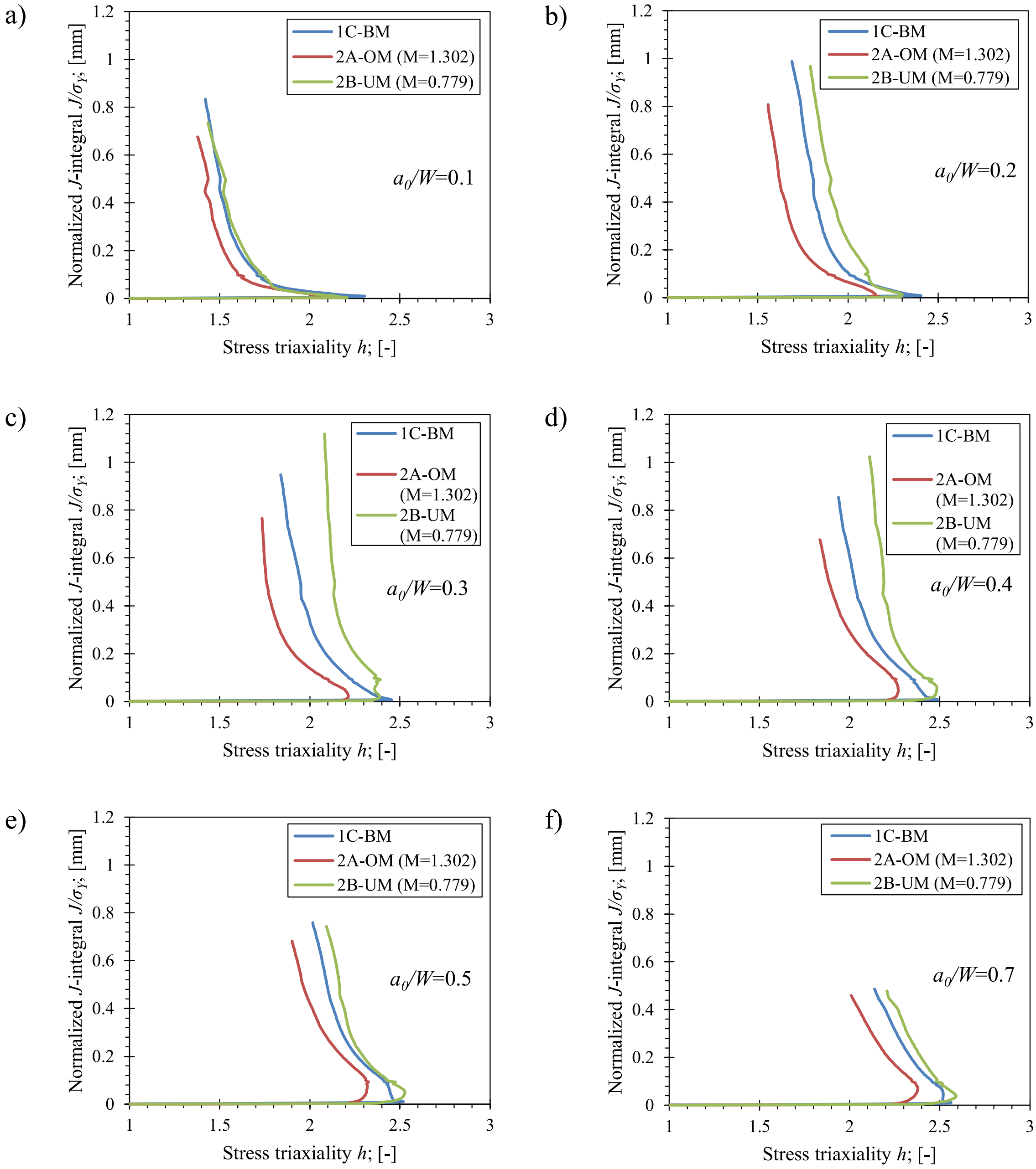

Figure 4.23 Stress triaxiality *h* for the welded OM and UM SE(B) specimens with a) a_0/W=0.1, b) a_0/W=0.2, c) a_0/W=0.3, d) a_0/W=0.4, d) a_0/W=0.5 and d) a_0/W=0.7. The distances to the weld root are L_W/W=0.36 and L_W/W=0.415 for the OM and the UM welds respectively. the results of the base material (FEM series 1C-BM) are plotted for a reference.

The opposite can be observed for the UM weld. In case of shallow cracks, i.e. $a/W<L_W/W$=0.415, the plastic zone is initially developed in the softer UM weld material (σ_{YS}=533.5 MPa). The base material with comparatively higher yield strength (σ_{YS}=686.7 MPa) presents a barrier that obscures spreading of the plastic zone. Only at sufficiently high load, the

plastic zone can spread into the base material, as demonstrated in Figure 4.22 a), Figure 4.22 b) and Figure 4.22 c). At the same time, the computed stress triaxiality h for the UM weld is higher than the one of the base material, as shown in Figure 4.23 a), Figure 4.23 b) and Figure 4.23 c).

The behaviour of the UM weld is understood as, the plastic zone originating from the crack tip is confined in the weld material with lower yield strength and only limited plastic deformation takes place in the base material. For that reason, the hydrostatic stress in front of the crack tip increases in comparison to homogeneous situation [153]. Hence, the higher crack driving force, which corresponds to the higher values of η_{pl} with respect to the base material for $0.2 \leq a_0/W \leq 0.5$, as demonstrated in Figure 4.20. Again, similar behaviour was reported by Kim et al.[58], Donato and Ruggieri [60], Zhou et al. [155] and Zerbst [63].

Such behaviour is observed until the crack length is similar to the distance to the weld root, as demonstrated in Figure 4.22 d). The narrow weld root limits plastic zone to a small area in front of the crack tip. This additionally increases the hydrostatic stress in front of the crack tip, which results in increased stress triaxiality, as demonstrated in Figure 4.23 d). This results in increased η_{pl} values with the maximum observed when the crack tip is located in the weld root, as demonstrated in Figure 4.20. Similarly, increased η_{pl} due to reduction of the weld width was reported in researches such as Zhou et al. [155] and Zerbst [63].

When the crack extends beyond the weld root, i.e. $a/W > L_W/W$, the plastic zone develops normally in the UM weld material without interaction of the adjacent base material. This results in a rapid decrease of the stress triaxiality for deeper cracks in the OM weld material to a similar level that was observed in the base material, as shown in the Figure 4.23 e) and Figure 4.23 f). Correspondingly, drop of η_{pl} can be observed as well, where values for the cracks with $a_0/W \geq 0.5$ are similar to the one for the base material, as demonstrated in Figure 4.20.

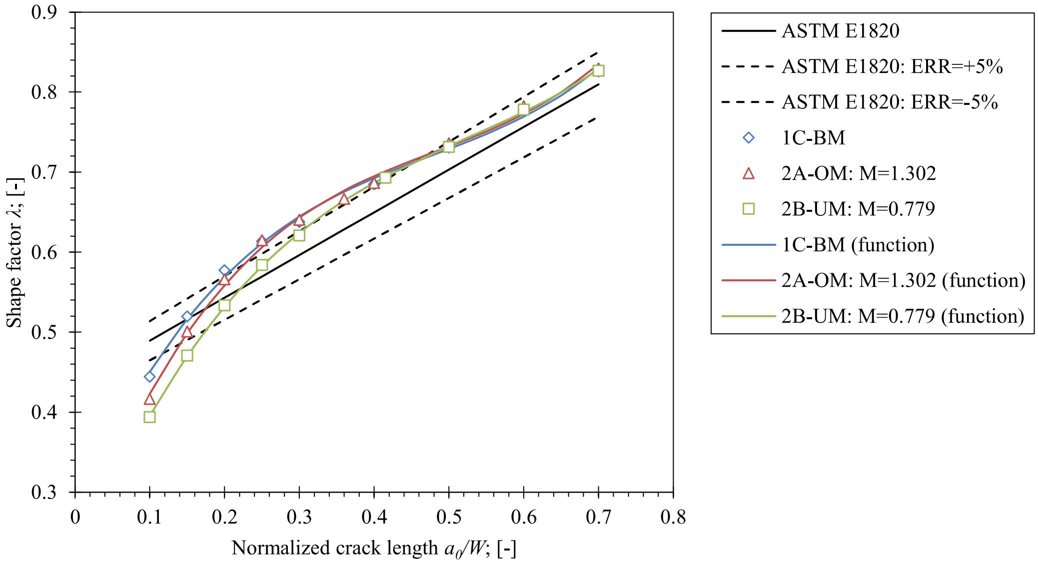

Figure 4.24 The comparison of the calibrated λ factors for the welded OM and UM SE(B) specimens with standard solution according to ASTM E1820. The results for the base material (FEM series 1C-BM) are plotted for a reference.

Table 4.11 The proposed λ solutions for the welded OM and UM SE(B) specimens.

FEM series	λ functions in range $0.1 \leq a_0/W \leq 0.7$	R^2 [-]
2A-OM	$\lambda = 3.000\left(\frac{a}{W}\right)^3 - 4.333\left(\frac{a}{W}\right)^2 + 2.442\left(\frac{a}{W}\right) + 0.220$	0.997
2B-UM	$\lambda = 2.229\left(\frac{a}{W}\right)^3 - 3.505\left(\frac{a}{W}\right)^2 + 2.254\left(\frac{a}{W}\right) + 0.203$	1.000

The geometry factor λ has been determined on the basis of LLD and CMOD according to the procedure, described in Chapter 4.2.2. The obtained results are presented in Figure 4.24. Deviation of $\lambda(a/W)$ relationships can be observed for shallow cracks with $a/W<0.5$. This is attributed to variations in deformation of the weld due to mismatching. For deep cracks with $a/W>0.5$, results are in good agreement. In this case, deep cracks have tips located beyond the weld root where the adjacent base material does not interact with the plastic zone in the weld. Therefore, in this case λ is dependent mainly on the shape of the fracture specimen and the roller setup. The corresponding calibrated λ functions are presented in Table 4.11.

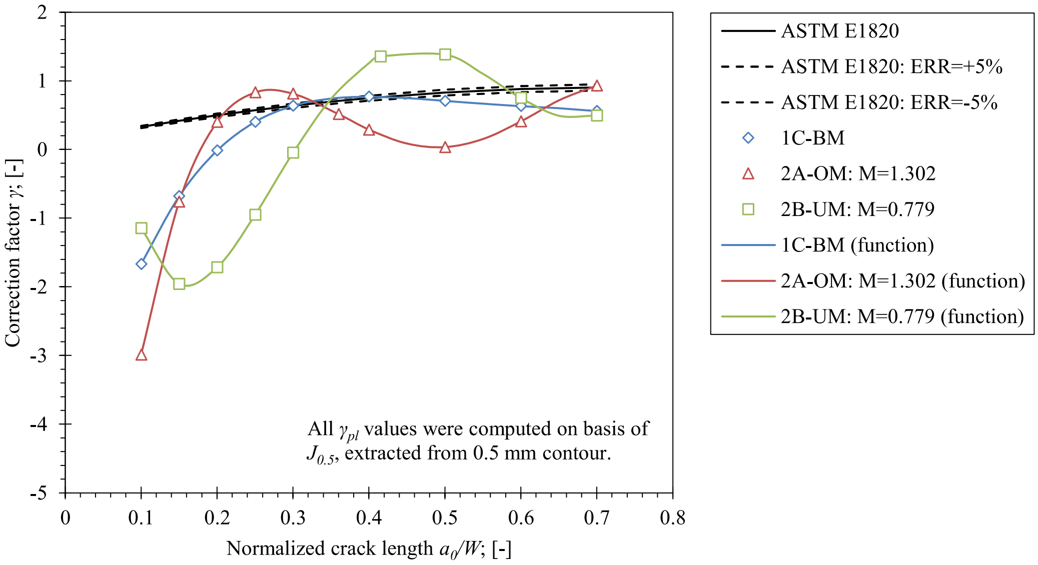

Figure 4.25 The comparison of the calibrated γ_{pl} factors for the welded SE(B) specimens with standard solution according to ASTM E1820 [60]. The results for the base material (series 1C-BM) are plotted for a reference.

Table 4.12 The proposed γ_{pl} functions for the welded OM and UM SE(B) specimens, valid for the *J*-integral, extracted from 0.5 mm contour.

FEM series	γ_{pl} functions for 0.5 mm contour in range $0.1 \leq a_0/W \leq 0.7$	R^2 [-]
2A-OM	$\gamma_{pl} = -350.776\left(\frac{a}{W}\right)^4 + 691.443\left(\frac{a}{W}\right)^3 - 476.044\left(\frac{a}{W}\right)^2 + 133.556\left(\frac{a}{W}\right) - 12.237$	1.000
2B-UM	$\gamma_{pl} = -451.632\left(\frac{a}{W}\right)^5 + 1422.106\left(\frac{a}{W}\right)^4 - 1562.720\left(\frac{a}{W}\right)^3 + 734.779\left(\frac{a}{W}\right)^2 - 136.680\left(\frac{a}{W}\right) + 6.601$	1.000

Finally, functions of the crack growth correction factors γ_{pl} were developed according to the procedure, described in Chapter 4.2.2, and are presented in Figure 4.25. The presented results indicate that in general, *J* is underestimated for the shallow cracks with $a/W<0.2$ and therefore positive correction due to the rack growth is needed in Equation (3.34). For the OM welds, *J* is overestimated when the crack tip is located close to the weld root ($a/W \approx L_W/W=0.36$), while little correction due to crack growth is needed once the crack tip is located beyond the weld root. The opposite behaviour can be observed for the UM weld. Here, *J* is underestimated for cracks shorter than the distance to the weld root ($a/W<L_W/W=0.415$).

4.6 Influence of the Yield Strength Mismatching on Fracture Behaviour of the Single Mismatched Welds

The results, presented in the previous chapter, indicate that η_{pl}, λ and γ_{pl} factors are influenced by the material properties, i.e. yield strength mismatching of the weld. The recent studies [58], [60] and [63], focused on fracture behaviour of an idealized straight butt welds with longitudinal crack at midplane, show that η_{pl} depends on the level of weld mismatch M. Because the dependency of η_{pl} on M is not known for surface cracked welded SE(B) specimens, a FEM based investigation was conducted in the scope of this research. Here, the FEM series 3A-OM and 3B-UM with pronounced strength mismatch were analysed. Plastic properties of the OM and the UM weld material models in Table 4.4 were artificially shifted in order to obtain pronounced yield strength mismatching weld materials with M=1.5 (σ_{YS}=1024.2 MPa) and M=0.5 (σ_{YS}=266.1 MPa), respectively. Remaining features of the FEM models were configured the same way as described in Chapter 4.5. The calibrated η_{pl} values were computed by using the slope method [60], as described in Chapter 4.2.1. The J-integral $J_{0.5}$, extracted from the 0.5 mm contour, was used for calibration of the η_{pl} factor. The obtained results are presented in Figure 4.26 that shows similarities in fracture behaviour of the welded SE(B) specimens with original and enhanced weld mismatching levels.

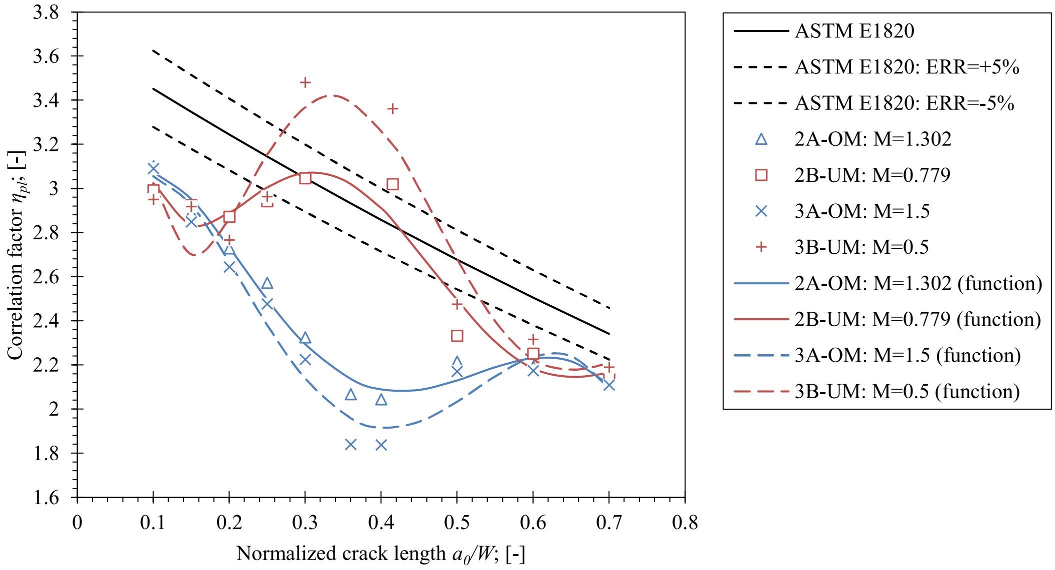

Figure 4.26 the comparison of the calibrated η_{pl} factors for the welded SE(B) specimens with various levels of weld yield strength mismatch M. Solution according to ASTM E1820 standard [60] is plotted as a reference.

Table 4.13 The proposed η_{pl} solutions for the welded OM and UM SE(B) specimens with weld yield strength mismatching factors M=1.5 and M=0.5, respectively. The listed equations are based on the J-integral, extracted from the 0.5 mm contour.

FEM series	η_{pl} functions for 0.5 mm contour in range $0.1 \le a_0/W \le 0.7$	R^2 [-]
3A-OM	$\eta_{pl} = 97.960\left(\frac{a}{W}\right)^5 - 316.782\left(\frac{a}{W}\right)^4 + 326.940\left(\frac{a}{W}\right)^3 - 132.696\left(\frac{a}{W}\right)^2 + 17.447\left(\frac{a}{W}\right) + 2.339$	0.957
3B-UM	$\eta_{pl} = -715.044\left(\frac{a}{W}\right)^5 + 1647.962\left(\frac{a}{W}\right)^4 - 1395.160\left(\frac{a}{W}\right)^3 + 522.880\left(\frac{a}{W}\right)^2 - 83.327\left(\frac{a}{W}\right) + 7.365$	0.880

According to Figure 4.26, the OM welds with M=1.302 (FEM series 2A-OM) and M=1.5 (FEM series 3A-OM) show similar shape of $\eta_{pl}(a/W)$ functions with peak values when the crack tip is near the narrow weld root, i.e. $a_0/W \approx L_W/W$=0.36. The minimum value, produced by $\eta_{pl}(a/W)$ function for M=1.5, is 8 % lower in comparison to the original mismatch level M=1.302. Both functions show close agreement for shallow cracks with $a_0/W \le 0.2$ and for deep cracks with $a_0/W \ge 0.6$. The opposite behaviour can be observed in case of the UM welds. Here, $\eta_{pl}(a/W)$ functions produce peak values when the crack tip is located near the narrow weld root, i.e. $a_0/W \approx L_W/W$=0.415. The peak value of $\eta_{pl}(a/W)$ function for the weld with yield strength mismatch level M=0.5 is 11 % higher than the one for M=0.779. Again, both functions show close agreement for shallow cracks with $a_0/W \le 0.2$ and for deep cracks with $a_0/W \ge 0.6$.

Correlation of η_{pl}(a/W) functions, presented in Figure 4.26, with equivalent strain fields, presented in Figure 4.27 for weld with M=1.5 (FEM series 3A-OM) and Figure 4.21 for weld with M=1.302 (FEM series 2A-UM), shows similar plastic zone patterns for both OM welds. Both cases show strong interference of the adjacent base material with development of plastic zone in case of the shallow cracks with $a_0/W \le 0.3$. Here, the plastic zone easily develops into the base material with lower yield strength (σ_{YS}=682.8 MPa) in comparison to the OM welds with M=1.5 (σ_{YS}=1024.2 MPa) and M=1.302 (σ_{YS}=889.0 MPa). However, such behaviour is more pronounced in case of the enhanced yield strength mismatch level M=1.5. This is particularly obvious when the crack tip is located in the weld root as shown Figure 4.27 d). Here, larger area of adjacent base material is more plastically deformed than in case of

M=1.302, as shown in Figure 1.21 d). This results in reduced peak stress triaxiality for mismatch level M=1.5 in comparison to M=1.302, which explains reduction of the η_{pl} values, shown in Figure 4.26. On the contrary, the adjacent base material shows little interference with the plastic zone for deep cracks with $a_0/W\leq0.5$, where the crack tips are located beyond the narrow weld root. This results in good agreement of the stress triaxiality h, as shown in Figure 4.29 a) and Figure 4.29 f), and η_{pl} values, shown in Figure 4.26, for both OM welds with M=1.5 and M=1.302. Additionally, thorough investigation of stress triaxiality in terms of $h(J/\sigma_{YS})$ curves indicates that the OM welds exhibit close agreement throughout the investigated crack length range $0.1\leq a_0/W\leq0.7$. This is particularly visible for constraint loss after the peak h due to onset of large plastic zone. The results in Figure 4.26 also indicate that interference of the base material with development of the plastic zone results in reduction of peak triaxiality h for cracks with tips located in the weld root, i.e. $a_0/W\approx L_W/W$=0.36, and shallower. Again, this correlates with reduced η_{pl} values for welds with enhanced yield stress mismatching M=1.5.

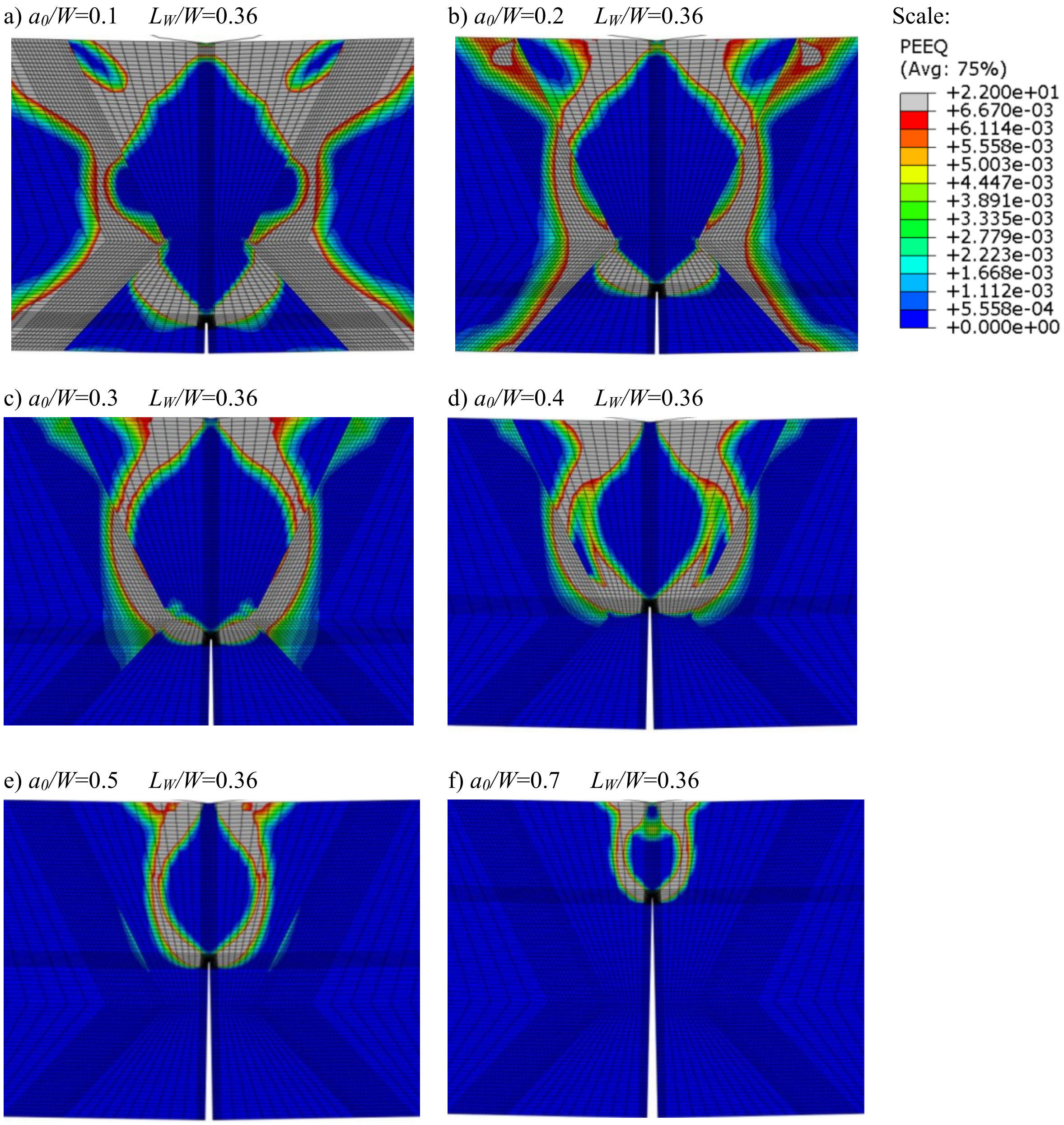

a) a_0/W=0.1 L_W/W=0.36

b) a_0/W=0.2 L_W/W=0.36

c) a_0/W=0.3 L_W/W=0.36

d) a_0/W=0.4 L_W/W=0.36

e) a_0/W=0.5 L_W/W=0.36

f) a_0/W=0.7 L_W/W=0.36

Figure 4.27 The plastic zone for the modelled welded SE(B) specimens with M=1.5 and crack lengths a) a_0/W=0.1, b) a_0/W=0.2, c) a_0/W=0.3, d) a_0/W=0.4, e) a_0/W=0.5 and f) a_0/W=0.7. The equivalent plastic strain (PEEQ) fields were obtained at the limit load F/F_Y=1 from results of the FEM series 3A-OM.

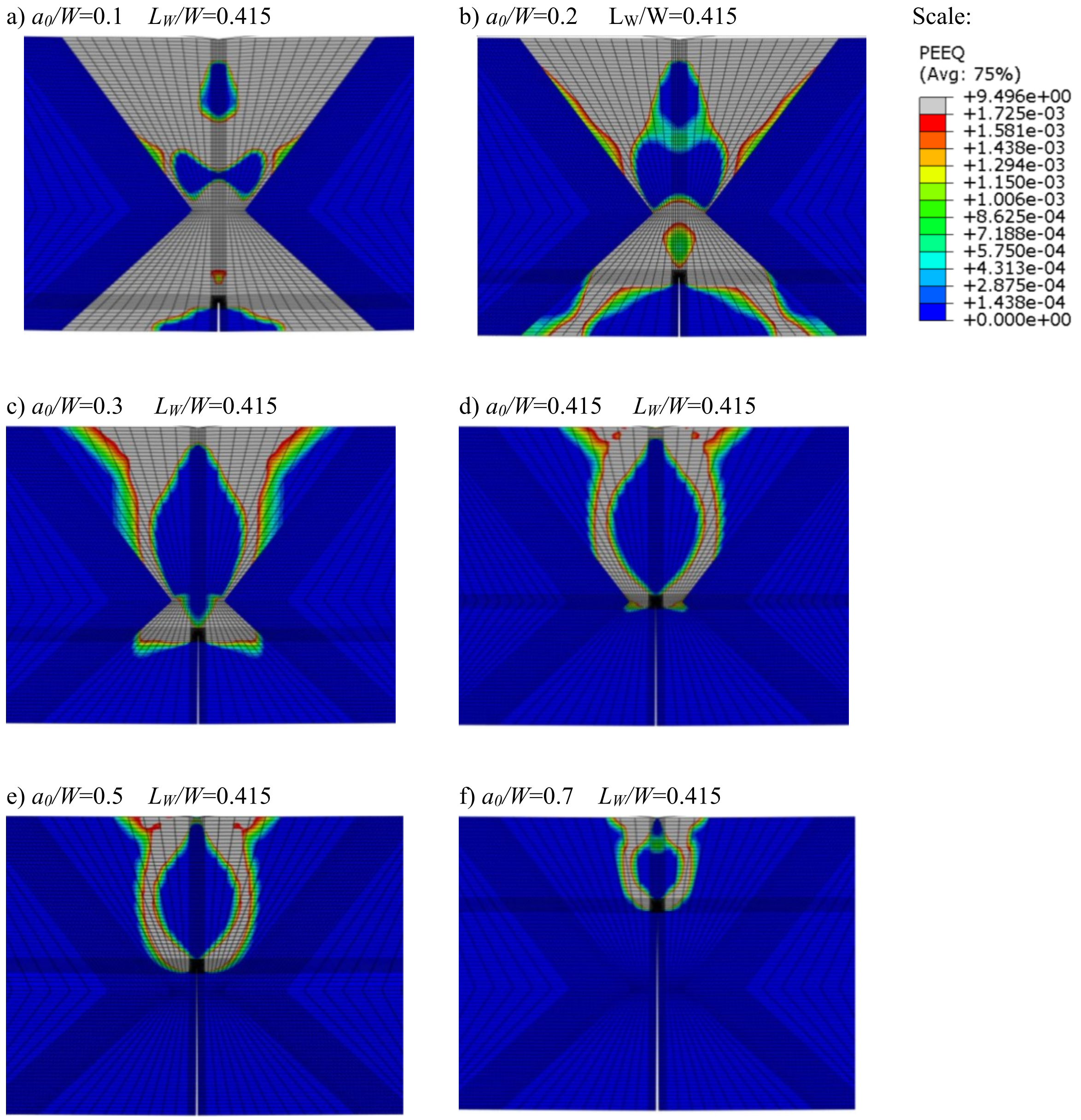

a) a_0/W=0.1 L_W/W=0.415

b) a_0/W=0.2 L_W/W=0.415

c) a_0/W=0.3 L_W/W=0.415

d) a_0/W=0.415 L_W/W=0.415

e) a_0/W=0.5 L_W/W=0.415

f) a_0/W=0.7 L_W/W=0.415

Figure 4.28 The plastic zone for the modelled welded SE(B) specimens with M=0.5 and crack lengths a) a_0/W=0.1, b) a_0/W=0.2, c) a_0/W=0.3, d) a_0/W=0.4, e) a_0/W=0.5 and f) a_0/W=0.7. The equivalent plastic strain (PEEQ) fields were obtained at the limit load F/F_Y=1 from results of the FEM series 3B-UM.

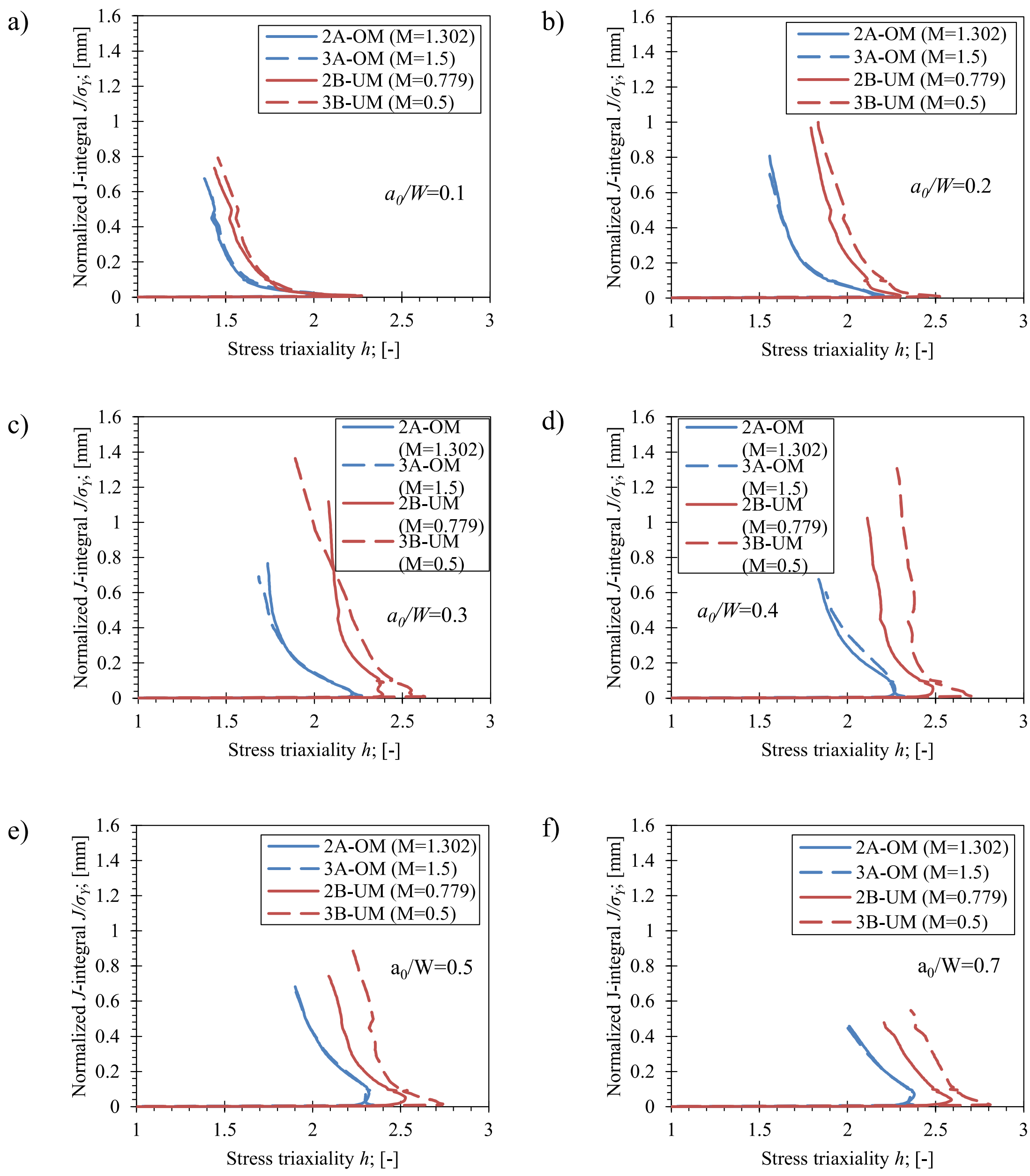

Figure 4.29 Stress triaxiality h for the welded OM and UM SE(B) specimens with a) a_0/W=0.1, b) a_0/W=0.2, c) a_0/W=0.3, d) a_0/W=0.4, e) a_0/W=0.5 and f) a_0/W=0.7. The distances to the weld root are L_W/W=0.36 and L_W/W=0.415 for the OM and the UM welds respectively

The UM welds exhibit higher variations of $\eta_{pl}(a/W)$ functions under different yield strength mismatching levels M, as demonstrated in Figure 4.26. Further correlation of $\eta_{pl}(a/W)$ functions with equivalent strain fields, presented in Figure 4.28 for the welds with M=0.5 (FEM series 3B-UM) and Figure 4.22 for the welds with M=0.779 (FEM series 2B-UM), show variations in the plastic zone patterns for both UM welds. In both cases, the plastic zone is limited mainly within the weld material. This is particularly distinctive for shallow cracks with $a_0/W<0.3$. The cause for such behaviour is the base material having higher yield strength (σ_{YS}=682.8 MPa) in comparison to undermatched welds with M=0.5 (σ_{YS}=266.1 MPa) and M=0.779 (σ_{YS}=532.1 MPa). Equivalent plastic strain fields for the shallow cracked undermatched welds with M=0.779, shown in Figure 4.22 a), Figure 4.22 b) and Figure 4.22 c), indicate that the weld material and relatively small area of the base material are subjected to plastic deformation. However, the presented principle of the plastic zone development is more pronounced for the UM welds with M=0.5. Here, the plastic zone is completely confined within the weld material due to relatively large difference in yield strength of the base and the weld material, as demonstrated in Figure 4.28 a), Figure 4.28 b) and Figure 4.28 c). As a result, stress triaxiality h is increased with respect to the actual weld mismatch level M=0.779, as demonstrated in Figure 4.29. This is particularly obvious when the crack tip is located close the narrow weld root, i.e. $a_0/W\approx L_W/W=0.415$, as demonstrated in Figure 4.29 d). The corresponding strain patterns for M=0.5, shown in Figure 4.28 d), and M=0.779, shown in Figure 4.22 d), indicate that the plastic zone is completely confined within a narrow region of the UM weld root. On the contrary, the adjacent base material shows little interference with plastic zone for deep cracks with $a_0/W\geq0.5$, where the cracks have tips located beyond the weld root. This results in close agreement with η_{pl} values, as shown in Figure 4.26 for both the UM welds with M=0.5 and M=0.779. Moreover, the investigation of the stress triaxiality in terms of $h(J/\sigma_{YS})$ curves, presented in Figure 4.29, indicates consistently higher triaxiality values for the welds with M=0.5 in comparison to the actual mismatching weld with M=0.779. This is attributed to more severe confinement of the plastic deformation in the UM weld in case of the former. As a result, the welds with M=0.5 show higher stress triaxiality even after constraint loss due to large plastic deformation onset throughout the investigated crack length range $0.1\leq a_0/W\leq0.7$.

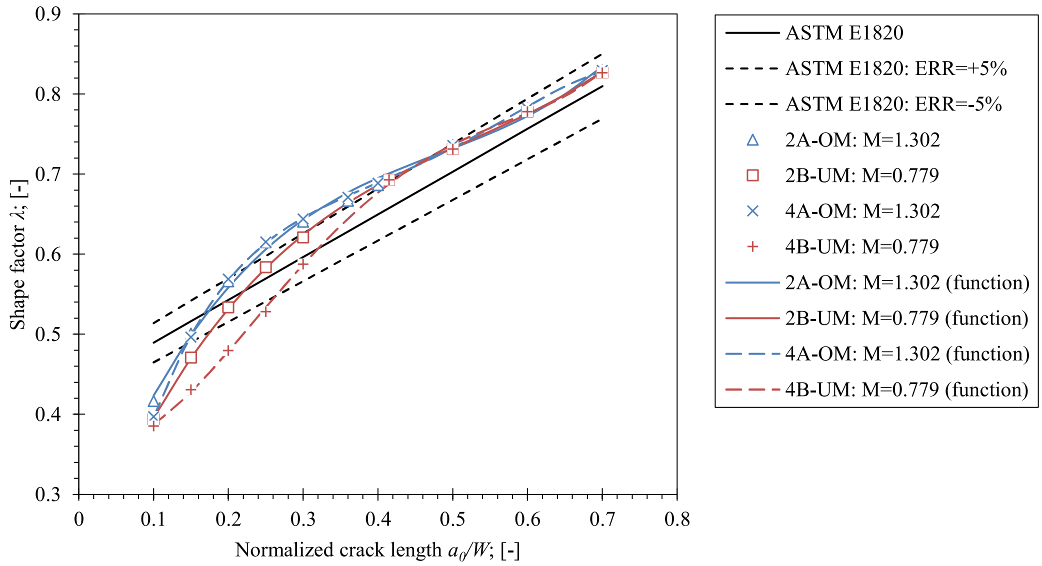

Figure 4.30 The comparison of the calibrated λ factors for the welded OM and UM SE(B) specimens with standard solution according to ASTM E1820 [60].

Table 4.14 The proposed λ solutions for the welded SE(B) specimens with pronounced overmatching(M=1.5) and undermatching (M=0.5).

FEM series	λ functions in range $0.1 \le a_0/W \le 0.7$	R^2 [-]
3A-OM	$\lambda = 3.547\left(\frac{a}{W}\right)^3 - 5.285\left(\frac{a}{W}\right)^2 + 2.972\left(\frac{a}{W}\right) + 0.127$	0.998
3B-UM	$\lambda = -0.469\left(\frac{a}{W}\right)^3 - 0.141\left(\frac{a}{W}\right)^2 + 1.135\left(\frac{a}{W}\right) + 0.256$	0.998

The geometry factors λ have been determined on the basis of LLD and CMOD according to the procedure, described in Chapter 4.2.2. The computed results are presented in Figure 4.31. In general, good agreement of $\lambda(a/W)$ functions for the OM welds with M=1.302 and M=1.5 can be observed in the analysed crack length range $0.1 \le a_0/W \le 0.7$. This is due to similar deformation behaviour of both OM welds. On the contrary, significant deviation between $\lambda(a/W)$ functions of the UM welds is observed for cracks with $a_0/W<0.5$. Here, the UM welds with M=0.5 show lower λ values than the UM welds with actual mismatch level M=0.779. This is attributed to distinctive differences in deformation behaviour due to interference of the adjacent base material with the plastic zone, as demonstrated in Figure 4.22 and Figure 4.28. The computed λ values for the deep cracks with $a_0/W \ge 0.5$, and various levels of yield strength mismatch in range $0.5 \le M \le 1.5$, seems to be in a good agreement. This indicates that in this case

λ is potentially dependent mainly on the shape of the fracture specimen and the roller setups, as it was discussed in Chapter 4.4 and Chapter 4.5. The corresponding calibrated $\lambda(a/W)$ functions are presented in the Table 4.14.

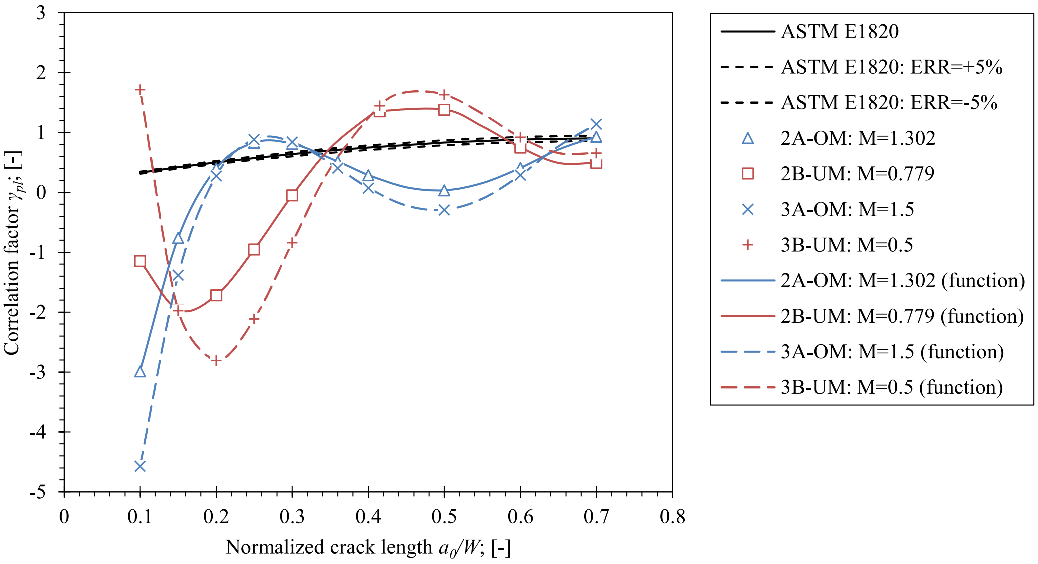

Figure 4.31 The comparison of the calibrated γ_{pl} factors for the welded OM and UM SE(B) specimens with standard solution according to ASTM E1820 [60].

Table 4.15 The proposed γ_{pl} functions for the welded OM and UM SE(B) specimens, valid for the *J*-integral, extracted from the 0.5 mm contour.

FEM series	γ_{pl} functions for 0.5 mm contour in range $0.1 \leq a_0/W \leq 0.7$	R^2 [-]
3A-OM	$\gamma_{pl} = -501.441\left(\frac{a}{W}\right)^4 + 992.155\left(\frac{a}{W}\right)^3 - 683.944\left(\frac{a}{W}\right)^2 + 191.723\left(\frac{a}{W}\right) - 17.844$	1.000
3B-UM	$\gamma_{pl} = -1503.250\left(\frac{a}{W}\right)^5 + 4096.377\left(\frac{a}{W}\right)^4 - 4175.130\left(\frac{a}{W}\right)^3 + 1940.616\left(\frac{a}{W}\right)^2 - 391.926\left(\frac{a}{W}\right) + 25.285$	0.999

The crack growth correction factors γ_{pl} were developed according to the procedure, described in the Chapter 4.2.2. The computed results are presented in Figure 4.31. The largest deviations of the results are observed for shallow cracks with $a_0/W<0.15$. In general, the results indicate that the analysed OM and UM welds require positive correction of J_{pl} for shallow cracks that are shorter than the distance to the weld root ($a_0/W<L_W/W$=0.36 for OM and $a_0/W<L_W/W$=0.415 for UM). Once the crack tip is located beyond the weld root, J_{pl} must be reduced due to the crack growth, which is indicated with positive values of γ_{pl} factor. Moreover, the OM welds require only minor corrections in crack lengths in range $0.4\leq a_0/W\leq 0.6$. Variations in γ_{pl} due to different yield strength mismatch levels M seem to be lesser for the OM welds than the UM welds. This is attributed to significant variations in deformation behaviour of the UM weld with M=0.5 and M=0.779

4.7 Influence of the Heat Affected Zone on Fracture Behaviour of the Single Mismatched Welds

Critical engineering assessment procedures, such as BS 7910 [4] and FITNET [1], [2], rely only on weld material properties for evaluation of integrity of welded structures by incorporating the mismatch factor M into correction of the FAD chart. Investigation of idealized welds with straight fusion lines and central crack, conducted by Koo et al. [156], showed that properties of the HAZ have an influence on the η_{pl} factor. Their conclusion was that narrow, moderately hardened HAZ with M=1.2 or moderately softened HAZ with M=0.8 cause ±3 % variations of η_{pl} values. Therefore, the effect of the HAZ on η_{pl} could be discarded in this particular case. However, fabricated welds in S690 QL plates have highly hardened HAZ with yield strength mismatch ratio M=1.518, as reported in Chapter 3.3.1 and Chapter 3.3.2. For that reason, the effect of HAZ on η_{pl}, λ and γ_{pl} factors was investigated through the computational analysis of the FEM series 4A-OM and 4B-UM. The modelled HAZ, as shown in Figure 4.32, has elastic and plastic material properties, presented in Table 4.4. The average width of the HAZ was determined through inspection of weld metallographic samples with optical microscope and it measured 2.8 mm (width of complete HAZ, including fine- and coarse-grained regions). The modelled OM and UM welds had yield strength mismatching M=1.302 and M=0.779, respectively. The remaining features of the FEM models were configured in the same way as described in Chapter 4.5. The calibrated η_{pl} values were computed by using the slope method [89], as described in Chapter 4.2.1. The J-integral $J_{0.5}$, extracted from the 0.5 mm contour, was used for the calibration of the η_{pl} factor. The obtained results are presented in Figure 4.33 that shows similar trends in behaviour of the UM welds and completely the opposite behaviour of the OM weld in presence of the HAZ. The corresponding calibrated functions $\eta_{pl}(a/W)$ are listed in Table 4.16.

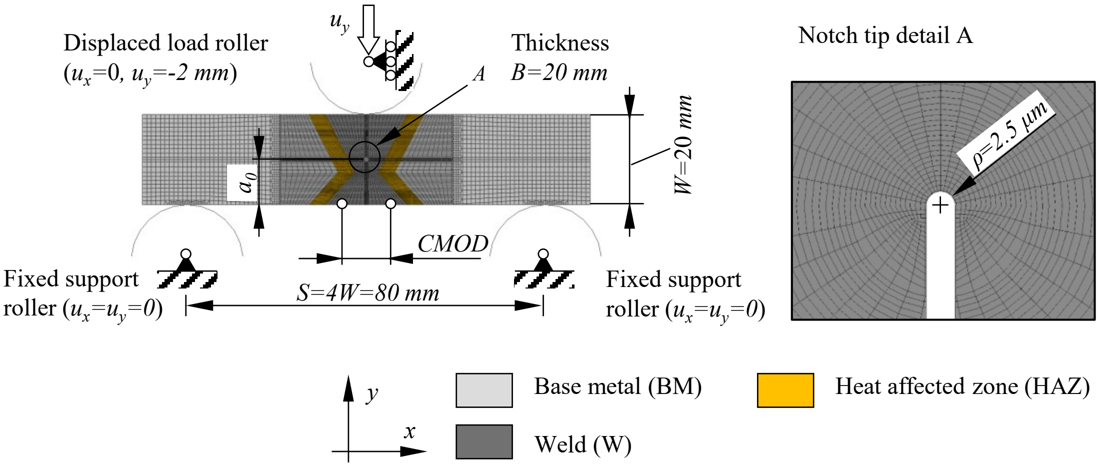

Figure 4.32 The configuration of the FEM for analysis of the single mismatched welds with HAZ.

According to Figure 4.33, the OM welds with M=1.302 and no HAZ (FEM series 2A-OM) show different shape of $\eta_{pl}(a/W)$ function than the OM welds with the same mismatch level and modelled HAZ (FEM series 3A-OM).It is important to note, that in case of the former, the plastic zone spreads into the base material due to comparatively higher yield strength of the OM weld material. the corresponding deformation behaviour of the OM welds with the absent HAZ has been presented in Chapter 4.5. To continue, the OM weld with the present HAZ shows lower η_{pl} values for shallow cracks with a_0/W<0.2. Figure 4.34 a) and Figure 4.34 b) show that the plastic zone is partially restricted to the OM weld with lower yield strength (σ_{YS}=889.0 MPa) than the HAZ (σ_{YS}=974.3 MPa in average), which acts as a barrier. This correlates with an increased peak triaxiality h in comparison to the OM weld with the absent HAZ, as demonstrated in Figure 4.36 a) and Figure 4.36 b). Additionally, lower constraint loss is observed after large scale plasticity onset which is a result of present HAZ. At yield limit load onset, adjacent regions of the base material and part of the HAZ plastically deform. With increasing, the crack length a_0/W, η_{pl} constantly rises until maximum value, when the crack tip at a_0/W=0.3 is located in front of the narrow weld root. Here, the plastic zone is confined in the narrow region of the OM weld material between layers of the HAZ, as demonstrated in Figure 4.34 c). This further increases hydrostatic pressure in front of the crack tip, which manifests in increased peak triaxiality h, as demonstrated in Figure 4.36 c). The described phenomena is less prominent when the crack tip passes the narrow weld root, i.e. $a_0/W \geq L_W/W$=0.36. Here, the bands of plastic deformation for a_0/W=0.4, originating from the crack tip, seems to be less obstructed by the layers of HAZ, as demonstrated in Figure 4.34 d). This correlates with reduced difference of stress triaxiality records $h(J/\sigma_{YS})$ between the OM welds with the present and absent HAZ, as demonstrated in Figure 4.36 d). For the deep cracks with $a_0/W \geq 0.5$, the plastic zone develops within the OM weld material without interaction of the HAZ, as demonstrated in Figure 4.34 e) and Figure 4.34 f). These plastic deformation patterns are the similar to deformation patterns of the OM welds with absent HAZ, shown in Figure 4.21 e) and Figure 4.21 f). This results in almost identical stress triaxiality between both OM welds, as demonstrated in Figure 4.36 e) and Figure 4.36 f). Consequentially, values of η_{pl} for the OM welds with present and absent HAZ are in good agreement with $a_0/W \geq 0.5$.

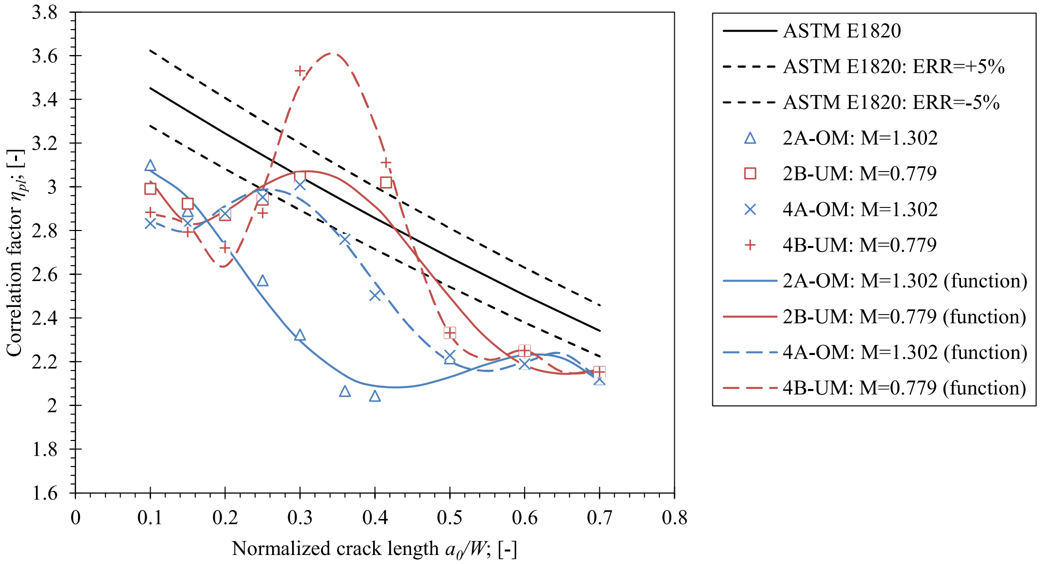

Figure 4.33 The comparison of calibrated η_{pl} factors for the welded OM and UM SE(B) specimens with HAZ and standard solution according to ASTM E1820. The results for the OM (FEM series 2A-OM) and the UM (FEM series 2B-UM) welds with no HAZ are plotted as a reference.

Table 4.16 The proposed η_{pl} functions for the welded OM and UM SE(B) specimens with HAZ, valid for the J-integral, extracted from 0.5 mm contour.

FEM series	η_{pl} functions for 0.5 mm contour in range $0.1 \le a_0/W \le 0.7$	R^2 [-]
4A-OM	$\eta_{pl} = 331.230\left(\frac{a}{W}\right)^6 - 1450.460\left(\frac{a}{W}\right)^5 + 2048.235\left(\frac{a}{W}\right)^4 - 1283.56\left(\frac{a}{W}\right)^3 + 376.673\left(\frac{a}{W}\right)^2 - 48.880\left(\frac{a}{W}\right) + 5.056$	0.988
4B-OM	$\eta_{pl} = 47028.960\left(\frac{a}{W}\right)^7 - 135988.425\left(\frac{a}{W}\right)^6 + 159730.047\left(\frac{a}{W}\right)^5 - 97624.037\left(\frac{a}{W}\right)^4 + 33048.434\left(\frac{a}{W}\right)^3 - 6106.258\left(\frac{a}{W}\right)^2 + 564.973\left(\frac{a}{W}\right) - 17.308$	0.985

The opposite to the OM welds, the UM welds with the HAZ (FEM series 4B-UM) have exhibited less variation of $\eta_{pl}(a/W)$ in comparison to the UM welds with the absent HAZ (FEM series 2BOM), as demonstrated in Figure 4.33. It is important to note, that the former show peak values of η_{pl} when the crack tip is located in the narrow weld root. This is due to plastic deformation being confined in the UM weld material with lower yield strength than the base material. This behaviour has been discussed in Chapter 4.5 for the UM welds with absent HAZ. Similarly, plastic zone is restricted to the UM weld material when the layers of HAZ are modelled. However, the described phenomena is more prominent as the HAZ has significantly higher yield strength (σ_{YS}=974.3 MPa) than the UM weld material (σ_{YS}=532.1 MPa). This is confirmed by analysing patterns of equivalent plastic strain, shown in Figure 4.35. It is obvious that plastic deformation is restricted to the UM weld material throughout the entire range of the analysed crack lengths $0.1 \le a0/W \le 0.7$. The development of plasticity for shallow cracks with $a_0/W \le 0.3$ in the UM welds is obstructed by the HAZ, as demonstrated in Figure 4.35 a), Figure 4.35 b) and Figure 4.35c). This causes an increased hydrostatic pressure in front of the crack tip and consequentially, an increased stress triaxiality, as demonstrated by $h(J/\sigma_{YS})$ curves in Figure 4.36 a), Figure 4.36 b) and Figure 4.36 c). Stress triaxiality starts to decrease once the crack tip is located in the weld root, as demonstrated in Figure 4.36 d). This is due to the lesser interference of the HAZ with plastic deformation as demonstrated in Figure 4.34 d). For deep cracks with the length greater than the distance to the weld root i.e., $a_0/W > L_W/W$=0.415, the development of the plastic zone is not interfered by the HAZ as demonstrated in Figure 4.34 e) and Figure 4.34 f). Therefore, stress triaxiality in terms of $h(J/\sigma_{YS})$ curves is independent of the HAZ as demonstrated in Figure 4.36 e) and Figure 4.36 f).

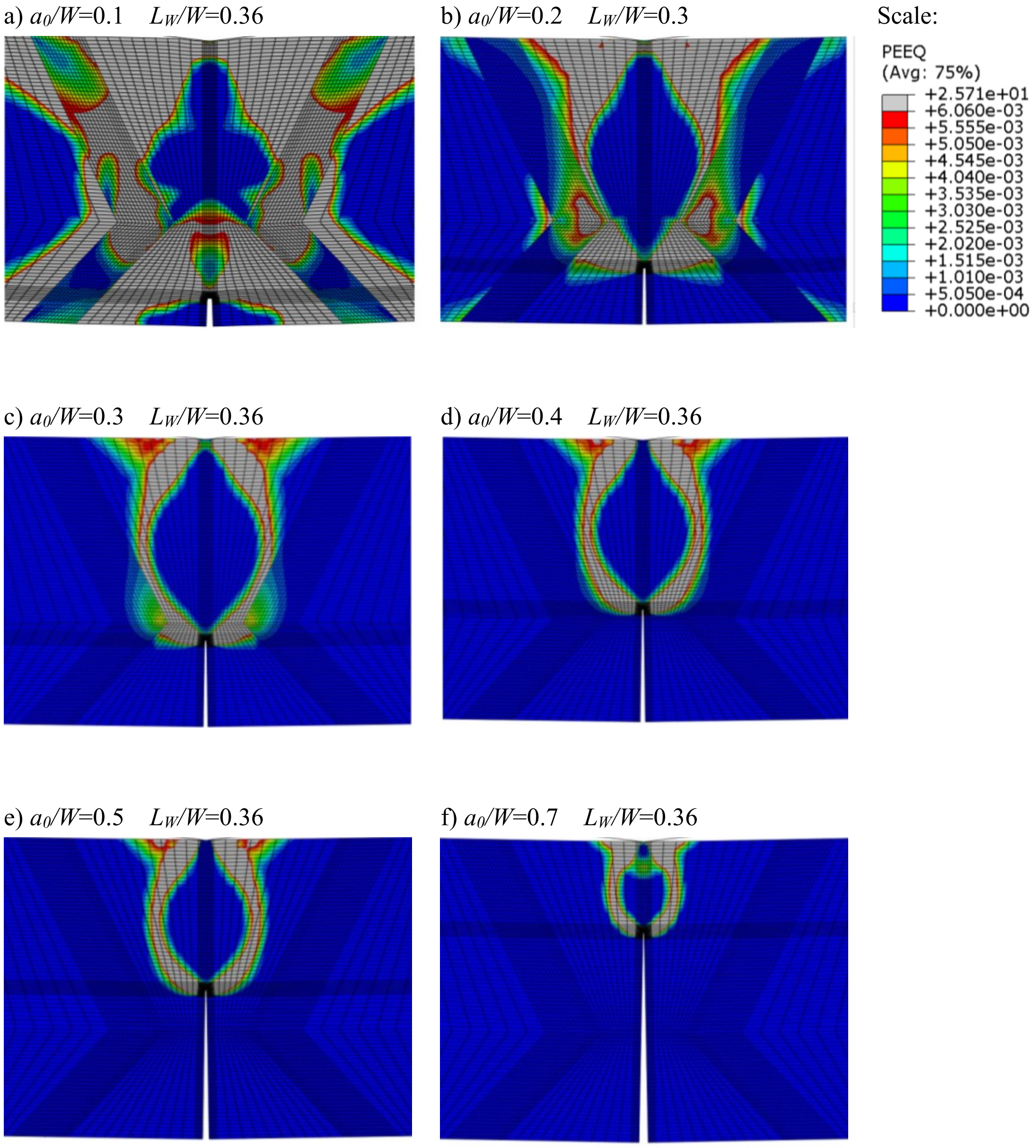
a) a_0/W=0.1 L_W/W=0.36

b) a_0/W=0.2 L_W/W=0.3

c) a_0/W=0.3 L_W/W=0.36

d) a_0/W=0.4 L_W/W=0.36

e) a_0/W=0.5 L_W/W=0.36

f) a_0/W=0.7 L_W/W=0.36

Figure 4.34 The plastic zone for the modelled SE(B) specimens with the OM weld, the HAZ and the crack lengths a) a_0/W=0.1, b) a_0/W=0.2, c) a_0/W=0.3, d) a_0/W=0.04, e) a_0/W=0.5 and f) a_0/W=0.7. Equivalent plastic strain fields were obtained at the yield limit load F/F_Y=1 from the results of the FEM series 4A-OM.

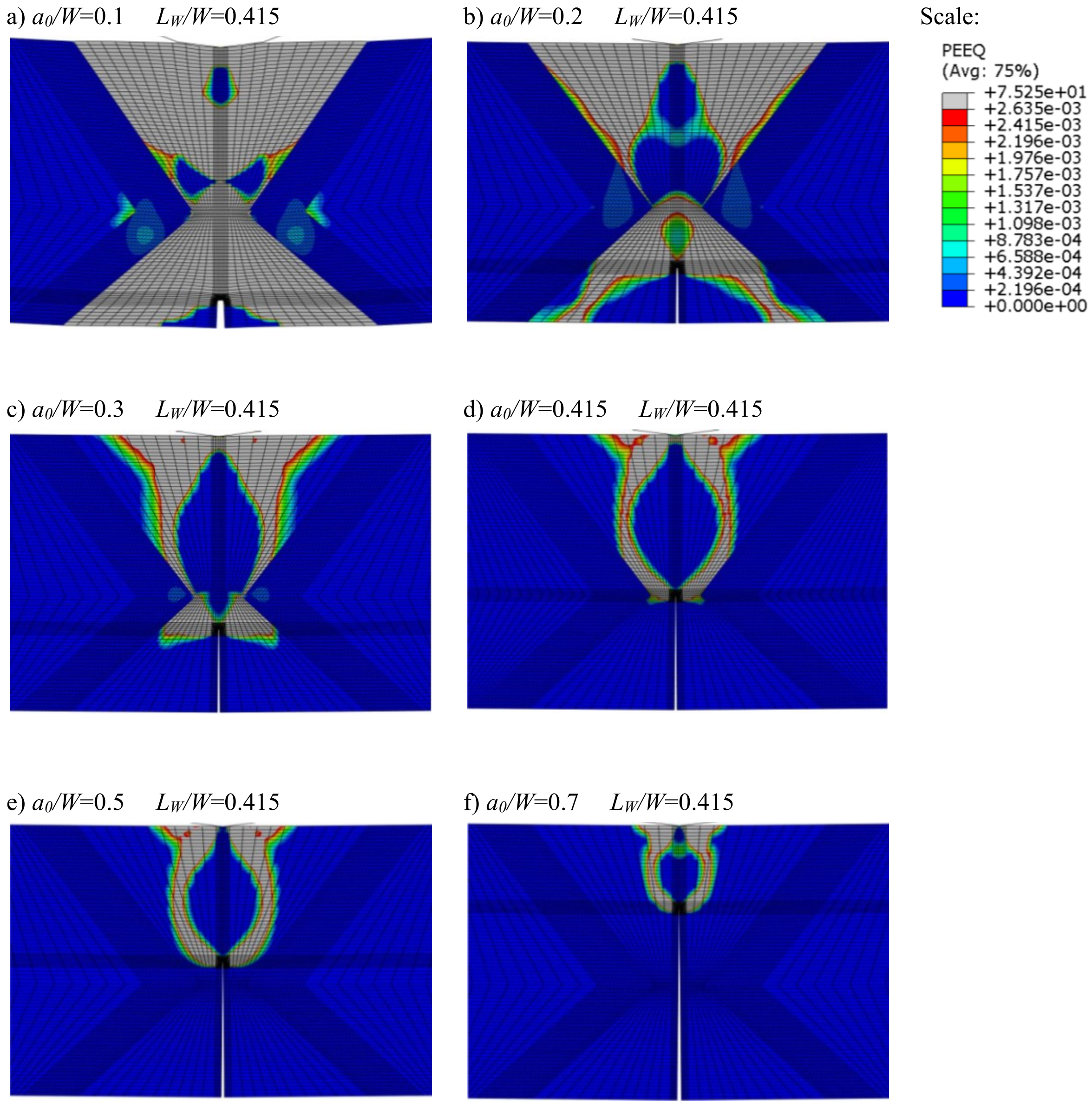

a) a_0/W=0.1 L_W/W=0.415

b) a_0/W=0.2 L_W/W=0.415

c) a_0/W=0.3 L_W/W=0.415

d) a_0/W=0.415 L_W/W=0.415

e) a_0/W=0.5 L_W/W=0.415

f) a_0/W=0.7 L_W/W=0.415

Figure 4.35 The plastic zone for the modelled SE(B) specimens with the UM weld, the HAZ and the crack lengths a) a_0/W=0.1, b) a_0/W=0.2, c) a_0/W=0.3, d) a_0/W=0.4 e) a_0/W=0.5 and f) a_0/W=0.7. The equivalent plastic strain fields were obtained at the yield limit load F/F_Y=1 from the results of the FEM series 4B-UM.

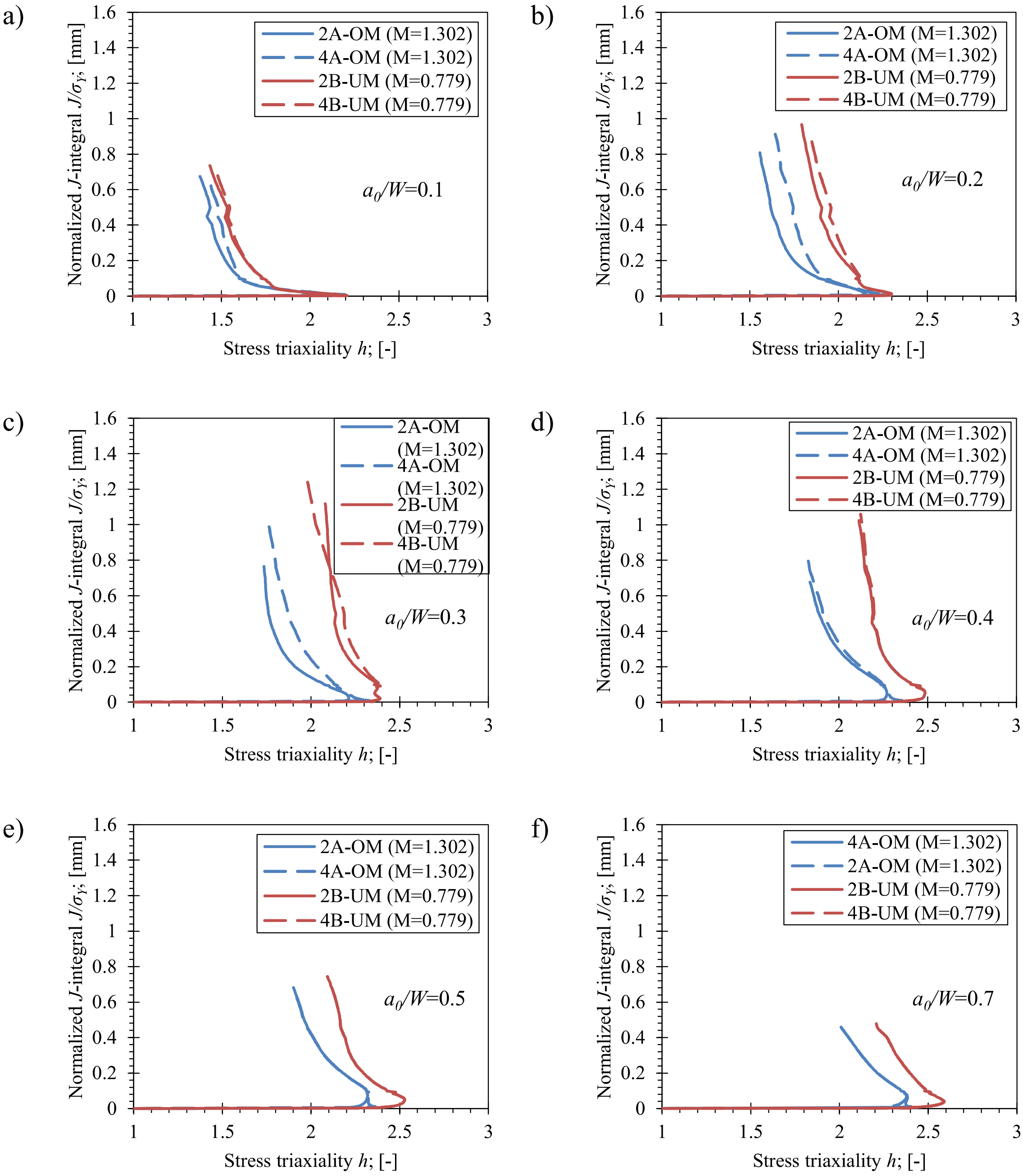

Figure 4.36 The stress triaxiality *h* for the modelled SE(B) specimens with the OM weld, the HAZ and the crack lengths a) a_0/W=0.1, b) a_0/W=0.2, c) a_0/W=0.3 d) a_0/W=0.4, e) a_0/W=0.5 and f) a_0/W=0.7. The corresponding distances to the weld root are L_W/W=0.36 and L_W/W=0.415 for the OM and the UM welds respectively.

The geometry factors λ have been determined on basis of LLD and CMOD according to the procedure, described in Chapter 4.1.2. The computed results are presented in Figure 4.37, while the corresponding calibrated functions are listed in Table 4.17. An overview of the presented

$\lambda(a/W)$ functions indicates that during monotonous loading, the HAZ has negligible effect on the ratio λ between CMOD and LLD of the SE(B) specimens with the OM weld. The opposite can be observed for the UM welds, where values of geometry factor λ are reduced for the cracks with $a_0/W<0.415$. This reduction is more prominent in presence of the HAZ. The correlation of the corresponding $\lambda(a/W)$ functions in Figure 4.37 with plastic strain patterns for $a_0/W<0.415$ in Figure 4.35 indicates, that the reduction of λ is clearly related to the interference of high strength material (base material or HAZ), adjacent to the UM weld, with the plastic zone at the crack tip. According to Figure 4.37, the UM weld with the HAZ show lower λ values than the UM weld without the HAZ. This is attributed to the higher yield strength mismatching between the UM weld material and the HAZ. This can be interpreted in a following manner: CMOD reduces for the given LLD, if the yield strength mismatching between the softer weld and the harder adjacent material increases. However, for deeper cracks with $a_0/W>0.4$ all $\lambda(a/W)$ functions seem to be in good agreement, regardless the weld configuration.

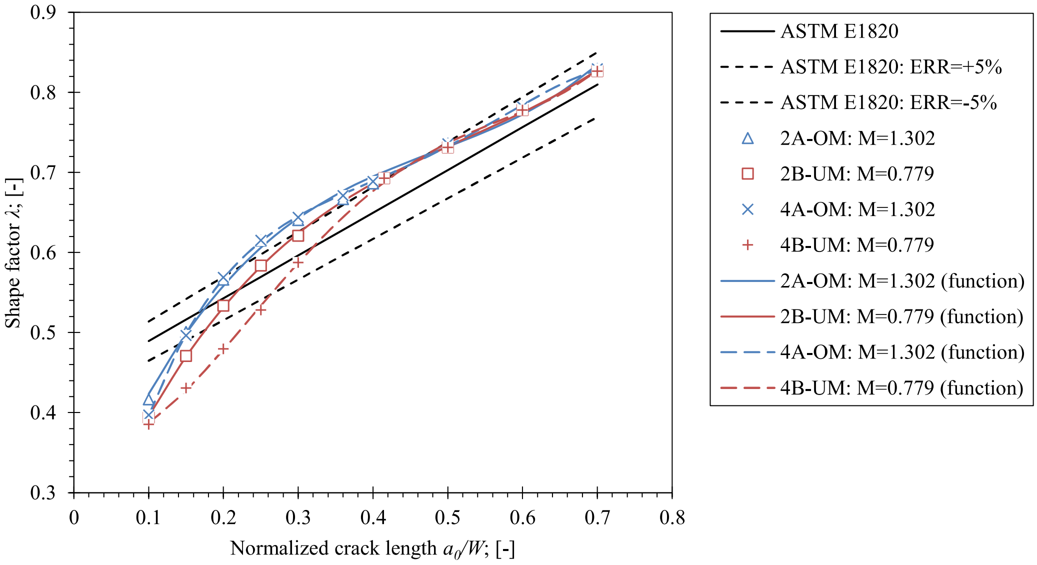

Figure 4.37 The comparison of the calibrated λ factors for the welded OM and UM SE(B) specimens with the HAZ and standard solution according to ASTM E1820. The results for the OM (FEM series 2A-OM) and the UM (FEM series 2B-UM) welds with no HAZ are plotted as a reference.

Table 4.17 The proposed λ functions for the welded OM and UM SE(B) specimens with the HAZ.

FEM series	λ functions in range $0.1\leq a_0/W\leq 0.7$	R^2 [-]
4A-OM	$\lambda = -10.245\left(\frac{a}{W}\right)^4 + 19.949\left(\frac{a}{W}\right)^3 - 14.029\left(\frac{a}{W}\right)^2 + 4.670\left(\frac{a}{W}\right) + 0.051$	1.000
4B-UM	$\lambda = 9.135\left(\frac{a}{W}\right)^4 - 14.811\left(\frac{a}{W}\right)^3 + 7.403\left(\frac{a}{W}\right)^2 - 0.401\left(\frac{a}{W}\right) + 0.367$	1.000

Finally, the crack growth correction factors γ_{pl} were developed according to the procedure, described in Chapter 4.1.2. The computed results are presented in Figure 4.38, while the corresponding calibrated γ_{pl} functions are listed in Table 4.18. Figure 4.38 shows diverse results, where the OM welds seem to be in closest agreement. In general, the presented $\gamma(a/W)$ functions indicate that plastic component of J_{pl} for the OM welds has to be increased for short cracks $a_0/W\leq 0.3$, hence the negative γ_{pl} values. For deeper cracks with $a_0/W>0.3$, the OM welds require only moderate correction of J_{pl}. Similar observations can be made for the UM welds as well. However, here it seems that $\gamma_{pl}(a/W)$ function for the UM weld with the HAZ diverges for short cracks with $a_0/W\leq 0.25$. This is attributed to the mathematical formulation of γ_{pl} with Equation (4.6) that involves derivatives of highly curved η_{pl} and λ functions.

To sum up, the results in form of η_{pl}, λ and γ_{pl} functions, presented in this chapter, indicate that the HAZ has significant effect on shallow cracks with length less than the distance to the weld root i.e., $a_0/W\leq L_W/W=0.36$ and $a_0/W\leq L_W/W=0.415$ for the OM and the UM welds, respectively. Therefore, the HAZ will be considered in the all subsequent FEM.

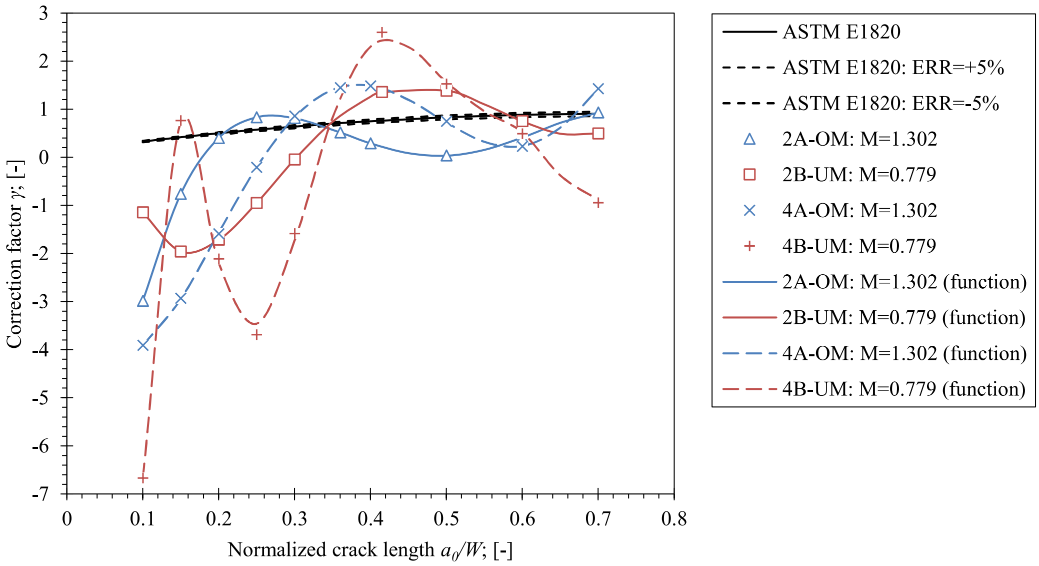

Figure 4.38 The comparison of the calibrated γ_{pl} factors for the welded OM and UM SE(B) specimens with the HAZ and standard solution according to ASM E1820. Results for the OM (FEM series 2A-OM) and the UM (FEM series 2B-UM) welds with no HAZ are plotted as a reference.

Table 4.18 The proposed η_{pl} functions for the welded OM and UM SE(B) specimens with the HAZ, valid for the *J*-integral, extracted from 0.5 mm contour.

FEM series	γ_{pl} functions for 0.5 mm contour in range $0.1 \leq a_0/W \leq 0.7$	R^2 [-]
4A-OM	$\gamma_{pl} = -950.940\left(\frac{a}{W}\right)^7 + 1328.569\left(\frac{a}{W}\right)^6 - 867.867\left(\frac{a}{W}\right)^5 + 1319.388\left(\frac{a}{W}\right)^4 - 1356.790\left(\frac{a}{W}\right)^3 + 533.901\left(\frac{a}{W}\right)^2 - 59.507\left(\frac{a}{W}\right) - 2.070$	1.000
4B-UM	$\gamma_{pl} = 225611.290\left(\frac{a}{W}\right)^7 - 695680.200\left(\frac{a}{W}\right)^6 + 884749.038\left(\frac{a}{W}\right)^5 - 596700.983\left(\frac{a}{W}\right)^4 + 227990.721\left(\frac{a}{W}\right)^3 - 48687.034\left(\frac{a}{W}\right)^2 + 5308.992\left(\frac{a}{W}\right) - 227.197$	1.000

4.8 Influence of Fusion Line Position on Fracture Behaviour of the Single Mismatched Welds

The results for the OM and the UM welds with the modelled HAZ that are presented in Chapter 4.7 are valid for the SE(B) specimens with weld root positions L_W/W=0.36 and L_W/W=0.415 for the OM and the UM welds, respectively. These dimensions were incorporated in the FEM in order to obtain calibrated η_{pl}, λ and γ_{pl} factors that are compatible with actually tested SE(B) specimens with the OM and the UM welds, designated as SEB-38 and SE(B)-40 in Table 3.10, respectively.

However, additional FEM were modelled and computed in order to investigate if solutions of η_{pl}, λ and γ_{pl} factors are dependent of the weld root position L_W. Therefore, two additional FEM series were produced in order to further investigate the OM welds. These were 5A-OM with L_W/W=0.390 and 5B-OM with L_W/W=0.652, that resembled tested fracture specimens with designations SE(B)-37 and SE(B)-39, respectively. Moreover, two additional FEM series were produced in order to further investigate the UM welds as well. These were 5C-UM with L_W/W=0.440 and 5D-UM with L_W/W=0.469 that resembled tested fracture specimens with designations SE(B)-41 and SE(B)-42, respectively. The computed FEM series are listed in the simulation matrix, available in Table 4.2, while the aforementioned tested specimens are listed in Table 3.10. Furthermore, the HAZ was considered in all of the computed FEM, while other features of the FEM were the same as described in Chapter 4.7. The calibrated values of η_{pl} were computed using the slope method [89], as described in Chapter 4.2.1. The J-integral $J_{0.5}$, extracted from the 0.5 mm contour, was used for calibration of the η_{pl} factors.

The computed η_{pl} solutions are presented in Figure 3.39, while the corresponding calibrated functions are listed in Table 4.19. The shapes of the computed $\eta_{pl}(a/W)$ functions seem to be similar within each group of the computed OM and UM SE(B) samples with the HAZ. Closer inspection of the computational results revealed that all the computed OM SE(B) specimens showed similar deformation behaviour as the reference FEM series 4A-OM. Furthermore, the computed UM SE(B) specimens showed similar deformation behaviour as reference FEM series 4B-UM. The principle of how plastic zone and the corresponding stress triaxiality h are being developed in the OM and the UM welds with the HAZ was presented detailly in Chapter 4.7, and will not be discussed here. What is important to note, is that peak values of η_{pl} are being shifted along the a_0/W axis with respect to the distance to the weld root L_W/W. Greater distance to the weld root L_W/W causes η_{pl} values to shift towards higher a_0/W, as demonstrated in Figure 4.39. On the contrary, shorted distance to the weld root L_W/W causes peak values of η_{pl} to shift towards lower a_0/W. Therefore, the FEM series 5A-OM with L_W/W=0.390 and 5B-OM with L_W/W=0.652 have peaks at a_0/W=0.3 and a_0/W=0.5, respectively. Additionally, both FEM series 5C-UM with L_W/W=0.440 and 5D-UM with L_W/W=0.469 have peaks at a_0/W=0.4, as the difference in distance to the weld root L_W/W between both FEM configurations is relatively small.

Next, the geometry factors λ were determined according to the procedure, described in Chapter 4.2.2. The computed results are presented in Figure 4.40, while the corresponding calibrated λ functions are listed in Table 4.20. The results in Figure 4.40 indicate that $\lambda(a/W)$ functions are in close agreement within the computed groups of the OM and the UM welds. This potentially means that the shape of $\lambda(a/W)$ is predominantly dependent on the level of yield strength mismatch between the weld material and the HAZ, while adjusting the distance to the weld root L_W/W for the same geometry of the weld causes only minimal variations.

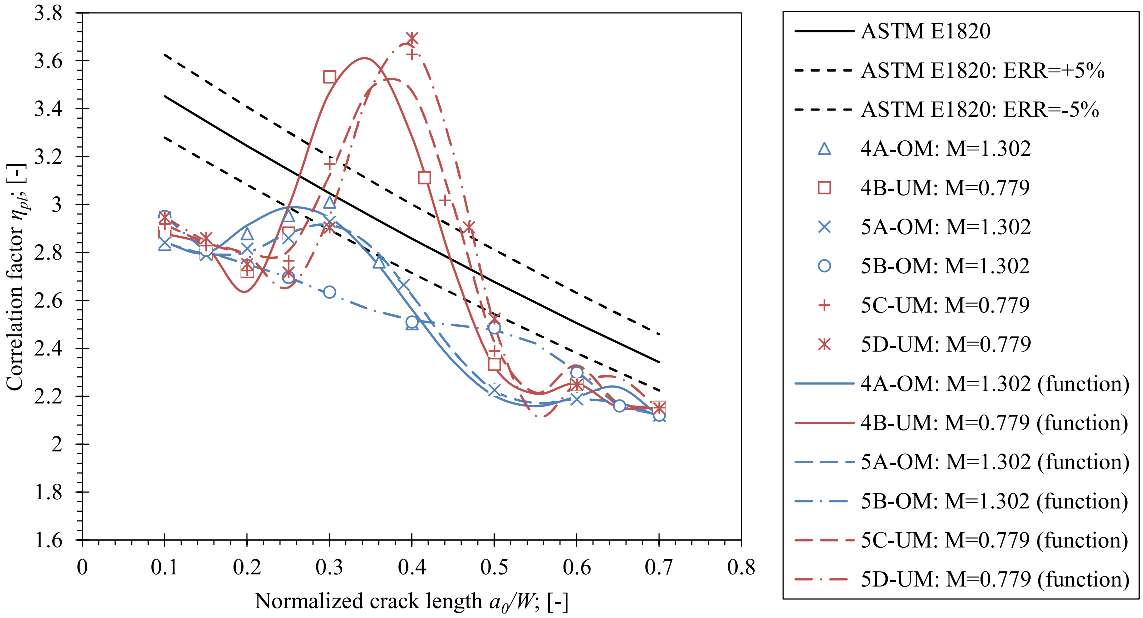

Figure 4.39 The comparison of the calibrated η_{pl} factors for the welded OM and UM SE(B) specimens with the HAZ and different weld root positions L_W/W. Standard solution according to ASTM E1820 [60] is plotted as a reference.

Table 4.19 The proposed η_{pl} functions for the welded OM and UM SE(B) specimens with the HAZ and different weld root positions L_W/W. Functions, listed in the table, are valid for the J-integral, extracted form 0.5 mm contour.

FEM series	η_{pl} functions for 0.5 mm contour in range $0.1 \leq a_0/W \leq 0.7$	R^2 [-]
5A-OM	$\eta_{pl} = 9326.608\left(\frac{a}{W}\right)^7 - 26541.464\left(\frac{a}{W}\right)^6 + 30339.524\left(\frac{a}{W}\right)^5 - 17783.174\left(\frac{a}{W}\right)^4 + 5671.773\left(\frac{a}{W}\right)^3 - 971.287\left(\frac{a}{W}\right)^2 + 82.192\left(\frac{a}{W}\right) + 0.163$	0.999
5B-OM	$\eta_{pl} = 1301.539\left(\frac{a}{W}\right)^6 - 3035.747\left(\frac{a}{W}\right)^5 + 2777.363\left(\frac{a}{W}\right)^4 - 1269.313\left(\frac{a}{W}\right)^3 + 304.998\left(\frac{a}{W}\right)^2 - 37.709\left(\frac{a}{W}\right) + 4.692$	1.000
5C-UM	$\eta_{pl} = 261853.203\left(\frac{a}{W}\right)^8 - 815506.912\left(\frac{a}{W}\right)^7 + 1057087.435\left(\frac{a}{W}\right)^6 - 739511.343\left(\frac{a}{W}\right)^5 + 303191.732\left(\frac{a}{W}\right)^4 - 74187.621\left(\frac{a}{W}\right)^3 + 10560.220\left(\frac{a}{W}\right)^2 - 800.594\left(\frac{a}{W}\right) + 27.659$	0.976
5D-UM	$\eta_{pl} = 325252.100\left(\frac{a}{W}\right)^8 - 1039776.000\left(\frac{a}{W}\right)^7 + 1385672.000\left(\frac{a}{W}\right)^6 - 998189.000\left(\frac{a}{W}\right)^5 + 421925.800\left(\frac{a}{W}\right)^4 - 106457.000\left(\frac{a}{W}\right)^3 + 15597.500\left(\frac{a}{W}\right)^2 - 1212.580\left(\frac{a}{W}\right) + 41.192$	0.993

Finally, the crack growth correction factors γ_{pl} were developed according to the procedure, described in Chapter 4.2.2. The computed results are presented in Figure 4.40, while the corresponding calibrated functions are listed in Table 4.21. Figure 4.40 indicates that $\gamma_{pl}(a/W)$ functions are in close agreement with the computed group of the OM welds. Here, $\gamma_{pl}(a/W)$ functions indicate, that J_{pl} for shallow cracks with $a_0/W<0.3$ is underestimated by the first term in Equation (3.33). Therefore, J_{pl} should be increased by incorporating the negative values of γ_{pl} in Equation (3.33). Moreover, only minor correction of the J_{pl} due to the crack growth is needed for the OM welds with deeper cracks $a_0/W \geq 0.3$. On the contrary to the OM welds, the UM welds show large scatter of the calibrated γ_{pl} factors. This is attributed to the mathematical formulation of γ_{pl} with Equation (4.6) that involves derivatives of highly curved η_{pl} and λ functions. For that reason, $\gamma_{pl}(a/W)$ functions for the UM welds are difficult to interpret.

Although, it seems that in general, J_{pl} should be increased with negative γ_{pl} values for shallow cracks with a_0/W<0.4 and decreased with positive γ_{pl} values for deeper cracks with a_0/W≥0.4.

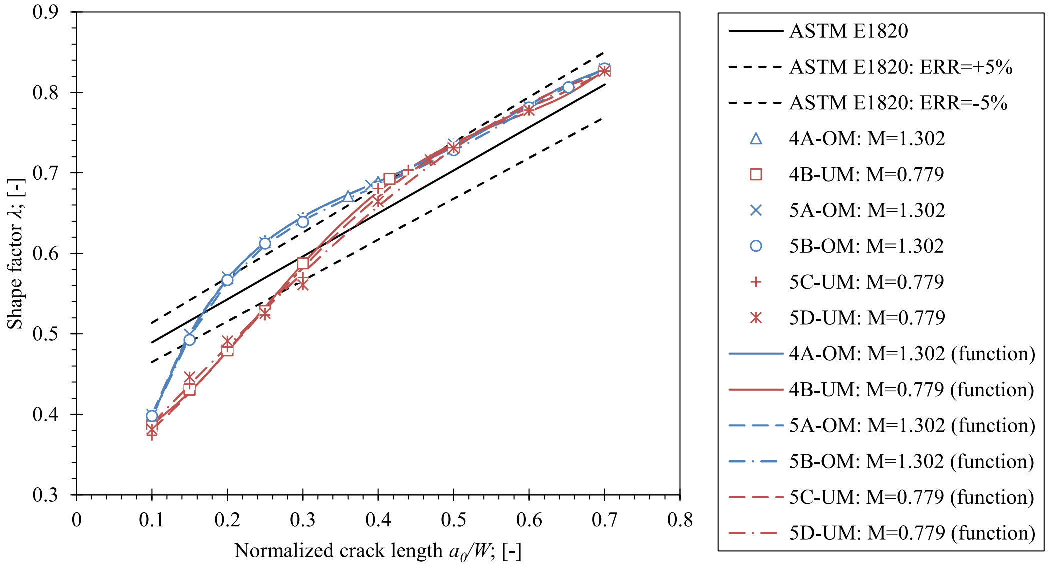

Figure 4.40 The comparison of the calibrated λ factors for the welded OM and UM SE(B) specimens with the HAZ and different weld root positions L_W/W. Standard solution according to ASTM E1820 is plotted as a reference.

Table 4.20 The proposed λ functions for the welded OM and UM SE(B) specimens with the HAZ and different weld root positions L_W/W.

FEM series	λ functions in range $0.1 \leq a_0/W \leq 0.7$	R^2 [-]
5A-OM	$\lambda = -10.201\left(\frac{a}{W}\right)^4 + 19.793\left(\frac{a}{W}\right)^3 - 13.870\left(\frac{a}{W}\right)^2 + 4.610\left(\frac{a}{W}\right) + 0.059$	1.000
5B-OM	$\lambda = -10.046\left(\frac{a}{W}\right)^4 + 19.686\left(\frac{a}{W}\right)^3 - 13.865\left(\frac{a}{W}\right)^2 + 4.611\left(\frac{a}{W}\right) + 0.056$	0.996
5C-UM	$\lambda = 5.247\left(\frac{a}{W}\right)^4 - 8.700\left(\frac{a}{W}\right)^3 + 4.180\left(\frac{a}{W}\right)^2 + 0.257\left(\frac{a}{W}\right) + 0.321$	0.997
5D-UM	$\lambda = 0.011\left(\frac{a}{W}\right)^4 - 0.576\left(\frac{a}{W}\right)^3 + 0.098\left(\frac{a}{W}\right)^2 + 0.972\left(\frac{a}{W}\right) + 0.291$	0.997

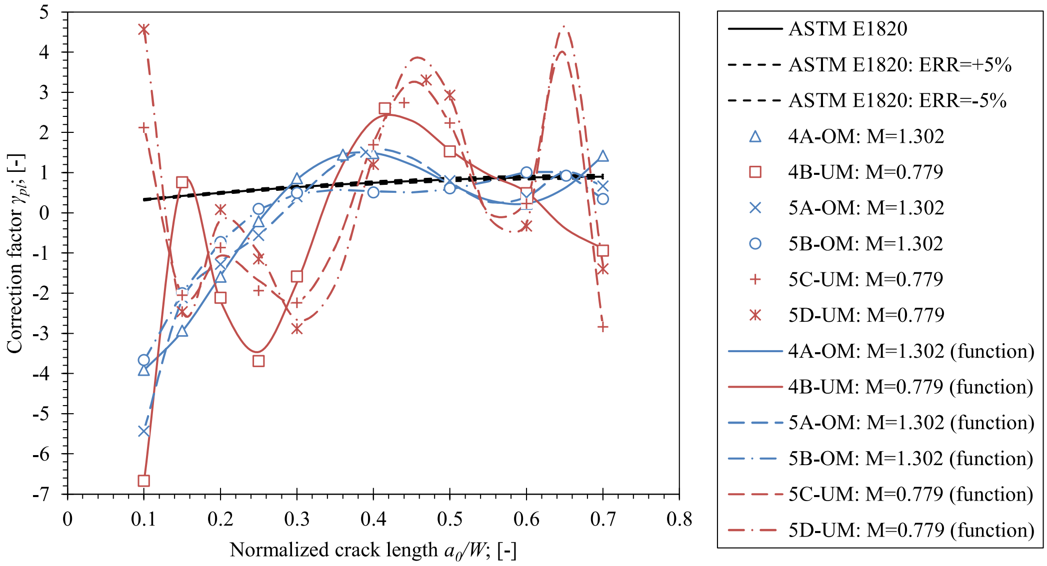

Figure 4.41 The comparison of the calibrated γ_{pl} factors for the welded OM and UM SE(B) specimens with the HAZ and different weld root positions L_W/W. Standard solution according to ASTM E1820 [60] is plotted as a reference.

Table 4.21 The proposed η_{pl} functions for the welded OM and UM SE(B) specimens with the HAZ and different weld root positions L_W/W. The functions, listed in the table, are valid for the J-integral, extracted from 0.5 mm contour.

FEM series	γ_{pl} functions for 0.5 mm contour in range 01≤a_0/W≤0.7	R^2 [-]
5A-OM	$\gamma_{pl} = -20599.622\left(\frac{a}{W}\right)^6 + 50145.762\left(\frac{a}{W}\right)^5 - 48055.216\left(\frac{a}{W}\right)^4 + 23052.207\left(\frac{a}{W}\right)^3 - 5841.527\left(\frac{a}{W}\right)^2 + 759.026\left(\frac{a}{W}\right) - 41.628$	1.000
5B-OM	$\gamma_{pl} = -982.223\left(\frac{a}{W}\right)^5 + 1667.428\left(\frac{a}{W}\right)^4 - 920.958\left(\frac{a}{W}\right)^3 + 135.272\left(\frac{a}{W}\right)^2 + 31.587\left(\frac{a}{W}\right) - 7.428$	1.000
5C-UM	$\gamma_{pl} = -519324.977\left(\frac{a}{W}\right)^7 + 1410582.681\left(\frac{a}{W}\right)^6 - 1562901.108\left(\frac{a}{W}\right)^5 + 909950.015\left(\frac{a}{W}\right)^4 - 298920.928\left(\frac{a}{W}\right)^3 + 55187.821\left(\frac{a}{W}\right)^2 - 5291.124\left(\frac{a}{W}\right) + 201.593$	0.995
5D-UM	$\gamma_{pl} = -751762.000\left(\frac{a}{W}\right)^7 + 2078746.000\left(\frac{a}{W}\right)^6 - 2348573.000\left(\frac{a}{W}\right)^5 + 1396375\left(\frac{a}{W}\right)^4 - 468780.000\left(\frac{a}{W}\right)^3 + 88352.570\left(\frac{a}{W}\right)^2 - 8618.220\left(\frac{a}{W}\right) + 333.523$	0.994

4.9 Fracture Behaviour of the Double Mismatched Welds

The fracture behaviour of double mismatched welds with surface crack has been studied in scope of researches conducted by Predan et al. [13] and Starčevič et al. [71]. Focus of the listed studies was to determine the crack driving force only for specific cases of double mismatched welds and show concepts of how such welds deform under monotonous loading. Current PhD thesis is an attempt to implement the findings of the listed researches into the existing fracture testing procedure [6]. This is done through calibration of η_{pl}, λ and γ_{pl} factors in the existing analytical framework for evaluation of the crack driving force from P-CMOD records of tested fracture specimens. For that reason, two FEM series 6A-OM-UM and 6B-UM-OM were produced and computed. Double mismatched welds in FEM were configured to resemble a crack traversing from OM to UM part of the weld for 6A-OM-UM series and from UM to OM part of the weld for 6B-UM-OM series. These two types of welds are denoted as OM-UM and UM-OM, respectively.

It is important to note that stationary cracks were incorporated in FEM with lengths a_0/W in range, provided in the analysis matrix in Table 4.2. In general, welds were simplified, as described in Chapter 4.3.1. The corresponding geometry of the modelled welds is presented in Table 4.1. The curved fusion lines were modelled at the OM-UM and the UM-OM interfaces, as it was assumed that it might affect the strain patterns near the weld root. Additionally, it is important to note, that the position of the weld is here addressed in terms of normalized distance to the fusion line L_f/W, as demonstrated in Figure 4.7. This is on the contrary to the single material welds, where the position of the weld in the SE(B) specimen was determined with the normalized distance to the weld root L_W/W. However, the fusion line represents the boundary between the OM and the UM part of the weld that has a significant impact on the crack driving force for the traversing crack [13]. The curved fusion lines were modelled at normalized distances L_f/W=0.5 for the FEM series 6A-OM-UM and L_f/W=0.435 for the FEM series 6B-UM-OM. This closely resembles the actual tested specimens with designations SE(B)-26 and SE(B)-10, respectively, as listed in Table 3.10. The method of the fracture testing is presented in Chapter 3.5.3, while the corresponding results are presented in Chapter 3.5.5. Yield strength mismatching of the OM and the UM parts of the weld was M=1.302 and M=0.779, respectively. The HAZ has been incorporated in the FEM as well, with the average mechanical properties, listed in Table 4.4. The remaining features of the FEM were the same as described in Chapter 4.7. The configurations of FEM in series 6A-OM-UM and 6B-UM-OM are presented in Figure

4.42. The calibrated η_{pl} values were computed by using the slope method [89], as described in Chapter 4.2.1. The *J*-integral $J_{0.5}$, extracted from 0.5 mm contour, was used for calibration of the η_{pl} factor. The obtained results are presented in Figure 4.43, while the corresponding calibrated functions $\eta_{pl}(a/W)$ are listed in Table 4.22.

According to Figure 4.43, the double mismatched welds show significantly different behavior than the single material welds. To begin with, the OM-UM welds show increased values of η_{pl} for the shallow cracks with $a_0/W \leq 0.3$. The corresponding fields of equivalent plastic strain, shown in Figure 4.44 a), Figure 4.44 b) and Figure 4.44 c), indicate that large scale plastic deformation initially occurs in the UM part of the weld that undergoes complete yielding at limit load onset. At this point, parts of the OM weld material, the HAZ and the base material exhibit plastic deformation as well. However, the analysed SE(B) specimens with the OM-UM welds and $a_0/W \leq 0.2$ exhibit yielding of net-cross section at significantly higher loads than simulated, due to the interference of the HAZ with the plastic zone. For that reason, Figure 4.44 a) and Figure 4.44 b) show equivalent plastic strain fields from the final analysis increment. Similarly, Figure 4.45 a) and Figure 4.45 b) show Von Mises stress fields from the final analysis increment. Moreover, the inspection of stress triaxiality *h* in Figure 4.48 a), Figure 4.48 b) and Figure 4.48 c) indicate that constraint of the material at the crack tip is lower than in the UM-OM and single material welds. This is correlated to the plastic zone being developed mostly in the UM part of the weld, ahead of the crack tip. Additionally, the corresponding Von Mises stress fields, shown in Figure 4.45 a), Figure 4.45 b) and Figure 4.45 c), indicate that stress is concentrated primarily in the OM part of the weld. This indicated that the OM part off the weld provides load bearing capacity after the yielding of material in the UM part of the weld has begun.

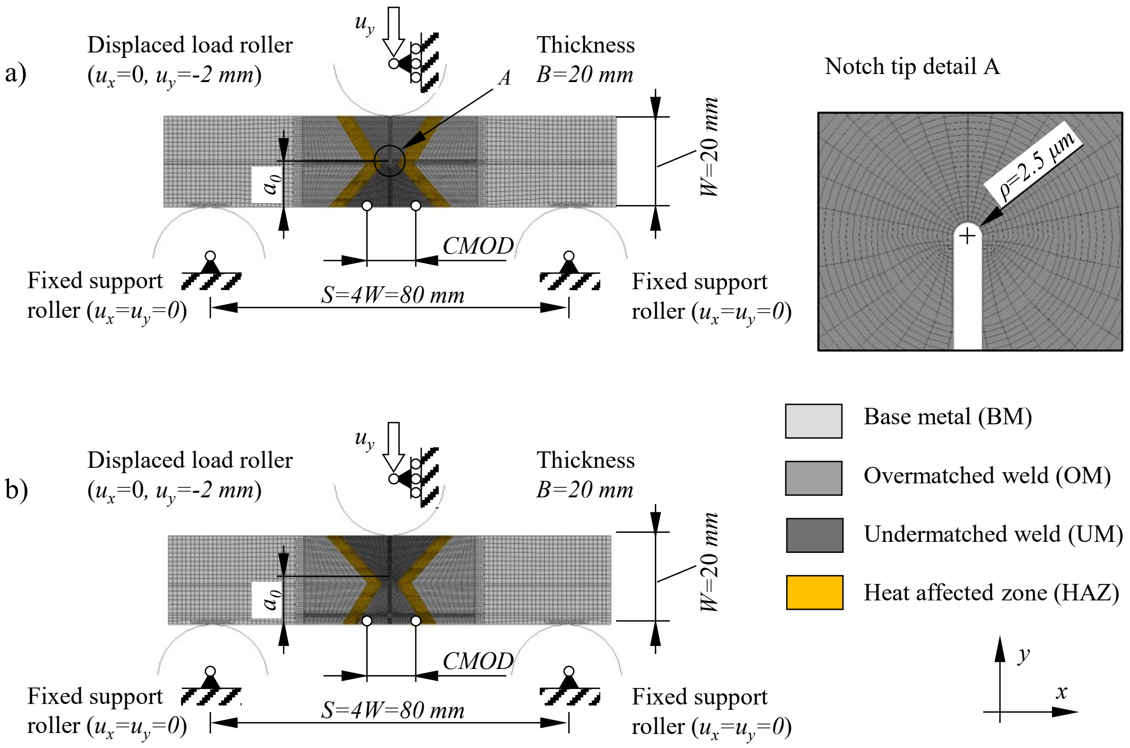

Figure 4.42 The configuration of the FEM for analysis of the double mismatched OM-UM and UM-OM welds with the HAZ.

As the crack tip approaches the OM-UM interface, the η_{pl} seems to increase almost exponentially. Considering that η_{pl} is directly correlated with the plastic component of the J-integral J_{pl}, i.e. the crack driving force, then the aforementioned increase of the η_{pl} is in line with the results, reported by Predan et al. [13]. The maximum value of η_{pl} factor is observed at a_0/W=0.4, where crack tip is located in the OM weld material, in front of the OM-UM interface. the corresponding strain patterns in Figure 4.44 d) indicate, that plastic deformation of the OM weld material is confined between the layers of HAZ, resulting in increased hydrostatic pressure in front of the crack tip due to the concentrated stress, as demonstrated in Figure 4.45 d). Consequentially, stress triaxiality h is further increased, as demonstrated in Figure 4.48 d).

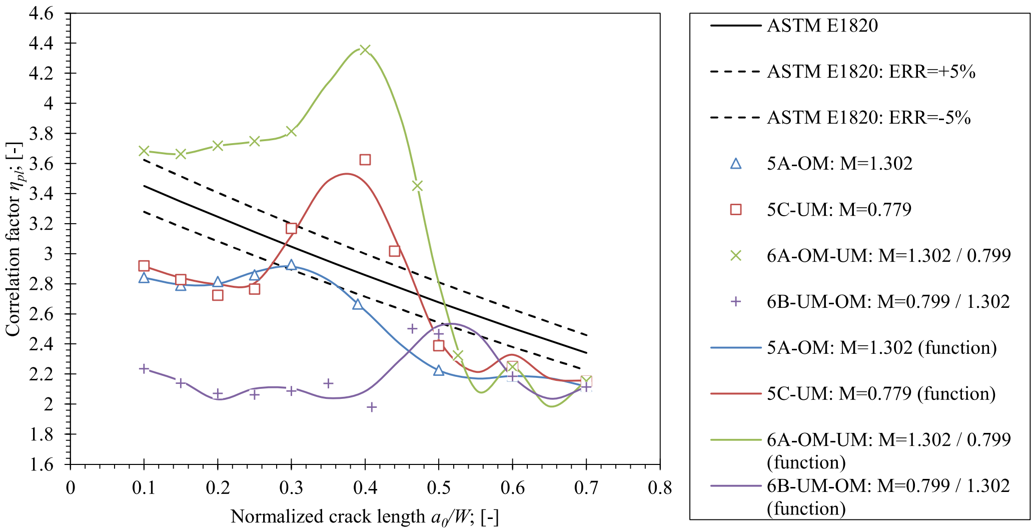

Figure 4.43 The comparison of the calibrated η_{pl} factors for the welded double mismatched OM-UM and UM-OM SE(B) specimens with the HAZ and standard solution according to ASTM E1820. Results for the single material OM (FEM series 5A-OM) and UM (5B-UM) welds are plotted as a reference.

Table 4.22 The proposed η_{pl} functions for the SE(B) specimens with the double mismatched welds and the HAZ. The functions, listed in the table, are valid for the *J*-integral, extracted form 0.5 mm contour.

FEM series	η_{pl} functions for 0.5 mm contour in range $0.1 \leq a_0/W \leq 0.7$	R^2 [-]
6A-OM-UM	$\eta_{pl} = 2118882.170\left(\frac{a}{W}\right)^9 - 7205366.759\left(\frac{a}{W}\right)^8 + 10434782.104\left(\frac{a}{W}\right)^7 - 8412335.471\left(\frac{a}{W}\right)^6 + 4145128.116\left(\frac{a}{W}\right)^5 - 1290762.224\left(\frac{a}{W}\right)^4 + 253445.775\left(\frac{a}{W}\right)^3 - 30204.692\left(\frac{a}{W}\right)^2 + 1979.547\left(\frac{a}{W}\right) - 50.607$	1.000
6B-UM-OM	$\eta_{pl} = -160078.400\left(\frac{a}{W}\right)^8 + 512111.553\left(\frac{a}{W}\right)^7 - 684994.442\left(\frac{a}{W}\right)^6 + 497600.394\left(\frac{a}{W}\right)^5 - 213475.202\left(\frac{a}{W}\right)^4 + 55050.014\left(\frac{a}{W}\right)^3 - 8275.992\left(\frac{a}{W}\right)^2 + 657.445\left(\frac{a}{W}\right) - 18.794$	0.817

Values of η_{pl} suddenly decrease if the crack tip is located at vicinity of the OM-UM interface. In this case, bands of plastic deformation, originating from the crack tip, are no longer restricted by the HAZ, as demonstrated in Figure 4.44 e). Additionally, stress is highly concentrated in the remaining OM weld material in front of the crack tip, as demonstrated in Figure 4.45 e). This indicates that the remaining quantity of the OM weld material has a lower resistance to relatively large deformations of the UM weld material. As a result, stress triaxiality is reduced, as demonstrated in Figure 4.48 e). This is a departure from the previously reported results by Predan et al. [13] that is here attributed to a strain field that is heavily influenced by the geometry of the weld and nearby layers of the HAZ. Once the crack crosses the OM-UM interface, η_{pl} values decrease even further and are in good agreement with the one of the single material UM weld. Plastic deformation is no longer obstructed by the HAZ or the OM-UM interface, as demonstrated in Figure 4.44 f) and Figure 4.44 g). At the same time, stress triaxiality h is in close agreement with the single material UM weld, as demonstrated in Figure 4.48 f) and Figure 4.48 g).

Moreover, the simulated SE(B) specimens with the UM-OM welds showed significantly lower values of η_{pl} in comparison to the single material welds for cracks with $a_0/W<0.4$. The inspection of the corresponding equivalent plastic strain fields, shown in Figure 4.46 a), Figure 4.46 b) and Figure 4.46 c), indicates that large scale plastic deformation initially occurs in the UM part of the weld, similar to the OM-UM welds. However, the UM weld material is located in front of the UM-OM interface and surrounds the crack in this case. Additionally, load bearing capacity of the UM-OM welds is provided by the OM weld material with higher yield strength (σ_{YS}=889.0 MPa) than the base (σ_{YS}=682.8 MPa) and the UM weld (σ_{YS}=532.1 MPa) materials. This is indicated by von Mises stress fields, shown in Figure 4.47 a), Figure 4.47 b) and Figure 4.47 c), where elevated stress in the OM part of the weld is observed after severe yielding of the UM part of the weld. Additionally, spreading of the plastic zone from the UM weld material into the base material is restricted by the overmatched HAZ. As a result, full net cross section yielding occurs at higher loads, that exceed the simulated loads. For that reason, equivalent plastic strain fields, shown Figure 4.46 a) and Figure 4.46 b), and von Mises stress fields, shown in Figure 4.45 a) and Figure 4.45 b), were obtained from the last simulation increment, where the maximum load was computed. Furthermore, the UM-OM welds for $a_0/W<0.4$ show the highest recorded triaxiality h of the all simulated weld configurations. As the crack tip approaches the UM-OM interface, the η_{pl} seems to slightly increase as the plastic zone becomes restricted to the progressively narrower UM part of the weld due to the nearby HAZ. However, η_{pl} suddenly decreases as the crack tip is located in UM weld material, 0.5 mm apart the UM-OM interface, which corresponds to the crack length a_0/W=0.409. This is in line with the results, published by Predan et al. [120]. The plastic zone is here predominantly localized at the vicinity of the crack tip in the UM weld material and then spreads around the OM weld material along the interface with the HAZ, as shown in Figure 4.46 d). Figure 4.47 d) shows, that stresses near the crack tip are lower than the stresses around the shorter cracks with $a_0/W<0.4$. The corresponding stress triaxiality is the highest of the all simulated weld configurations with crack length approx. $a_0/W=0.4$. It is important to note, that sudden loss of triaxiality for the UM-OM weld in Figure 4.47 d) occurs, as the location of extraction of h that is proportional to J, and is defined by Equation (4.13), crosses the UM-OM interface. This part of the corresponding $h(J/\sigma_Y)$ curve should be considered as invalid, and is here plotted only for demonstrative purpose. Once the crack tip passes the UM-OM interface, fracture behaviour of th UM-OM weld becomes similar to the single material OM weld. Therefore, η_{pl} and crack tip constraint in terms of h are in good agreement with both types of welds with $a_0/W\geq0.5$, as demonstrated in Figure 4.43, Figure 4.48 f) and Figure 4.48 g), respectively. Figure 4.46f) and Figure 4.46 g) show normal development of plastic deformation in the OM weld material with no interference of the HAZ.

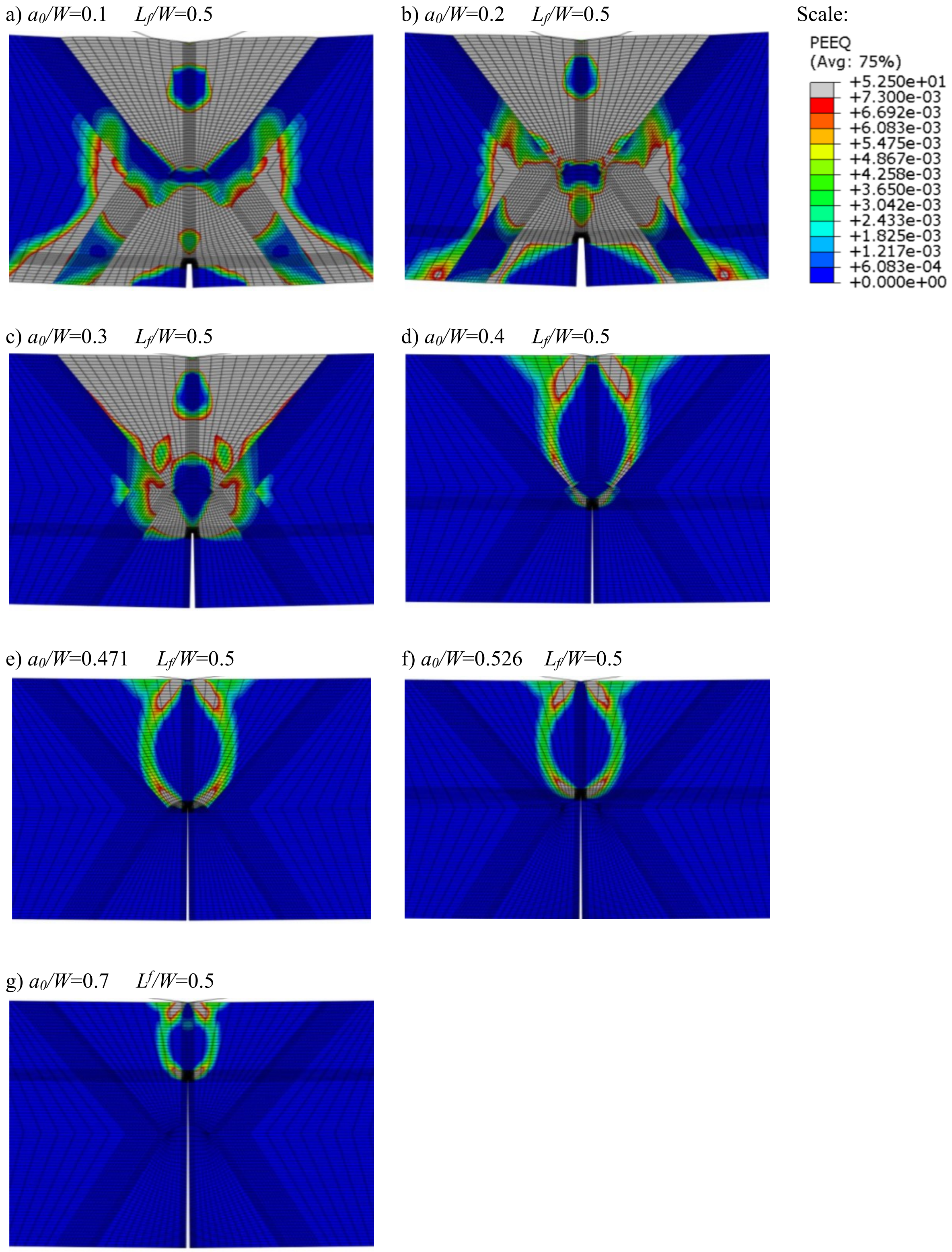

a) a_0/W=0.1 L_f/W=0.5

b) a_0/W=0.2 L_f/W=0.5

c) a_0/W=0.3 L_f/W=0.5

d) a_0/W=0.4 L_f/W=0.5

e) a_0/W=0.471 L_f/W=0.5

f) a_0/W=0.526 L_f/W=0.5

g) a_0/W=0.7 L^f/W=0.5

Figure 4.44 Plastic zone for the modelled SE(B) specimens with the double mismatched OM-UM weld and crack lengths a) a_0/W=0.1, b) a_0/W=0.2, c) a_0/W=0.3, d) a_0/W=0.4, e) a_0/W=0.471 f) a_0/W=0.526 and g) a_0/W=0.7. The equivalent plastic strain fields were obtained at yield limit load F/F_Y=0.1 from the results of the FEM series 6A-OM-UM. The exception are strain fields for a) and b) that were obtained from the last simulation increment.

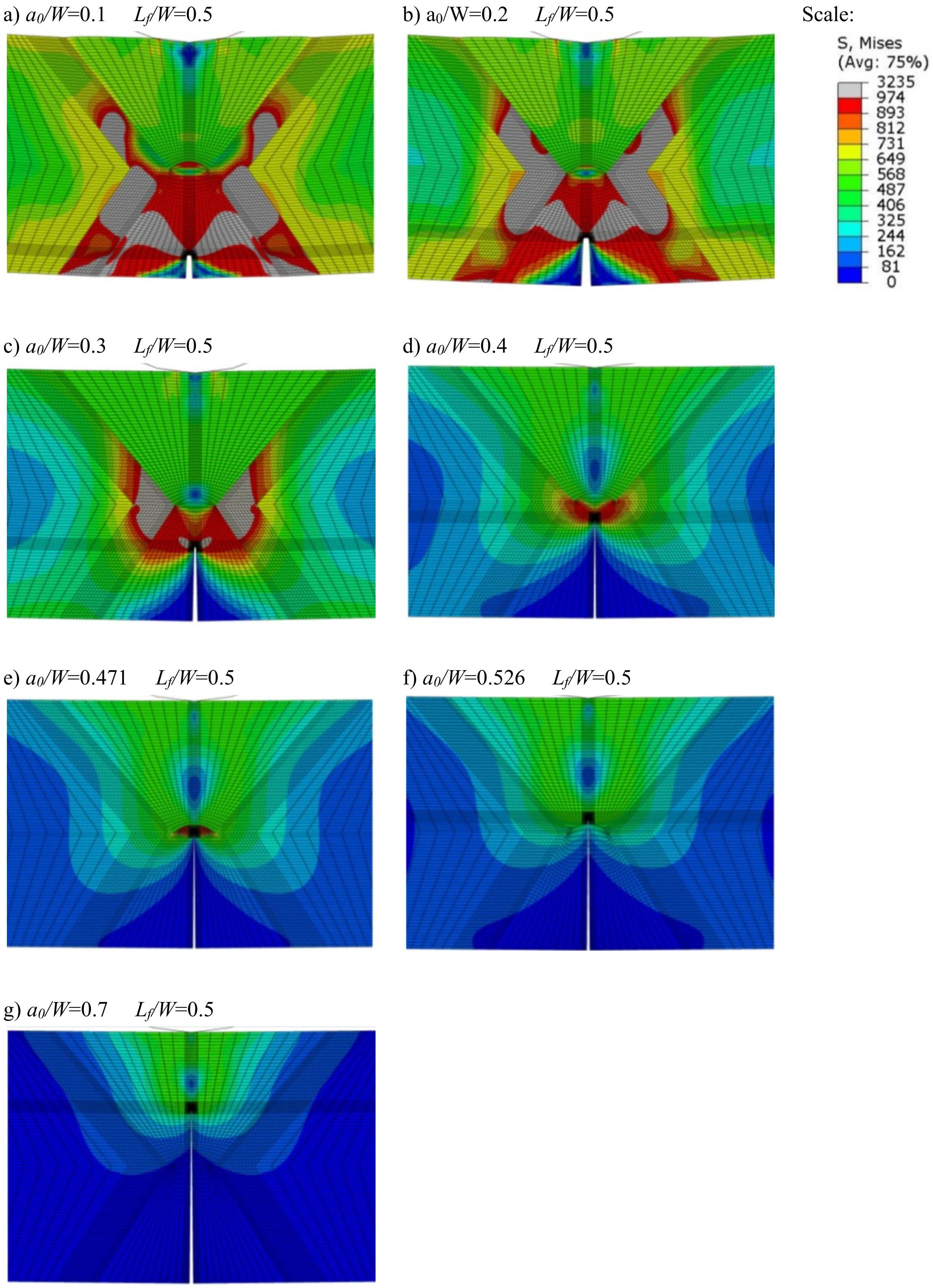
a) a_0/W=0.1 L_f/W=0.5

b) a_0/W=0.2 L_f/W=0.5

Scale:

c) a_0/W=0.3 L_f/W=0.5

d) a_0/W=0.4 L_f/W=0.5

e) a_0/W=0.471 L_f/W=0.5

f) a_0/W=0.526 L_f/W=0.5

g) a_0/W=0.7 L_f/W=0.5

Figure 4.45 Von Mises stress field for the modelled SE(B) specimens with the double mismatched OM-UM weld and crack lengths a) a_0/W=0.1, b) a_0/W=0.2, c) a_0/W=0.3, d) a_0/W=0.4, e) a_0/W=0.471, f) a_0/W=0.526 and g) a_0/W=0.7. Von Mises stress fields were obtained at limit load onset F/F_Y=1 from the results of the FEM series 6A-OM-UM. The exception are strain fields for a) and b) that were obtained from the last simulation increment.

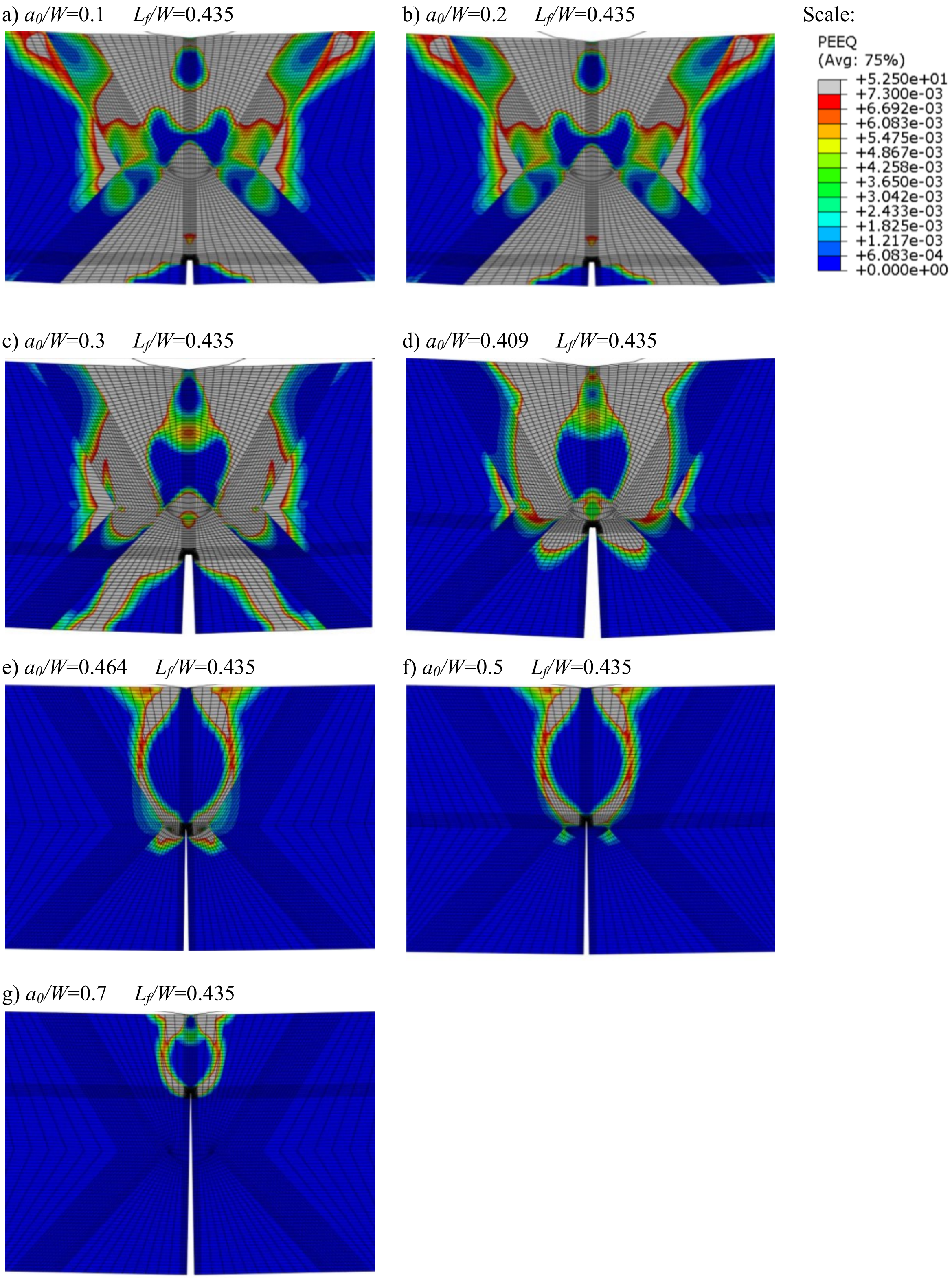
a) a_0/W=0.1 L_f/W=0.435

b) a_0/W=0.2 L_f/W=0.435

Scale:

c) a_0/W=0.3 L_f/W=0.435

d) a_0/W=0.409 L_f/W=0.435

e) a_0/W=0.464 L_f/W=0.435

f) a_0/W=0.5 L_f/W=0.435

g) a_0/W=0.7 L_f/W=0.435

Figure 4.46 Plastic zone for the modelled SE(B) specimens with the double mismatched UM-OM weld and crack lengths a) a_0/W=0.1, b) a_0/W =0.2, c) a_0/W=0.3, d) a_0/W=0.409, e) a_0/W=0.464, f) a_0/W=0.5 and g) a_0/W=0.7. The equivalent plastic strain fields were obtained at yield limit load F/F_Y=0.1 from the results of the FEM series 6B-UM-OM. The exception are stain fields for a) and b) that were obtained at the last recorded load in the simulation.

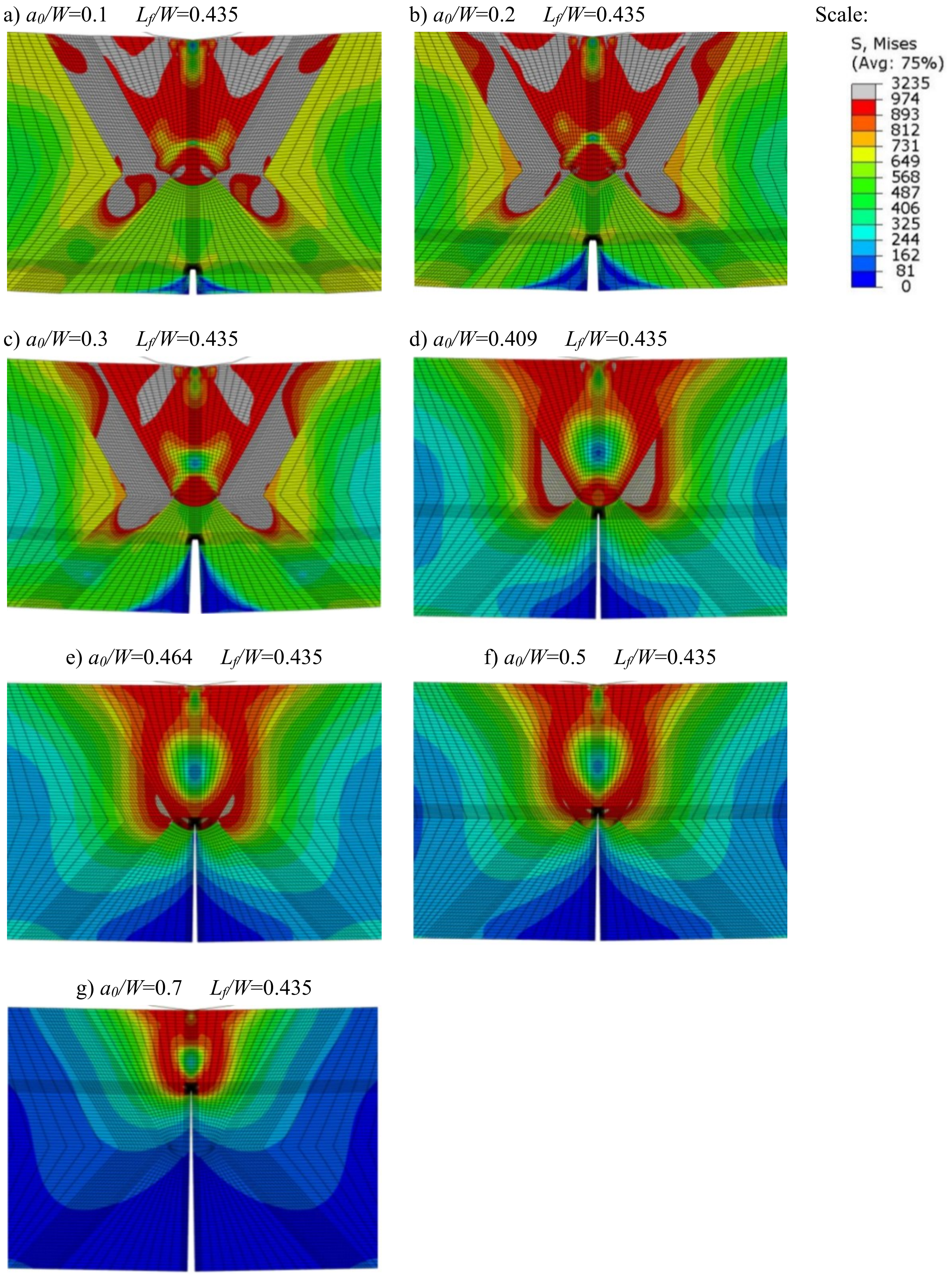

a) a_0/W=0.1 L_f/W=0.435

b) a_0/W=0.2 L_f/W=0.435

c) a_0/W=0.3 L_f/W=0.435

d) a_0/W=0.409 L_f/W=0.435

e) a_0/W=0.464 L_f/W=0.435

f) a_0/W=0.5 L_f/W=0.435

g) a_0/W=0.7 L_f/W=0.435

Figure 4.47 Von Mises stress field for the modelled SE(B) specimens with the double mismatched UM-OM weld and crack lengths a) a_0/W=0.1, b) a_0/W=0.2, c) a_0/W=0.3, d) a_0/W=0.409, e) a_0/W=0.464, f) a_0/W=0.5 and g) a_0/W=0.7. Von Mises stress fields were obtained at yield limit load F/F_Y=1 from the results of the FEM series 6B-UM-OM. The exceptions are stress fields for a) and b) that were obtained at the last recorded load in simulation.

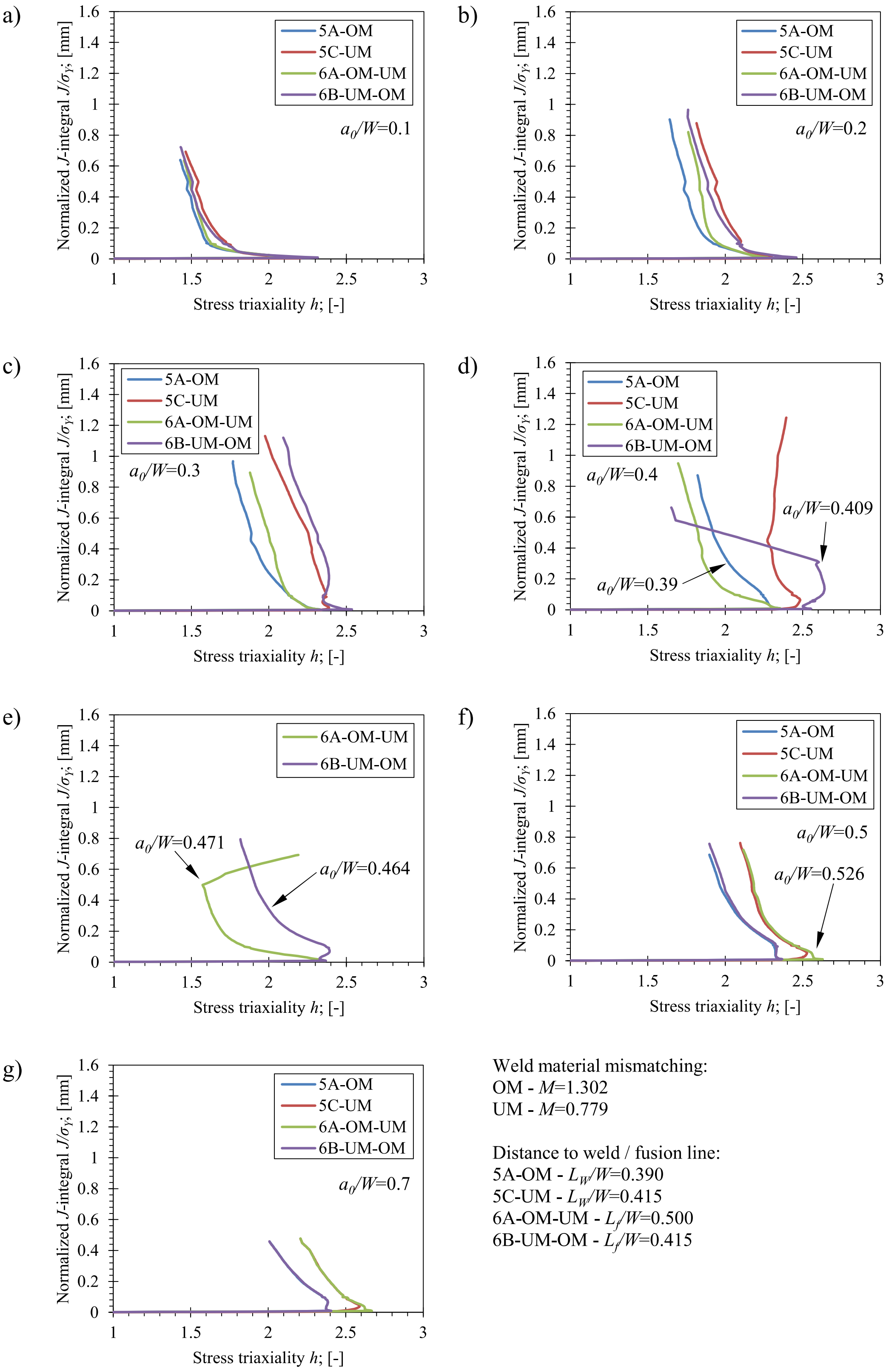

Weld material mismatching:
OM - M=1.302
UM - M=0.779

Distance to weld / fusion line:
5A-OM - L_W/W=0.390
5C-UM - L_W/W=0.415
6A-OM-UM - L_f/W=0.500
6B-UM-OM - L_f/W=0.415

Figure 4.48 Stress triaxiality h for the modelled SE(B) specimens with the double mismatched OM-UM and UM-OM welds with crack lengths a) a_0/W=0.1, b) a_0/W=0.2, c) a_0/W=0.3, d) a_0/W=0.4, e) a_0/W=0.47, f) a_0/W=0.5 and g) a_0/W=0.7. The corresponding distances to the fusion line are L_f/W=0.5 and L_f/W=0.435 for the OM-UM and the UM-OM welds respectively.

To sum up, the aforementioned observations clearly indicate that the OM weld material bears the highest stress once large-scale plasticity occurs in the analysed SE(B) specimens. This is due to higher yield strength (σ_{YS}=889.0 MPa) as compared to the base (σ_{YS}=682.8 MPa) and the UM weld (σ_{YS}=532.1 MPa) materials. However, in the case of the OM-UM welds, the OM weld material is highly stressed due to substantial plastic deformations of the surrounding material. This results in increased η_{pl}, although stress triaxiality is low due to relatively uniform Von Mises stress field in front of the crack tip. The opposite can be concluded for the UM-OM welds. Here, the OM weld material still provides most of the bearing capacity for the analysed SE(B) specimens. But, the UM weld material deforms less near the UM-OM interface. Again, this is a consequence of higher yield strength of the OM weld material. As result, η_{pl} reduces as the crack tip is located near the OM-UM interface. Stress triaxiality is relatively low due to fairly uniform strain field between the crack tip and the OM weld material. The presented conclusions are mostly in line with previously published results by Predan et al. [13].

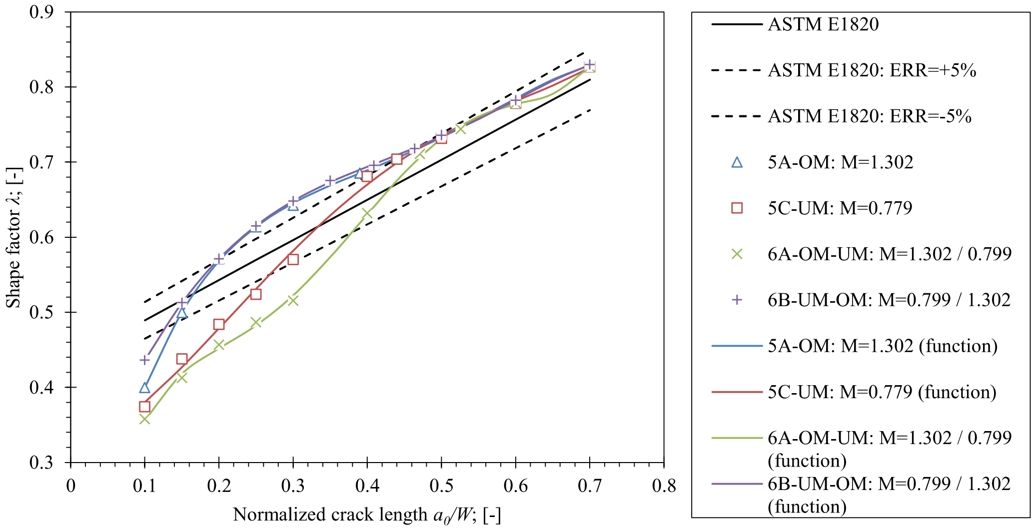

Figure 4.49 The comparison of the calibrated λ factors for SE(B) specimens with the OM-UM and the UM-OM welds. Standard solution according to ASTM E1820 [60] and the results for the OM (FEM series 5A-OM) and the UM (FEM series 5B-UM) welds are plotted as a reference.

Table 4.23 The proposed λ functions for SE(B) specimens with the double mismatched OM-UM and UM-OM weld. The HAZ is considered in the results as well.

FEM series	λ functions in range $0.1 \leq a_0/W \leq 0.7$	R^2 [-]
6A-OM-UM	$\lambda = 88.115\left(\frac{a}{W}\right)^5 - 176.758\left(\frac{a}{W}\right)^4 + 129.796\left(\frac{a}{W}\right)^3 - 42.847\left(\frac{a}{W}\right)^2 + 7.100\left(\frac{a}{W}\right) - 0.038$	0.999
6B-UM-OM	$\lambda = -9.607\left(\frac{a}{W}\right)^5 + 14.164\left(\frac{a}{W}\right)^4 - 3.505\left(\frac{a}{W}\right)^3 - 3.464\left(\frac{a}{W}\right)^2 + 2.450\left(\frac{a}{W}\right) + 0.228$	1.000

The geometry factors λ have been determined on the basis of LLD and CMOD according to the procedure, described in Chapter 4.2.2. The computed results are presented in Figure 4.49, while the corresponding calibrated functions are listed in Table 4.23. Figure 4.49 shows that $\lambda(a/W)$ functions for the double mismatched UM-OM and the single material OM welds are in close agreement. This suggests that the SE(B) specimens would have similar CMOD for the same given LLD in both cases. On the contrary, the OM-UM welds show deviation from the UM welds, for cracks with $0.15 \leq a_0/W < 0.5$. Here, the crack tip approaches the OM-UM interface and the quantity of the OM weld material in front of the crack tip reduces. However, according to Figure 4.49, it seems, that small quantity of the OM weld material between the crack tip and the OM-UM interface alters the compliance of the SE(B) specimen after large scale yielding starts. Therefore, the computed CMOD is lower for the OM-UM welds in comparison to the UM welds for the given LLD. Presented $\lambda(a/W)$ functions are again in good agreement, once the crack surpasses the OM-UM interface, i.e. has length $a_0/W \geq 0.5$. This further indicates that the material in front of the crack tip dictates how the fracture specimen, i.e. SE(B) specimen, is going to deform under load.

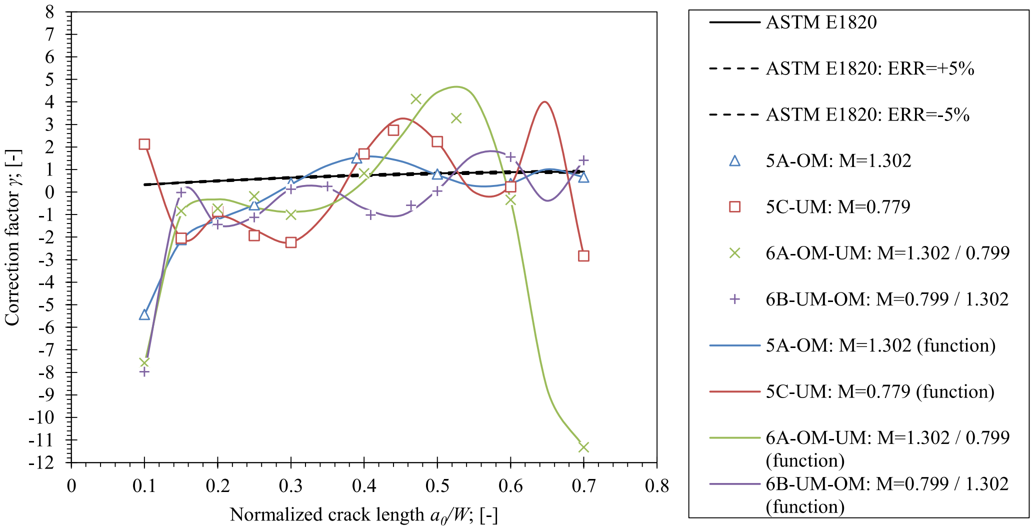

Figure 4.50 The comparison of the calibrated γ_{pl} factors for the welded double mismatched OM-UM and UM-OM SE(B) specimens with the HAZ and the standard solution according to ASTM E1820 [60]. Results for the single material OM (FEM series 6A-OM-UM) and UM (FEM series 6B-UM-OM) welds are plotted as a reference.

Finally, crack growth correction factors γ_{pl} were computed according to the procedure, described in Chapter 4.2.2. The computed results are presented in Figure 4.50. The corresponding calibrated functions are listed in Table 4.24. Figure 4.50 shows scattered results of the analysed SE(B) specimens containing the single material and the double mismatched welds. The scatter of the results is attributed to mathematical definition of the γ_{pl} factors, given by Equation (4.6), that is based on variable $\eta_{pl}(a/W)$ and $\lambda(a/W)$ functions and their corresponding derivatives. However, it seems that the first term in Equation (3.33) underestimates J_{pl} for shallow cracks with $a_0/W<0.4$. Therefore, J_{pl} must be increased due to crack growth during fracture test by the negative γ_{pl} values in the second term of Equation (3.33). The opposite can be observed for deeper cracks with $a_0/W>0.4$. Here, the first term of Equation (3.33) overestimates J_{pl} due to crack growth during fracture testing. Therefore, J_{pl} has to be reduced by inserting the positive γ_{pl} into the second term of Equation (3.33). For the double mismatched welds, transition from underestimated to overestimated J_{pl} occurs when crack traverses the UM-OM or the OM-UM interface.

Table 4.24 The proposed γ_{pl} functions for the SE(B) specimens with the double mismatched OM-UM and UM-OM welds. The HAZ is considered in the results. The proposed factors are valid for the *J*-integral, extracted from 0.5 mm contour.

FEM series	γ_{pl} functions for 0.5 mm contour in range $0.1 \leq a_0/W \leq 0.7$	R^2 [-]
6A-OM-UM	$\gamma_{pl} = 207356.837\left(\frac{a}{W}\right)^7 - 541222.599\left(\frac{a}{W}\right)^6 + 582745.630\left(\frac{a}{W}\right)^5$ $- 337946.354\left(\frac{a}{W}\right)^4 + 114944.922\left(\frac{a}{W}\right)^3$ $- 23030.760\left(\frac{a}{W}\right)^2 + 2513.017\left(\frac{a}{W}\right) - 115.035$	0.996
6B-UM-OM	$\lambda = -85253.127\left(\frac{a}{W}\right)^9 - 296747.597\left(\frac{a}{W}\right)^8 + 1846800.762\left(\frac{a}{W}\right)^7$ $- 3284024.015\left(\frac{a}{W}\right)^6 + 2958127.567\left(\frac{a}{W}\right)^5$ $- 1535492.338\left(\frac{a}{W}\right)^4 + 474353.810\left(\frac{a}{W}\right)^3$ $- 85230.343\left(\frac{a}{W}\right)^2 + 8134.030\left(\frac{a}{W}\right) - 316.354$	1.000

4.10 Influence of Fusion Line Position on Fracture Behaviour of the Double Mismatched Welds

The results for the double mismatched welds, presented in Chapter 4.9, are valid for the SE(B) specimens with positions of fusion lines, i.e. interface between the OM and the UM weld materials, L_f/W=0.5 and L_f/W=0.435 for the OM-UM and the UM-OM welds respectively. These dimensions were incorporated into the FEM in order to obtain calibrated η_{pl}, λ and γ_{pl} factors that are compatible with the actually tested SE(B) specimens with the OM-UM and the UM-OM welds, designated as SE(B)-26 and SE(B)-10 in Table 3.10, respectively. Additional FEM were modelled and computed in order to provide necessary factors to estimate the *J*-integral for the other tested SE(B) specimens, having fusion line between the OM and the UM weld material positioned at different L_f/W distances. For that reason, two additional series per weld configuration were created. In case of the OM-UM weld, the FEM series 7A-OM-UM with L_f/W=0.525 and 7B-OM-UM with L_f/W=0.583 were created, and are valid for SE(B)-60 and SE(B)-58 specimens, respectively. In case of the UM-OM weld, the FEM series 7C-UM-OM with L_f/W=0.360 and 7D-UM-OM with L_f/W=0.528 were created and are valid for SE(B)-9 and SE(B)-52 specimens, respectively. All mentioned SE(B) specimens are listed in Table 3.10. The details, regarding the mentioned FEM series are available in the simulation matrix in Table 4.2. All other features of the created FEM were kept the same as described in Chapter 4.9. The calibrated values of η_{pl} were computed using the slope method [89], as described in

Chapter 4.2.1. *J*-integral $J_{0.5}$, extracted from 0.5 mm contour, was used for calibration of the η_{pl} factor. The obtained results are presented in Figure 4.51, while the corresponding calibrated functions are listed in Table 4.25. The shapes of the computed $\eta_{pl}(a/W)$ functions seem to be similar within each group of the simulated SE(B) samples, containing the OM-UM and the UM-OM welds. The closer inspection of the computational results revealed that all simulated SE(B) specimens with the OM-UM weld have similar deformation behaviour under monotonous loading as the FEM series 6A-OM-UM. Additionally, the SE(B) specimens with the UM-OM weld have similar deformation behaviour as the FEM series 6B-UM-OM. The principle of how plastic zone and stress triaxiality *h* are developed under the effect of yield strength mismatched materials, adjacent to the crack tip, was detailly presented in Chapter 4.9. For that reason, it will not be discussed here. However, it is important to note, that position of the fusion line L_f/W shifts $\eta_{pl}(a/W)$ functions along the a_0/W axis. Higher L_f/W shifts transitions from high to low values of the $\eta_{pl}(a/W)$ functions towards larger a_0/W, and vice versa. This observation was observed for the single material welds as well, as discussed in the Chapter 4.8. Therefore, the FEM series 7A-OM-UM with L_f/W=0.525 and 7B-OM-UM with L_f/W=0.583 have peaks at a_0/W=0.4 and a_0/W=0.5, respectively. Similarly, the FEM series 7C-OM-UM with L_f/W=0.360 and 7D-UM-OM with L_f/W=0.528 have minimum values of η_{pl} at a0/W=0.334 and a_0/W=0.501, respectively.

Next, the geometry factors λ were determined according to the procedure, described in Chapter 4.2.2. The computed results are presented in Figure 4.52. The corresponding calibrated λ functions are listed in Table 4.26. Figure 4.52 indicates that functions $\lambda(a/W)$ are in close agreement within the computed groups of the OM-UM and the UM-OM configurations of welds. However, minor scatter can be observed for the UM-OM weld configurations. This is due to different L_f/W dimensions for each computed FEM series. On the contrary, functions $\lambda(a/W)$ for the UM-OM welds seems to be less susceptible to variations in L_f/W. Once the crack surpasses the interface between the UM and the OM weld materials, results are in good agreement for all computed FEM series.

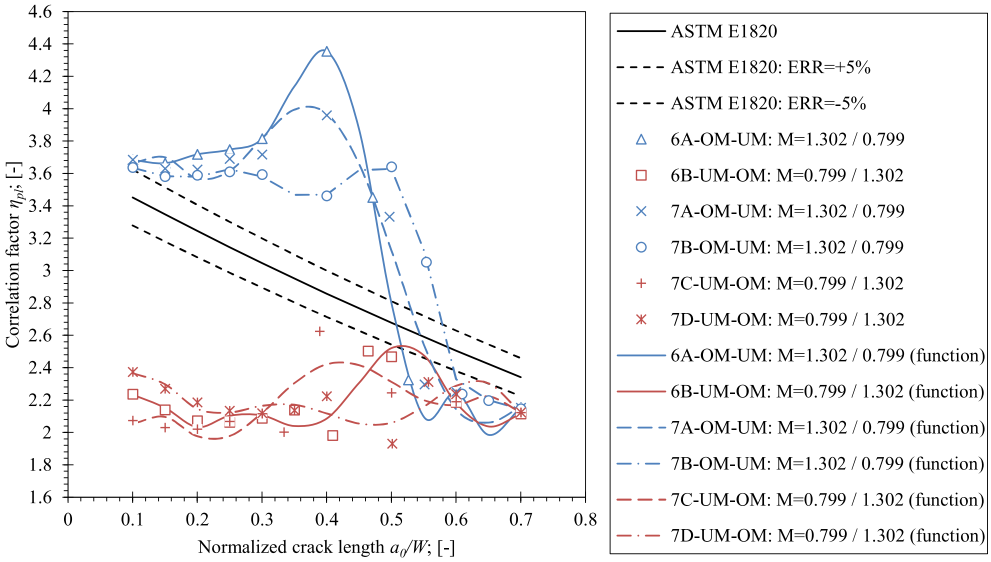

Figure 4.51 The comparison of the calibrated η_{pl} factors for the SE(B) specimens, containing the double mismatched OM-UM and UM-OM welds and different positions L_f/W of the fusion line between the OM and the UM weld materials. Standard solution according to ASTM E1820 is plotted as a reference.

Table 4.25 The proposed η_{pl} functions for the SE(B) specimens, containing the OM-UM and the UM-OM welds with different positions L_f/W of fusion line between the OM and the UM weld materials. Functions, listed in the table, are valid for the J-integral, extracted form 0.5 mm contour.

FEM series	η_{pl} functions for 0.5 mm contour in range $0.1 \le a_0/W \le 0.7$	R^2 [-]
7A-OM-UM	$\eta_{pl} = -5139.723\left(\frac{a}{W}\right)^6 + 12639.810\left(\frac{a}{W}\right)^5 - 11954.662\left(\frac{a}{W}\right)^4 + 5464.118\left(\frac{a}{W}\right)^3 - 1255.474\left(\frac{a}{W}\right)^2 + 136.573\left(\frac{a}{W}\right) - 1.828$	0.973
7B-UM-UM	$\eta_{pl} = -531204.737\left(\frac{a}{W}\right)^9 + 1650929.105\left(\frac{a}{W}\right)^8 - 2147543.247\left(\frac{a}{W}\right)^7 + 1521885.880\left(\frac{a}{W}\right)^6 - 641482.794\left(\frac{a}{W}\right)^5 + 165066.080\left(\frac{a}{W}\right)^4 - 25653.432\left(\frac{a}{W}\right)^3 + 2299.839\left(\frac{a}{W}\right)^2 - 107.597\left(\frac{a}{W}\right) + 5.635$	1.000
7C-OM-UM	$\eta_{pl} = -3651.875\left(\frac{a}{W}\right)^6 + 8871.399\left(\frac{a}{W}\right)^5 - 8403.191\left(\frac{a}{W}\right)^4 + 3904.028\left(\frac{a}{W}\right)^3 - 919.016\left(\frac{a}{W}\right)^2 + 102.491\left(\frac{a}{W}\right) - 2.153$	0.577
7D-OM-UM	$\eta_{pl} = 10624.682\left(\frac{a}{W}\right)^7 - 31254.384\left(\frac{a}{W}\right)^6 + 37265.902\left(\frac{a}{W}\right)^5 - 23146.494\left(\frac{a}{W}\right)^4 + 8004.162\left(\frac{a}{W}\right)^3 - 1519.650\left(\frac{a}{W}\right)^2 + 143.405\left(\frac{a}{W}\right) - 2.809$	0.612

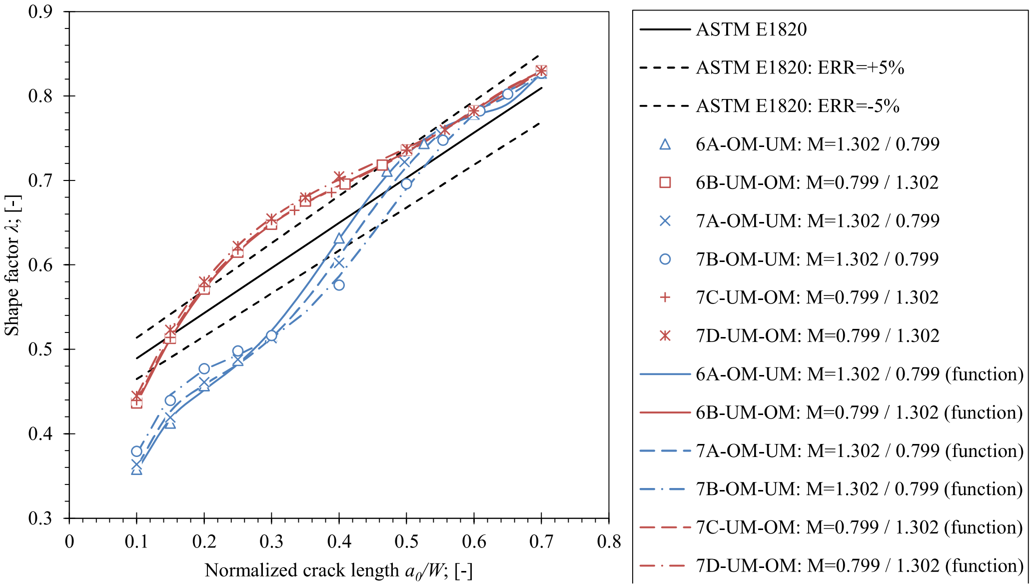

Figure 4.52 The comparison of the calibrated λ factors for the SE(B) specimens, containing the double mismatched OM-UM and UM-OM welds with different positions L_f/W of the fusion line between the OM and the UM weld materials. Standard solution according to ASTM E1820 is plotted as a reference.

Table 4.26 The proposed λ functions for the SE(B) specimens, containing the OM-UM and the UM-OM welds with different positions L_f/W of the fusion line between the OM and the UM weld materials.

FEM series	λ functions in range $0.1 \leq a_0/W \leq 0.7$	R^2 [-]
7A-OM-UM	$\lambda = 76.101\left(\frac{a}{W}\right)^5 - 160.620\left(\frac{a}{W}\right)^4 + 124.678\left(\frac{a}{W}\right)^3 - 43.551\left(\frac{a}{W}\right)^2 + 7.481\left(\frac{a}{W}\right) - 0.061$	0.999
7B-UM-UM	$\lambda = 52.310\left(\frac{a}{W}\right)^5 - 121.946\left(\frac{a}{W}\right)^4 + 104.431\left(\frac{a}{W}\right)^3 - 40.011\left(\frac{a}{W}\right)^2 + 7.356\left(\frac{a}{W}\right) - 0.052$	0.999
7C-OM-UM	$\lambda = -11.405\left(\frac{a}{W}\right)^5 + 16.744\left(\frac{a}{W}\right)^4 - 4.501\left(\frac{a}{W}\right)^3 - 3.481\left(\frac{a}{W}\right)^2 + 2.498\left(\frac{a}{W}\right) + 0.227$	1.000
7D-OM-UM	$\lambda = -0.640\left(\frac{a}{W}\right)^5 - 2.265\left(\frac{a}{W}\right)^4 + 7.552\left(\frac{a}{W}\right)^3 - 6.865\left(\frac{a}{W}\right)^2 + 2.914\left(\frac{a}{W}\right) + 0.215$	1.000

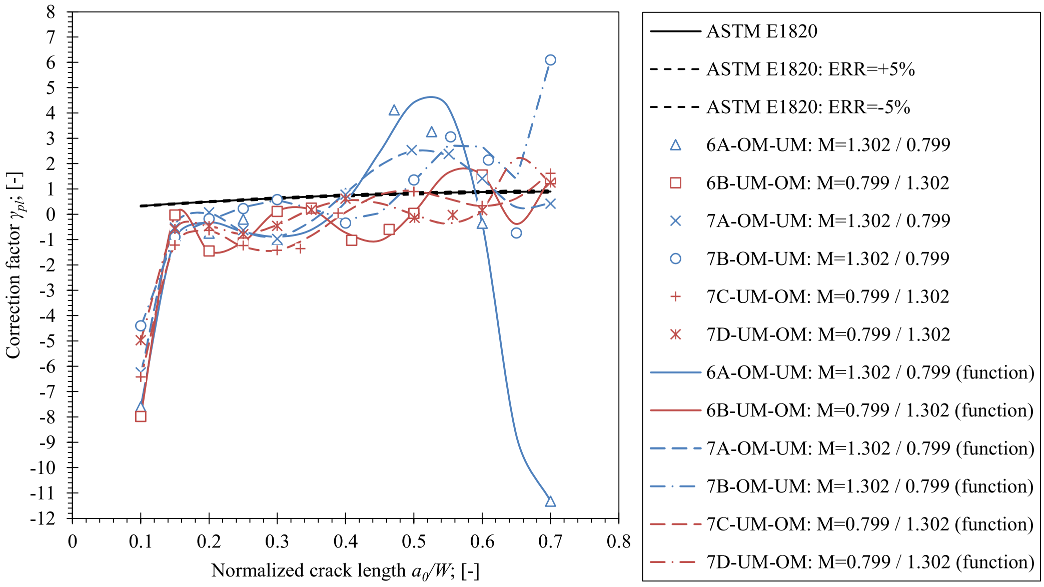

Figure 4.53 The comparison of the calibrated γ_{pl} factors for the SE(B) specimens, containing the double mismatched OM-UM and UM-OM welds with different positions L_f/W of the fusion line between the OM and the UM weld materials. Standard solution according to ASTM E1820 is plotted as a reference.

Finally, the crack growth correction factors γ_{pl} were computed according to the procedure, described in Chapter 4.2.2. The obtained results are presented in Figure 4.53, while the corresponding functions are listed in Table 4.27. Figure 4.53 indicates that $\lambda(a/W)$ functions for the OM-UM weld configurations are in relatively good agreement. In general, it seems that the first term in Equation (3.33) underestimates J_{pl} for shallow cracks with $a_0/W<0.4$. Therefore, J_{pl} must be increased due to crack growth during fracture test by the negative γ_{pl} values in the second term of Equation (3.33). The opposite can be observed for deeper cracks with $a_0/W>0.4$. Here, the first term of Equation (3.33) overestimates J_{pl} due to crack growth during fracture testing. Therefore, J_{pl} has to be reduced by inserting the positive γ_{pl} into the second term of Equation (3.33). Large scatter of results can be observed for $a_0/W>0.6$, which is attributed to mathematical definition of the γ_{pl} factors, given by Equation (4.6), that is based on variable $\eta_{pl}(a/W)$ and $\lambda(a/W)$ functions and their corresponding derivatives. Similar observations can be made for the UM-OM configurations of welds as well. However, here it seems, that the results are in closer agreement throughout the range of the analysed crack lengths $0.1\leq a_0/W\leq 0.7$. Again, some variations of $\lambda(a_0/W)$ are noted. However, these variations are attributed to the mathematical formulation of the γ_{pl} factor.

Table 4.27 The proposed γ_{pl} functions for the SE(B) specimens, containing the OM-UM and the UM-OM welds with different positions L_f/W of fusion line between the OM and the UM weld materials. Functions listed in the table, are valid for the J-integral, extracted from 0.5 mm contour.

FEM series	γ_{pl} functions for 0.5 mm contour in range $0.1 \leq a_0/W \leq 0.7$	R^2 [-]
7A-OM-UM	$\gamma_{pl} = 23809.802\left(\frac{a}{W}\right)^7 - 76351.247\left(\frac{a}{W}\right)^6 + 107497.999\left(\frac{a}{W}\right)^5 - 84594.227\left(\frac{a}{W}\right)^4 + 39041.832\left(\frac{a}{W}\right)^3 - 10245.062\left(\frac{a}{W}\right)^2 + 1384.664\left(\frac{a}{W}\right) - 73.897$	1.000
7B-UM-UM	$\gamma_{pl} = 210602.947\left(\frac{a}{W}\right)^7 - 562476.065\left(\frac{a}{W}\right)^6 + 613941.818\left(\frac{a}{W}\right)^5 - 353713.950\left(\frac{a}{W}\right)^4 + 115997.657\left(\frac{a}{W}\right)^3 - 21698.560\left(\frac{a}{W}\right)^2 + 2161.803\left(\frac{a}{W}\right) - 89.856$	1.000
7C-OM-UM	$\gamma_{pl} = -8484.655\left(\frac{a}{W}\right)^7 + 7182.067\left(\frac{a}{W}\right)^6 + 19053.551\left(\frac{a}{W}\right)^5 - 34612.474\left(\frac{a}{W}\right)^4 + 22624.322\left(\frac{a}{W}\right)^3 - 7097.704\left(\frac{a}{W}\right)^2 + 1060.185\left(\frac{a}{W}\right) - 60.857$	1.000
7D-OM-UM	$\gamma_{pl} = -1077374.981\left(\frac{a}{W}\right)^9 + 3608148.668\left(\frac{a}{W}\right)^8 - 5165243.830\left(\frac{a}{W}\right)^7 + 4100860.135\left(\frac{a}{W}\right)^6 - 1949639.367\left(\frac{a}{W}\right)^5 + 553643.990\left(\frac{a}{W}\right)^4 - 85789.992\left(\frac{a}{W}\right)^3 + 4859.875\left(\frac{a}{W}\right)^2 + 317.404\left(\frac{a}{W}\right) - 38.999$	1.000

4.11 Summary and Conclusions

Correction coefficients η_{pl} and γ_{pl} were calibrated on the basis of extensive parametrical FEA study. The study incorporated plane strain FEM that had implemented small strain approach and the elastic-plastic material models for various parts of the weld joint. The material models were established on the basis of experimental results, obtained by tensile testing of micro and AWMTT tensile specimens, as described in Chapter and Chapter, respectively. The geometry of the welds was simplified, as described in Chapter 4.3.1. The FEM of the base material were verified by comparing the computed solution with the published solutions ([45], [37], [38], [46], [47], [136] and [49]) and a solution, provided by the ASTM E1820 standard [6]. The correction parameters η_{pl} and γ_{pl} were computed on the basis of computational results using the slope method, developed by Donato et al. [60] and a differential approach, modified by Zhu et al [49]. It is important to note, that the γ_{pl} was computed indirectly from the η_{pl}, the geometry factor λ and their derivatives.

First of all, the correction factors were calibrated for the base material in conjunction with the various fixture setups. The results showed, that the oversized fixed support rollers reduce the η_{pl} values by 12 % in comparison to the standard support rollers. Moreover, the diameter of the load roller has a significant impact on the computed geometry factor λ. The increase of the load roller diameter causes an increase of the geometry factor λ. Furthermore, the computed γ_{pl} showed a significant deviation from the standard solution. Considering that the γ_{pl} depends on the correction factor η_{pl}, the geometry factor λ and their derivatives, it was concluded that the crack growth correction factor γ_{pl} is a mathematical parameter. Therefore, the interpretation of this parameter is rather difficult. It is important to note, that the convergence analysis of the *J*-integral was conducted at the same time. Two valued of the *J*-integral were obtained from the contours 0.5 mm and 2.0 mm ahead of the crack tip (denoted as 0.5 mm contour and 2.0 mm contour, respectively). The convergence analysis showed that the *J*-integral values, extracted from the 0.5 mm contour are sufficiently accurate, and can be used for the computation of the η_{pl}. Therefore, the *J*-integral was extracted from the 0.5 mm contour in all subsequent FEM.

In the next step, fracture behaviour of the single material welds was analysed, and the corresponding correction factors were calibrated. The HAZ was not considered in the first iteration. Additionally, only the actual fixture setup was modelled. Furthermore, the stress field ahead of the crack tip was analysed and the corresponding stress triaxiality was computed. The obtained results showed that in case of the OM weld, the η_{pl} gradually decreased as the normalized crack length *a/W* increased, and reached the minimum when the crack tip was located in the narrow weld root. Analysis of the corresponding strain fields showed that the plastic deformation developed primarily in the base material that has a lower yield strength than the OM weld. This effect was more prominent when the crack tip was located in the narrow weld root and resulted in a reduced stress triaxiality ahead of the crack tip. The latter was associated with the reduction of the η_{pl}. The corresponding interpretation is that, in the case of the OM weld, the deformation energy, imposed on the SE(B) specimen, manifests in plastic deformation of the base material rather than the crack driving force. The opposite was observed in the case of the UM welds. Here, the plastic deformation is contained within the UM weld, that has lower yield strength than the base material. As a result, the stress triaxiality ahead of the crack tip was increased. Consequentially, the η_{pl} increased as well, and reached the maximum when the crack tip was located in the narrow weld root. As the plastic deformation was limited to the narrow weld, larger portion of the strain energy manifested in the crack driving force than in the plastic deformation. Furthermore, the geometry coefficient λ was affected only for the shallower cracks ($a/W<0.4$), where the interface between the weld and the base material interfered with the deformation filed. Once the crack tip passes the narrow weld root, the strain field is no longer obstructed. Here, the η_{pl} and λ are similar to the one of the base material, and are mainly dependent on the shape and dimensions of the fracture specimen.

The presence of the HAZ alters fracture behaviour of the single material welds. In case of the OM welds, the HAZ contains the plastic deformation within the weld. As a result, the stress triaxiality ahead of the crack tip increases. Consequentially the η_{pl} increases as well, and reaches the maximum when the crack tip is located within the narrow weld root. Therefore, due to the confinement of the plastic deformation within the weld, the crack driving force is increased. Similar effect was observed in the UM welds as well. However, it was less prominent, as the base material itself can contain the plastic deformation within the weld, due to the higher yield strength in comparison to the UM weld. It is important to note that once the crack tip passed the narrow weld root, the plastic deformation developed primarily in the weld and was no longer obstructed by the HAZ. In this case, the fracture behaviour of the welded SE(B) specimen is similar to the one of the homogeneous material, and is no longer dependent on the configuration of the weld. Additionally, varying the position off the weld root had no significant effect on the fracture behaviour of the specimen. The only noted difference was that the peak values of stress triaxiality or the η_{pl} moved towards the deeper or shallower crack lengths in accordance with the position of the weld root. The main conclusion of this part of the study was that the HAZ significantly alter the deformation field ahead of the crack tip and consequentially the fracture behaviour of the SE(B) specimen. Therefore, the HAZ was considered in all subsequent FEM.

In the continuation of this research, it was observed that the double mismatched welds have a significant impact on the fracture behaviour of the SE(B) specimens. In case of the double mismatched welds with a crack in the UM weld material, the plastic zone is confined within the weld, between the crack tip and the OM weld material (located ahead of the crack tip). The cause for such behaviour are the OM weld material and the nearby HAZ, that have higher yield strength than the UM weld material. This results in the increased stress triaxiality. However, the η_{pl} is decreased as the OM weld material provides the load bearing capacity. As a result, the crack driving force decreases. This effect is the most prominent when the crack tip is located in the UM weld material, near the interface with the OM weld material. Once the crack tip passes the interface between the UM and the OM weld materials, the strain field is no longer obstructed by the HAZ and the fracture behaviour is similar to the homogeneous material.

The opposite fracture behaviour was observed in case of the double mismatched welds with a crack in the OM weld material. Here, the plastic zone developed predominantly in the UM weld material and in the base material. As a result, the stress triaxiality was reduced reduced. In contrary, the η_{pl} increased as the small amount of the OM material ahead of the crack tip can no longer provide a sufficient load bearing capacity, and the specimen undergoes large bending deformations. As a result, the crack driving force increases. This effect is the most prominent when the crack tip is located near the interface between the OM and the UM weld material. Additionally, the λ was significantly reduced for the shallow cracks in comparison to the single material welds. However, once the crack tip passes the interface between the UM and the OM weld materials, the strain field is no longer obstructed by the HAZ. Therefore, the fracture behaviour of the double mismatched weld becomes similar to the homogeneous material.

The above described observations clearly indicate, that the material ahead of the crack tip has a significant impact on fracture behaviour of the double mismatched welds. The OM weld material ahead of the crack tip decreases the crack driving force, while the UM weld material ahead of the crack tip increases the crack driving force. This observation is in line with the results of Predan et al. [13].

5 POST-PROCESSING OF FRACTURE TOUGHNESS TESTING RESULTS

5.1 Introduction

Results, described in Chapter 4 showed that configurations of the weld have a significant impact on stress field in the vicinity of the crack tip located in the weld, and consequently on fracture behaviour of the fracture specimen. For that reason, the correction parameters η_{pl} and γ_{pl} had to be calibrated, as described in Chapter 4. The current chapter presents the results, expressed as the J-R resistance curves, that were obtained by implementing the calibrated correction factors into the J-integral calculation procedure, presented in Chapter 3.5. The computed J-R curves, obtained with the calibrated and the standard correction factors will be compared and the differences will be analysed in scope of this chapter.

5.2 Influence of Fixture Configuration on Fracture Toughness of the Base Material

The influence of fixture configuration was determined for the tested base material SE(B) specimens that are listed in Table 3.10. The corresponding J-integral was computed according to the procedure, described in Chapter 3.5.3. the J-integral was here computed using two different sets of η_{pl}, λ and γ_{pl} factors. The first set included standard values of the aforementioned factors, provided in ASTM E1820 [6]. The second set included η_{pl}, λ and γ_{pl} factors that were calibrated for the fixture with fixed load and support rollers that have diameter d_S=d_L=25 mm. Such fixtures were used in the actual fracture tests. Procedure for calibration of η_{pl}, λ and γ_{pl} factors with analysis of the FEM series 1C-BM is described in Chapter 4.4, while the corresponding calibrated functions are listed in Table 4.5, Table 4.7 and Table 4.8. Factors η_{pl}, λ and γ_{pl} were calibrated on the basis of the J-integral $J_{0.5}$, that was extracted from 0.5 mm contour in the FEM. The obtained results, in terms of critical J_{Ic} at the fracture onset and the J-integral resistance curves J-R, are presented and compared in Table 5.1 and Figure 5.1. According to Table 5.1, J_{Ic}, computed with the calibrated factors, is lower than J_{Ic}, computed with the standard factors, by 13.1 % at maximum. Similar can be observed for J-R curves in Figure 5.1. Here, J-R curves that were computed with the calibrated factors show lower resistance to stable crack growth than J-R curves that were computed with the standard factors. This indicates that using standard η_{pl}, λ and γ_{pl} factors leads to the overestimated J-integral if the non-standard fixtures are used for fracture testing.

Table 5.1 The characteristic dimensions and fracture toughness for the tested SE(B) specimens, extracted from the base material. The computed fracture toughness is based on the standard and the calibrated η_{pl}, λ and γ_{pl} factors.

Specimen:	SE(B)-01	SE(B)-02	SE(B)-05
Fatigue precrack length a_0 [mm]	10.67	10.65	10.27
Normalized crack length a_0/W [-]	0.534	0.533	0.515
Final crack length a_p [mm]	11.72	11.78	11.08
Standard equations			
Critical J-integral J_{Ic} [kJ/m^2]	293	451	421
$J_{0.5}$ based equations, calibrated for fixed load and support rollers with d_S=d_L=25 mm			
Critical J-integral J_{Ic} [kJ/m^2]	265	399	366
Deviation from standard solution [%]	-9.6	-9.4	-13.1

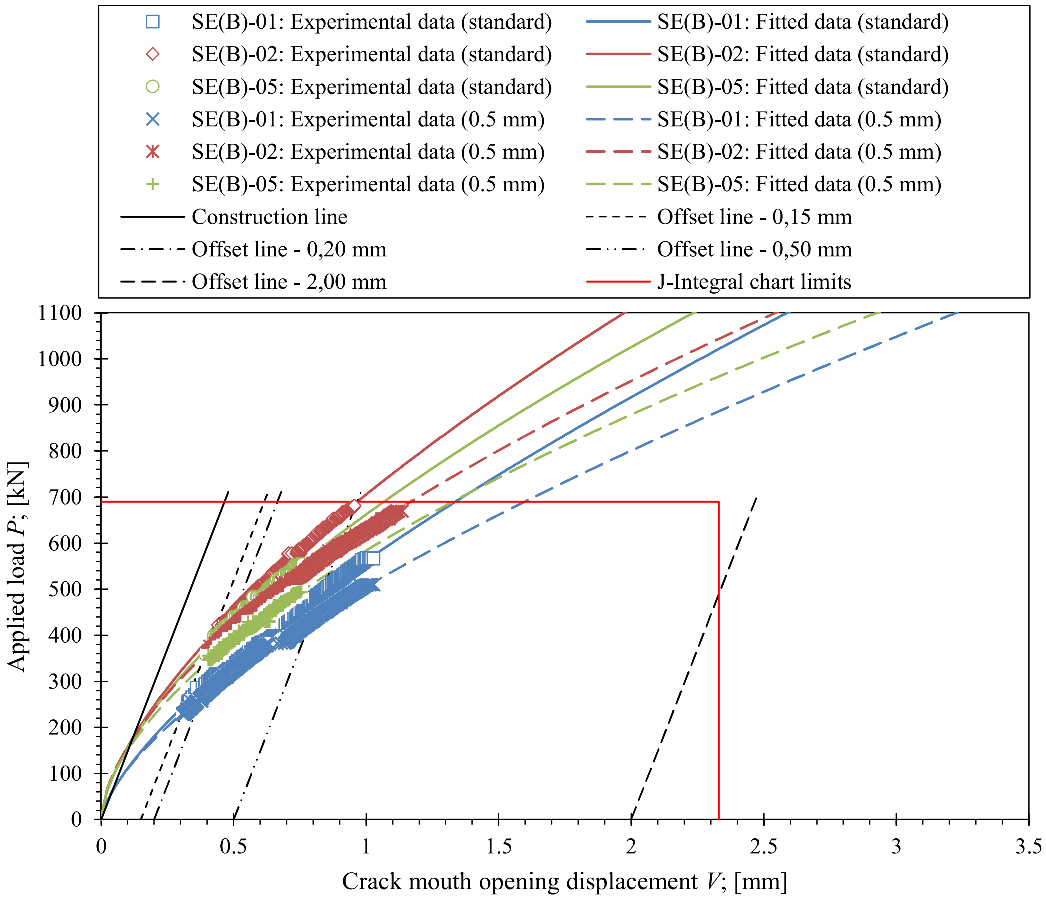

Figure 5.1 J-R curves for the tested base material SE(B) specimens. J-R curves were computed, using equations according to ASTM E1820 and the calibrated equations for the fixed rollers setup.

5.3 Influence of the J-integral Contour Size on Fracture Toughness of the Base material

Influence of the *J*-integral was determined for 0.5 mm and 2.0 mm contours, where the *J*-integral values $J_{0.5}$ and $J_{2.0}$ were extracted. Two corresponding sets of η_{pl}, λ and γ_{pl} factors were calibrated, as described in Chapter 4.4. This was done through parametrical analysis of the FEM series 1C-BM that resembles the actual fixture and the SE(B) specimen setup during fracture testing. Two sets of η_{pl}, λ and γ_{pl} factors were calibrated on the basis of the *J*-integral $J_{0.5}$ and $J_{2.0}$ that were extracted from 0.5 mm and 2.0 mm contours in the FEM, respectively. The corresponding calibrated functions for η_{pl} and γ_{pl} are presented in Table 4.5 and Table 4.7 for the first set, and in Table 4.6 and Table 4.8 for the second set. The calibrated functions for λ are presented in Table 4.7, and are dependent only on the measured LLD and CMOD. The calibrated factors, based on $J_{0.5}$ and $J_{2.0}$ were then implemented in the computation of the *J*-integral for the tested base material SE(B) specimens, that are listed in Table 3.10.

Table 5.2 The characteristic dimensions and the fracture toughness of the base material SE(B) specimens for $J_{0.5}$ and $J_{2.0}$ based factors.

Specimen:	SE(B)-01	SE(B)-02	SE(B)-05
Fatigue precrack length a_0 [mm]	10.67	10.65	10.27
Normalized crack length a_0/W [-]	0.534	0.533	0.515
Final crack length a_p [mm]	11.72	11.78	11.08
$J_{0.5}$ based factors			
Critical *J*-integral J_{Ic} [kJ/m^2]	265	399	366
$J_{2.0}$ based factors			
Critical *J*-integral J_{Ic} [kJ/m^2]	268	405	371
Deviation from $J_{0.5}$ based solution [%]	1.1	1.5	1.4

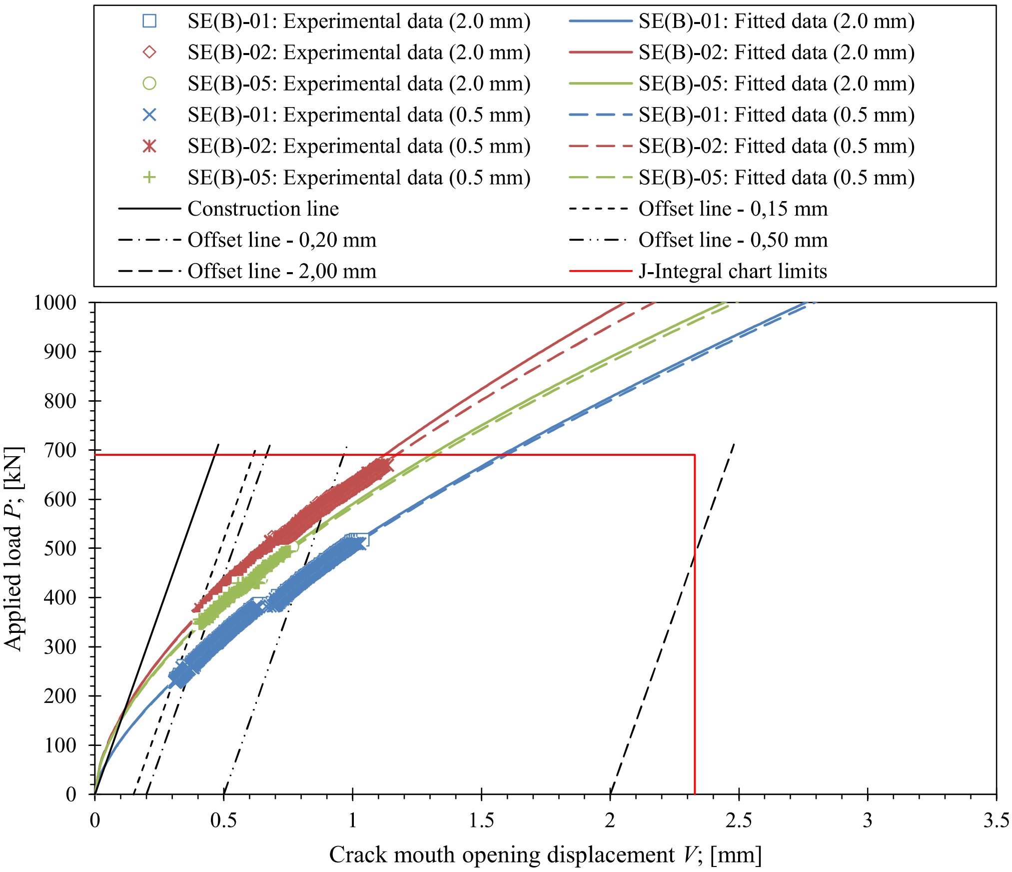

Figure 5.2 The comparison of *J*-R curves for the tested base material SE(B) specimens, obtained with the calibrated factors on the basis of the *J*-integral $J_{0.5}$ and $J_{2.0}$, extracted from the 0.5 mm and 2.0 mm contours, respectively.

Critical J_{Ic} at the crack onset and *J*-R curves were produced for both sets of factors and are presented in Table 5.2 and Figure 5.2. The observed difference in J_{Ic}, computed by $J_{0.5}$ and $J_{2.0}$ based η_{pl}, λ and γ_{pl} factors, is 1.5 % at maximum. Furthermore, *J*-R curves in Figure 5.2 indicate close agreement between $J_{0.5}$ and $J_{2.0}$ based solutions. Therefore, it can be concluded that η_{pl}, λ and γ_{pl} factors, calibrated for the 0.5 mm contour, enable accurate estimation of the *J*-integral from the recorded *P*-CMOD history during fracture testing. For that reason, the 0.5 mm contour was used for the calibration of η_{pl}, λ and γ_{pl} factors in all subsequent cases of the single material and the double mismatched welds.

5.4 Influence of the Heat Affected Zone on Fracture Toughness of the Single Mismatched Welds

Extensive parametrical FEA of SE(B) specimens with the single material welds has been conducted in scope of this research, as described in Chapter 4.6 and Chapter 4.7. The obtained results indicated that yield strength mismatching of the weld material and the HAZ, with respect to the base material, has a significant effect on development of plastic zone at the tip of the crack. This further affects the η_{pl}, λ and γ_{pl} factors. Therefore, it is assumed, that configuration of the weld has a significant effect on the J-integral, computed from P-CMOD history, that was recorded during fracture testing. In order to verify this assumption, η_{pl}, λ and γ_{pl} factors that were calibrated for the single material welds with no HAZ and the single material welds with the HAZ, as described in Chapter 4.6 and Chapter 4.7. These factors are here implemented into analytical calculation of the J-integral from the experimental data for the single material OM and UM welds. The representative specimen, extracted from the OM weld, was SE(B)-38. The corresponding J-integral has been computed with three sets of η_{pl}, λ and γ_{pl} factors. The first set, was obtained from ASTM E1820 standard [6]. The second set was adjusted for the single material OM weld with no HAZ, and was obtained from the FEM series 2A-OM. The third set was adjusted for the OM weld with the HAZ, and was obtained from the FEM series 4A-OM. Common to the all three listed sets of η_{pl}, λ and γ_{pl} factors is that they were calibrated for 0.5 mm contour, and the actual fixture with fixed rollers. The computed critical J_{Ic} and J-R curves for the OM weld are presented in Table 5.3 and Figure 5.3, respectively. Comparison of the results in Table 5.3 indicates that η_{pl}, λ and γ_{pl} factors, calibrated for the OM weld and the OM weld with the HAZ, produce 34.2 % and 8.3 % lower J_{Ic} than the standard factors. Furthermore, the inspection of J-R curves in Figure 5.3 indicates that the J-integral is reduced throughout the entire range of ductile crack growth Δa, if η_{pl}, λ and γ_{pl} factors, calibrated for the OM weld and the OM weld with the HAZ, are used.

Similar procedure of the J-integral computation has been repeated for specimen SE(B)-40 that was extracted from the single material UM weld. The corresponding J-integral has been computed with three sets of η_{pl}, λ and γ_{pl} factors. Again, the first set was obtained from ASTM E1820 standard [6] and was used as a reference. The second set was adjusted for the single material UM weld with no HAZ and was obtained from the FEM series 2B-UM. The third set was adjusted for the UM weld with the HAZ and was obtained from the FEM series 4B-UM. All three sets of η_{pl}, λ and γ_{pl} factors were adjusted for 0.5 mm contour and the actual fixture with fixed rollers. The computed critical J_{Ic} and J-R curves for the UM weld are presented in Table 5.4 and Figure 5.4, respectively. The comparison of the results in Table 5.4 indicates that η_{pl}, λ and γ_{pl} factors, calibrated for the UM weld and the UM weld with the HAZ, produce 6.3 % and 8.9 % lower J_{Ic} than the standard factors. Additionally, the inspection of J-R curves in Figure 5.4 shows that that the J-integral was reduced throughout the entire range of ductile crack Δa growth.

To sum up, the described observations indicate that the computed fracture toughness in terms of the J-integral is overestimated if η_{pl}, λ and γ_{pl} factors, calibrated for the homogeneous material, are used. The effect of the weld material and the HAZ on development of plastic zone, and consequentially, on the crack growth, is significant and must not be neglected. This is obvious in case of the OM weld. Here, the HAZ with higher yield strength than the OM weld material, restricts plastic deformation in the weld, as discussed in Chapter 4.7. This results in a significant difference in J_{Ic}, produced with η_{pl}, λ and γ_{pl} factors that were calibrated for the OM weld and the OM weld with the HAZ. Therefore, the HAZ should always be considered when calibrating correction factors for the J-integral calculation.

Table 5.3 The characteristic dimensions and the fracture toughness for the tested specimen SE(B)-38, extracted from the OM weld.

Specimen:	SE(B)-38
Fatigue precrack length a_0 [mm]	8.58
Normalized crack length a_0/W [-]	0.431
Final crack length a_p [mm]	9.89
Normalized distance to weld root L_W/W [-]	0.360
standard equations	
Critical J-integral J_{Ic} [kJ/m^2]	193
$J_{0.5}$ based equations, calibrated for OM weld	
Critical J-integral J_{Ic} [kJ/m^2]	127
Deviation from standard solution [%]	-34.2
$J_{0.5}$ based equations, calibrated for OM weld with HAZ	
Critical J-integral J_{Ic} [kJ/m^2]	177
Deviation from standard solution [%]	-8.3

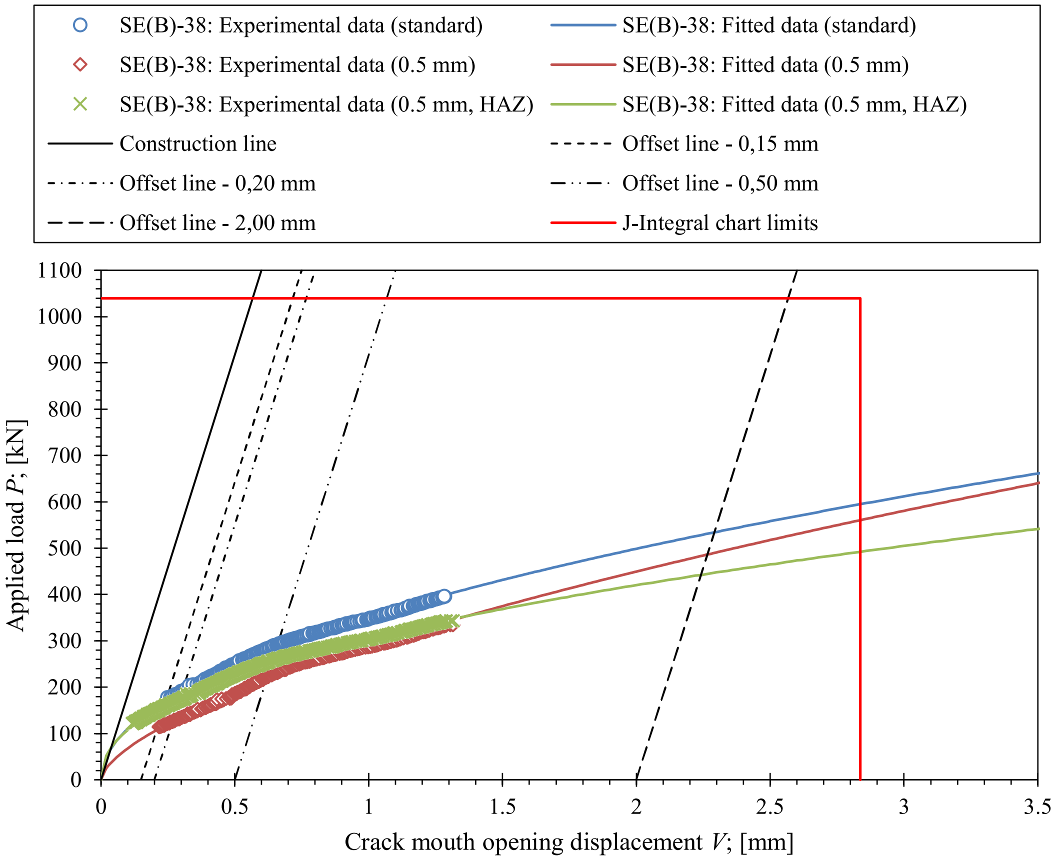

Figure 5.3 The comparison of *J*-R curves for SE(B)-38 specimen, containing the OM weld. The Presented *J*-R curves were obtained with the standard equations according to ASTM E1820 and $J_{0.5}$ based equations, calibrated for the OM weld and the OM weld with the HAZ.

Table 5.4 The characteristic dimensions and the fracture toughness for the tested specimen SE(B)-40, that was extracted from the UM weld.

Specimen:	SE(B)-40
Fatigue precrack length a_0 [mm]	9.02
Normalized crack length a_0/W [-]	0.45
Final crack length a_p [mm]	9.99
Normalized distance to weld root L_W/W [-]	0.415
standard equations	
Critical J-integral J_{Ic} [kJ/m^2]	336
$J_{0.5}$ based equations, calibrated for UM weld	
Critical *J*-integral J_{Ic} [kJ/m^2]	315
Deviation from standard solution [%]	-6.3
$J_{0.5}$ based equations, calibrated for UM weld with HAZ	
Critical *J*-integral J_{Ic} [kJ/m^2]	306
Deviation from standard solution [%]	-8.9

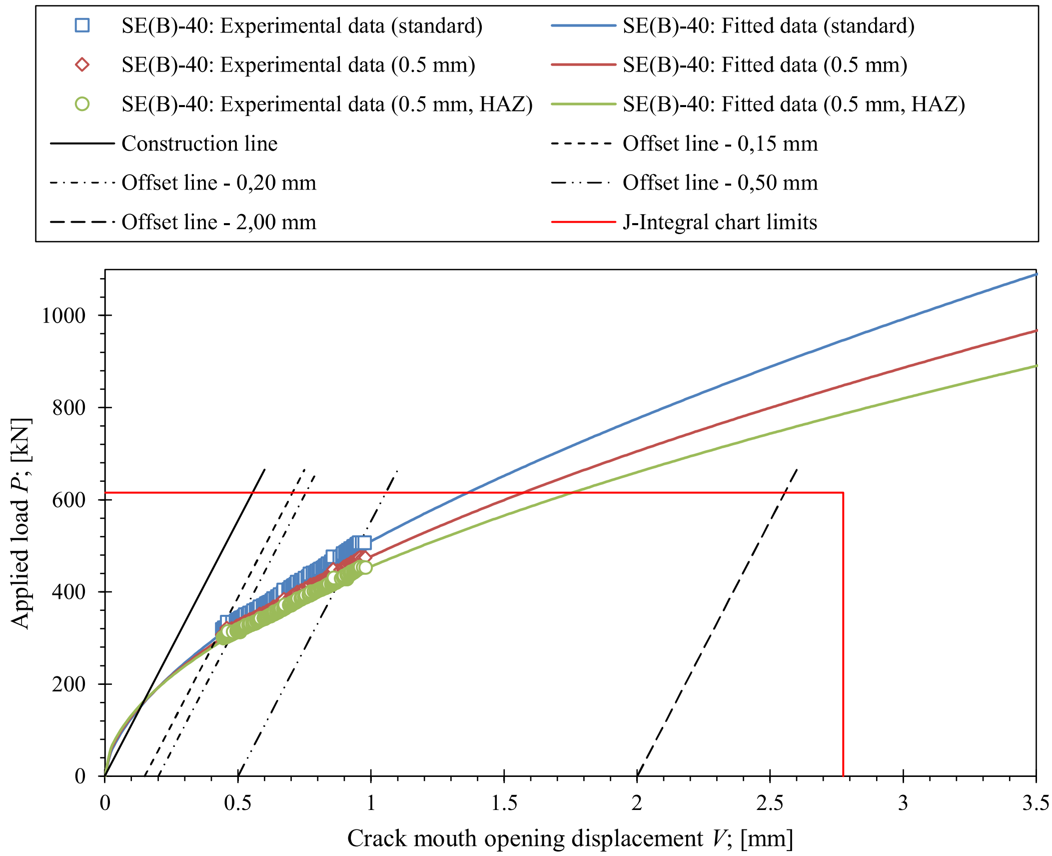

Figure 5.4 Comparison of J-R curves for SE(B)-40 specimen, containing the UM weld. The presented J-R curves were obtained with the standard equations according to ASTM E1820 and $J_{0.5}$ based equations, calibrated for the UM weld and the UM weld with the HAZ.

5.5 Fracture toughness of the Single Mismatched Welds

Experimental data of the remaining fracture toughness tests for the single material OM and UM welds was reanalysed in the same way, as discussed in Chapter 5.4. The J-integral was recomputed, using η_{pl}, λ and γ_{pl} factors that were calibrated for the OM and the UM welds with the HAZ and the fixture with fixed rollers. Factors that had been calibrated from the numerical results of the FEM series 5A-OM, 4A-OM and 5B-OM were applied in the computation of the J-integral for specimens SE(B)-37, SE(B)-38 and SE(B)-39, respectively, extracted from the OM weld. Furthermore, factors that had been calibrated from the numerical results of the FEM series 4B-UM, 5C-UM and 5D-UM were applied in the computation of the J-integral for specimens SE(B)-40, SE(B)-41 and SE(B)-42, respectively, extracted from the UM weld. Additionally, the reference J-integral was computed according to ASTM E1820 [6]. Finally, J-R curves were constructed on the basis of the computed J-integral and the estimated ductile crack extension by the NDRM. Critical J_{Ic} at the fracture onset was determined from J-R curves according to ASTM E1820 [6]. The comparison of the results for the OM welds in Table 5.5 indicates that η_{pl}, λ and γ_{pl} factors, calibrated for the OM weld with the HAZ, produce 8.3 % lower J_{Ic} than the standard factors. Additionally, Figure 5.5 shows that J-R curves, obtained with the calibrated factors, exhibit lower resistance to crack growth than the J-R curves, obtained with the standard factors. This was observed throughout the entire range of ductile crack extension Δa. Similar observations can be made for the UM welds as well. Here, the comparison of the results in Table 5.6 indicates that η_{pl}, λ and γ_{pl} factors, calibrated for the OM weld with the HAZ, produce 12.8 % lower J_{Ic} than the standard factors. Moreover, Figure 5.6 shows that the J-R curves, obtained with the calibrated factors, exhibit lower resistance to crack growth than the J-R curves, obtained with the standard factors. Presented observations further support conclusions that were made in the previous chapter. The J-integral should be always computed with η_{pl}, λ and γ_{pl} factors that are calibrated for welds that are being tested and for fixtures that are used for fracture testing.

Table 5.5 The characteristic dimensions and fracture toughness for the tested SE(B) specimens, extracted from the OM weld.

Specimen:	SE(B)-37	SE(B)-38	SE(B)-39
Fatigue precrack length a_0 [mm]	8.44	8.58	8.85
Normalized crack length a_0/W [-]	0.424	0.431	0.444
Final crack length a_p [mm]	11.34	9.89	10.96
Normalized distance to weld root L_W/W [-]	0.390	0.360	0.652
standard equations			
Critical J-integral J_{Ic} [kJ/m^2]	158	193	204
$J_{0.5}$ based equations, calibrated for OM weld with HAZ			
Critical J-integral J_{Ic} [kJ/m^2]	147	177	193
Deviation from $J_{0.5}$ based solution [%]	-7.0	-8.3	-5.4

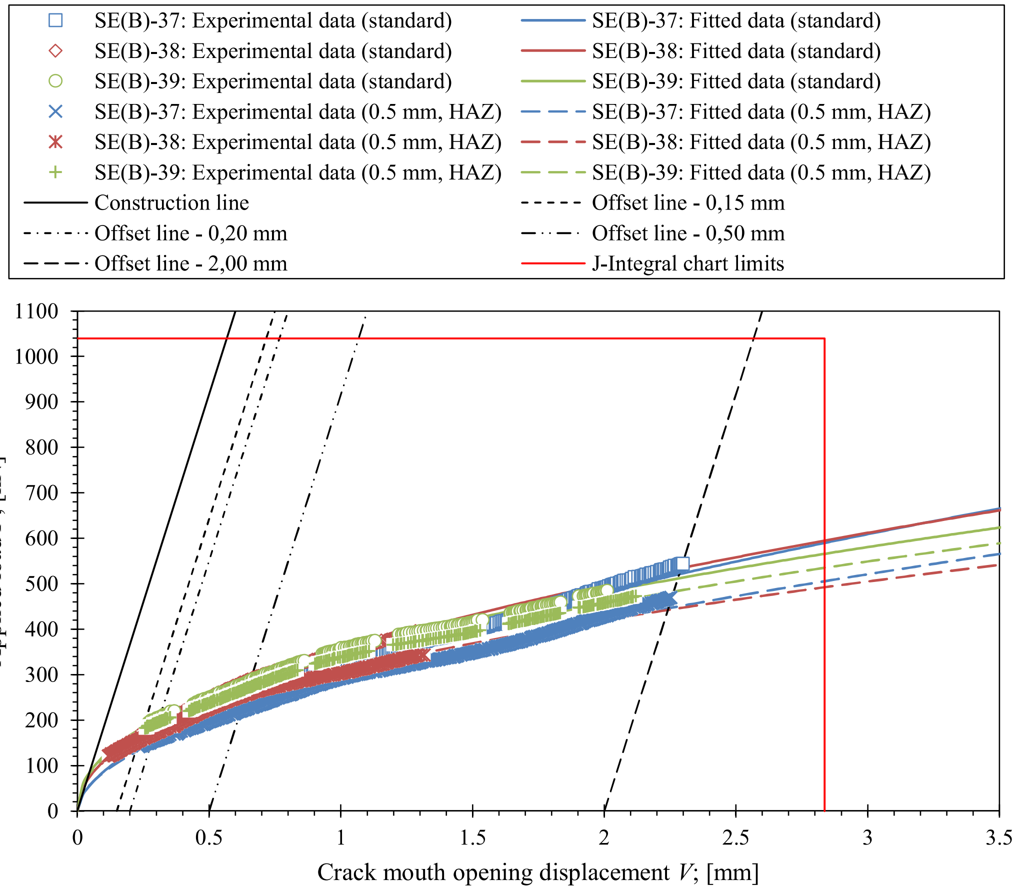

Figure 5.5 The comparison of *J*-R curves for the tested SE(B) specimens, extracted from the OM weld. The presented *J*-R curves were obtained with standard equations according to ASTM E1820 and $J_{0.5}$ based equations, calibrated for the OM weld with the HAZ.

Table 5.6 The characteristic dimensions and the fracture toughness for the tested SE(B) specimens, extracted from the UM weld.

Specimen:	SE(B)-40	SE(B)-41	SE(B)-42
Fatigue precrack length a_0 [mm]	9.02	8.99	9.23
Normalized crack length a_0/W [-]	0.448	0.447	0.459
Final crack length a_p [mm]	9.99	10.16	10.38
Normalized distance to weld root L_W/W [-]	0.415	0.440	0.469
standard equations			
Critical *J*-integral J_{Ic} [kJ/m^2]	336	445	293
$J_{0.5}$ based equations, calibrated for UM weld with HAZ			
Critical *J*-integral J_{Ic} [kJ/m^2]	306	388	287
Deviation from $J_{0.5}$ based solution [%]	-8.9	-12.8	-2.0

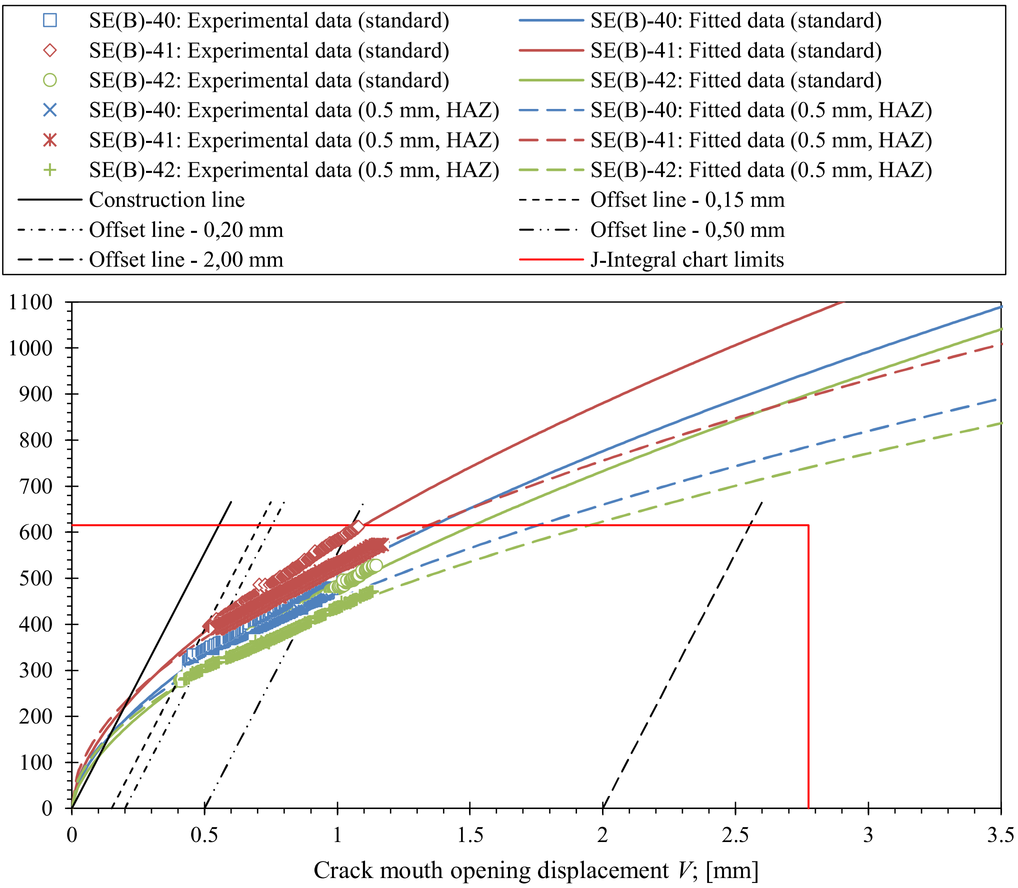

Figure 5.6 The comparison of *J*-R curves for the tested SE(B) specimens, extracted form the UM weld. The presented *J*-R curves were obtained with standard equations according to ASTM E1820 and $J_{0.5}$ based equations, calibrated for the UM weld with the HAZ.

5.6 Fracture Toughness of the Double Mismatched Welds

The experimental data of fracture toughness tests for the double mismatched welds was reanalysed in the same way, as discussed in Chapter 5.4. The *J*-integral was recomputed, using η_{pl}, λ and γ_{pl} factors, that were calibrated for the double mismatched OM-UM and UM-OM welds. Factors that had been calibrated from the numerical results of FEM series 6A-OM-UM, 7A-OM-UM and 7B-OM-UM were applied in the computation of the *J*-integral for specimens SE(B)-26, SE(B)-60 and SE(B)-58, respectively. These specimens were notched in the OM part of the weld. Furthermore, factors that had been calibrated from the numerical results of FEM series 6B-UM-OM, 7C-UM-OM and 7D-UM-OM, were applied in the computation of the *J*-integral for specimens SE(B)-10, SE(B)-9 and SE(B)-52, respectively. These specimens were notched in the UM part of the weld. Additionally, the reference *J*-integral was computed according to ASTM E1820 [6] for the all tested specimens. J-R curves were constructed and the corresponding J_{IC} was determined according to ASTM E1820 [6]. The comparison of the results for the SE(B) specimens, notched in the OM part of the weld, in Table 5.7 indicates that the calibrated factors provide 17.2 % higher J_{Ic} than the standard factors. Furthermore, Figure 5.7 indicates that J-R curves, obtained with the calibrated factors, exhibit higher resistance to crack growth for $\Delta a \leq 0.5$ mm and lower resistance to crack growth for $\Delta a > 0.5$ mm in comparison to the standard J-R curves. This explains higher J_{Ic} for the calibrated factors. Similar observations can be made for the SE(B) specimens that were notched in the UM part of the weld. The results in Table 5.8 indicate that the calibrated factors provided 28.2 % lower J_{Ic} than the standard factors. Moreover, Figure 5.8 indicates that J-R curves, obtained with the calibrated factors, show lower resistance to fracture than the J-R curves, obtained with the standard factors, throughout the entire range of the measured ductile crack extension Δa. However, the results had to be critically assessed in case of the SE(B) specimens, extracted from the double mismatched welds and notched in the UM part of the weld. The corresponding η_{pl}, λ and γ_{pl} factors were calibrated for the crack that propagates in plane. However, the analysis of the fractured surfaces in Chapter 3.4.6 shows that severe crack path deviation occurs after the local unstable crack growth. From there on, the crack is growing along the interface between the OM part of the weld and the HAZ. This is attributed to the severe plastic deformation that origins at the crack tip in the UM part of the weld, and is forced to develop around the OM part of the weld, as demonstrated in Figure 4.47. Therefore, the standard and the calibrated η_{pl}, λ and γ_{pl} factors provide fault solution and should not be used for the computation of J-integral for UM-OM welds.

Table 5.7 The characteristic dimensions and fracture toughness for the tested SE(B) specimens, extracted from the double mismatched weld and notched in the OM part of the weld.

Specimen:	SE(B)-26	SE(B)-58	SE(B)-60
Fatigue precrack length a_0 [mm]	9.30	10.30	10.37
Normalized crack length a_0/W [-]	0.466	0.514	0.518
Final crack length a_p [mm]	10.79	11.46	11.25
Normalized distance to fusion line L_f/W [-]	0.500	0.525	0.583
standard equations			
Critical J-integral J_{Ic} [kJ/m^2]	287	441	366
$J_{0.5}$ based equations, calibrated for OM-UM weld with HAZ			
Critical J-integral J_{Ic} [kJ/m^2]	336	517	366
Deviation from $J_{0.5}$ based solution [%]	17.1	17.2	0.0

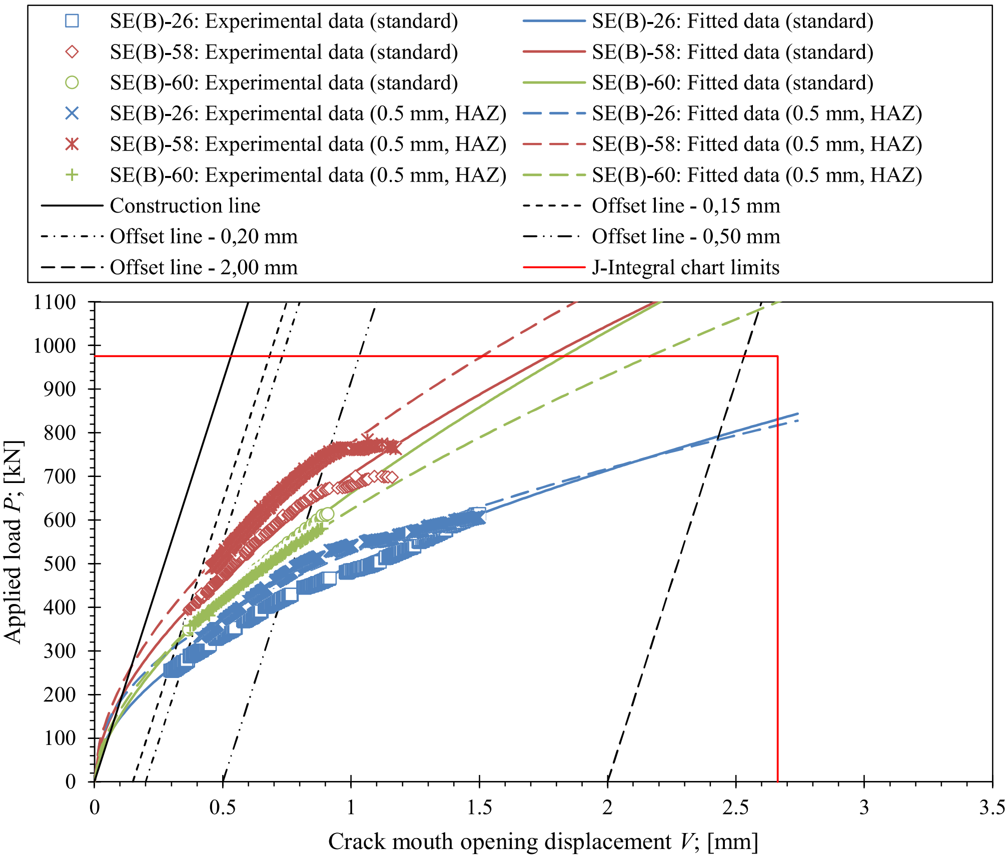

Figure 5.7 The comparison of the *J*-R curves for the tested SE(B) specimens, extracted from the double mismatched weld with notch in the OM part of the weld. The presented *J*-R curves were obtained with the standard equations according to ASTM E1820 and $J_{0.5}$ based equations, calibrated for the OM-UM weld with the HAZ.

Table 5.8 The characteristic dimensions and fracture toughness for the tested SE(B) specimens, extracted from the double mismatched weld and notched in the UM part of the weld.

Specimen:	SE(B)-9	SE(B)-10	SE(B)-52
Fatigue precrack length a_0 [mm]	6.07	8.27	9.58
Normalized crack length a_0/W [-]	0.304	0.414	0.478
Final crack length a_p [mm]	7.73	9.75	10.88
Normalized distance to fusion line L_f/W [-]	0.360	0.435	0.528
standard equations			
Critical *J*-integral J_{Ic} [kJ/m^2]	1080	341	312
$J_{0.5}$ based equations, calibrated for UM-OM weld with HAZ			
Critical *J*-integral J_{Ic} [kJ/m^2]	870	246	224
Deviation from $J_{0.5}$ based solution [%]	-19.4	-27.9	-28.2

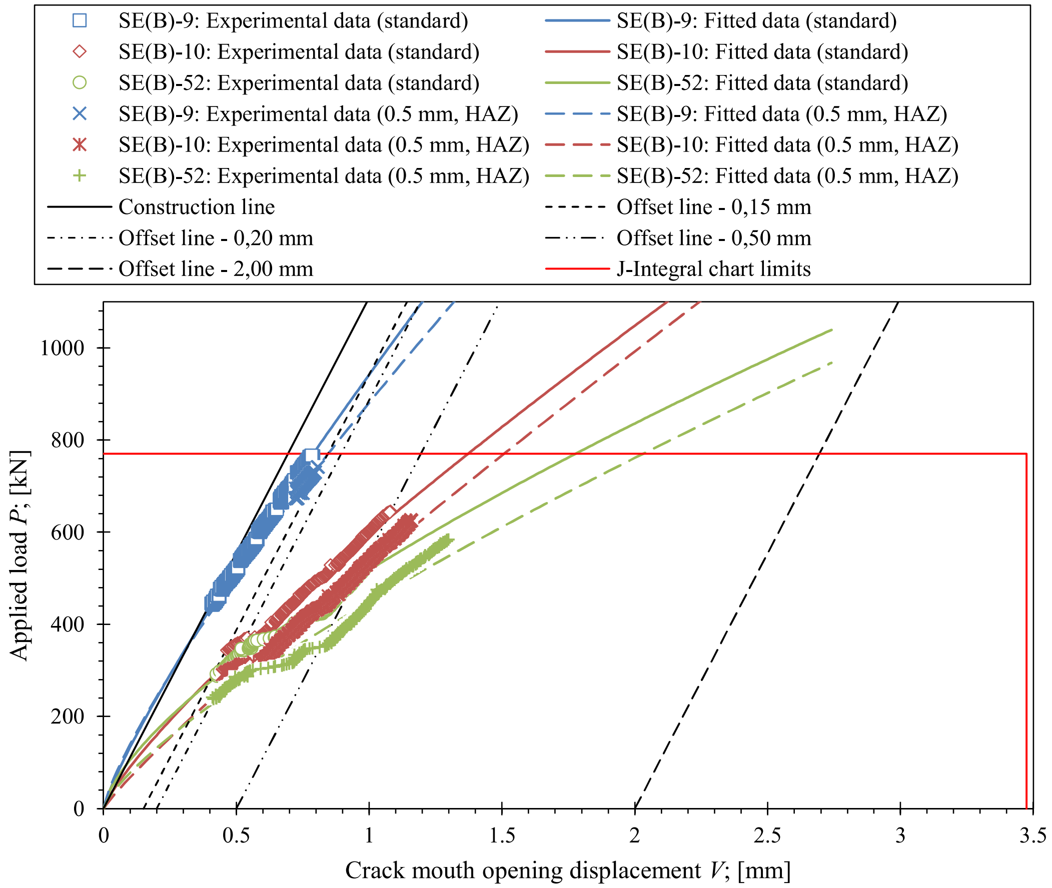

Figure 5.8 The comparison of the *J*-R curves for the tested SE(B) specimens, extracted from the double mismatched weld with notch in the UM part of the weld. The presented *J*-R curves were obtained with the standard equations according to ASTM E1820 and the $J_{0.5}$ based equations, calibrated for the UM-OM weld with the HAZ.

5.7 Verification of the Obtained Results

The results, obtained with the NDRM and the UCM as described in Chapter 3.5.5 and Chapter 3.5.7, respectively, were postprocessed once more using the corrected η_{pl} and γ_{pl} factors. For the SE(B)-09 specimen (the UM-OM weld), the corrected η_{pl} and γ_{pl} factors were computed using the equations that are valid for the $J_{0.5}$ and are given in Table 4.25 and Table 4.27, respectively. For the SE(B)-26 specimen (the OM-UM weld), the corrected η_{pl} and γ_{pl} factors were computed using the equations that are valid for the $J_{0.5}$ and are given in Table 4.22and Table 4.24, respectively. The obtained J-R curves are presented in Figure 5.9 and Figure 5.10 for the specimens SE(B)-09 and SE(B)-26, respectively. The corresponding fracture toughness values are presented in the Table 5.9. It is important to add, that the fitted functions of the UCM and NDRM *J*-R curves were not computed for the SE(B)-09 specimen, as none of the J_i-a_i data sets was within the 0.15 mm and 2.0 mm offset (i.e. exclusion) lines. As a result, the corresponding fracture toughness, expressed as J_{Ic} and K_{JIc}, could not be determined.

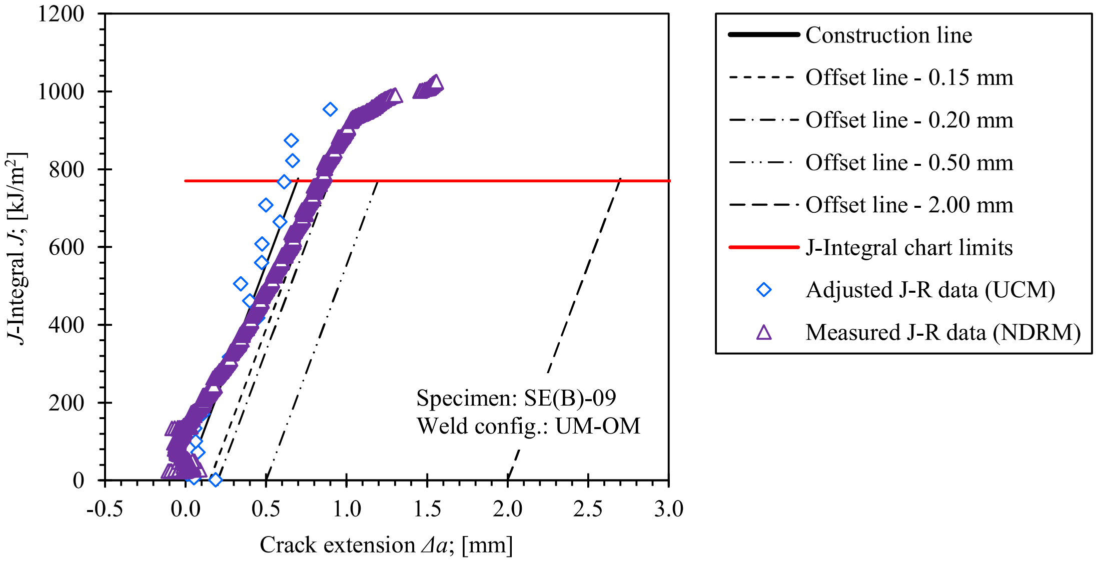

Figure 5.9 The corrected UCM and NDRM *J*-R resistance curves for the fracture test of the SE(B)-09 specimen (UM-OM weld).

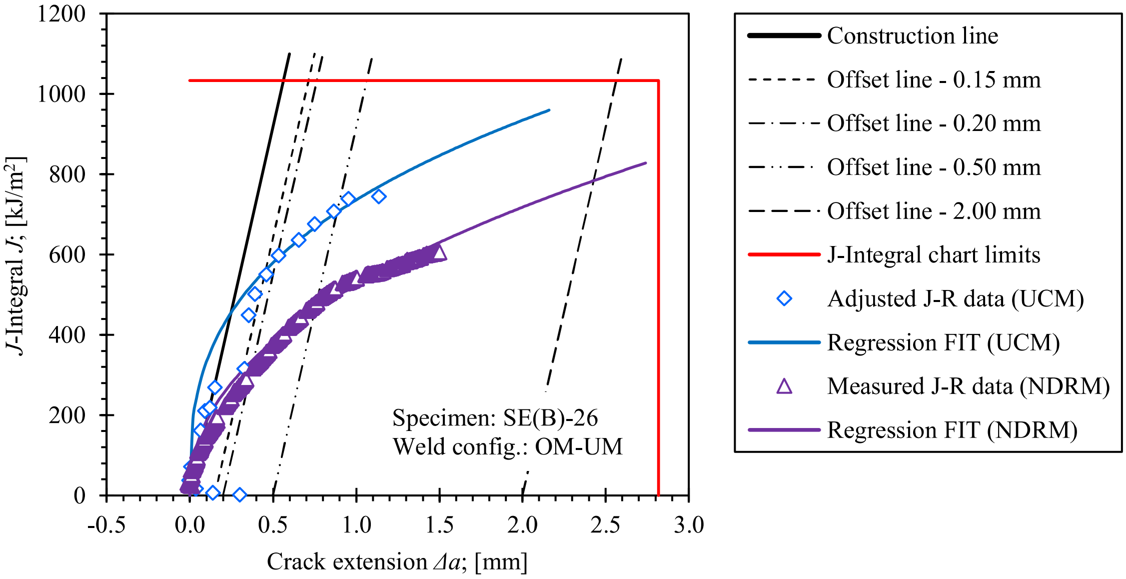

Figure 5.10 The corrected UCM and NDRM *J*-R resistance curves for the fracture test of the SE(B)-26 specimen (OM-UM weld).

Table 5.9 The corrected results for the fracture tests of the SE(B)-09 and SE(B)-26 specimens.

Specimen	SE(B)-09		SE(B)-26	
Test method	NDRM	UCM	NDRM	UCM
Measured fatigue precrack length a_0; [mm]	6.07		9.30	
Measured final crack length a_p; [mm]	7.73		10.79	
Distance to fusion line L_f; [mm]	7.20		10.00	
Estimated ductile crack growth Δa; [mm]	1.67	0.90	1.50	1.14
Estimated final crack length $a_0+\Delta a$; [mm]	7.73	6.97	10.79	10.44
Critical J-integral J_{Ic}; [kJ/m^2]	n.a.	n.a.	336	559
Critical SIF K_{JIc}; [MPam$^{1/2}$]	n.a.	n.a.	295	381

The comparison of the results shows that the UCM and the NDRM *J*-R curves are in close agreement for small ductile crack growth, i.e. Δa<0.4 mm. This indicates that the accuracy of the NDRM method is sufficient at least for the small ductile crack growth. From here on, the UCM *J*-R curves deviate from the NDRM *J*-R curves. The reasons for such deviation are is the influence of the interface between the OM and the UM weld material, crack tunnelling and the crack path deviation. Moreover, the UCM fails to accurately predict the total ductile crack growth, as shown in the Table 5.9. Here, the UCM predicts the total ductile crack growth Δa that is, in comparison to the NDRM, 0.77 mm shorter in case of the SE(B)-09 specimen and 0.36 mm shorter in case of the SE(B)-26 specimen. Moreover, the inaccurate ductile crack growth estimation has an effect on the η_{pl} and γ_{pl} values. Due to that, the computed plastic component of the *J*-integral J_{pl} that is based on the Δa determined by the UCM, is not the same as the J_{pl} that is based on the Δa, determined by the NDRM. In case of the NDRM, the Δa is calibrated on the basis of the physically measured fatigue precrack a_0 and the final crack length a_p, and is considered to be accurate. Therefore, it can be concluded, that the UCM does not produce accurate *J*-R curves for the tested SE(B) specimens with the OM-UM and the UM-OM configurations of the welds.

5.8 Summary and Conclusions

This chapter provided an overview of the J-R resistance curves that were obtained using the NDRM and sets of the standard and the calibrated η_{pl} and γ_{pl} factors. The latter were calibrated specifically for each tested SE(B) specimen configuration.

The obtained results for the fracture test of the base material SE(B) specimens, presented in Chapter 5.2, show that the configuration of the fixtures has a significant impact on the fracture behaviour of the tested SE(B) specimens. Using the standard η_{pl} and γ_{pl} factors in computation of the J-integral leads to the overestimation of the material resistance to stable tearing (i.e. the ductile crack growth), as demonstrated in Figure 5.1. Correspondingly, the critical J_{Ic} could be overestimated by approx. 13 % if the fixture with the fixed oversized rollers is used during the test and the standard η_{pl} and γ_{pl} factors are applied in the J computation. Therefore, it is necessary to properly calibrate the correction factors if the configuration of the fixture differs from the standard one. It is also important that the converged J-integral is used for the calibration of the correction parameters. The results of the sensitivity analysis, presented in Chapter 5.3, showed that the correction factors, calibrated on the basis of $J_{0.5}$ and $J_{2.0}$ (i.e. the J-integral extracted form the 0.5 mm and the 2.0 mm contours) differ. However, the difference between the $J_{0.5}$ and the $J_{2.0}$ was less than 2%, as demonstrated in Figure 5.2A ge. For that reason, the correction parameters were calibrated on the basis of the $J_{0.5}$ for all the remaining SE(B) specimens. The main advantage of the 0.5 mm contour is its small size, that enables to fit the contour in a single material region in the narrow weld root of the double mismatched weld. Additionally, the effect of the HAZ has to be considered as well, which is demonstrated in Chapter 5.4. Therefore, it is necessary to incorporate the HAZ into the FEM, that are used for the calibration of the correction factors.

Inspection of the J-R curves for the single material welds (Chapter 5.5) and the double mismatched welds (Chapter 5.6) showed that in general, the standard correction parameters lead to overestimation of the tearing resistance. An exception are the OM-UM welds, where standard correction factors lead to underestimation of the tearing resistance of the weld, as demonstrated on Figure 5.7.

Finally, the J-R resistance curves that were obtained with the NDRM and the UCM were compared. The comparison showed, that the NDRM correctly estimates the total ductile crack growth Δa, while the UCM failed to do so. Moreover, the UCM showed deviations of the J-R curve at larger ductile crack growth Δa>0.4 mm. The reason for that is influence of the interface between the OM and the UM weld material, the crack tunnelling effect and the crack path deviation. A severe crack path deviation was observed in the broken OM-UM welds, as shown in Figure 3.59 d). The UCM was used only as a reference in scope of this research, and another comprehensive study that would investigate application of the UCM to fracture testing of the double mismatched welds is needed.

6 CONCLUSIONS

The aim of this research was to estimate fracture toughness of welds with pronounced strength heterogeneity and to assess if the NDRM could be used for evaluation of the stable crack extension. This was done through experimental characterization of weld material mechanical properties and through extensive parametric FEA of welded joints with pronounced strength heterogeneity.

6.1 Experimental Work

Experimental work included fabrication of welded sample plates, metallography, hardness measurements, tensile testing of standard and miniature specimens and fracture testing. Sample plates were fabricated by MAG welding of S690 QL steel, that is normally used in highly loaded constructions. Welds with pronounced strength heterogeneity were artificially fabricated by using highly OM and UM weld materials.

Metallography was conducted on samples of weld and base material, indicating relatively high presence of bainite and martensite in the microstructure of weld. Portion of both microconstituents varied in the weld due to complex thermal history that is result of the weld material deposition in multiple passes. This resulted in highly variable local mechanical properties that were initially recognized by measuring indentation hardness. Measured hardness profiles showed high local variations of hardness, where hardness can change by 350 HV within a distance of 3 mm.

Local mechanical properties in various parts of the weld were determined by tensile testing of micro specimens. The results showed that yield strength mismatch M could vary from 0.697 for the UM weld to 1.518 for the fine grained HAZ. The comparison of local mechanical properties with the measured hardness profiles showed good correlations between yield strength, ultimate tensile strength and indentation hardness.

Average mechanical properties were determined by tensile testing of standard round bar specimens. The obtained average material properties were compared to the local material properties. The comparison showed that the average and the local true stress strain records were in close agreement. Therefore, it was concluded, that material models could be developed from average mechanical properties and then implemented into simplified FEM of SE(B) specimens.

Fracture properties of welds and base material were determined by fracture testing of SE(B) specimens that were extracted from the single material welds, the double mismatched welds and the base material. SE(B) specimens that were extracted from the welds were surface notched. As a result, planar cracks with straight fronts were relatively simple to produce without applying any of special techniques for modification of residual stresses. The results of fracture tests indicated that the double mismatched welds, tested in scope of this project, have improved fracture properties in comparison to the single material welds.

6.2 Numerical Work

Numerical work included extensive programme of parametrical plane strain FEA for SE(B) specimens with welds and notches in different configurations. In total, three different configurations of fixtures and nine different configurations of mismatched welds were analysed. Reference values of η_{pl}, λ and γ_{pl} factors were obtained through simulation of the SE(B) specimens that contained only homogeneous BM for all three different fixture setups. The corresponding results showed, that in the *J*-integral is reduced by 12 % if a fixture with fixed oversized rollers was used instead of the standard fixture according to ASTM E1820. This means, that fracture toughness is overestimated by 12 % if the *J*-integral is computed with standard η_{pl}, λ and γ_{pl} factors, while non-standard fixtures are used during fracture testing. This observation emphasizes the importance of respecting the test boundary conditions set forward by the standard. The analysis of the *J*-integral convergence in the homogeneous material has been conducted as well. Obtained results indicated that difference in the *J*-integral values, extracted from contours at distances 0.5 mm and 2.0 mm apart from the crack tip, is less than 1.5 %. This proved, that reasonably accurate *J*-integral can be obtained from 0.5 mm contour in all subsequent FEA. Another benefit of smaller contour is that the crack tip can be modelled closer to the interface between the OM and the UM weld material. As a result, variations in the crack driving force at the vicinity of the interface can be more accurately determined.

FEA of the single material welds showed that plastic zones developed primarily in the BM if the weld material had comparatively higher yield strength (OM weld). This caused reduction of the material constraint in front of the crack tip, and consequently a reduction of the local crack driving force. The opposite was observed for the weld material with lower yield strength (UM weld), where the BM material acted as a barrier that contained the plastic zone in the weld. This resulted in increased material constraint in front of the crack tip and increased crack driving force. It is important to note, that material constraint has been characterized with stress triaxiality *h*, that was extracted at a certain distance ahead of the crack tip, where stress field is no longer affected by incorrect deformation of the crack tip due to small strain approach.

Considering the HAZ in the FEM changed the behaviour of the single material welds. This was especially noted in case of the OM welds where the HAZ had comparatively higher yield strength. There, the HAZ acted as a barrier that contained plastic zone primarily in the weld, resulting in increased material constraint and crack driving force. Correspondingly, the *J*-integral that had been computed from the experimental data, was reduced by 8.3 % in comparison to the standard solution, if η_{pl}, λ and γ_{pl} factors, calibrated on the basis of the SE(B) sample with the OM weld and the HAZ, were used. In case of the UM welds, plastic zone was further contained in the weld and only slight increase of material constraint and crack driving force was observed. The *J*-integral, computed from the experimental data, was reduced by 8.9 % in comparison to the standard solution. This indicates that the effect of HAZ on fracture behaviour must be considered in the narrow parts of the weld, where it interacts with the zone of plastic deformation.

Finally, the double mismatched welds were analysed. Substantial increase of the crack driving force has been observed before the crack that was located in the OM weld material, traversed interface between the OM and the UM weld materials. Correspondingly, the *J*-integral that had been computed from the experimental data with new calibrated η_{pl}, λ and γ_{pl} factors, was increased by 17 % with respect to the standard solution. The opposite was observed when crack, located in the UM weld material, traversed the interface between the UM and the OM weld materials. In this case, a severe reduction of the local crack driving force and material constraint was observed. The reason for that is the OM material, located in front of the crack tip, was highly stressed and carried the majority of the imposed load. As a result, the plastic zone developed around the OM part of the weld at interface with the HAZ. This explaines crack path deviations, observed on the fractured surfaces after fracture testing. The crack path deviation presents several challenges for measurement of the crack length. Practical methods that are normally used in fracture testing are unloading compliance technique (UCT) and direct current potential drop (DCPD) method. The UCT is very sensitive to variations in the compliance of the fracture specimen and requires planar crack with a straight front in order to accurately measure stable crack extension Δa. If the shape of the crack deviates or the crack front is not straight (i.e. crack tunnelling), then that influences the compliance of the fracture specimen and the UCT yields inaccurate measurements of Δa. On the other hand, the DCPD method might give wrong measurements, as ductile crack growth is measured only from reduction of net cross section, regardless of crack growth path.

6.3 Perspectives for Future Work

Researchers and engineers are striving hard for constant improvement in standards, codes and techniques to enhance the prediction capabilities of failures in welded structures which results in economic and operational safety. The current standards for determination of fracture toughness for welds are based on the established procedures for fracture testing of homogeneous metallic materials. It is well known that welds have highly heterogeneous structure which can have an effect on the fracture behaviour. Therefore, this thesis is a small step towards the establishment of a unified approach for fracture testing of welds. The main contribution of this work to scientific community is a demonstration of how the heterogeneous structure of the weld affects the fracture behaviour, and how to resolve this challenge. The corresponding outcome is that the J-computation procedure should be properly calibrated in order to compensate the effects of the weld heterogeneity. Additionally, it is important to take care that the fixtures are designed well and in conformance with the requirements of the standards. Any deviations from the standard specifications might result in a significant impact on the fracture behaviour of the tested fracture specimen. However, it is important to continue with such studies and to validate the solution that is proposed in this thesis on different types of welds and base materials.

Additional recommendation for the future work would be to revise the application of the 95 % secant method (specified in the ASTM E399 standard [5]) and the unloading compliance method (specified in the ASTM E1820 standard [6]) to the fracture testing of welds.

The 95 % secant method is applied if a significant unstable fracture occurs during the stable tearing of the fracture specimen. In this case the standard ASTM E1820 for measurement of fracture toughness refers to the ASTM E399 standard for measurement of linear elastic plane-strain fracture toughness K_{Ic}. The latter specifies how to apply the 95% secant method. This thesis showed that 95 % secant method produces overly conservative fracture toughness in case of the significant unstable fracture that is preceded by a significant plastic deformation. This was observed in testing of the double mismatched welds with a fatigue precrack in the UM weld material. These welds showed the highest load bearing capacity among all tested welds, but the lowest fracture toughness due to restrictions of the 95 % secant method. For that reason, the 95 % secant method should be revised and modified if needed.

Finally, the unloading compliance method was implemented in this work as a reference for verification of the normalization data reduction method. The obtained results showed that the heterogeneous structure of the weld has a significant impact on the accuracy of the unloading compliance method. Additionally, the crack tunnelling and the crack path deviations were observed on the fracture surfaces of the broken specimens. One solution would be to implement the side grooves that would maintain the straight crack front and a planar crack. However, the increased stress triaxiality due to the side grooves can lead to an unstable fracture. therefore, the unloading compliance method should be revised, and a procedures and solutions to counteract the crack tunnelling and the crack path deviations should be developed.

7 LITERATURE

[1] M. Koçak, S. Webster, J. J. Janosch, R. A. Ainsworth, and R. Koers, “FITNET Fitness-for-service (FFS) - Procedure (Volume 1).” GKSS Research Center, Geesthacht, 2008.

[2] M. Koçak, I. Hadley, S. Szavai, Y. Tkach, and N. Taylor, “FITNET Fitness-for-service (FSS) - Annex (Volume 2).” GKSS Research Center, Geesthacht, 2008.

[3] GKSS-Forschungszentrum Geesthacht, *EFAM ETM 97 - the ETM method for assessing the significance of crack-like defects in engineering structures*. Geesthacht: GKSS Research Center, 1998.

[4] “BS 7910:2013 ‘Guide to methods for assessing the acceptability of flaws in metallic structures.’” BSI Standards Limited, Chiswick Tower, 2015.

[5] “ASTM E399-12e3 ‘Standard Test Method for Linear-Elastic Plane-Strain Fracture Toughness KIc of Metallic Materials.’” ASTM International, West Conshohocken, 2013.

[6] “ASTM E1820-15 ‘Standard Test Method for Measurement of Fracture Toughness.’” ASTM International, West Conshohocken, 2016.

[7] “BS 7448-1:1991 ‘Fracture mechanics toughness test, Part-1. Method for determination of KIc, critical CTOD and critical J values of metallic materials.’” BSI Standards Limited, Chiswick Tower, 2003.

[8] “BS 7448-2:1997 ‘Fracture mechanics toughness test, Part-2. Method for determination of KIc, critical CTOD and critical J values of welds in metallic materials.’” BSI Standards Limited, Chiswick Tower, 2004.

[9] “BS 7448-3:2005 "Fracture mechanics toughness test, Part-3. Method for determination of fracture toughness of metallic materials at rates of increase in stress intensity factor greater than 3.0 MPa·m0.5^-1.” BSI Standards Limited, Chiswick Tower, 2007.

[10] “BS 7448-4:1997 "Fracture mechanics toughness test, Part-4. Method for determination of fracture resistance curves and initiation values for stable crack extension in metallic materials.” BSI Standards Limited, Chiswick Tower, 2003.

[11] “ISO 12135 ‘Metallic materials — Unified method of test for the determination of

quasistatic fracture toughness.'" International Organization for Standardization, Geneva, 2016.

[12] S. Hertelé, N. Gubeljak, and W. De Waele, "Advanced characterization of heterogeneous arc welds using micro tensile tests and a two-stage strain hardening ('UGent') model," *Int. J. Press. Vessel. Pip.*, vol. 119, pp. 87–94, 2014, doi: 10.1016/j.ijpvp.2014.03.007.

[13] J. Predan, N. Gubeljak, and O. Kolednik, "On the local variation of the crack driving force in a double mismatched weld," *Eng. Fract. Mech.*, vol. 74, no. 11, pp. 1739–1757, 2007, doi: 10.1016/j.engfracmech.2006.09.015.

[14] E. Østby, Z. L. Zhang, and C. Thaulow, "Constraint effect on the near tip stress fields due to difference in plastic work hardening for bi-material interface cracks in small scale yielding," *Int. J. Fract.*, vol. 111, no. 1, pp. 87–103, 2001, doi: 10.1023/A:1010992906312.

[15] K. H. Schwalbe and M. Koçak, *Proceedings of the International Conference on Mis-Matching of Welds. ESIS 17*. London: Mechanical Engineering Publ., 1994.

[16] K. H. Schwalbe and M. Koçak, *Proceedings of the Second International Symposium on Mis-Matching of Interfaces and Welds*. Geesthacht: GKSS Research Centre, 1997.

[17] Y. J. Kim and K. H. Schwalbe, "Mismatch effect on plastic yield loads in idealized weldments. I. Weld centre cracks," *Eng. Fract. Mech.*, vol. 68, no. 2, pp. 183–199, 2001, doi: 10.1016/S0013-7944(00)00094-1.

[18] S. Hao, A. Cornec, and K. H. Schwalbe, "Plastic stress-strain fields and limit loads of a plane strain cracked tensile panel with a mismatched welded joint," *Int. J. Solids Struct.*, vol. 34, no. 3, pp. 297–311, 1997, doi: 10.1016/S0020-7683(96)00021-2.

[19] P. Gilles and C. Franco, "A new estimation scheme for cracks in mis-matching welds – the ARAMIS method," *Proceedings of International Conference of Mis-Matching Welds ESIS 17*. Mechanical Engineering Publications Ltd, London, UK, 1994.

[20] S. H. Kim, J. J. Han, and Y. S. Kim, "Mismatch limit loads of circumferential cracked pipes in V-groove welds," *Proc. ASME 2013 Press. Vessel. Pip. Conf.*, 2013.

[21] N. Gubeljak, "The effect of strength mis-match on welded joint fracture behaviour," University of Maribor, Faculty of Mechanical Engineering, 1998.

[22] "ISO 15653:2010 'Metallic materials — Method of test for the determination of quasistatic fracture toughness of welds.'" International Organization for Standardization, Geneva, 2010.

[23] I. Milne, R. O. Ritchie, and B. Kaihaloo, Eds., *Comprehensive Structural Integrity*. Elsevier Science Ltd., 2007.

[24] X. K. Zhu and J. A. Joyce, "J-Resistance curve testing of HY80 steel using SE(B) specimens and normalization method," *Eng. Fract. Mech.*, vol. 74, no. 14, pp. 2263–2281, 2007, doi: 10.1016/j.engfracmech.2006.10.018.

[25] J. Yang, G. Z. Wang, F. Z. Xuan, S. T. Tu, and C. J. Liu, "Out-of-plane constraint effect on local fracture resistance of a dissimilar metal welded joint," *Mater. Des.*, vol. 55, pp. 542–550, 2014, doi: 10.1016/j.matdes.2013.10.034.

[26] J. Yang, G. Z. Wang, F. Z. Xuan, S. T. Tu, and C. J. Liu, "An experimental investigation of in-plane constraint effect on local fracture resistance of a dissimilar metal welded joint," *Mater. Des.*, vol. 53, pp. 611–619, 2014, doi: 10.1016/j.matdes.2013.07.058.

[27] X. K. Zhu and J. A. Joyce, "Review of fracture toughness (G, K, J, CTOD, CTOA) testing and standardization," *Eng. Fract. Mech.*, vol. 85, pp. 1–46, 2012, doi: 10.1016/j.engfracmech.2012.02.001.

[28] T. L. Anderson, *Fracture Mechanics - Fundamental and Applications*, Third edit. Boca Raton: CRC Press, Taylor & Francis Group, LLC, 2005.

[29] J.R.Rice, "'A Path Independent Integral and the Approximate Analysis of Strain Concentration by Notches and Cracks,'" *J. Appl. Mech.*, vol. 35, no. 2, p. 379, 1968.

[30] J. A. Begley and J. D. Landes, "The J Integral as a Fracture Criterion," in *Fracture Toughness: Part II*, H. Corten, Ed. West Conshohocken, PA: ASTM International, 1972, pp. 1–23.

[31] D. Landes and J. A. Begley, "The Effect of Specimen Geometry on JIC," in *Fracture*

Toughness: Part II, H. Corten, Ed. West Conshohocken, PA: ASTM International, 1972, pp. 24–39.

[32] J. R. Rice, P. C. Paris, and J. G. Merkle, "Some Further Results of J-Integral Analysis and Estimates.," *ASTM Spec. Tech. Publ.*, no. September, pp. 231–245, 1972, doi: 10.1520/stp49643s.

[33] J. Sumpter and C. Turner, "Method for Laboratory Determination of Jc," in *Cracks and Fracture*, 100 Barr Harbor Drive, PO Box C700, West Conshohocken, PA 19428-2959: ASTM International, pp. 3-3–16.

[34] G. R. Irwin and D. C. Washington, "G. R. Irwin, 'Analysis of stresses and strains near the end of a crack traversing a plate'. J. Applied Mechanics, 24,(1957) 361–364." pp. 361–364, 1957.

[35] G. Clarke and J. Landes, "Evaluation of the J Integral for the Compact Specimen," *J. Test. Eval.*, vol. 7, no. 5, p. 264, 1979, doi: 10.1520/JTE10222J.

[36] J. D. G. Sumpter, "Jc determination for shallow notch welded bend specimens," *Fatigue Fract. Eng. Mater. Struct.*, vol. 10, no. 6, pp. 479–493, 1987, doi: 10.1111/j.1460-2695.1987.tb00498.x.

[37] M. T. Kirk and R. H. Dodds, "J and CTOD Estimation Equations for Shallow Cracks in Single Edge Notch Bend Specimens," *J. Test. Eval.*, vol. 21, no. 4, p. J. Test. Eval., 1993, doi: https://doi.org/10.1520/JTE11948J.

[38] M. Nevalainen and R. H. Dodds, "Numerical investigation of 3-D constraint effects on brittle fracture in SE(B) and C(T) specimens," *Int. J. Fract.*, vol. 74, no. 2, pp. 131–161, 1995, doi: 10.1007/BF00036262.

[39] J. A. Joyce, *Manual on Elastic-Plastic Fracture: Laboratory Test Procedures*. West Conshohocken: ASTM International, 1996.

[40] S. J. Garwood, J. N. Robinson, and C. E. Turner, "The measurement of crack growth resistance curves (R-curves) using the J integral," *Int. J. Fract.*, vol. 11, no. 3, pp. 528–530, 1975, doi: 10.1007/BF00033539.

[41] H. A. Ernst, P. C. Paris, and J. D. Landes, “Estimations on J-Integral and Tearing Modulus T From a Single Specimen Test Record.,” *ASTM Spec. Tech. Publ.*, pp. 476–502, 1981.

[42] H. Ernst, P. C. Paris, M. Rossow, and J. W. Hutchinson, “Analysis of Load-Displacement Relationship To Determine J-R Curve and Tearing Instability Material Properties,” *Astm Stp 677*. pp. 581–599, 1979.

[43] J. Hutchinson and P. Paris, “Stability Analysis of,” in *Elastic-Plastic Fracture*, 100 Barr Harbor Drive, PO Box C700, West Conshohocken, PA 19428-2959: ASTM International, pp. 37-37–28.

[44] X.-K. Zhu, B. N. Leis, and J. A. Joyce, “Experimental Estimation of J-R Curves from Load-CMOD Record for SE(B)Specimens,” *J. ASTM Intl. ASTM Spec. Tech. Publ.*, vol. 5, no. 5, pp. 66–15, 2008, doi: 10.1520/JAI101532.

[45] S. X. Wu, Y. W. Mai, and B. Cotterell, “Plastic η-factor (ηp),” *Int. J. Fract.*, vol. 45, no. 1, pp. 1–18, 1990, doi: 10.1007/BF00012606.

[46] Y. J. Kim and K. H. Schwalbe, “On Experimental J Estimation Equations Based on CMOD for SE(B) Specimens,” *J. Test. Eval.*, vol. 29, no. 1, pp. 67–71, 2001, doi: 10.1520/jte12393j.

[47] Y. J. Kim, J. S. Kim, S. M. Cho, and Y. J. Kim, “3-D constraint effects on J testing and crack tip constraint in M(T), SE(B), SE(T) and C(T) specimens: Numerical study,” *Eng. Fract. Mech.*, vol. 71, no. 9–10, pp. 1203–1218, 2004, doi: 10.1016/S0013-7944(03)00211-X.

[48] G. H. B. Donato and C. Ruggieri, “Estimation Procedures for J and CTOD Fracture Parameters Using Three-Point Bend Specimens.” pp. 149–157, Sep. 25, 2006, doi: 10.1115/IPC2006-10165.

[49] X. K. Zhu, B. N. Leis, and J. A. Joyce, “Experimental estimation of J-R curves from load-CMOD record for SE(B) specimens,” *J. ASTM Int.*, vol. 5, no. 5, pp. 1–15, 2008, doi: 10.1520/JAI101532.

[50] M. H. Sharobeam and J. D. Landes, “The load separation criterion and methodology in

ductile fracture mechanics," *Int. J. Fract.*, vol. 47, no. 2, pp. 81–104, 1991, doi: 10.1007/BF00032571.

[51] M. H. Sharobeam and J. D. Landes, "The load separation and ηpldevelopment in precracked specimen test recordsdevelopment in precracked specimen test records," *Int. J. Fract.*, vol. 59, no. 3, pp. 213–226, 1993, doi: 10.1007/BF02555184.

[52] J. A. Joyce, "Application of the key curve method to determining JR curves for A533B steel." Naval Academy, Annapolis, MD, 1980.

[53] K. H. Schwalbe *et al.*, "EFAM ETM 97 – the ETM method for assessing the significance of crack-like defects in engineering structures, comprising the versions ETM 97/1 and ETM 97/2." GKSS Research Center, Geesthacht, 1998.

[54] N. Gubeljak, M. D. Chapetti, J. Predan, and J. D. Landes, "CTOD-R curve construction from surface displacement measurements," *Eng. Fract. Mech.*, vol. 78, no. 11, pp. 2286–2297, 2011, doi: 10.1016/j.engfracmech.2011.05.002.

[55] J. Džugan and H. W. Viehrig, "Application of the normalization method for the determination of J-R curves," *Mater. Sci. Eng. A*, vol. 387–389, no. 1-2 SPEC. ISS., pp. 307–311, 2004, doi: 10.1016/j.msea.2004.01.067.

[56] X. K. Zhu, P. S. Lam, and Y. J. Chao, "Application of normalization method to fracture resistance testing for storage tank A285 carbon steel," *Int. J. Press. Vessel. Pip.*, vol. 86, no. 10, pp. 669–676, 2009, doi: 10.1016/j.ijpvp.2009.03.009.

[57] J. Tang, Z. Liu, S. Shi, and X. Chen, "Evaluation of fracture toughness in different regions of weld joints using unloading compliance and normalization method," *Eng. Fract. Mech.*, vol. 195, no. February, pp. 1–12, 2018, doi: 10.1016/j.engfracmech.2018.03.022.

[58] Y. J. Kim, J. S. Kim, K. H. Schwalbe, and Y. J. Kim, "Numerical investigation on J-integral testing of heterogeneous fracture toughness testing specimens: Part I - Weld metal cracks," *Fatigue Fract. Eng. Mater. Struct.*, vol. 26, no. 8, pp. 683–694, 2003, doi: 10.1046/j.1460-2695.2003.00676.x.

[59] C. Eripret and P. Hornet, "Fracture toughness testing procedures for strength mis-

matched structures," in *Mis-matching of interfaces and welds*, K. H. Schwalbe and M. Koçak, Eds. Geestchacht: GKSS Research Center, 1997.

[60] G. H. B. Donato, R. Magnabosco, and C. Ruggieri, "Effects of weld strength mismatch on J and CTOD estimation procedure for SE(B) specimens," *Int. J. Fract.*, vol. 159, no. 1, pp. 1–20, 2009, doi: 10.1007/s10704-009-9377-9.

[61] L. L. S. Mathias, D. F. B. Sarzosa, and C. Ruggieri, "Effects of specimen geometry and loading mode on crack growth resistance curves of a high-strength pipeline girth weld," *Int. J. Press. Vessel. Pip.*, vol. 111–112, pp. 106–119, 2013, doi: 10.1016/j.ijpvp.2013.06.003.

[62] U. Zerbst *et al.*, "Review on fracture and crack propagation in weldments - A fracture mechanics perspective," *Eng. Fract. Mech.*, vol. 132, pp. 200–276, 2014, doi: 10.1016/j.engfracmech.2014.05.012.

[63] U. Zerbst, "Application of fracture mechanics to welds with crack origin at the weld toe: a review Part 1: Consequences of inhomogeneous microstructure for materials testing and failure assessment," *Weld. World*, vol. 63, no. 6, pp. 1715–1732, 2019, doi: 10.1007/s40194-019-00801-5.

[64] R. Nikhil, S. A. Krishnan, G. Sasikala, B. S. Dutt, and A. Moitra, "Evaluation of Plastic 'Eta' Factor for Welds of SS316L(N) with High Strength Mismatch Ratio," *J. Mater. Eng. Perform.*, vol. 28, no. 1, pp. 79–86, 2019, doi: 10.1007/s11665-018-3811-y.

[65] N. Gubeljak, "Fracture behaviour of specimens with surface notch tip in the heat affected zone (HAZ) of strength mis-matched welded joints," *Int. J. Fract.*, vol. 100, no. 2, pp. 155–167, 1999, doi: 10.1023/A:1018794316336.

[66] O. Kolednik, "The yield stress gradient effect in inhomogeneous materials," *Int. J. Solids Struct.*, vol. 37, no. 5, pp. 781–808, 2000, doi: 10.1016/S0020-7683(99)00060-8.

[67] N. Gubeljak, O. Kolednik, J. Predan, and M. Oblak, "Effect of strength of mismatch interface on crack driving force," *Key Eng. Mater.*, vol. 251–252, pp. 235–243, 2003, doi: 10.4028/www.scientific.net/kem.251-252.235.

[68] J. Predan, N. Gubeljak, O. Kolednik, and F. D. Fischer, "The change of the local crack

driving force in an under-match welded joint,” *Adv. Fract. Mech. life Saf. assessments Proc. [Elektronski vir]*, p. 8 f., 2004.

[69] N. K. Simha, F. D. Fischer, O. Kolednik, J. Predan, and G. X. Shan, “Crack tip shielding or anti-shielding due to smooth and discontinuous material inhomogeneities,” *Int. J. Fract.*, vol. 135, no. 1–4, pp. 73–93, 2005, doi: 10.1007/s10704-005-3944-5.

[70] J. Predan, N. Gubeljak, and O. Kolednik, “On the local variation of the crack driving force in a double mismatched weld,” *Eng. Fract. Mech.*, vol. 74, no. 11, pp. 1739–1757, 2007, doi: 10.1016/j.engfracmech.2006.09.015.

[71] L. Starčevič, N. Gubeljak, and J. Predan, “The numerical modelling approach with a random distribution of mechanical properties for a mismatched weld,” *Materials (Basel).*, vol. 14, no. 19, 2021, doi: 10.3390/ma14195896.

[72] Acroni d.o.o., “High strength heavy plates.” Acroni, d.o.o., Jesenice, Slovenia, pp. 1–12, 2022, [Online]. Available: https://sij.acroni.si/assets/Uploads/High-strength-heavy-plates-Acroni.pdf.

[73] Elektrode Jesenice d.o.o., “Welding consumables.” Elektrode Jesenice d.o.o., Jesenice, Slovenia, 2022, [Online]. Available: https://sij.elektrode.si/assets/magazine-files/ElektrodWeldinConsumables.compressed.pdf.

[74] “ISO 15792-1 ‘Welding consumables - Test methods - Part 1: Test methods for all-weld metal test specimens in steel, nickel and nickel alloys.’” International Organization for Standardization, 2000.

[75] M. D. Arsić, D., V. Lazić, R. R. Nikolić, S. Aleksandrović, B. Hadzima, “Optimal welding technology of high strength steel S690QL,” *Mater. Eng. -Materialove Inz.*, vol. 22, no. 1, pp. 33–47, 2015.

[76] Certilas Nederland BV, “Cooling times (Delta T8/5) S355 till S960,” 2022. https://certilas.nl/en/content/cooling-times-delta-t85-s355-till-s960.

[77] C. Chen, S. P. Chiew, M. S. Zhao, C. K. Lee, and T. C. Fung, “Influence of cooling rate on tensile behaviour of S690Q high strength steel butt joint,” *J. Constr. Steel Res.*, vol. 173, p. 106258, 2020, doi: 10.1016/j.jcsr.2020.106258.

[78] "DIN EN 1011-2:2005 'Schweißen - Empfehlungen zum Schweißen metallischer Werkstoffe - Teil 2: Lichtbogenschweißen von ferritischen Stählen.'" Deutsches Institut für Normung, Berlin, 2001.

[79] S. Hertelé, W. De Waele, M. Verstraete, R. Denys, and N. O'Dowd, "J-integral analysis of heterogeneous mismatched girth welds in clamped single-edge notched tension specimens," *Int. J. Press. Vessel. Pip.*, vol. 119, pp. 95–107, 2014, doi: 10.1016/j.ijpvp.2014.03.006.

[80] M. Perović, S. Baloš, D. Kozak, D. Bajić, and T. Vuherer, "Utjecaj kinematičkih faktora zavarivanja trenjem miješanjem na karakteristike zavarenog spoja kovanih ploča od legure aluminija EN AW 7049 A," *Teh. Vjesn.*, vol. 24, no. 3, pp. 723–728, 2017, doi: 10.17559/TV-20160417122830.

[81] M. S. Zhao, C. K. Lee, T. C. Fung, and S. P. Chiew, "Impact of welding on the strength of high performance steel T-stub joints," *J. Constr. Steel Res.*, vol. 131, pp. 110–121, 2017, doi: 10.1016/j.jcsr.2016.12.023.

[82] "ASTM E384-17 'Standard Test Method for Microindentation Hardness of Materials.'" ASTM International, West Conshohocken, 2017.

[83] R. Pamnani, V. Karthik, T. Jayakumar, M. Vasudevan, and T. Sakthivel, "Evaluation of mechanical properties across micro alloyed HSLA steel weld joints using Automated Ball Indentation," *Mater. Sci. Eng. A*, vol. 651, pp. 214–223, 2016, doi: 10.1016/j.msea.2015.10.104.

[84] W. Guo, L. Li, S. Dong, D. Crowther, and A. Thompson, "Comparison of microstructure and mechanical properties of ultra-narrow gap laser and gas-metal-arc welded S960 high strength steel," *Opt. Lasers Eng.*, vol. 91, no. November 2016, pp. 1–15, 2017, doi: 10.1016/j.optlaseng.2016.11.011.

[85] E. L. Stevens, J. Toman, A. C. To, and M. Chmielus, "Variation of hardness, microstructure, and Laves phase distribution in direct laser deposited alloy 718 cuboids," *Mater. Des.*, vol. 119, pp. 188–198, 2017, doi: 10.1016/j.matdes.2017.01.031.

[86] A. R. H. Midawi, C. H. M. Simha, and A. P. Gerlich, "Assessment of yield strength

mismatch in X80 pipeline steel welds using instrumented indentation,” *Int. J. Press. Vessel. Pip.*, vol. 168, no. October, pp. 258–268, 2018, doi: 10.1016/j.ijpvp.2018.09.014.

[87] M. Tümer, F. G. Warchomicka, H. Pahr, and N. Enzinger, “Mechanical and microstructural characterization of solid wire undermatched multilayer welded S1100MC in different positions,” *J. Manuf. Process.*, vol. 73, no. November 2021, pp. 849–860, 2022, doi: 10.1016/j.jmapro.2021.11.021.

[88] S. Naib, P. Štefane, W. De Waele, N. Gubeljak, and S. Hertelé, “Calibration of Hardness Transfer Functions Based on Micro Tensile and All Weld Metal Tensile Tests of Heterogeneous Welds,” no. June, p. 468, 2018, doi: 10.3390/icem18-05372.

[89] R. Lacalle *et al.*, “Influence of the Flame Straightening Process on Microstructural, Mechanical and Fracture Properties of S235 JR, S460 ML and S690 QL Structural Steels,” *Exp. Mech.*, vol. 53, no. 6, pp. 893–909, 2013, doi: 10.1007/s11340-013-9723-8.

[90] K. Kumar *et al.*, “Use of miniature tensile specimen for measurement of mechanical properties,” *Procedia Eng.*, vol. 86, pp. 899–909, 2014, doi: 10.1016/j.proeng.2014.11.112.

[91] T. H. Hyde, W. Sun, and J. A. Williams, “Requirements for and use of miniature test specimens to provide mechanical and creep properties of materials: a review,” *Int. Mater. Rev.*, vol. 52, no. 4, pp. 213–255, 2007, doi: 10.1179/174328007x160317.

[92] M. Koçak, “Structural integrity of welded structures: Process - Property - Performance (3p) relationship,” *Proc. Int. Conf. Adv. Weld. Sci. Technol. Constr. Energy Transp. AWST 2010, held Conj. with 63rd Annu. Assem. IIW 2010*, no. December, 2010.

[93] S. Naib, W. De Waele, P. Štefane, N. Gubeljak, and S. Hertelé, “Crack driving force prediction in heterogeneous welds using Vickers hardness maps and hardness transfer functions,” *Eng. Fract. Mech.*, vol. 201, 2018, doi: 10.1016/j.engfracmech.2018.07.020.

[94] “ASTM E345-16 ‘Standard Test Methods of Tension Testing of Metallic Foil.’” ASTM International, West Conshohocken, 2016.

[95] “ASTM E8/E8M-13a ‘Standard Test Methods for Tension Testing of Metallic

Materials.'" ASTM International, West Conshohocken, 2013.

[96] GOM Metrology, "GOM metrology products - 3D Testing." https://www.gom.com/en/products/3d-testing.

[97] "ASTM E111-04 'Standard Test Method for Young's Modulus, Tangent Modulus, and Chord Modulus.'" ASTM International, West Conshohocken, 2004.

[98] "ASTM E646-07 'Standard Test Method for Tensile Strain-Hardening Exponents (n - Values) of Metallic Sheet Materials.'" ASTM International, West Conshohocken, 2007.

[99] J. R. Davis, Ed., *Tensile Testing*, 2nd editio. Materials park, Ohio: ASM International, 2004.

[100] W. Ramberg and W. R. Osgood, "Description of stress-strain curves by three parameters," *Natl. Advis. Comm. Aeronaut.*, p. Technical Note No. 902, 1943, [Online]. Available: http://hdl.handle.net/2060/19930081614.

[101] D. Kujawski, P. S. Patwardhan, and R. A. Nalavde, "An estimation of true Ramberg-Osgood curve parameters for materials with and without Luder's strain using yield and ultimate strengths," *Fatigue Fract. Eng. Mater. Struct.*, vol. 43, no. 9, pp. 2147–2156, 2020, doi: 10.1111/ffe.13248.

[102] Y. Bao, "Dependence of ductile crack formation in tensile tests on stress triaxiality, stress and strain ratios," *Eng. Fract. Mech.*, vol. 72, no. 4, pp. 505–522, 2005, doi: 10.1016/j.engfracmech.2004.04.012.

[103] N. E. Dowling, *Mechanical Behavior of Materials: Engineering Methods for Deformation, Fracture and Fatigue*, 4th Ed. Hralow: Pearson Education Limited, 2013.

[104] J. L. González-Velázquez, *Mechanical Behavior and Fracture of Engineering Materials*, 1st Ed. Cham: Springer Cham, 2020.

[105] B. Marandet and G. Sanz, "Evaluation of the Toughness of Thick Medium Strength Steels by LEFM and Correlations Between KIc and CVN," in *ASTM STP 631*, 1977, pp. 72–95.

[106] K. Wallin, M. Valo, R. Rintamaa, K. Törrönen, and R. Ahlstrand, “Descriptive characteristics of different types of test for irradiation embrittlement,” *Nucl. Eng. Des.*, vol. 159, no. 1, pp. 69–80, 1995, doi: 10.1016/0029-5493(95)01054-L.

[107] V. S. Barbosa, L. A. C. de Godois, K. E. Bianchi, and C. Ruggieri, “Charpy impact energy correlation with fracture toughness for low alloy structural steel welds,” *Theor. Appl. Fract. Mech.*, vol. 113, no. February, p. 102934, 2021, doi: 10.1016/j.tafmec.2021.102934.

[108] T. H. E. Influence, O. F. Testing, S. On, and T. H. E. Notch, “Testing Samples Size Effect,” vol. 48, no. 4, pp. 253–256, 2009.

[109] M. Dunđer, T. Vuherer, I. Samardžić, and D. Marić, “Analysis of heat-affected zone microstructures of steel P92 after welding and after post-weld heat treatment,” *Int. J. Adv. Manuf. Technol.*, vol. 102, no. 9, pp. 3801–3812, 2019, doi: https://doi.org/10.1007/s00170-019-03513-8.

[110] A. Ilić *et al.*, “Analysis of influence of thewelding procedure on impact toughness of welded joints of the high-strength low-alloyed steels,” *Appl. Sci.*, vol. 10, no. 7, 2020, doi: 10.3390/app10072205.

[111] “ASTM E23-16b ‘Standard Test Methods for Notched Bar Impact Testing of Metallic Materials.’” ASTM International, West Conshohocken, 2016.

[112] P. O. Marushchak, R. T. Bishchak, T. Vuherer, and E. Procedure, “for Continuous Casting of Blanks With Fused Layers,” vol. 48, no. 6, pp. 14–23, 2013.

[113] A. P. Sorochak, P. O. Maruschak, O. P. Yasniy, T. Vuherer, and S. V. Panin, “Evaluation of dynamic fracture toughness parameters of locomotive axle steel by instrumented Charpy impact test,” *Fatigue Fract. Eng. Mater. Struct.*, vol. 40, no. 4, pp. 512–522, 2017, doi: 10.1111/ffe.12510.

[114] “ISO 14556 ‘Steel - Charpy V-notch pendulum impact test - Instrumented test method.’” International Organization for Standardization, 2000.

[115] L. R. Botvina, V. M. Blinov, M. R. Tyutin, I. O. Bannykh, and E. V. Blinov, “Fracture of high-nitrogen 05Kh20G10N3AMF steel during impact loading,” *Russ. Metall.*, vol.

2012, no. 3, pp. 239–247, 2012, doi: 10.1134/S0036029512030044.

[116] "ASTM E2298-15 'Standard Test Method for Instrumented Impact Testing of Metallic Materials.'" ASTM International, West Conshohocken, 2015.

[117] T. Kobayashi, "On the information about fracture characteristics obtained from instrumented impact test of A533 steel for reactor pressure vessel," *Eng. Fract. Mech.*, vol. 19, no. 1, pp. 67–79, Jan. 1984, doi: 10.1016/0013-7944(84)90069-9.

[118] N. D. Alexopoulos, A. Stylianos, and J. Campbell, "Dynamic fracture toughness of Al-7Si-Mg (A357) aluminum alloy," *Mech. Mater.*, vol. 58, pp. 55–68, 2013, doi: 10.1016/j.mechmat.2012.11.005.

[119] W. Jia *et al.*, "Study on Intrinsic Influence Law of Specimen Size and Loading Speed on Charpy Impact Test," *Materials (Basel).*, vol. 15, no. 11, p. 3855, 2022, doi: 10.3390/ma15113855.

[120] Schaeffler Technical Documentation, *Schaeffler Technical Pocket Guide*, 3rd, revis ed. Herzogenaurach: Schaeffler Technologies AG & Co. KG, 2021.

[121] M. Toyoda and F. Minami, "Evaluation procedure of structural reliability of weldments based on CTOD results," *Proc. 8th Intn. Conf. Offshore Mech. Arct. Engng.*, vol. 3, pp. 717–724, 1989.

[122] M. G. Avalons and F. Keppens, "Master thesis: 'Deformation and fracture behavior of heterogeneous welds containing defects.'" Ghent Unniversity, Ghent, 2017.

[123] S. Naib, P. Štefane, W. De Waele, N. Gubeljak, and S. Hertelé, "Tearing resistance of heterogeneous welds in Single Edge notched Tensile (SE(T)) testing," *Eng. Fract. Mech.*, vol. 214, pp. 194–211, 2019, doi: 10.1016/j.engfracmech.2019.02.017.

[124] L. G. F. De Andrade and G. H. Bolognesi Donato, "Effects of crack tunneling and plasticity on the elastic unloading compliance technique for SE(B) - Current limitations and proposals," *Procedia Struct. Integr.*, vol. 13, pp. 1908–1914, 2018, doi: 10.1016/j.prostr.2018.12.271.

[125] J. Landes, Z. Zhou, K. Lee, and R. Herrera, "Normalization Method for Developing J-R

Curves with the LMN Function," *ournal Test. Eval. 19*, vol. 19, no. 4, pp. 305–311, 1991, doi: https://doi.org/10.1520/JTE12574J.

[126] T. L. Panontin and M. R. Hill, "The effect of residual stresses on brittle and ductile fracture initiation predicted by micromechanical models," *Int. J. Fract.*, vol. 82, no. 4, pp. 317–333, 1996, doi: 10.1007/bf00013236.

[127] W. G. Xu and F. M. Burdekin, "Effects of residual stresses on constraint and fracture behaviour of wide plates," *Proc. R. Soc. A Math. Phys. Eng. Sci.*, vol. 454, no. 1977, pp. 2505–2528, 1998, doi: 10.1098/rspa.1998.0268.

[128] J. Liu, Z. L. Zhang, and B. Nyhus, "Residual stress induced crack tip constraint," *Eng. Fract. Mech.*, vol. 75, no. 14, pp. 4151–4166, 2008, doi: 10.1016/j.engfracmech.2008.03.010.

[129] X. B. Ren, Z. L. Zhang, and B. Nyhus, "Effect of residual stresses on the crack-tip constraint in a modified boundary layer model," *Int. J. Solids Struct.*, vol. 46, no. 13, pp. 2629–2641, 2009, doi: 10.1016/j.ijsolstr.2009.02.009.

[130] N. Gubeljak, M. Koçak, and I. Rak, "Assessment of fatigue precracking methods for fracture toughness testing of Q+T weldments," *ECF 11 Mech. Mech. Damage Fail. Proc. 11th Bienn. Eur. Confernece Fract.*, 1996.

[131] K. H. Schwalbe, J. Heerens, U. Zerbst, H. Pisarski, and M. Koçak, "EFAM GTP 02 - the GKSS test procedure for determining the fracture behaviour of materials." GKSS Research Center, Geesthacht, 2002.

[132] P. Dong and J. Zhang, "Residual stresses in strength-mismatched welds and implications on fracture behavior," *Eng. Fract. Mech.*, vol. 64, no. 4, pp. 485–505, 1999, doi: 10.1016/S0013-7944(99)00088-0.

[133] K. H. Schwalbe, J. D. Landes, and J. Heerens, "Classical Fracture Mechanics Methods," in *Comprehensive Structural Integrity, Online Update Fracture of Materials from Nano to Macro*, R. O. Milne and B. K. Ritchie, Eds. Oxford: Elsevier, 2007, pp. 3–42.

[134] E. Kreyszig, *Advanced Engineering Mathematics*, 9th Ed. New York: John Wiley & Sons, Inc., 2006.

[135] J. K. Pieterse and J. W. Lewis, “Fitting curves to your data using least squares,” 2022. https://jkp-ads.com/articles/leastsquares.asp.

[136] G. H. B. Donato and C. Ruggieri, “Estimation Procedures for J and CTOD Fracture Parameters Using Three-Point Bend Specimens,” *6th Int. Pipeline Conf.*, pp. 1–9, 2006, [Online]. Available: http://proceedings.asmedigitalcollection.asme.org/proceeding.aspx?articleid=1597148.

[137] S. Kumar, A. Kumar, P. K. Singh, and J. Chattopadhyay, “Plastic eta factor and blunting line for characterization of fracture toughness of dissimilar metal weld,” *Fatigue Fract. Eng. Mater. Struct.*, vol. 42, no. 5, pp. 1191–1202, 2019, doi: 10.1111/ffe.12985.

[138] S. Lindqvist and J. Kuutti, “Dependence between η -factor and crack location relative to a fusion boundary between hard and soft materials in a SE(B) specimen,” *Int. J. Fract.*, vol. 211, no. 1–2, pp. 281–293, 2018, doi: 10.1007/s10704-018-0288-5.

[139] G. H. B. Donato, “Effects of side-grooves and 3-D geometries on compliance solutions and crack size estimations applicable to C(T), SE(B) and clamped SE(T) specimens,” *Proc. ASME 2013 Press. Vessel. Pip. Conf. PVP2013*, pp. 1–10, 2013.

[140] R. G. Savioli and C. Ruggieri, “J and CTOD estimation formulas for C(T) fracture specimens including effects of weld strength overmatch,” *Int. J. Fract.*, vol. 179, no. 1–2, pp. 109–127, 2013, doi: 10.1007/s10704-012-9781-4.

[141] S. Hertelé, N. O’Dowd, K. Van Minnebruggen, M. Verstraete, and W. De Waele, “Fracture Mechanics Analysis of Heterogeneous Welds: Validation of a Weld Homogenisation Approach,” *Procedia Mater. Sci.*, vol. 3, no. 0, pp. 1322–1329, 2014, doi: 10.1016/j.mspro.2014.06.214.

[142] R. F. Souza, C. Ruggieri, and Z. Zhang, “A framework for fracture assessments of dissimilar girth welds in offshore pipelines under bending,” *Eng. Fract. Mech.*, vol. 163, pp. 66–88, 2016, doi: 10.1016/j.engfracmech.2016.06.011.

[143] M. Kuna, *Finite Elements in Fracture Mechanics*, vol. 201. Dordrecht: Springer Netherlands, 2013.

[144] Dassault Systemes, “Abaqus Analysis User Manual.” Dassault Systemes, Vélizy-

Villacoublay, France, 2018.

[145] Dassault Systemes, *Modeling Fracture and Failure with Abaqus*. Vélizy-Villacoublay, France: Dassault Systemes, 2012.

[146] J. R. Rice, “Limitations to the small scale yielding approximation for crack tip plasticity,” *J. Mech. Phys. Solids*, vol. 22, no. 1, pp. 17–26, 1974, doi: 10.1016/0022-5096(74)90010-6.

[147] M. C. Burstow, I. C. Howard, and R. A. Ainsworth, “The effects of material strength mismatching on constraint at the limit load of welded three-point bend specimens,” *Int. J. Fract.*, vol. 89, no. 2, pp. 117–142, 1998, doi: 10.1023/A:1007480827982.

[148] M. C. Burstow, I. C. Howard, and R. A. Ainsworth, “The influence of constraint on crack tip stress fields in strength mismatched welded joints,” *J. Mech. Phys. Solids*, vol. 46, no. 5, pp. 845–872, 1998, doi: 10.1016/S0022-5096(97)00098-7.

[149] M. C. Burstow and I. C. Howard, “Damage mechanics models of ductile crack growth in welded specimens,” *Fatigue Fract. Eng. Mater. Struct.*, vol. 23, no. 8, pp. 691–708, 2000, doi: 10.1046/j.1460-2695.2000.00317.x.

[150] Z. Liu, X. Wang, J. Tang, C. Deng, H. Zhao, and X. Chen, “The effects of in-plane and out-of-plane constraints on J-R curves for X80 steel: A study using clamped SENT specimens,” *Eng. Fract. Mech.*, vol. 206, no. December 2018, pp. 342–358, 2019, doi: 10.1016/j.engfracmech.2018.12.004.

[151] B. Younise, M. Rakin, N. Gubeljak, B. Medjo, and A. Sedmak, “Effect of material heterogeneity and constraint conditions on ductile fracture resistance of welded joint zones - Micromechanical assessment,” *Eng. Fail. Anal.*, vol. 82, no. August, pp. 435–445, 2017, doi: 10.1016/j.engfailanal.2017.08.006.

[152] B. S. Henry and A. R. Luxmoore, “The stress triaxiality constraint and the Q-value as a ductile fracture parameter,” *Eng. Fract. Mech.*, vol. 57, no. 4, pp. 375–390, 2002, doi: 10.1016/s0013-7944(97)00031-3.

[153] K. Van Minnebruggen, S. Hertelé, M. A. Verstraete, W. De Waele, and R. M. Denys, “Constraint analysis of defects in strength mismatched girth welds of (pressurized) pipe

and Curved Wide Plate tensile test specimens," *Eng. Fract. Mech.*, vol. 131, pp. 128–141, 2014, doi: 10.1016/j.engfracmech.2014.07.018.

[154] N. P. O'Dowd and C. F. Shih, "Family of crack-tip fields characterized by a triaxiality parameter-I. Structure of fields," *J. Mech. Phys. Solids*, vol. 39, no. 8, pp. 989–1015, 1991, doi: 10.1016/0022-5096(91)90049-T.

[155] H. Zhou, F. Biglari, C. M. Davies, A. Mehmanparast, and K. M. Nikbin, "Evaluation of fracture mechanics parameters for a range of weldment geometries with different mismatch ratios," *Eng. Fract. Mech.*, vol. 124–125, pp. 30–51, 2014, doi: 10.1016/j.engfracmech.2014.03.006.

[156] J. M. Koo, Y. Huh, and C. S. Seok, "Influence of the strength mismatch of a narrow gap welded joint of SA508 on the plastic η factor," *J. Mater. Eng. Perform.*, vol. 21, no. 11, pp. 2451–2459, 2012, doi: 10.1007/s11665-012-0187-2.

Primož Štefane, mag. inž. str | Curriculum Vitae

Education

Doctoral study programme – University of Maribor, Faculty of Mechanical Engineering Oct. 2014 - current

Master study programme – University of Maribor, Faculty of Mechanical Engineering Oct. 2012 – Sep. 2014
Title of master thesis: *Fracture behaviour of structural steel in temperature transition region*

Academic study programme – University of Maribor, Faculty of Mechanical Engineering Oct. 2009 – Sep. 2012
Title of bachelor thesis: *Determination of test's load cases for axle pin of wind turbine*

Work Experience

Simulations engineer – Rimac Technology (Croatia) Apr. 2022 - current

University research and teaching assistant – University of Maribor, Faculty of Mechanical Engineering (Slovenia) Nov. 2014 – Mar. 2022

Mechanical design engineer – University of Maribor, Faculty of Mechanical Engineering, Laboratory of Machine Parts and Structures (Slovenia) Mar. 2014 – Aug. 2014

Mechanical design engineer – EMO Orodjarna d.o.o. (Slovenia) Apr. 2012 – May. 2012

Mechanical engineer – Kostroj Strojegradnja d.o.o. (Slovenia) 2011 – 2014 (12 months altogether)

Experiences abroad

Visiting researcher – University of Ghent, SOETE Laboratory (Belgium) June 2017
Fracture testing of heterogeneous welds in low constraint conditions

Certificates

Cambridge English C1 Advanced – Score 195 Issued Aug. 2021, No expiration date
Credential ID: 954194CUY 6878

Important publications

P. Štefane, S. Naib, S. Hertelé, W. de Waele, N. Gubeljak, "Crack tip constraint analysis in welded joints with pronounced strength and toughness heterogeneity," *Theoretical and Applied Fracture Mechanics*, vol. 103, pp. 1-13, 2019.

P. Štefane, S. Hertelé, S. Naib, W. de WAELE, N. Gubeljak, "Effects of fixture configurations and weld strength mismatch on J-integral calculation procedure for SE(B) specimens," *Materials*, vol. 15, no. 3, pp. 1-24, 2022

Univerza v Mariboru

Fakulteta za strojništvo

(ime članice UM)

IZJAVA O AVTORSTVU IN ISTOVETNOSTI TISKANE IN ELEKTRONSKE OBLIKE DOKTORSKE DISERTACIJE

Ime in priimek študenta/-ke: Primož Štefane

Študijski program: STROJNIŠTVO

Naslov doktorske disertacije: Application of normalization method to fracture toughness testing of welds with pronounced strength heterogeneity

Mentor/-ica: Nenad Gubeljak

Somentor/-ica: Stijn Hertelé

Podpisani/-a študent/-ka Primož Štefane

- izjavljam, da je zaključno delo rezultat mojega znanstvenoraziskovalnega dela;
- izjavljam, da sem pridobil/-a vsa potrebna soglasja za uporabo podatkov in avtorskih del v zaključnem delu in jih v zaključnem delu jasno in ustrezno označil/-a;
- na Univerzo v Mariboru neodplačno, neizključno, prostorsko in časovno neomejeno prenašam pravico shranitve avtorskega dela v elektronski obliki, pravico reproduciranja ter pravico ponuditi zaključno delo javnosti na svetovnem spletu preko DKUM in drugih informacijskih zbirk in ponudnikov; sem seznanjen/-a, da bodo dela, deponirana/objavljena v DKUM, dostopna široki javnosti pod pogoji licence **Creative Commons BY-NC-ND**, kar vključuje tudi avtomatizirano indeksiranje preko spleta in obdelavo besedil za potrebe tekstovnega in podatkovnega rudarjenja in ekstrakcije znanja iz vsebin; uporabnikom se dovoli reproduciranje brez predelave avtorskega dela, distribuiranje, dajanje v najem in priobčitev javnosti samega izvirnega avtorskega dela, in sicer pod pogojem, da navedejo avtorja in da ne gre za komercialno uporabo;
- dovoljujem objavo svojih osebnih podatkov, vezanih na zaključek študija (ime, priimek, leto zaključka študija, naslov zaključnega dela) na spletnih straneh Univerze v Mariboru in v publikacijah Univerze v Mariboru;
- izjavljam, da je tiskana oblika zaključnega dela istovetna elektronski obliki zaključnega dela, ki sem jo oddal/-a za objavo v DKUM;
- izjavljam, da sem seznanjen s pogoji Proquesta za oddajo in javno objavo doktorske disertacije v podatkovno zbirko ProQuest Dissertations & Theses Global (http://contentz.mkt5049.com/lp/43888/382619/PQDTauthoragreement.pdf).

Uveljavljam permisivnejšo obliko licence Creative Commons: CC BY-ND 4.0

(*navedite obliko*)

Kraj in datum:

Maribor, 13.09.2022

Podpis študenta/-ke: